OPTICAL IMAGING OF CARDIAC ATRIAL ACTIVATION AND REPOLARISATION IN GENETICALLY ALTERED MODELS

By

Ting Yue Yu

A thesis submitted to
The University of Birmingham
for the degree of
DOCTOR OF PHILOSOPHY

Physical Sciences of Imaging in the Biomedical Sciences
School of Chemistry
College of Engineering and Physical Sciences
The University of Birmingham
September 2015

Abstract

A method for developing an optical mapping system to quantify electrical activation and repolarisation in murine left atria was created. The spread of activation is important in understanding the mechanisms for the rhythm of the heart in healthy and diseased states as cardiovascular disease is the leading cause of death worldwide.

The activation spread was recorded using a novel 2nd generation high resolution (128x2048 pixels) CMOS camera with the voltage sensitive dye di-4-ANEPPS. Algorithms for automatic quantification of action potential duration and conduction velocities were implemented in MATLAB. Optical mapping results were validated against monophasic action potentials and microelectrode measurements showing comparable duration measurements.

A genetic mouse model of atrial fibrillation was used (Pitx2c$^{+/-}$) and was found to have a shorter action potential duration in the left atrium compared to wild-type mice. The results showed a preferential antiarrhythmic effect of the sodium channel blocker, flecainide, to the left atrium of Pitx2c$^{+/-}$ mice.

A second mouse model was used to mimic arrhythmogenic right ventricular cardiomyopathy (plako$^{+/-}$). No significant changes were witnessed in young sedentary cohorts at baseline and flecainide slowed conduction in both WT and plako$^{+/-}$. In endurance trained mice, a prolongation of the effective refractory period was seen after flecainide treatment. Plako$^{+/-}$ sedentary mice treated with dihydrotestosterone showed a prolongation in action potential duration.

Declaration

I hereby declare that the work presented here in this thesis titled, “Optical Imaging of Cardiac Atrial Activation and Repolarisation in Genetically Altered Models” is the work of my own, unless otherwise stated. The work here was written and submitted by me to the School of Chemistry, University of Birmingham, United Kingdom as fulfilment of the degree of Doctor of Philosophy.

I further declare that this work has not been submitted to any other university for the award of any other degree, diploma or equivalent course.

TING YUE YU

ID: 0803108

Acknowledgements

First and foremost, I would like to take this opportunity to thank my supervisors Dr Larissa Fabritz and Dr Hamid Dehghani but also Professor Paulus Kirchhof. It is with their knowledge and tutelage I can call myself a scientist. I also thank all the members of the PSIBS doctoral training centre, for their support in and out of my studies. In addition, thank you to Fahima Syeda who has helped me since I started in the lab, and for imparting me with her wisdom.

I would also like to thank Birmingham University Lacrosse Club, for showing me a life outside the lab and for all the truly incredible memories. Thank you to Victoria Salisbury, for being a great friend and for listening to all my worries. Many thanks to Natalie Poulter for all the hugs. Special thanks to Eric Pitkeathly for all those years we lived together, without him I wouldn't be the person I am today, we have come a long way since being undergraduates.

Finally, I thank my family. No words can ever express my gratitude.

Dedication

To my loving grandparents - a lifetime of sacrifice.

Project outcomes

The outcomes of this thesis were as follows

Publications

Published in peer review

- A regional reduction in I_{to} and I_{KACh} in the murine posterior left atrial myocardium is associated with action potential prolongation and increased ectopic activity. A. P. Holmes*, **T. Y. Yu***, S .Tull, F. Syeda, S. M. Kuhlmann, S. M. O'Brien, P. Patel, K. L. Brain, D. Pavlovic, N. A. Brown, L. Fabritz, P. Kirchhof. *PLOS ONE. Vol 11, issue 5, pp 1-17.* 2016.
- Optical mapping design for murine atrial electrophysiology. **T.Y. Yu,** H. Dehghani, K.L. Brain, F. Syeda, A.P. Holmes, P. Kirchhof, L. Fabritz. *Computer methods in biomechanics and biomedical engineering: Imaging & Visualization.* Vol 1163, special issue, pp 1-9. 2015.
- An automated system using spatial oversampling for optical mapping in murine atria. Development and validation with monophasic and transmembrane action potentials. **T.Y. Yu,** F. Syeda, A.P. Holmes, B. Osborne, H. Dehghani, K.L. Brain, P. Kirchhof, L. Fabritz. *Progress in Biophysics and Molecular Biology.* Vol 115, issue 2-3, pp 340-8. 2014
- Can preload-reducing therapy prevent disease progression in arrhythmogenic right ventricular cardiomyopathy? Experimental evidence and concept for a clinical trial. L. Fabritz, L. Fortmuller, **T.Y. Yu**, M. Paul, P, Kirchhof*. Progress in Biophysics and Molecular Biology.* Vol. 110, issue 2-3, pp 340-6. 2012.

In review

- PITX2 modulates atrial membrane potential and reduced PITX2 potentiates the antiarrhythmic effects of sodium-channel blockers. F. Syeda, A. P.

Holmes, **T. Y. Yu**, S. Tull, S. M. Kuhlmann, D. Pavlovic , D. Betney, G. Riley, J. P. Kucera, F. Jousset, J. de Groot, S. Rohr, N. Brown, L. Fabritz, P. Kirchhof. Reviewed by the *Journal of the American College of Cardiology*. 2015.

Conference proceedings and posters

- New Optical Mapping Design and Automated Algorithms for Cardiac Electrophysiology. *Medical Image Understanding and Analysis (MIUA),* City University, London, UK. pp 265-270. 9th -11th July 2014
- Advancing Optical Imaging of Electrical Activation of the Heart Using Mutant Murine Models. *Inter-disciplinary inter-doctoral training centre (ID2)*, Oxford, UK. 26th - 27th June 2014.
- Advancement of optical mapping through automated algorithms and second generation CMOS detectors to reveal murine atrial activation patterns and regional variation of action potential duration. *British Cardiovascular Society,* Manchester, UK. 2nd - 3rd June 2014.
- Pitx2c deficiency modulates the effect of flecainide, atrial conduction, refractoriness and arrhythmia inducibility. *American Heart Association,* Chicago, USA. 15th - 19th November 2014.
- Optical Mapping of the Heart for Cardiovascular Diseases. *Inter-disciplinary inter-doctoral training centre (ID2)*, Birmingham, UK. 24th - 25th June 2015.

Prizes

- New Optical Mapping Design and Automated Algorithms for Cardiac Electrophysiology. *Medical Image Understanding and Analysis,* City University, London, UK, 2014. For best research poster.
- Optical Mapping of the Heart for Cardiovascular Diseases. *Inter-disciplinary inter-doctoral training centre (ID2)*, Birmingham, UK, 2015. For best research poster.

Contents

Figures

List of abbreviations

AAD	Antiarrhythmic drug
AAS	Androgenic anabolic steroids
AF	Atrial fibrillation
ANEP	Amino-Naphthyl-Ethenyl-Pyridinium
ANOVA	Analysis of variance
AoV	Aortic valve
AP	Action potential
APD	Action potential duration
APD30	Action potential duration at 30% repolarisation
APD50	Action potential duration at 50% repolarisation
APD70	Action potential duration at 70% repolarisation
ARVC	Arrhythmogenic right ventricular cardiomyopathy
AV node	Atrioventricular node
bpm	Beats per minute
Ca^{2+}	Calcium ion
CCD	Charged coupled device
CHD	Coronary heart disease
CMOS	Complementary metal-oxide semiconductor
CL	Cycle length
CV	Conduction velocity
CVD	Cardiovascular disease

ΔF/F	Fractional change in fluorescence
Di-4-ANEPPS	Di-4-amino-naphthyl-ethylene-pyridinium-propyl-sulfonate
DHT	Dihydrotestosterone
DNA	Deoxyribonucleic acid
E	Electric field
ECF	Extracellular fluid
ECG	Electrocardiogram
ERP	Effective refractory period
Flec	Flecainide
fr	Frame rate
HEK	Human embryonic kidney
hERG	human ether-a-go-go related gene
Hg	Mercury
ICF	Intracellular fluid
I_{Kr}	Potassium rectifier current (rapid)
I_{Ks}	Potassium rectifier current (slow)
$I_{K,slow}$	Slowly inactivating potassium current
I_{to}	Transient outward potassium current
K^+	Potassium ion
KHB	Krebs-Henseleit buffer
kHz	Kilohertz
K_VLQT	Potassium channel protein

K_V	Voltage-gated potassium channel
LA	Left atrium
LAA	Left atrial appendage
LA-PV	Left atrial pulmonary vein
LED	Light emitting diode
LV	Left ventricle
MAP	Monophasic action potential
mRNA	Messenger ribonucleic acid
mV	Millivolt
MV	Mitral valve
Na^+	Sodium ion
NA	Numerical aperture
$Na_V1.5$	Voltage-gated sodium channel subunit 1.5
OAP	Optical action potential
PDA	Photodiode array
Pitx2	Paired like homeodomain transcription factor 2
Plako	Plakoglobin
PV	Pulmonary valve
QE	Quantum efficiency
QRS	QRS complex of an electrocardiogram
RA	Right atrium
RAA	Right atrial appendage

RH	Rina Hildesheim
RNA	Ribonucleic acid
ROI	Region of interest
RV	Right ventricle
SA node	Sinoatrial node
S1	Train of 8 stimuli
S2	Early 9th stimulus
Sed	Sedentary
SEM	Standard error of the mean
SG	Savitzky-Golay
SNP	Single nucleotide polymorphism
SNR	Signal to noise ratio
TAP	Transmembrane action potential
TIFF	Tagged image file format
TH	Tungsten Halogen
TMP	Transmembrane potential
TV	Tricuspid valve
Vm	Membrane voltage
WT	Wild-type
Xe	Xenon

Project aims and objectives

The aims of this thesis were to:

- Develop a high resolution optical mapping system to measure the action potential duration (APD) and conduction velocity (CV) of the left atrium (LA) of the mouse.
- Develop novel automated software to analyse the images created by the optical mapping system.
- Investigate the Pitx2c deficient mouse model and its role in atrial fibrillation by use of the optical mapping system and measuring APD and CV differences in the LA.
- Test whether flecainide, an antiarrhythmic drug, has a preferential effect on the LA of the Pitx2c$^{+/-}$ model compared to wild-type.
- Investigate atria of a plakoglobin deficient mouse, a model of arrhythmogenic right ventricular cardiomyopathy (ARVC), by measuring CV values and APD between genotypes.
- Ascertain whether flecainide has a preferential effect to the plako$^{+/-}$ model.
- Determine whether endurance training can exacerbate an ARVC phenotype in the atria of the plako$^{+/-}$ model.
- Investigate whether flecainide shows a preferential effect on the endurance trained plako$^{+/-}$ model of the LA.
- Test the effects of anabolic androgen steroid doping by administering dihydrotestosterone to the plako$^{+/-}$ model and measuring the APD and CV values.

1. Biological introduction

This introduction provides a broad overview of the heart and cardiovascular disease.

1.1. The heart

The heart is a muscular organ which pumps blood around the body of humans and other animals via a system of vessels. The blood provides the body with oxygen and vital nutrients to sustain life [1]. The heart performs a cycle of relaxation and contraction in a single beat and must remain to do so for the remainder of one's life, undergoing an estimated 3 billion beats in a lifetime [2].

1.1.1. Anatomy and blood flow

The heart is a single organ but acts as a double pump, one to circulate deoxygenated blood to the lungs where it is oxygenated and the other to deliver oxygenated blood to the rest of body. In humans and other mammals such as mice, the heart is divided into four chambers; left and right atria which sit towards the top of the organ and the left and right ventricles at the bottom. Between the atria and ventricles are valves which help regulate the direction of blood flow [3]. The right atrium (RA) receives deoxygenated blood from the superior and inferior venae cavae where it is pumped to the right ventricle (RV) through the tricuspid valve (TV) (see Figure 1.1). Subsequently, the RV pumps blood through the pulmonary valve (PV) to the pulmonary artery then onto the lungs. The left atrium (LA) contracts and circulates oxygenated blood from the lungs to the left ventricle (LV) via the mitral valve. Contraction of the LA subsequently pumps blood through

the aortic valve to the aorta to the rest of the body [4]. Collectively, these atrial and ventricular events form the cardiac cycle. When the heart is in the contracting phase of the cardiac cycle, this is known as systole. Diastole is the part of the cardiac cycle when the heart is relaxing and refills with blood [3].

The ventricles are much thicker and stronger than the atria and the LV is stronger than the RV. This corresponds to the greater forces needed by the LV to pump blood through the high pressure system of the body. The atrial walls are thinner than the ventricular walls, as they only need to pump blood to the ventricles.

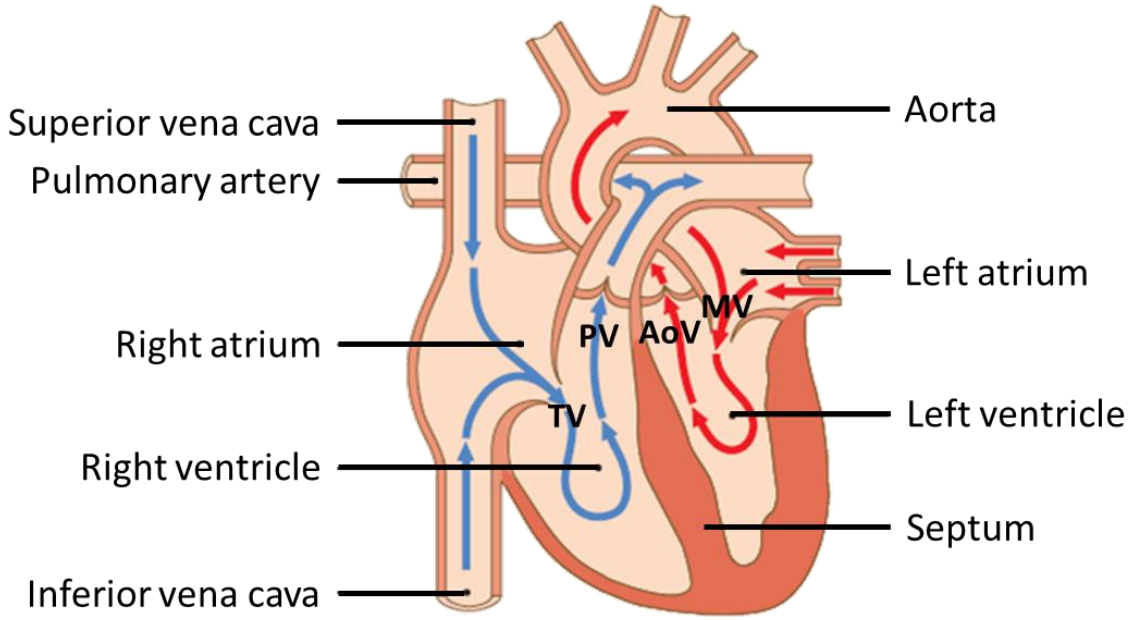

Figure 1.1. Anatomy and direction of blood flow through the heart.

The blue arrows show deoxygenated blood circulating from the superior and inferior venae cavae to the right atrium and ventricles, which leaves via the pulmonary artery to the lungs. Red arrows show oxygenated blood circulating from the left atrium to the left ventricle exiting via the aorta to the rest of the body. The direction of blood flow is regulated by four valves; tricuspid valve (TV), pulmonary valve (PV), aortic valve (AoV) and the mitral valve (MV). These valves prevent the backflow of blood. Image adapted from *Davidson's Principles and Practice of medicine 22nd Edition. Elsevier. 2014.* [4].

Cardiac output is the volume of blood pumped by the heart per unit time and is calculated by the product of the stroke volume and heart rate, usually measured in litres/min. The stroke volume is the volume of blood ejected in each cardiac cycle and is dependent upon the end-diastolic volume (preload) of the ventricles, contractility and systolic aortic pressure (afterload) [1].

1.1.2. Cardiac muscle

The heart wall consists of multiple layers: the inner endocardium, the myocardium and the outer epicardium. In addition to this, the pericardium is a double-walled sac that surrounds the heart. The endocardium is a thin sheet of cells that line the internal walls of the heart and valve. The part of the pericardium that forms the outer-most border is called the parietal pericardium. The inner layer which is in contact with the myocardium is called the epicardium and contains a small amount of fluid to lubricate its movements against the pericardium [5]. The myocardium is the bulk tissue of the heart, the layer which performs the contractions. The myocardial tissue is mainly comprised of cardiomyocytes and a small portion of cardiac pacemaker cells and the conduction system of the heart.

Cardiomyocytes are striated muscle cells which have the ability to contract easily. These striations arise from the arrangement of protein filaments (actin and myosin). The cardiomyocytes are connected by junctions known as intercalated disks which allow for synchronised contraction of the muscle (Figure 1.2A). An intercalated disk allows electrical conduction via gap junctions, mechanical conduction via fascia adherens (adherent proteins) [4]. Within the cardiomyocytes are myofibrils - rod like units made from thick myosin and thin actin filaments (Figure 1.2B) [4]. Actin filaments are the major component of the I-band region

which is bisected by the Z-lines. Myosin filaments extend throughout the A-band region where they are cross linked at the centre by the M-line.

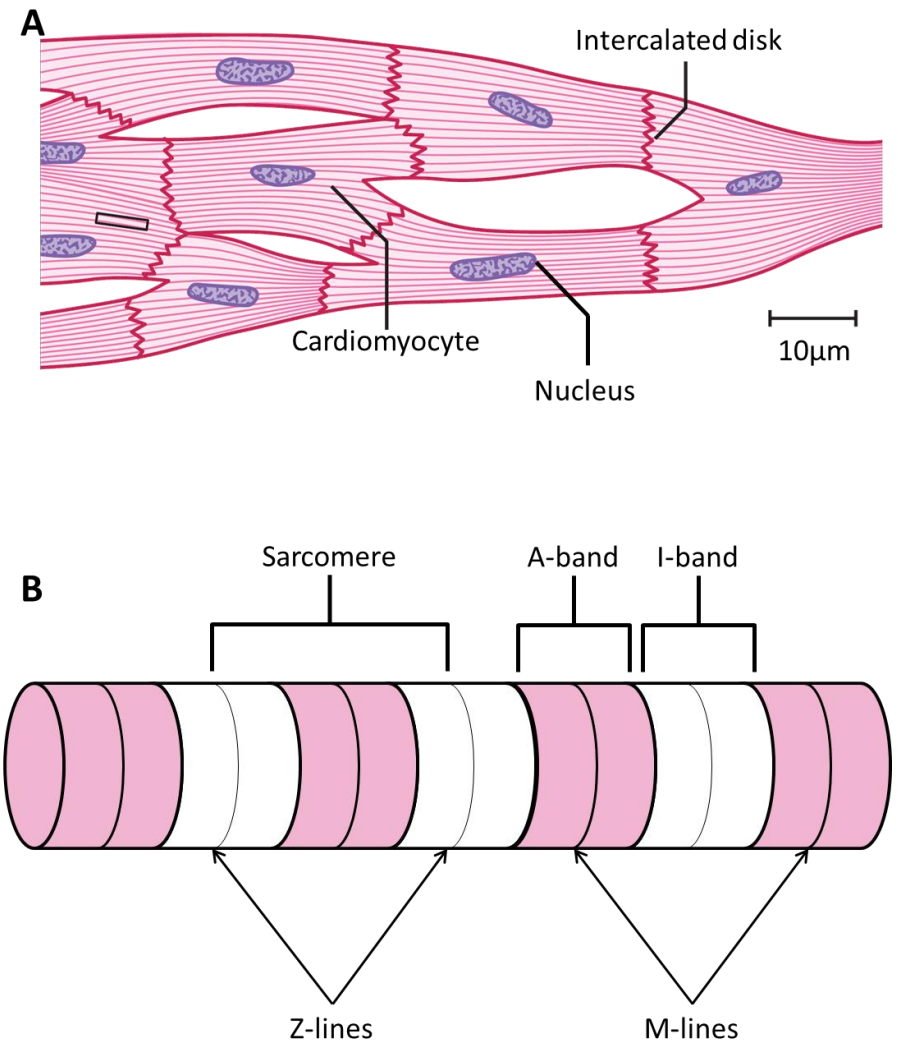

Figure 1.2. Schematic of cardiac muscle fibres and myofibril.

A) Shows a muscle fibre made from series of cardiomyocytes that are joined through intercalated disks. B) Represents the expanded region, which shows a myofibril section. Myofibrils are constructed of repeating sarcomeres within cardiomyocytes. Each sarcomere is defined as the structures bound between the Z-lines which lie within the I-band region. The main component of the I-band regions are actin filaments. The A-band comprises of thick myosin filaments which are crosslinked at the centre by the M-line. Image A) is adapted from *Davidson's Principles and Practice of medicine 22nd Edition. Elsevier. 2014*. [4]. *Image B) was created by the author of this thesis*.

1.1.3. Electrical conduction system of the heart

The heart beats in an orderly fashion to circulate blood throughout the body. This normal rhythmic activity is called sinus rhythm and consists on average of 65 to 100 beats per minute (bpm) [1], [4]. The contractions of the atria and ventricles are regulated by the transmission of electrical impulses which travel through a network of pacemaker cells and the conductions system [6], as shown in Figure 1.3. The sinoatrial (SA) node is responsible for the sinus rhythm of the heart. Situated in the RA of the heart, it can be thought of as the natural pacemaker. The SA node generates the electrical impulse that initiates contraction, which first excites the RA then the LA by travelling through Bachmann's bundle. The impulse travels through internodal pathways in the RA to the atrioventricular node. Subsequently, the impulse travels through the bundle of His where is divides into the left and right bundle branch located in the septum between the ventricles. The left and right bundle branches excite the LV and RV, respectively. Both bundle branches terminate in Purkinje fibres, where they spread throughout the myocardium in the ventricles [7]. The rate at which the impulse travels through the tissue of the heart is known as the conduction velocity (CV).

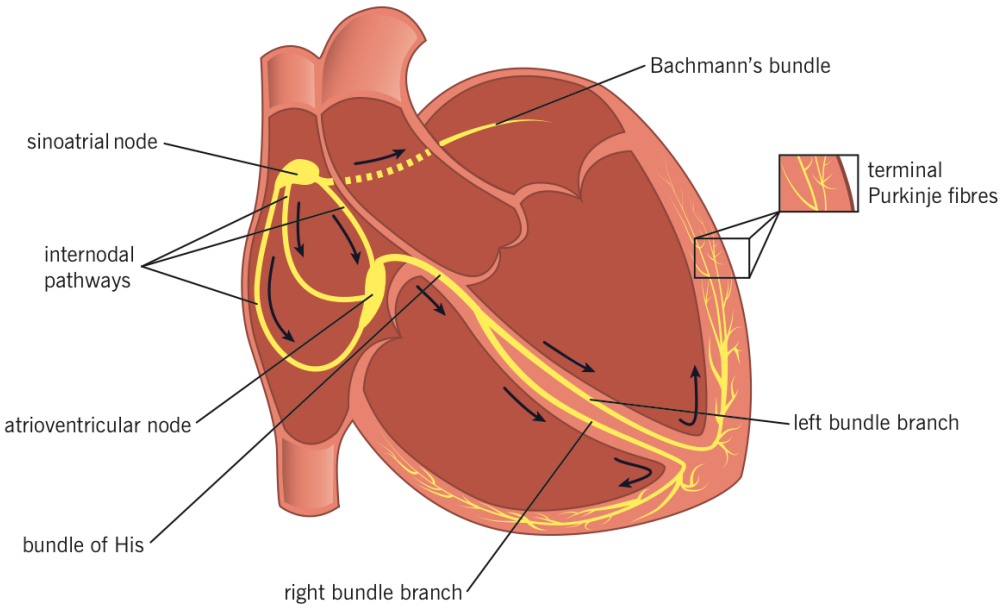

Figure 1.3. The cardiac electrical conduction system.

This illustrates the transmission of the electrical impulses through the heart. The impulse is initiated by the sinoatrial node in the right atrium where it travels to the atrioventricular node via internodal pathways. In addition to this, a pathway called Bachmann's bundle conducts the impulse to the right atrium from the left atrium. From the atrioventricular node, the impulse reaches the Bundle of his whereby it is divided to the left and right bundle branches. Finally, the impulse terminates in the Purkinje system where it spreads throughout the myocardium in the ventricles. Image extracted from *McMaster Physiology Review*. Retrieved from:

http://www.pathophys.org/physiology-of-cardiac-conduction-and-contractility/heart-conduction-colour/

1.1.4. Ion channels

Ion channels are proteins that form a pore on the cell membrane, their functions include the gating of the flow of ions across the interior and exterior of the cell [8]. Governing the flow of ions controls the electrical properties of the cell. The transmembrane potential (TMP) is the electrical potential difference between the intracellular (ICF) and extracellular (ECF) fluid of the cell. A cardiac ion channel is selective; it is only permeable to a single type of ion. Some channels are voltage-

gated; a specific TMP range is necessary for the channel to be open, outside of this range, it becomes impermeable to ions. Different types of voltage-gated ion channels have a particular ion selectivity and a particular voltage dependence [9]. There is also time dependence for some cardiac ion channels. Time dependent channels are configured to close a fraction of a second after opening and cannot be re-opened until the TMP returns to resting levels [9]. The different types of channels are a result of their protein structure which is encoded by specific genes. The key channels in the cardiomyocyte are (Figure 1.4): the potassium (K^+) channels which mediate the outflow of K^+ ions, sodium (Na^+) and calcium (Ca^{2+}) channels regulating the inflow of Na^+ and Ca^{2+} ions, the Na^+/Ca^{2+} exchanger which transports 3 Na^+ ions each Ca^{2+} ion [2].

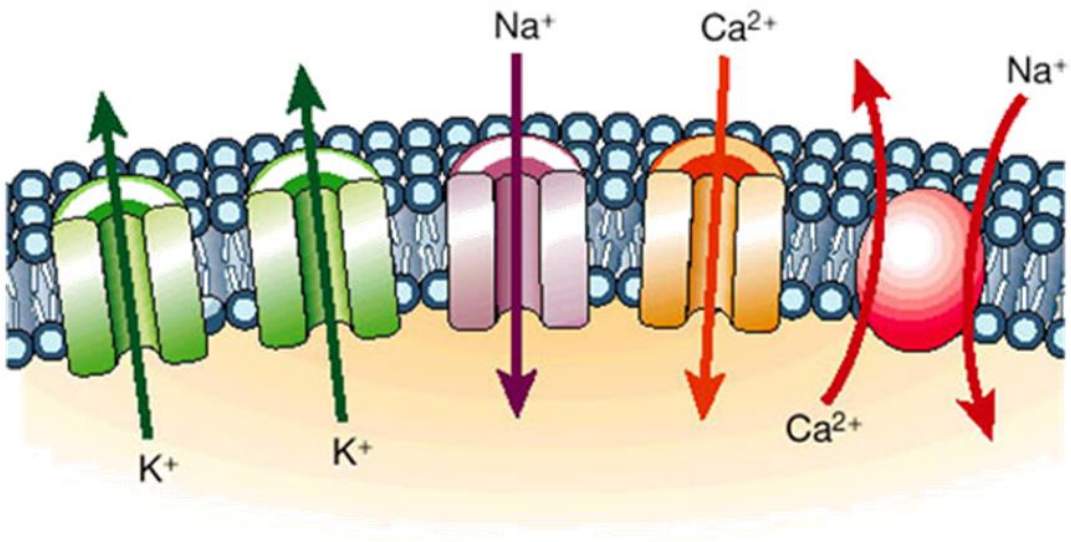

Figure 1.4. Cardiac ion channels.

This illustrates the key ion channels on the cardiomyocyte. The region in blue represents the cell membrane. Potassium (K^+) channels (green) mediate the outward K^+ ion current across the membrane. The influx of sodium (Na^+) and calcium (Ca^{2+}) ions are mediated by the Na^+ (purple) and Ca^{2+} (orange) channels, respectively. The Na^+/Ca^{2+} exchanger (red) transports 3 Na^+ ions for every Ca^{2+} ion. Image adapted from *Cardiac channelopathies. Nature. 2002* [2].

1.1.5. The cardiac action potential

The electromechanical activity of the heart is attributed to the generation of action potentials (AP) from cardiomyocytes. An AP is an electrical stimulation as a result of a series of ion fluxes which are mediated by channels in the membrane of the cardiomyocyte which leads to a contraction. The AP is comprised of five phases and is an abrupt reversal of the membrane potential to a positive value. An AP is initiated by a pacemaker cell of an adjacent cardiomyocyte. The morphology and amplitude of the AP is determined by differences in ion concentration across the cell membrane. Ion channels gate the flow of ions between the intracellular and the extracellular fluid. Figure 1.5 illustrates the AP and its phases are listed as follows [10]:

- Phase 0 – rapid depolarisation. The potential shifts towards a positive voltage range and is governed by the rapid opening of fast sodium (Na^+) channels causing an influx of Na^+ and the TMP rises to be slightly above 0mV. Fast Na^+ channels close as these are time dependent and remain open for only a short period. Note that the TMP requires a minimum potential in order to initial an AP, this is known as the threshold potential.
- Phase 1 – rapid repolarisation or peak upstroke. Potassium (K^+) channels open briefly and an outward flow of K^+ returns the TMP to approximately 0mV.
- Phase 2 – plateau phase. Maintained by a balance of positive inward and outward currents. This is the longest phase of the AP where Calcium (Ca^{2+}) ions enter the cell through the long-type Ca^{2+} channel and is balanced by the out flow of K^+.

- Phase 3 – repolarisation. The plateau phase begins to terminate and late repolarisation begins. The Ca^{2+} channels gradually close but K^{+} channels remain open. The persistent outflow of K^{+} brings the TMP towards the resting potential of -90mV.
- Phase 4 – resting membrane potential. At this phase the AP is typically held at approximately -90mV due to a constant outward leak of K^{+} and the closure of Ca^{2+} and Na^{+} channels.

The action potential duration (APD) is defined as the amount of time in which the voltage remains above the resting potential [11]. Looking at the specific times of the duration gives insight into the different phases of the AP.

Once an AP initiates, the cardiomyocyte is unable to initiate a new AP for a brief period of time, this is known as the effective refractory period (ERP). The ERP occurs due to the fast Na^{+} channels remaining closed until the cell fully repolarises [1]. The ERP can act as a protective mechanism against abnormal heart rhythms [12] and allows for adequate time for the chambers of the heart to fill with blood before contraction.

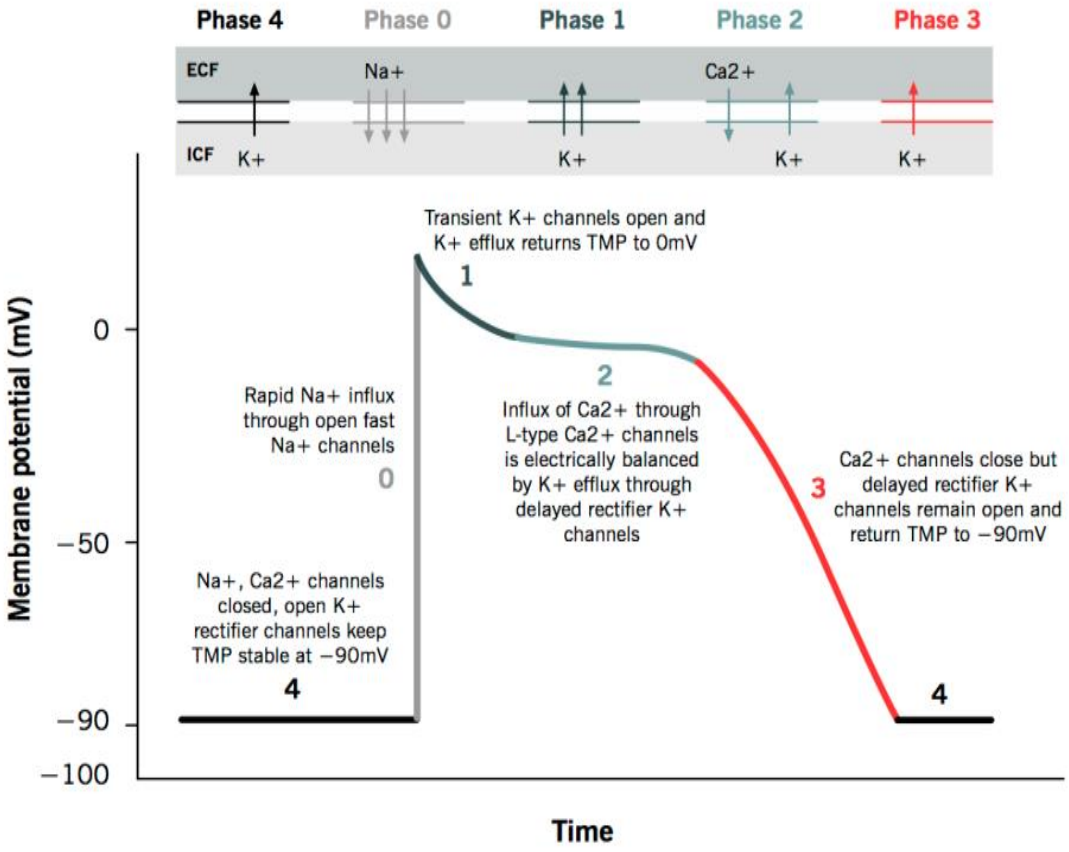

Figure 1.5. The cardiac action potential.

An AP is a short lasting event whereby the membrane voltage of a cardiomyocyte rapidly rises and falls. The top section illustrates the ionic movements between the extracellular (ECF) and the intracellular (ICF) fluid. The stages of an AP are described by five phases 0 to 4 at the bottom section of the image. At phase 0 the cells rapidly depolarise causing the potential to shift towards a positive voltage range caused by an influx of sodium ions (Na^+). Phase 1 is the rapid repolarisation; the AP upstroke reaches its peak voltage caused by an outflow of potassium ions (K^+). Phase 2 is the plateau phase, the longest of all the phases. The plateau is maintained by a balance of positive inward calcium ions (Ca^+) and outward K^+. Phase 3 is the repolarisation where the plateau begins to terminate Ca^{2+} channels begin to close but K^+ channels remain open. Phase 4 is the resting phase, whereby the transmembrane potential (TMP) of the AP is typically held at -90mV due to a constant outward leak of K^+. Image extracted from *McMaster Pathophysiology Review.* Retrieved from:

http://www.pathophys.org/physiology-of-cardiac-conduction-and-contractility/actionpotential/

1.1.6. The electrocardiogram

The electrocardiogram (ECG) is used to assess cardiac rhythm and conduction. The basis of an ECG is that the electrical depolarisation of the heart produces a small current which reaches the surface of the body [4]. If a series of electrodes are placed onto the skin on opposite sides of the heart, the electrical potentials can be recorded.

A normal ECG consists of a P wave, a “QRS complex” and a T wave. There exists a U wave and by definition it follows the T wave, however, this wave is inconsistent and not always seen [13]. The P wave represents the depolarisation of the atria. The QRS complex is caused by currents from the rapid depolarisation of the ventricles and is made up of three waves, the Q wave, R wave and the S wave. The T wave is caused by currents generated as the ventricles recover from the state of depolarisation; this is known as a repolarisation wave. The PR interval reflects the time of the electrical impulse to travel from the SA node to the AV node. The ST segment represents the period when the ventricle are depolarised. The QT segment is the measure of time between the start of the QRS complex to the end of the T wave. A lengthened QT interval is a marker for cardiac abnormalities, often referred to as long QT syndrome [14]. Between the cycles of the ECG waves, the recording returns to baseline, this is known as the isoelectric line. Figure 1.6 shows the AP waveforms of the heart from multiple regions forming the waves present in an ECG. ECGs are useful in understanding the electrical conduction system of the heart; they typically form a predictable pattern in a normal heart. Therefore, deviations from the norm can give indication of pathological abnormalities [15], hence the importance of ECG interpretation. The

placement of ECG electrodes plays an important factor of the waveform of the ECG [16]. The depolarisation of the heart towards a positive electrode produces a positive deflection, whereas away from the positive electrode creates a negative deflection. This differs from the repolarisation. As the heart repolarises, the impulse towards the positive electrode produces a negative inflection but away from the electrode generates a positive deflection [1]. For example, if the R wave of the QRS complex is greater than the S wave, this suggests the depolarisation is travelling towards the positive electrode. If the S wave is greater than the R wave, this suggests depolarisation away from the positive electrode.

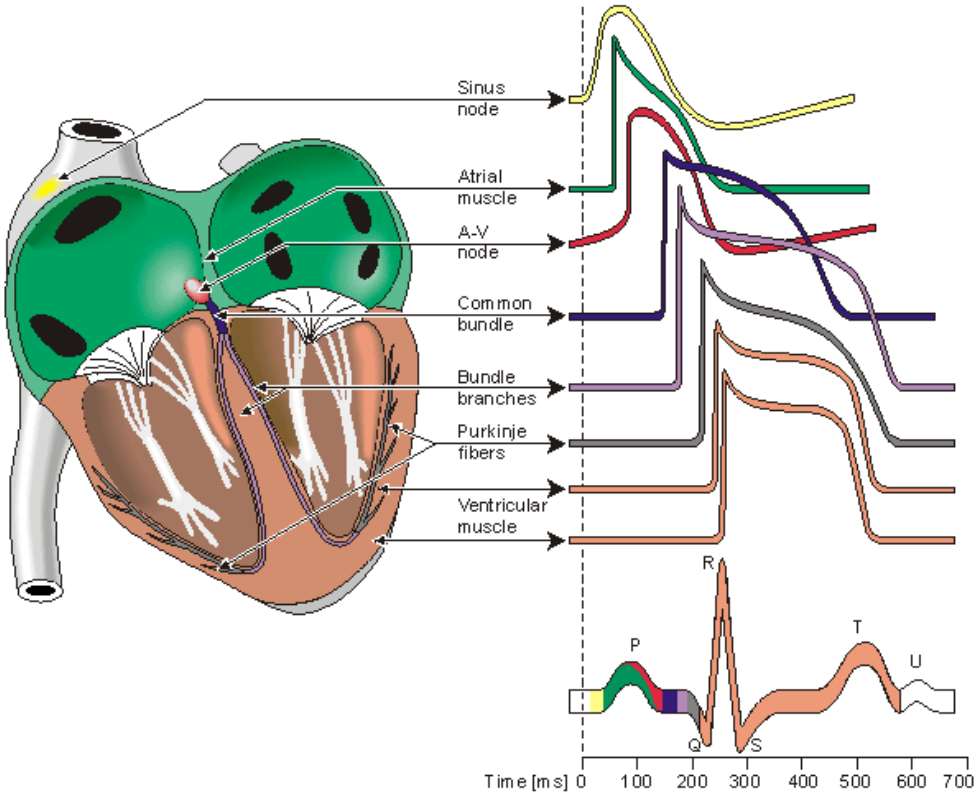

Figure 1.6. Action potential waveforms of the heart.

This shows the regional waveforms of the electrical activity from different parts of the heart forming an electrocardiogram (lower portion of the image). The electrical impulses spread from the heart to the surrounding tissue where they can be recorded by electrodes. The electrical impulse begins at the Sinoatrial (sinus) node and travels down to the atrioventricular (AV) node where it eventually ends in the ventricles. Image extracted from *Bioelectromagnetism - Principles and Applications of Bioelectric and Biomagnetic Fields. Part I. Oxford University Press. 1995* [17].

1.2. Cardiovascular disease

Cardiovascular disease (CVD) is defined as a group of diseases which affect the heart or blood vessels and they remain the leading cause of death worldwide [18]. It is estimated that 30% of all deaths worldwide were caused by CVD [19]. Within the UK, 27% of all deaths were caused by CVD [20]. There are many risk factors which contribute to the propensity of CVD. Some of these factors may be environmental or lifestyle such as obesity [21] and smoking [22], as well genetic predisposition [23].

The main causes of CVD death are coronary heart disease (CHD) and stroke. The heart has its own network of blood vessels on the surface of the heart called coronary arteries. CHD is when the blood supply is interrupted, this sometimes referred to as ischaemic heart disease. A stroke manifests when the blood flow to the brain is disrupted, this can either be ischaemic; due to a lack of blood flow or haemorrhagic, due to bleeding [24]. As a result, the function of the brain is impaired. In the UK 46% of CVD deaths were due to CHD and 26% were from stroke. Overall, CHD was responsible for 16% of all male deaths and 10% for women in the UK [19]. 6% of all UK deaths in men and 9% in women were caused by stroke [19]. It is clear that CVD presents itself as a significant burden. There is also a financial cost of CVD. In England, more than £6.8 billion was spent on treating CVD in 2012/2013 from the NHS [20]. In 2014, more than 313 million prescriptions were dispensed for CVD in England [20].

1.3. Cardiac arrhythmias

Cardiac arrhythmias are a group of conditions where the rhythm of the heart is irregular or the rate is abnormal. Tachycardia is the term for a fast heart rate, usually defined as over 100 bpm. Bradycardia means a slowed heart rate, which is defined as less than 60bpm [15]. Arrhythmias can arise when the electrical impulses are coming from another part of the heart or there is an impairment of the conduction system causing the impulse to take an unusual path [25]. Many types of arrhythmia have no symptoms but when they do present, they can range from the feeling of skipped beats to chest pains and unconsciousness [26]. Some arrhythmias are not serious but others can predispose one to more severe conditions such as stroke and heart failure [26]. The most common type of arrhythmia is atrial fibrillation (AF) [27], this an uncoordinated and rapid beating of the atria, leading to impaired atrial function [25]. More information on AF is provided in section 1.4.

Ectopic beats or extrasystoles are essentially premature extra beats which interrupt the normal rhythm of the heart. Extrasystoles can present themselves in either the atria, or the ventricle [25]. While the SA node typically regulates the sinus rhythm of the heart, an atrial extrasystole occurs when another region of the atria depolarises before the SA node triggers, causing a premature beat, this is also known as a premature atrial contraction. A similar action occurs in ventricular extrasystoles, where the ventricles depolarise before the triggering of the SA node [25].

Afterdepolarisations are abnormal depolarisations in the heart which interrupt the repolarisation phase of the AP and can be described as early or delayed. Early

afterdepolarisations (EADs) occur during the phase 2 of phase 3 of the AP. Delayed afterdepolarisations (DADs) begin during phase 4 of an AP but before another AP would normally occur. When an EAD or DAD has amplitude greater than the threshold potential, further APs can be initiated, referred to as a triggered response [28]. These triggered events can result in extrasystoles and tachycardia [28].

Re-entry is a form of arrhythmia that is caused by the electrical impulse not completing the normal circuit, but rather finding an alternative route. Conditions that facilitate re-entry include the presence of unidirectional block, where the passage of the electrical impulse is inhibited in on direction, and the rate of conducting the impulse is slow [29]. A model for re-entry is shown in Figure 1.7. In a normal system (Figure 1.7 *left*), where a conducting bundle forms a branch, the electrical impulse will travel down each branch. If these branches are connected by a common pathway the impulses will cancel each other. In the case for re-entry (Figure 1.7 *right*), there is a unidirectional block at branch (2). In such a block, the impulse can travel retrogradely from branch (3) to (2). As the impulse leaves the block, it can re-excite the tissue if it is beyond the ERP and re-enter at (1). An electrode at (*) would measure high frequency impulses. If the impulse left the block and found the tissue to be within the ERP the tissue would not re-excite. Hence, in this instance a longer ERP would be favourable.

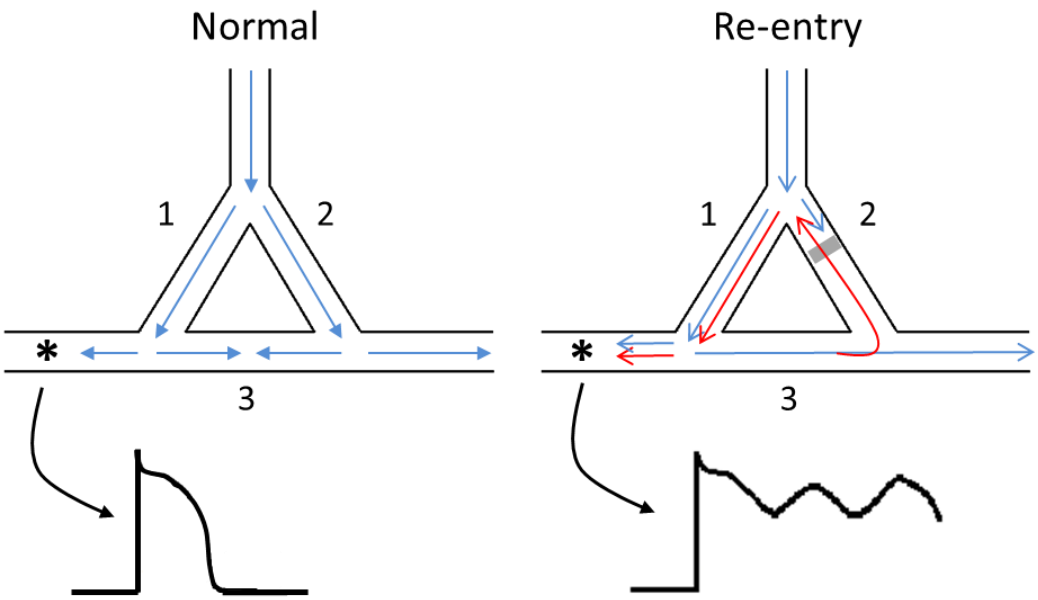

Figure 1.7. Re-entry model.

This illustrates the normal and re-entrant models. Conducting bundles branch to (1) and (2) and are met by a common pathway at (3). In the case of normal conduction, the impulse (blue arrows) divides at the top to branches (1) and (2) and at (3) they meet and cancel. If an electrode was placed at (*), it would witness a single AP. For the re-entrant model however, there is a unidirectional block (grey box) at branch (2). The impulse only travels down branch (1) and conducts to (3). Subsequently, the impulse travels to branch (2) (red arrow) and through the block. If the tissue after the block is within its refractory period the impulse ends. However, if it is outside of its refraction, the impulse continues, and can re-enter at branch (1). The electrode at (*) would measure a series of frequent impulses. *Image was created by the author of this thesis*.

1.3.1. Antiarrhythmic drugs

Antiarrhythmic drugs (AADs) or agents are a group of pharmaceuticals used to supress cardiac arrhythmias. AADs can either be used to control rate or rhythm. They can be classified according to whether they interfere with ion channels located on the cardiomyocyte or by whether they block receptors [30]. Here we shall discuss the class of AADs which act by blocking the Na^+ channel, often referred to as class I agents. Class I drugs can be further subcategorised into

three groups (Ia, Ib and Ic) [30]. Class Ia are drugs which prolong the AP by reducing the rate of the upstroke (phase 0). Class Ib agents do not reduce the rate of the upstroke but shorten the APD. Class Ic drugs reduce the upstroke rate, slow the CV and can prolong the ERP [30]. Na^+ channel blockers can convert regions of unidirectional block to bidirectional block, abolishing re-entry [31]. Class I agents depress the excitability of the cardiomyocytes [31]. These properties can be both pro- and antiarrhythmic [32].

Flecainide acetate or simply flecainide is a class Ic antiarrhythmic. It is used in a variety of arrhythmias such AF [33]. Flecainide was first synthesised in 1972 and successfully tested in humans in 1975, soon after in 1982 is was approved for use in Europe [34], [35]. Flecainide binds to the open Na^+ channel and causes a blockade. The main effect of the channel blockade is the slowing of CV and prolongation of the ERP. Flecainide is also known to a lesser extent inhibit the K^+ channels [36]. The effect of flecainide on the Na^+ channels increase as the heart rate increases, this is known as use-dependence [37], [38].

1.4. DNA and genetics

The propensity of CVD may be due to environmental factors but also genetic ones [23]. Therefore, this section is a brief highlight of some of the basic principles of genetics and deoxyribonucleic acid, commonly referred to as DNA. All living things are composed of cells. The heart is mainly composed of cells called cardiomyocytes. Within cells the nucleus can be found, where its genetic information is stored; information that specifies the form and function of all cells within an organism [39]. This information is stored in the form of DNA, strands of long molecules coiled to form a double helix (Figure 1.8). DNA is formed of

polymer chains of molecules called nucleotides. Each nucleotide is composed of a nitrogen containing nucleobase: adenine, thymine, cysteine and guanine (A, T, C and G, respectively) [39]. These nucleobases are classified into two types, purines (A and G) and pyrimidines (C and T). Two strands of DNA run in opposite directions, pairing the nucleobases forming a double helix. During assembly of the helical structure, a purine can pair only with a pyrimidine (A-T and G-C), and a pyrimidine with a purine (C-G and T-A). This pairing is known as a base pair [26]. The sequence of these base pairs specifies the form and function of a cell. Figure 1.8 illustrates the process of how DNA encodes the biological information of a cell as a protein product. Within cells, DNA is organised into coils called chromosomes. A gene is a sequence of DNA located on a region of the chromosome known as a locus. Introns and exons are nucleotide sequences within a gene. Exons are parts of the gene which codes for protein, introns however, do not [39]. A gene directly produces a single strand of mRNA (messenger ribonucleic acid), this is an identical sequence of one of the two strands of DNA – the DNA has been transcripted. Ribosomes are biological components which facilitate the synthesis of proteins specified by mRNA. Genes can exist in alternative forms, which are located at the same locus on the chromosome. These forms are known as alleles. Some alleles can result in different observable traits, known as phenotypes, such as hair and eye colour. Mammals such as humans and mice have two pairs of chromosomes; one of each pair is inherited from each parent [39]. This is also true for genes, one of the two copies of each gene from each parent. The genotype can be described as homozygous if two identical pairs of alleles at a particular locus are present, heterozygous if the two alleles are non-identical. In this thesis, the nomenclature

for a genotype that is heterozygous is denoted by a superscripted +/-, e.g. "genotype$^{+/-}$", i.e. it is deficient in a gene. Homozygous genotypes with two non-functioning alleles are denoted as "genotype$^{-/-}$". Homozygous genotypes with two functioning pairs of alleles are stated as wild type (WT) as these are considered the "normal" allele at that locus.

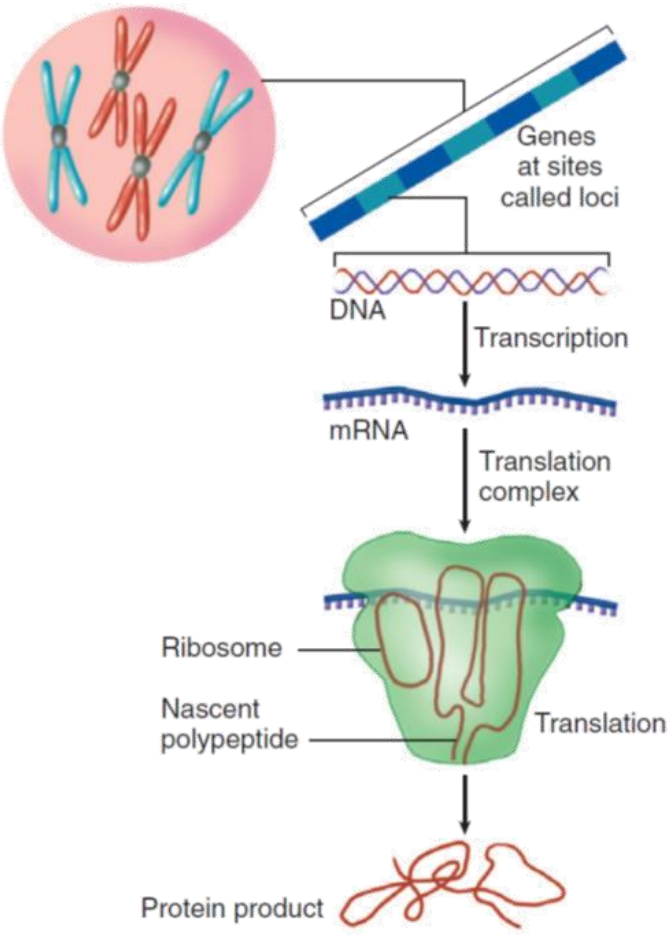

Figure 1.8. The flow of information from DNA to protein.

This depicts the storage of genetic information in the chromosomes (top left) and how protein is synthesised. Genes are regions of DNA on the chromosome that encode biological information. A gene directly produces a strand of mRNA. Ribosomes serve as a site for protein synthesis. The ribosome decodes the mRNA and produces a chain of amino acids (polypeptide). The polypeptide later becomes an active protein and performs functions in the cell. Image extracted from *Braunwald's Heart Disease. A Textbook of Cardiovascular Medicine. Elsevier. 2011* [26].

1.4.1. Single nucleotide polymorphism (SNP)

A single nucleotide polymorphism (SNPs) is a variation at a single position in a DNA sequence. Recall that DNA is a sequence of nucleotides (A, T, C and G). Differences in nucleotide sequences (Figure 1.9) that lead to structural change in the encoded protein are called mutations. A mutation is defined as occurring in less than 1% of a given populations. Hence, if more than 1% of a population does not carry the same nucleotide at a specific location in the DNA sequence, this is considered a SNP. Some SNP sequences are associated with diseases, whilst others are harmless or protective [26].

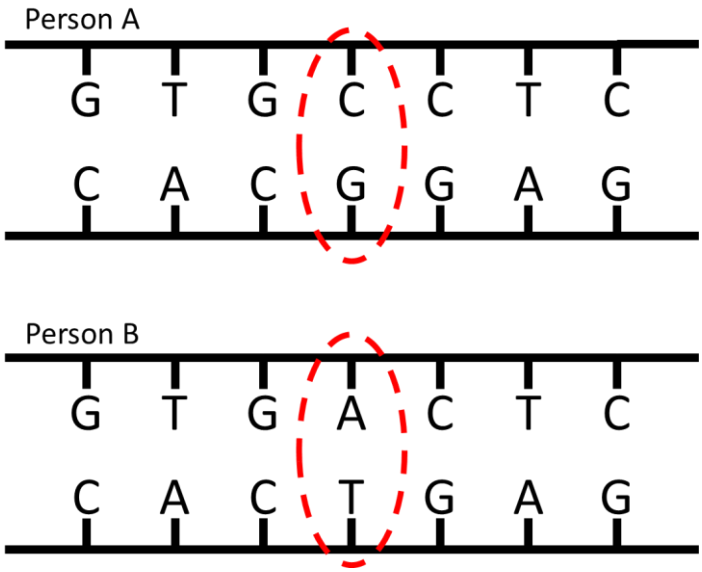

Figure 1.9. A single nucleotide polymorphism.

This shows a representation of the nucleotide sequence from two people. The base pairs highlighted in red shows the location of the polymorphism. If person B shares the same nucleotide base at that location with more than 1% of a given population and person A does not, Person A is considered to have the SNP. *Image was created by the author of this thesis*.

1.5. Atrial fibrillation

Atrial fibrillation (AF) is the most common sustained arrhythmia in man and a common cause of stroke and cardiac deaths, AF is more prevalent in the aging population [40] and affects up to 2% of the general population [27]. It is described by rapid and disorganised atrial activation [27]. Under sinus rhythm, the hearts beats at approximately 65 to 100 bpm and can rise to as much as 200 bpm during intense exercise [1]. During AF, atrial cells can depolarise at rates close to 400-600 times a minute [41]. Fortunately, each of these beats does not lead to a ventricular contraction as this would quickly result in loss of consciousness caused by a fall in blood pressure. The occurrence of AF is dependent on multiple factors such as re-entry. Re-entry can occur due to reduced refractoriness and slow conduction [29]. AF can be initiated by ectopy in the form of extrasystoles or afterdepolarisations [42]. Current management of AF include rate or rhythm control. Rate control methods target the ventricular rate by reducing rate of conduction of the atrioventricular (AV) node. The AV node is the key conduction bundle that link the electrical signals from the atria to the ventricles (Figure 1.3) [43]. Rhythm control attempts to convert the heart to sinus rhythm, e.g. by use of antiarrhythmic drugs such as flecainide. Flecainide works by blocking the Na^+ channels in the heart. The effect of flecainide on the Na^+ channels has been shown to increase as heart rate increases [27], [37], [44]. There have been many studies and good progress has been made in the characterisation of factors that cause AF, such as hypertension, diabetes and heart failure [29], [45], [46]. However, there is still a need for better therapies to prevent incident and recurrent AF [45], [47].

1.5.1. Role of Pitx2

Genome-wide association studies have found common gene variants or single nucleotide polymorphisms (SNP) associated with AF on chromosomes 4q25 [48], [49]. This region is in close proximity to the paired-like homeodomain transcription factor 2 (Pitx2) homeobox gene [50]. Pitx2 is a homeobox gene responsible for the left right asymmetry formation of the body [51].

Four isoforms (a, b, c and d) exist for Pitx2. The c-isoform mRNA has been shown to be expressed 100 fold higher in the LA compared to the other chambers of the heart and is crucial to the development of the sinoatrial node [52]. These variants are associated with altered mRNA expression of the transcription factor Pitx2 and show an increased risk of AF [49]. A severe insufficiency of the Pitx2 has been shown to lead to structural and electrical remodelling in the atria [53]. Other research groups found mouse models of homozygous deletion ($Pitx2^{-/-}$) leads to cardiac abnormalities [51]. A heterozygous ($Pitx2c^{+/}$) mouse model showed increased risk of AF inducibility [53]–[55].

1.6. Arrhythmogenic right ventricular cardiomyopathy

Arrhythmogenic right ventricular cardiomyopathy/dysplasia (ARVC/D) is a genetic form of cardiomyopathy, a disease of the heart muscle. It is an inherited disease which contributes significantly to the sudden death of young athletes [56], thereby suggesting that endurance training facilitates disease progression. ARVC has prevalence in the general population of approximately 1:2000 to 1:5000 [57] whereby men are more affected by women with the approximate ratio of 3:1 [58]. ARVC primarily affects the right ventricle and is characterised by arrhythmia and

fibrosis, a thickening and scarring of connective tissue, but ARVC may involve the left ventricle [59]. The right ventricle dilates at later stages leading to reduced contractility and ejection fraction of the heart [60], [61]. Pre-stages of the fibro-fatty infiltration and remodelling are often detected by ECG changes in ARVC patients, which can be used as a diagnostic marker [62], [63]. The tissue of the myocardium is replaced with fatty and fibrotic tissue. Alterations in the QRS complex of an ECG indicate that ARVC sufferers are susceptible to increased arrhythmias [64], [65].

ARVC is considered a disease of the desmosome. Desmosomes are intercellular junctions that connect intermediate filaments to the cell surface and provide strong adhesion between cells [66], see Figure 1.10. Mutations in the protein junctions in the desmosome of the intercalated disk result in an ARVC phenotype [67], [68]. These mutations lead to a change in morphological structure and which can result in cell death [59]. Conditions of mechanical stress can weaken the adhesiveness of the cells which leads to the hypothesis that environmental factors such as endurance training can exacerbate the phenotype and accelerate the development of ARVC [64].

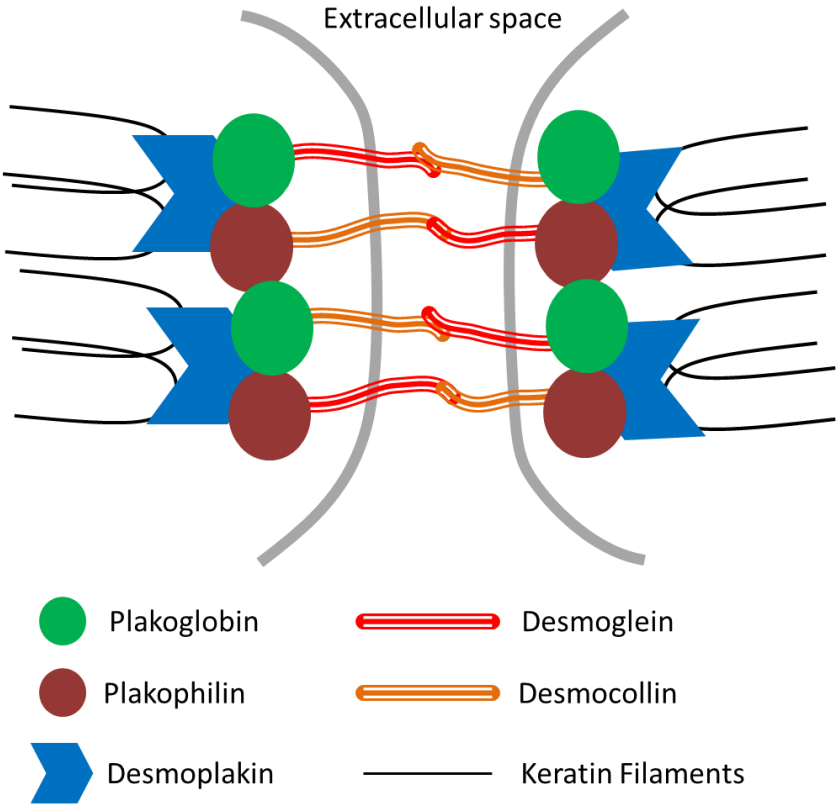

Figure 1.10. The desmosome.

This is a simplified model of the desmosome, which highlight the main protein-protein interactions. Desmosomes mediate cell-cell contact via a number of proteins: plakoglobin, plakophilin, desmoplakin, desmoglein and desmocollin. The keratin filaments are anchored to the desmosomal proteins which mediate through the cell wall (grey line). *Image was created by the author of this thesis*.

1.6.1. Role of plakoglobin

Previous studies have shown that the gene variants that code for plakoglobin is located on chromosome 17q21 [69]–[71]. Plakoglobin is a key constituent for the adherent junctions and is responsible for the tight adhesion between cardiomyocytes (see Figure 1.10) [69], [71]. It is involved in the area composita of adhering junctions. This area is thought to be the main component of the intercalated disk between cardiomyocytes and consists of adherent fascia proteins and desmosomal proteins [67], [68]. Transgenic mouse models have verified the

roles of junctional protein dysfunction in ARVC. Mice with homozygous deletion of plakoglobin (plako$^{-/-}$) do not survive gestation [72]. However, heterozygous (plako$^{+/-}$) mice develop the ARVC phenotype with age or endurance training which consists of enlarged right ventricle and inducible ventricular tachycardia [64].

1.7. Genetically altered murine models

Genetically altered murine models are becoming increasingly popular for the investigation of human cardiac arrhythmias [73]. Albeit some differences such as their small size and faster heart rates, they often provide a second best compared to the patient themselves. These models allow for control of multiple factors such as age, sex and diet reducing genetic and environmental variability [74]. Mice have a short gestation period, rapid maturation and their ease of genetic manipulation making them very attractive models. Mice and humans also have many homologous cardiac developmental pathways but also have considerable differences. One example of this is the faster resting heart rates of 600 beats/minute which is 10x faster than that of a human. Mice have also been shown to have a much shorter APD with no plateau phase [75]. The APD of a mouse is reported to be 10x less than their human counterpart; this is mainly due to the differences in relative abundance of repolarisation currents. One of the obvious differences is the lack of a plateau phase in the mouse AP compared to humans. The lack of a plateau is attributed to the predominance of activating outward potassium channels causing relatively short APDs at around 50% to repolarisation compared to the human AP [76]. The currents which play a large role in the repolarisation of the human heart are the rectifying potassium currents both rapid (I_{Kr}) and slow (I_{Ks}) [77]. The current I_{Kr} is mediated by the hERG (human

ether-a-go-go-related gene) channel and I_{Ks} by the K_VLQT1 channel. Both hERG and K_VLQT1 are proteins which form the channels to moderate the flow of outward potassium current [78]. These currents give rise to the long lasting plateau phase of the AP in a human but are not present in mice. The prominent currents in mice which are responsible for the repolarisation are three distinct potassium currents - slowly inactivating potassium current ($I_{K,slow1}$ and I_{Kslow2}) and the non-inactivating steady state current (I_{SS}) [73]. Studies have revealed that $I_{K,slow1}$ is mediated by the K_V1.5 channel protein and $I_{K,slow2}$ by K_V2.1 [79], [80]. The identity of the protein mediating the I_{SS} current remains to be found [73]. The differences in channel expression between mice and men give rise to the different currents which repolarise the cells causing their morphological differences in AP. Figure 1.11 shows the differences in ionic current and how they contribute to the morphology of a human and mouse AP.

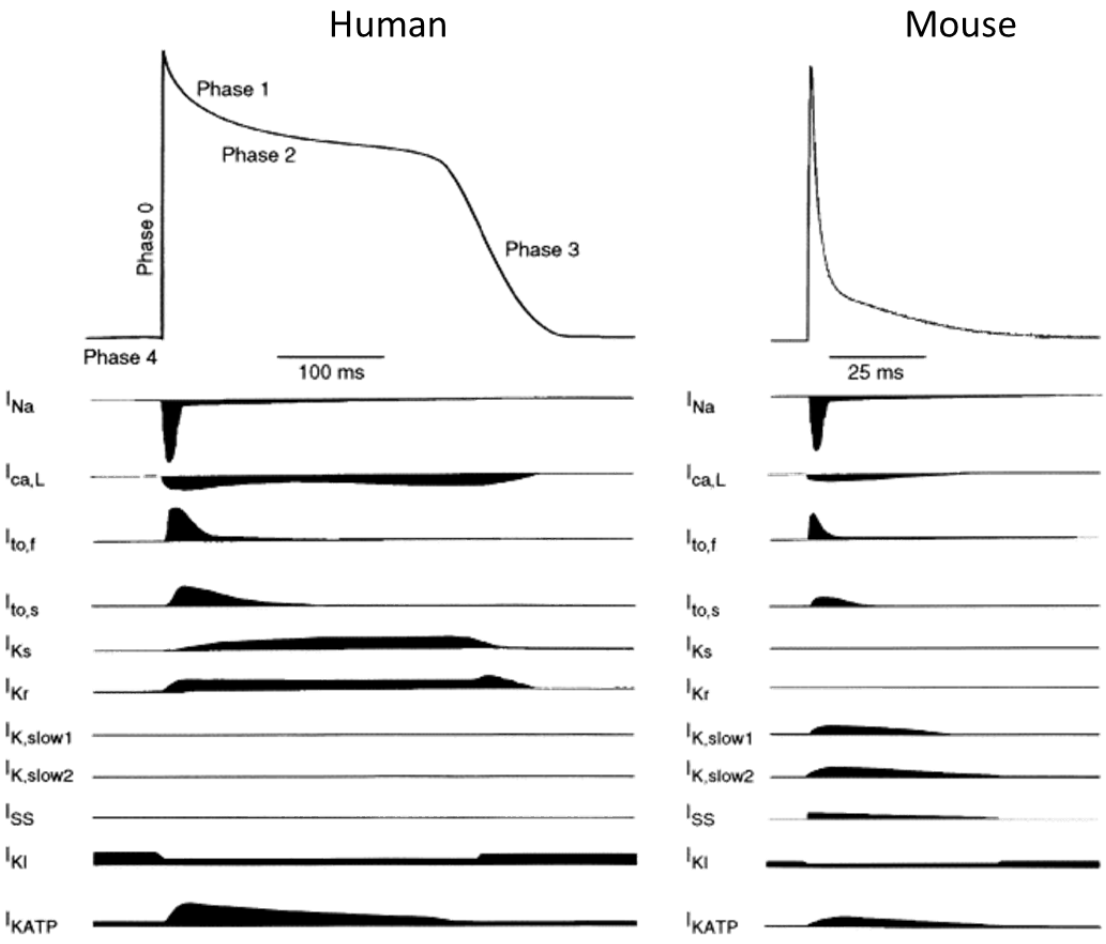

Figure 1.11. The human and mouse action potential.

This shows the morphological differences between a typical human (left) and mouse (right) AP. The currents can be seen below each of the APs. The inward currents such as the long type (L-type) calcium ($I_{Ca,L}$) and sodium (I_{Na}) are shown to appear below the line and outward currents are above. The main difference between the human and mouse AP is the plateau seen at phase 2. Inward potassium currents, I_{Kr} (rapid) and I_{Ks} (slow) are prominent in the human AP whereas this is true for the slowly inactivating potassium currents ($I_{K,slow1\&2}$) and the non-inactivating steady state current (I_{SS}) in mice. Image extracted from *Studying Cardiac Arrhythmias in the Mouse - A Reasonable Model for Probing Mechanisms? Trends in cardiovascular medicine. 2004* [73].

1.8. Action potential measurement techniques

To measure the millivolt changes in cardiac tissue, there have been numerous techniques developed. Some of these techniques involve direct contact but can also be non-contact. Monophasic action potential (MAP) electrodes are often used

in measurement of cardiac AP. The first MAP was developed over 30 years ago [81] and recorded signals by applying a point load to the myocardium. In simplest terms, the point of contact measures the voltage with respect to a reference electrode but the genesis of the MAP signal is still not understood [82].

MAP electrodes have often been used in conjunction with a Langendorff apparatus, a method of sustaining a whole isolated heart for a prolonged period of time [83], as shown in Figure 1.12. The Langendorff apparatus works by reverse perfusion. Blood normally leaves the heart by the aorta but here, buffer solution used to sustain the heart is flowed into the aorta. During reverse perfusion, the aortic valves close and the solution passes through the coronary ostia where it passes through the vascular bed. Subsequently, the solution reaches the coronary sinus and the atria. The MAP electrodes have the advantage over suction electrodes which were developed much earlier on, which caused damage to the tissues [81], [84]. The MAP electrode measures the potential from an aggregate of surrounding cells and can be difficult to use especially for small organs such as murine atria. The gold standard for measuring the cardiac AP is the microelectrode, which measures the voltage directly from a single cell. The microelectrode technique has been widely used in cardiac research [85]–[87] but has one main drawback; it only measures from a single point from a cell. Much information can be gathered from measurements of a single AP series such as its activation time, duration, effective refractory period (ERP). Despite this, it is often necessary to study the effects from multiple regions of the heart. Electrode arrays [88] and optical mapping [89], [90] techniques have been developed to overcome this drawback by taking measurements from multiple points simultaneously.

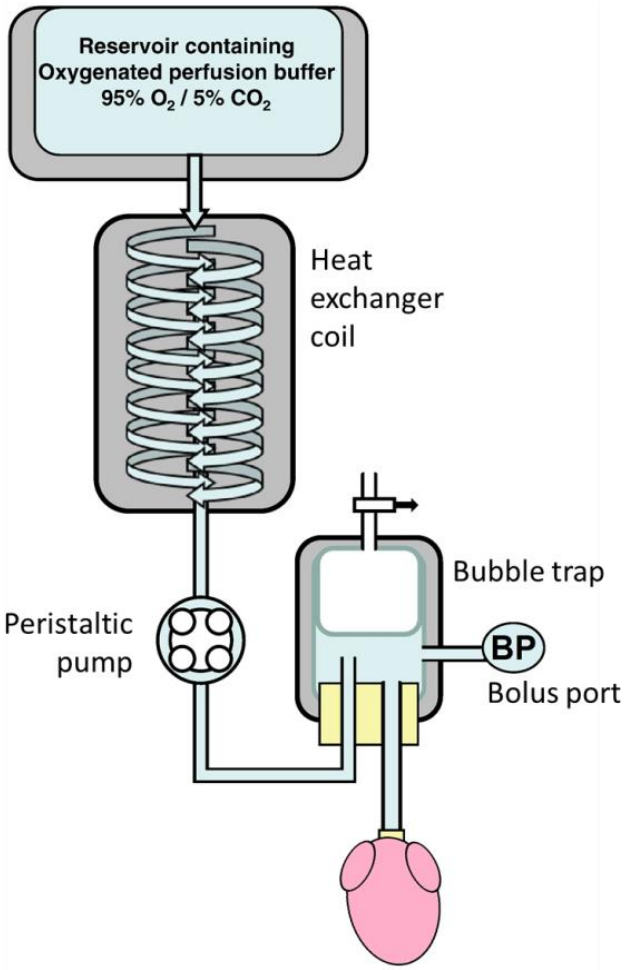

Figure 1.12. Scheme of a Langendorff apparatus.

This shows a simplified scheme of the Langendorff system. The heart is cannulated at the aorta, and is retrogradely perfused with buffer solution. The solution is directed from the reservoir to the heat exchanger coil by the peristaltic pump and the temperature is kept at approximately 37ºC. The solution subsequently reaches the bubble trap, where there is also a bolus port where drugs can be administered. For murine hearts, the pump is usually set to deliver 4ml per minute. This image was adapted from *Retrograde heart perfusion: the Langendorff technique of isolated heart perfusion. Journal of Molecular and cellular cardiology. 2011* [83].

1.9. The need for optical mapping

Optical mapping is an important tool in cardiac electrophysiology as understanding the spread of electrical activity allowed for better knowledge of the mechanisms responsible for cardiac arrhythmias. Microelectrode and monophasic action

potential (MAP) electrodes are useful tools for studying arrhythmias; however, they lack spatial resolution. Optical mapping has provided important insights into mechanisms of atrial arrhythmias in murine models [91], [92]. The ability to resolve spatially is important as cardiomyocytes depolarise, the AP propagates to other regions of the tissue. Measuring a single cell or an aggregate of neighbouring cells only provides information regarding that specific region. The depolarisation pattern is the basis for sinus rhythm and arrhythmias. Optical mapping can yield information such as conduction velocities by mapping the location of multiple APs. As such, investigations on re-entrant arrhythmias [93], [94] atrial [55] and ventricular fibrillation [95] and many other cardiac arrhythmias have benefited greatly from optical mapping.

2. Introduction to optical mapping

2.1. General principles

Optical mapping is an established imaging technique used for the measurement of electrical excitability in cardiac tissue [96]–[98] which was first demonstrated in 1976 [99], and is a valuable tool for aiding our understanding of arrhythmias [92]. This is a fluorescence imaging method based on voltage sensitive dyes that bind onto the lipid membranes on a cell. During an optical mapping experiment, a sample of cardiac tissue is perfused ex vivo and stained using the dye. The membrane bound dye is excited by a light source and emits at a longer wavelength similar to standard fluorescence techniques but the main difference lies in the dyes ability to sense local changes in electric fields [100]. The theory of how an excited fluorophore can emit a photon of lower energy is shown in Figure 2.1. These molecules react by changing their optical spectra which is recorded using appropriate filters and cameras. The result of this shift in spectra allowed us to visualise cardiac action potentials (APs) as relative changes in fluorescence. The motivation for the development of these dyes arises when high spatial and temporal resolution measurements are required, which contact methods such as microelectrodes do not provide. One of the main aims of an optical mapping system is to provide measurements with high signal to noise ratios (SNR) and high spatial and temporal resolution.

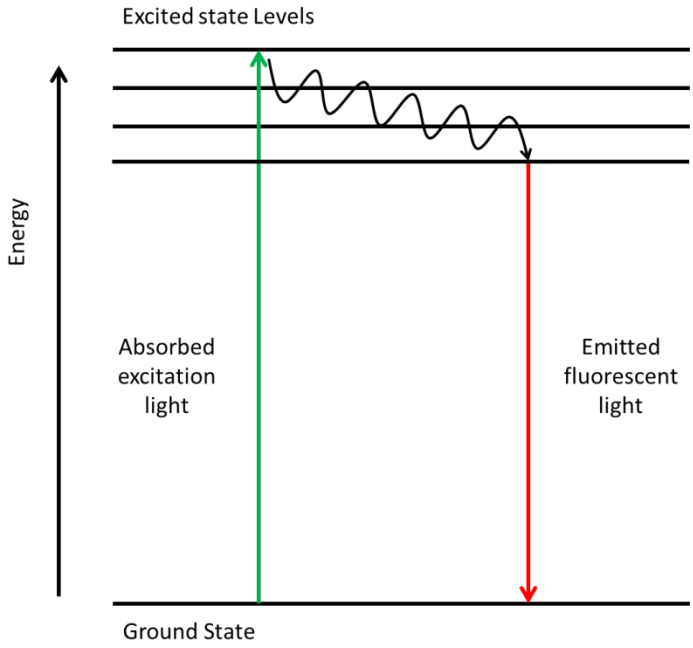

Figure 2.1. Jablonski diagram of fluorescence.

The fluorophore is excited by an incoming photon. The electron attached to the fluorophore's energy level reaches an excited state as indicated by the green upward arrow. As the electron returns to the ground state it emits a photon of lower energy compared to the excitation photon as indicated by the red downward arrow.

2.2. Voltage sensitive dyes

Voltage sensitive dyes are molecular probes that strongly bind onto the cell lipid bilayers. Whilst bound, the dye fluoresces with an intensity that is proportional to the membrane potential [101]. An ideal dye should have the following properties:

I. High sensitivity, large shifts in the fractional change in fluorescence in response to millivolt changes in potential, denoted by ΔF/F where F is the fluorescence.

II. Minimal photobleaching to maintain a high signal to noise ratio.

III. Minimal toxicity leading to reduced cellular damage.

IV. No physiological effects on the cardiac tissue which can skew results.

V. Fast responding to changes in potential across membranes.

Several useful families of compounds have found widespread use in cardiac electrophysiology [96], [100]. Styryl dyes are the most used group [96], such as the RH (Rina Hildesheim) and ANEP (Amino-Naphthyl-Ethenyl-Pyridinium) dyes. Di-4-ANEPPS (di-4-amino-naphthyl-ethylene-pyridinium-propyl-sulfonate) remains one of the most used dyes due to its relatively low cost [100]; its chemical structure can be seen on Figure 2.2. However, there have been studies to show that there is a significant slowing of conduction velocity with the use of di-4-ANEPPS [102]. The peak excitation and emission wavelength for di-4-ANEPPS is at 465nm and 635nm, respectively.

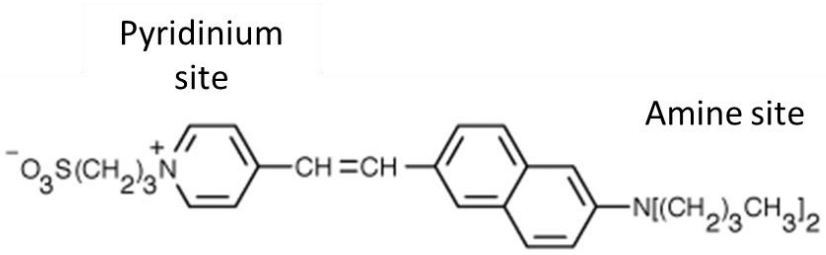

Figure 2.2. Chemical structure of di-4-ANEPPS.

This shows the chemical structure of di-4-amino-naphthyl-ethylene-pyridinium-propyl-sulfonate (di-4-ANEPPS), a voltage sensitive dye which responds to changes in membrane potential. The excitation wavelength is 465nm and its peak emission is 635nm. In the ground state the pyridinium site is slightly positively charged and the negative electron cloud resides on the $N[(CH_2)_3CH_3]_2$ amine site. The amine group is the site which binds onto the cell membrane. Image adapted from *ThermoFisher Scientific*. Retrieved from: https://www.thermofisher.com/order/catalog/product/D1199

2.2.1. Mode of action

Di-4-ANEPPS works by the principle of electrochromism (sometimes referred to as the Stark Effect). Upon excitation the charge density distribution of the dye shifts

from one end of the dye to another, this can be seen in Figure 2.3. Whilst at the ground state the pyridinium site is more positively charged (N^+) and negative electron cloud resides towards the amine group, thus being the electron acceptor and donor, respectively. During excitation this charge distribution reverses and the amine group becomes the electron acceptor [103]. As the cells polarise ($-V_m$) with an electric field E, it perturbs the spectrum of the dye by changing the energy difference between the ground and excited states. As a result, the emission spectra shift in wavelength or redshifts as seen in Figure 2.4. It can be seen that in order to gain the best fractional change in fluorescence (i.e. largest ΔF/F), the peak of the spectra should be avoided and the ideal selections are towards the tails of the spectrum.

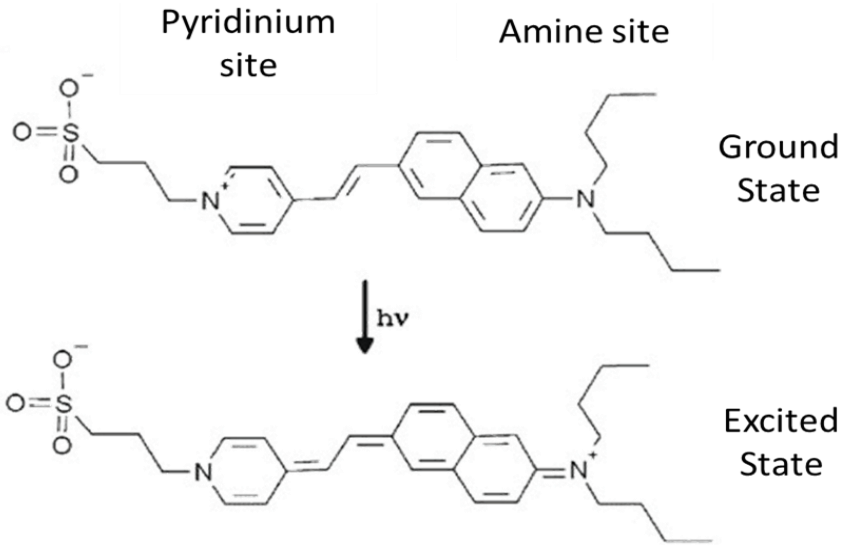

Figure 2.3. Di-4-ANEPPS ground and excited states

This shows the different charge distributions for di-4-ANEPPS during its ground and excited states. Upon excitation, the negative charge density shifts from the amine side to the pyridinium side of the molecule. This shift can be seen from the N region on the ground state which becomes N^+ when excited. The energy difference between the two states is shown as hv; where h is Planck's constant and v the frequency of the photon. Image adapted from *Design and Use of Organic Voltage Sensitive Dyes. Membrane Potential Imaging in the Nervous System: Methods and Application. Springer. 2011* [104].

Depending on whether measurements are made on either side of the peak emission wavelength, fluorescence changes will either increase or decrease as a result, this is seen in Figure 2.4B. Figure 2.5 shows how a long pass filter (red line) can result in a negative ΔF/F as cells depolarise from -90mV to 0mV, the red shaded regions represent the amount of photons that pass the filter for measurement. A long pass filter will allow for a large number of photons to pass through provided it is greater than that stated wavelength. In the case in Figure 2.5, light with a wavelength greater than 630nm will be passed and photons below this value were blocked. Long pass filters differ from band pass filters which only allow a small portion of photons to be transmitted depending on the window size.

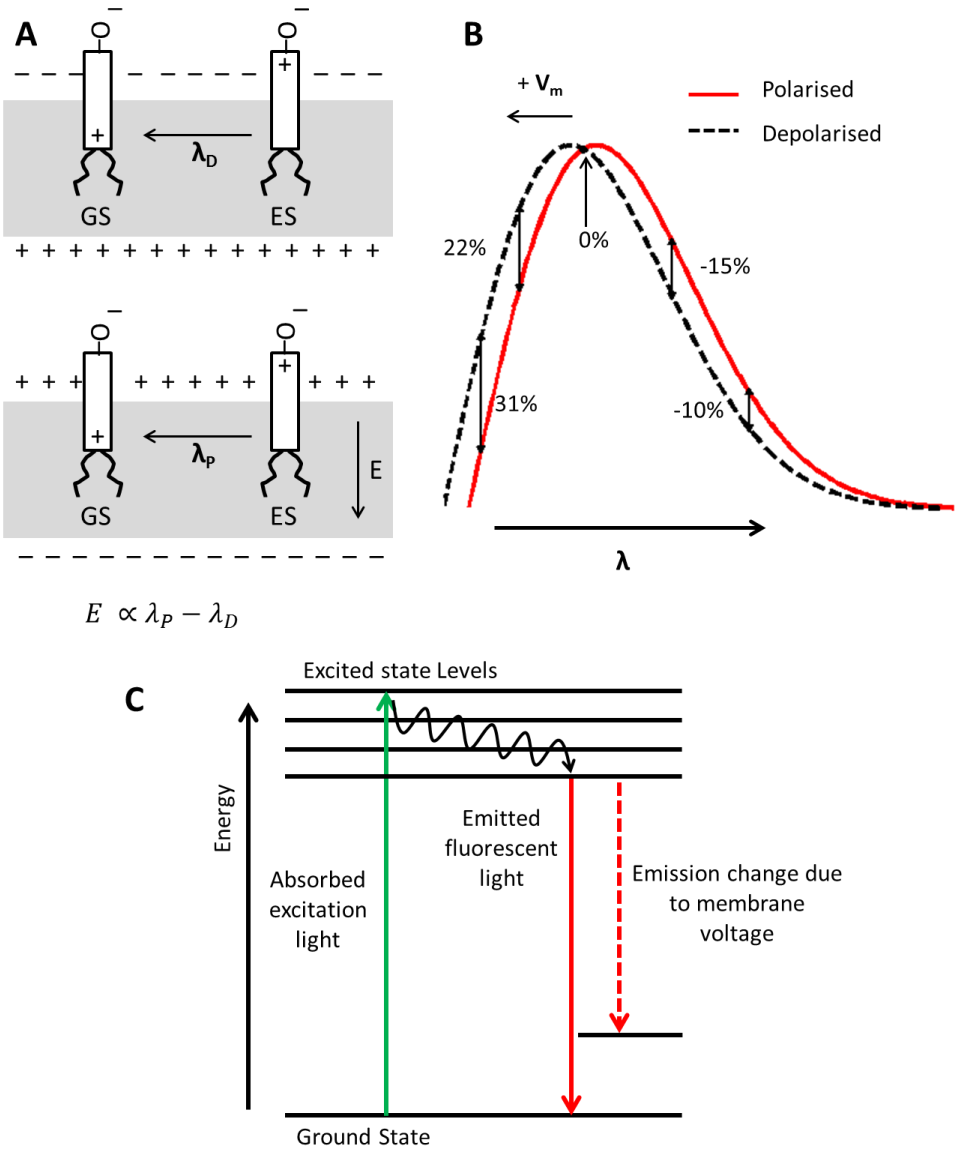

Figure 2.4. The shift in emission spectra in di-4-ANEPPS due to cell depolarisation (+V_m).

A) Shows the dye represented as the white rectangles bound onto the cell membrane (shown in grey). The dye goes from the excited state (ES) to the ground state (GS), but is perturbed by the electric field (E) in the membrane. This perturbation causes the emission wavelength to change from λ_D to λ_P (depolarised to polarised) which is proportional E. B) Represents the emission spectra for the dye at polarised (solid red) and depolarised phases (black dashed). The relative changes in fluorescence are indicated by the change in percentages for various choices of detection wavelength (λ). It can be seen that the choice in wavelength can have a significant effect on the sensitivity of the dye, for example, towards the peak of the dyes show almost 0% difference. This image was generated by plotting two skewed normal distributions in MATLAB and calculating their relative differences. C) The Jablonski diagram shows the excitation and emission of the dye. The electric field of the dye differentially stabilises the energy of the ground state hence a differing emission wavelength (dashed red line) during depolarisation. Images A) and B) were adapted from *Design and Use of Organic Voltage Sensitive Dyes. Membrane Potential Imaging in the Nervous System: Methods and Application*. Springer. 2011 [104].

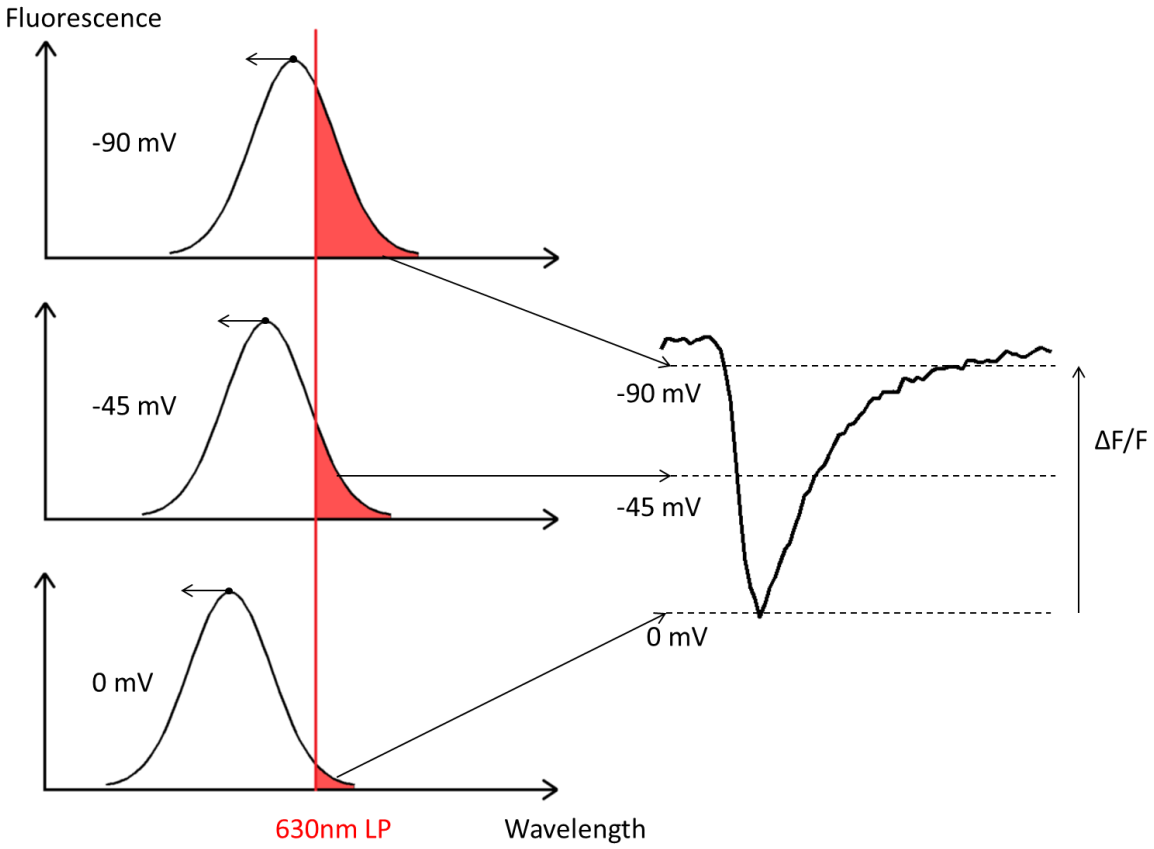

Figure 2.5. Principle of how voltage sensitive dyes generate an inverted action potential as a cardiac tissue depolarises.

This graphic shows as the cardiomyocytes depolarise they reach a more positive voltage, in this case from -90mV towards 0mV. The result of this change in voltage shifts the emission spectra of the dye. The 630nm long pass (LP) filter indicated by the red line allows for only photons with a wavelength of 630nm and above to pass. The red shaded regions represent the amount of photons that pass the filter for measurement. As the cells depolarise the quantity of light collected reduces (red regions become smaller) and created the inverted AP as seen on the right. *Image was created by the author of this thesis.*

Di-4-ANEPPS is frequently chosen due to its large fractional fluorescence changes (~8-10% per 100mV) and low toxicity and photobleaching [105], [106]. One problem with di-4-ANEPPS is that it can be internalised by the cell causing the fluorescence response to drop. This internalisation has prompted a redesign of the molecule to contain 2 octyl chains, di-8-ANEPPS, with a longer hydrocarbon tail. Increasing the length of the dye reduces the likelihood of it penetrating across

the bilayer and internalising, but also reduces its water solubility [100], something that needs to be taken under consideration.

ANEP dyes are also popular due to their linear response to changes in voltage. The measured light intensity increases corresponds proportionally to the membrane voltage. This linearity occurs at both tails of the emission spectra. For example if measurements were made above and below the emission peak, the ΔF/F would either increase or decrease by the same amount, this can be seen in Figure 2.6 for di-8-ANEPPS. The graph in Figure 2.6 was extracted from a study performed on simultaneous voltage and optical recording from cultured mouse hippocampal neurons [107]. The study showed that at wavelengths measured below 570 nm, depolarisation results in an increase in fluorescence and the opposite is seen at above 570 nm [107].

Optical mapping allows us to measure APs; but does not generally provide information on absolute voltage changes in the membrane. This is generally not considered a problem for looking at the propagation of excitation through cardiac tissue.

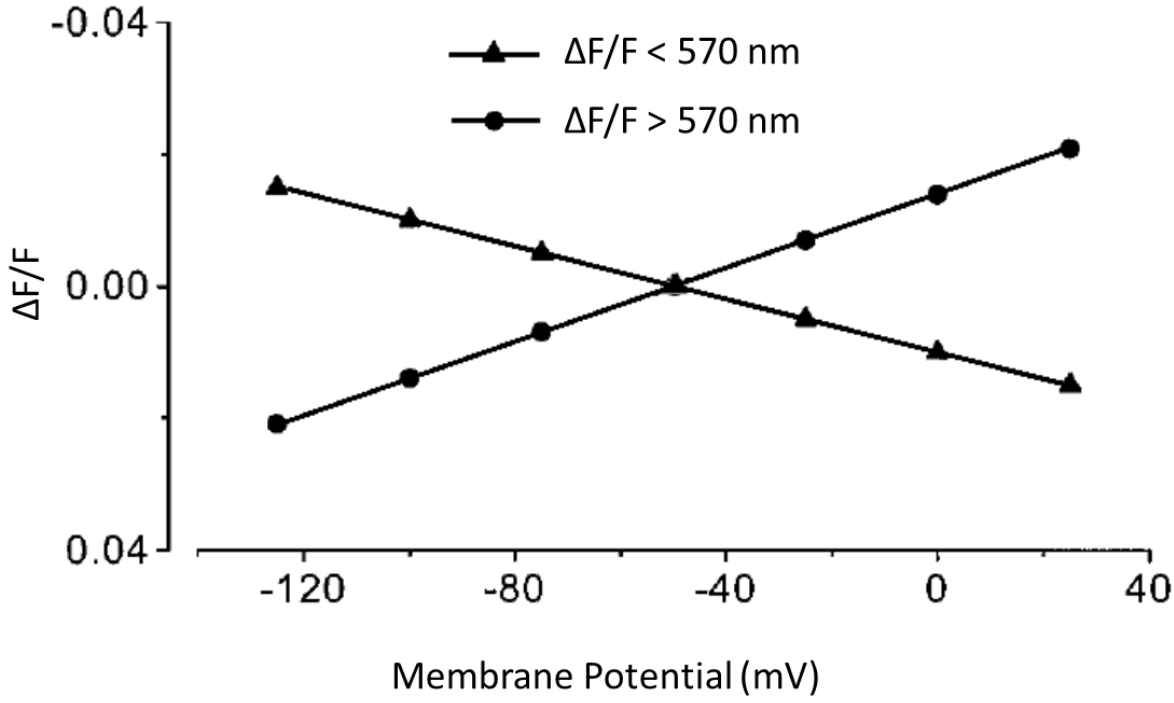

Figure 2.6. Linear response to membrane potential and fluorescent changes for di-8-ANEPPS.

The fractional change in fluorescence, ΔF/F in ANEP dyes had been shown to correspond linearly with membrane voltage. The above graph shows the response of di-8-ANEPPS from the membrane potential of cultured mouse hippocampal cells. Measurements made above and below the peak emission wavelength at 570nm show either an increase or decrease in ΔF/F but both show linearity in their responses. This graph was adapted from *High-speed, random-access fluorescence microscopy: II. Fast quantitative measurements with voltage-sensitive dyes. Biophysical Journal. 1999.* [107]

2.3. Optics

The type of optical objectives or lenses required is determined by the type and size of the tissue samples investigated. The purpose of these optical lenses are to focus the excitation light onto a sample and to collect its fluorescence onto a detector. The numerical aperture (NA) of a lens characterises the angular range in which it can image over, this is arguably the most important factor of a lens. The number of photons that can be collected from a lens is proportional to the square

of the NA. For very small samples, microscope objectives are the best choice for light detection with magnifications above 5x (NA = 0.25-1.3). For imaging the whole heart or larger preparations, much smaller magnifications are required and this is known as macroscopic imaging. Photographic lenses are much better suited for this as their magnifications are much lower (<10x) and yield greater light collection efficiency with numerical apertures of 0.36-0.58. Due to the macroscale of imaging, each optical AP is derived from multiple cells, which can be in the range of hundreds of cardiomyocytes. Therefore, each signal can be considered an average from multiple neighbouring cells.

2.3.1. Light Sources

Light sources are required to excite the voltage sensitive dyes and there are multiple types which are commonly used in optical mapping. These include: Tungsten-Halogen (TH) lamps, arc lamps, lasers and light emitting diode (LED) lamps. The choice of light source should be selected according to the preparation type, light intensity depending on the signal to noise ratio, imaging area and the cost.

2.3.2. Tungsten-Halogen (TH) Lamps

TH lamps are one of the most common sources, with a power of 100 or 250 W. They yield a moderate light intensity and a smooth spectrum over the visible range which is desirable for choosing excitation wavelengths [108]. The TH bulbs themselves have a long life-time and low cost. TH lamps provide moderate light intensity. For situations where this is insufficient, arc lamps can be considered. The most common arc lamps are xenon (Xe) and mercury (Hg).

2.3.3. Arc Lamps

Figure 2.7 shows that like the TH lamps, the Xe spectra are relatively flat over the visible range. Arc lamps produce a higher photon flux density per watt as the source itself is much smaller [109]. As a result of this higher photon flux, Xe lamps have been reported to yield two to three times more light than a TH lamp with similar Wattage [110]. Hg and Metal-Halide lamps exhibit multiple large peaks which can be seen in Figure 2.7 which makes this an ideal candidate for exciting the RH-237 dyes [108].

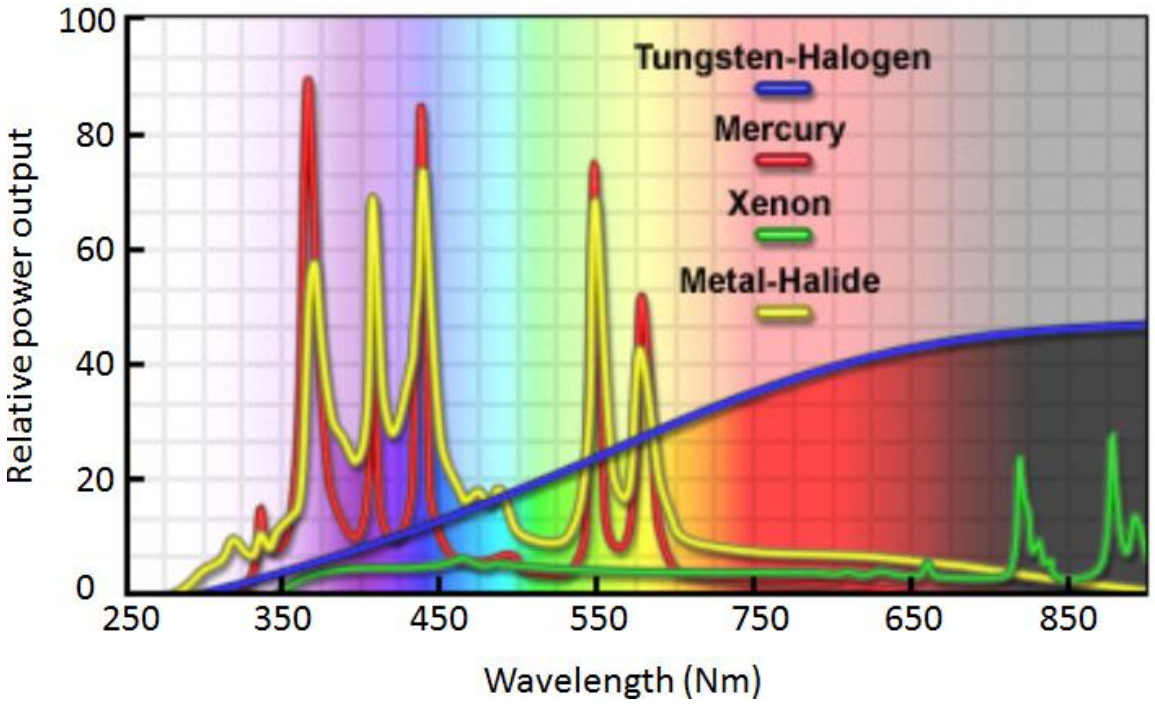

Figure 2.7. Spectral characteristics of commonly used light sources in optical imaging.

The spectral profiles for multiple excitation sources are shown here. These sources are ones commonly found in optical imaging. The distinct peaks are present in the halide and mercury lamps making them a good choice for specific dyes. The tungsten-halogen lamp shows good output intensity at the infrared region but little output in the ultraviolet. The xenon spectrum has strong peaks towards the 800nm region but low output in the visible range. However, the profile of the xenon is much more continuous compared to the other light sources. Image adapted from *Nikon Microscopy.* Retrieved from: **http://www.microscopyu.com/articles/livecellimaging/automaticmicroscope.html**

2.3.4. Lasers

Lasers produce monochromatic light, the photons emitted are of a single wavelength with high intensity which is very desirable. This light can be easily focused onto a small area. However, they come with multiple disadvantages, such as their high purchase and running costs and they consume large amounts of power [93]. The high intensity also comes at another cost of causing dyes to photobleach. To reduce this effect, the illumination times need to be minimised.

2.3.5. Light Emitting Diodes (LEDs)

LEDs provide an attractive alternative to lamps and laser sources due to their low power consumption, optical stability, and large choice in emission wavelengths. Whilst lasers provide photons of a specific wavelength, LEDs can yield light of narrow wavelengths, reducing the need for optical filtering and poses a long lifetime [111]. The bulbs themselves can be easily changed for other wavelengths. Some systems have optical feedback mechanisms to provide image stability and the ability for millisecond pulsing. Synchronising image acquisitions with LEDs illumination times can reduce the levels of photobleaching.

2.4. Detectors

In order to convert the fluorescence from optical mapping experiments to images, the emitted photons need to be transduced into electrical charges. Many options exist based on two dimensional arrays of silicon elements. Factors to consider for a detector are the quantum efficiency, spatial and temporal resolution. When imaging hearts of small animals such as mice, the heart rates are an order of

magnitude greater than that of humans hence the need for fast readout rates. To follow the course of a mouse AP, one should use an acquisition rate of at least 1000 frames/sec [112].

2.4.1. Photodiode arrays (PDA)

Photodiode arrays will convert incident photons to a proportional current. Each diode is connected individually to a current-voltage (I/V) converter, which limits the number of elements which are possible to be spaced onto a single chip. The advantage of PDAs is that it they have high quantum efficiency ~90% but are extremely limited by pixel size. The most popular choice for a PDA is a 16 x 16 element array by Hamamatsu Photonics Corp (Japan) [112]. Another advantage is that as the signals from the diodes are analogue, there is constant generation of current which leads to fast sampling rates.

2.4.2. Charged coupled devices (CCD)

CCDs provide a significant advantage over PDAs due to their higher spatial resolution. Each element in the CCD stores a photogenerated charge which is integrated over a period of time, after which it is transmitted to a read out amplifier. For each device only one amplifier is required, this allows for the manufacture of arrays with a large number of elements. The quantum efficiency of CCD chips can be above 80% which makes them comparable to PDAs, but the rates of data acquisition are much lower. This can be increased by binning pixels together, but this reduces the spatial resolution, defeating its main advantage. One of the most advanced CCD devices used in optical mapping have an 80 x 80 pixel array with a frame rate of 2000/sec from RedShirt Imaging (Fairfield, CT). For increase rates

and quantum efficiency, a 3 x 3 binning mode is possible bringing the number of elements to 23 x 23 at 5000 frames/sec [112].

2.4.3. Complementary metal-oxide semiconductor (CMOS)

CMOS detectors are a form of image sensor with each pixel housing a photodetector and an active amplifier. CMOS sensors typically have a faster readout than CCDs. Recent developments have shown that CMOS cameras have efficiencies close to CCD detectors whilst retaining its high speed acquisition [97]. Disadvantages of CMOS detectors are that each sensor typically reads row by row which can bring about rolling shutter effects skewing images. Despite this, the latest devices from Hamamatsu Photonics allow for reduction of the vertical imaging area to increase readout speed whilst maintaining its horizontal pixel count [90]. One of their most used devices, the ORCA flash 4.0, enables readout speeds of 1603 frames/sec at 128 x 2048 pixels. Figure 2.8 shows the spectral response with a maximal QE of over 70% at 600nm. The wide horizontal pixel range can allow for dual imaging without the need of a secondary camera by using an image splitter to divide the incoming light onto the sensor. Each of the images can be filtered at different wavelengths and for different dyes. The advantage of dual imaging is that multiple parameters can be measured such as membrane voltage and calcium without the need for a secondary camera [94], [113].

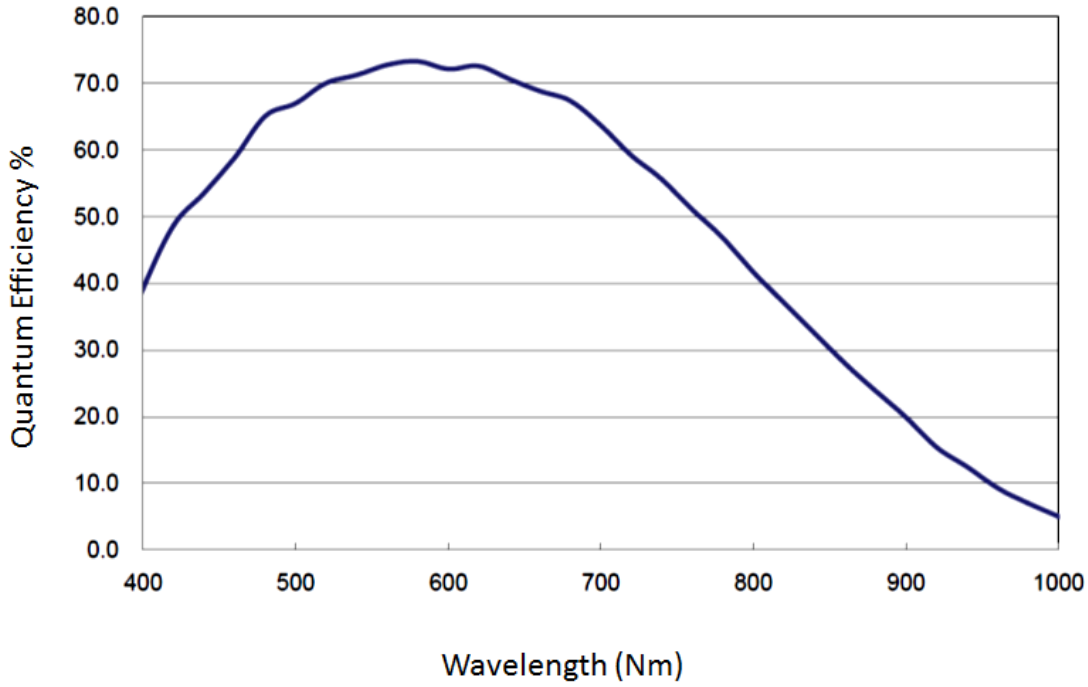

Figure 2.8. Spectral response of the Hamamatsu ORCA Flash 4.0 CMOS detector.

This graph shows the quantum efficiency in relation to the wavelength of the incident photons on the CMOS detector. The efficiency reaches a peak close to 600nm and at a wavelength of 465nm it has a good efficiency of over 50%, making it suitable for the fluorescence of di-4-ANEPPS which has an emission peak of 465nm. Image adapted from the *Hamamatsu technical notes for the ORCA Flash 4.0 September 2015.* Retrieved from: http://www.hamamatsu.com/resources/pdf/sys/SCAS0080E_C11440-22CU_tec.pdf

2.4.4. Contact maps

There exist other methods for imaging the depolarisation of cardiac tissue without the use of optics. This involves placing physical electrodes on the surface of the samples to form a contact map. Each electrode measures the depolarisation from a single cell or an aggregate of cells. Coupling multiple electrodes together can yield similar results to that of photodetectors as each electrode effectively represents a pixel in the image. The downside of contact mapping is the low resolution which is determined by the physical size of each electrode [88]. This method has limitations for measuring APDs in smaller samples such as the mouse atrium.

3. Materials and methods

3.1. Animals

All surgical procedures were performed according to the Animals (Scientific Procedures) Act, 1986 and were approved by the Home office and the local authorities.

3.2. Genetically altered models

Experiments were performed on heterozygous Plakoglobin deficient mice (plako$^{+/-}$) [64], [114] and Pitx2c$^{+/-}$ heterozygous mice [51], [55], [115].

3.3. Buffer solutions

For all experiments a standard bicarbonate buffered Krebs-Henseleit (KHB) solution was used containing in mM: NaCl 118; $NaHCO_3$ 24.88; KH_2PO_4 1.18; Glucose 5.55; Na-Pyruvate 5; $MgSO_4$ 0.83; $CaCl_2$ 1.8; KCl 3.52, equilibrated with 95% O2 and 5% CO2 and heated to 35-37°C. Under these conditions the pH was maintained at 7.4. All Chemicals used in buffer solutions were purchased from Sigma-Aldrich Corporation unless otherwise stated.

3.4. Data analysis

Values were expressed as mean ± standard error of the mean unless otherwise stated. Statistical analysis was performed using one way Analysis of Variance (ANOVA) with Bonferroni post hoc analysis where appropriate (GraphPad Prism 5.01). Significance was deemed as $p<0.05$ or considered very significant at $p<0.01$.

3.5. Surgical procedures

3.5.1. Murine anaesthesia

I initially weighed the mice and administered 50µl of heparin (LEO Laboratories Ltd, UK) by intraperitoneal injection. Heparin is an anticoagulant which prevents blood clots. A second intraperitoneal injection was administered by myself with 200mg/kg of pentobarbital sodium (Euthatal, Merial, UK) causing deep terminal anaesthesia. The pedal reflex was then checked to assure the mouse was under deep anaesthesia.

3.5.2. Heart isolation

Once the mouse exhibited no pedal reflex ensuring deep anaesthesia, it was then placed in the supine position on a polystyrene block with the limbs pinned down. Forceps were used to draw the skin from below the sternum and scissors were used to perform a bilateral dissection. The scissors were used to cut through the rib cage and to reveal the diaphragm. Perforating the diaphragm revealed the heart and the chest plate was pulled back. Curved forceps were used to scoop under the heart and fine scissors were used to sever the vessels releasing the whole heart which was then placed in a petri dish with cold KHB solution. The KHB solution was stored at 4ºC causing temporary cessation of cardiac activity known as cardioplegia. Cardioplegia temporarily stopped the heart from contracting which allowed for ease of cannulation. Lung and adipose tissue were often removed with the heart as a by-product of this procedure; these excess tissues were then discarded leaving behind the whole heart only. Subsequently, the hearts were transferred to a new petri dish with cold KHB on a custom stand

which housed a 2ml syringe and a cannula (outer diameter 1mm), as seen in Figure 3.1. The cannula was in such a position that it protruded into the dish below the solution. The aorta was identified and using forceps it was carefully stretched over the cannula ensuring the aortic valve was not blocked. Silk sutures held the aorta in place. Once on the cannula, 2ml of KHB was retrogradely perfused to remove the heart of any excess blood as seen in Figure 3.1. Time from first incision to coronary perfusion was kept below 5 minutes. On average samples were excised in approximately 2.5 minutes from the first incision of the thoracotomy limiting any tissue damage, coinciding with other studies [114], [116].

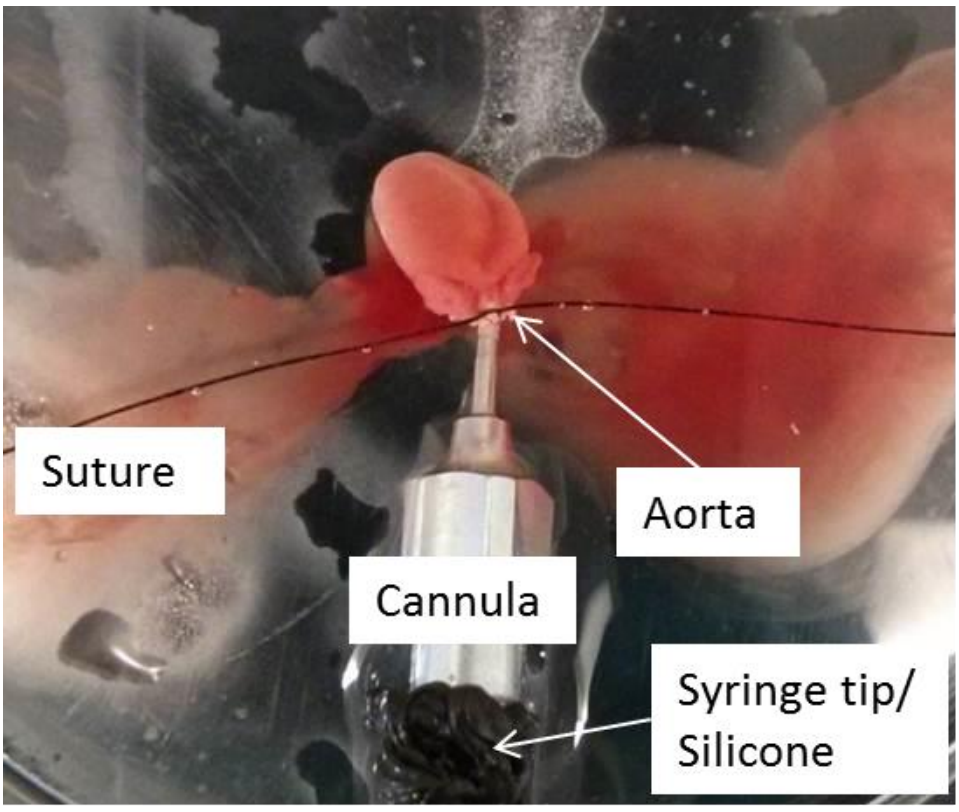

Figure 3.1. Cannulation of the ascending aorta.

This shows the heart cannulated at the aorta as indicated above. The cannula is connected secured by fine sutures, which can be seen as a fine black string across the image. The end of the cannula is connected to a 2ml syringe and held securely with black silicone, as indicated above. The heart is submerged in cold buffer solution to cause a temporary cessation of contractions of the heart. The syringe was filled with cold buffer (before cannulation) and depressed to expel the blood from the heart, as seen as the large red regions either side of the heart.

3.5.3. Langendorff perfusion and dye loading

The heart and cannula was transferred and mounted on a vertical Langendorff apparatus (Hugo Sachs, Germany) and perfused with KHB. The buffer was kept at 36-37°C, at constant perfusion pressure (100 ± 5mmHg) and coronary flow (4 ± 0.5ml/min). A small cannula made from a needle was inserted through the left ventricular wall to allow for any excess solution to drain as seen in Figure 3.2. Di-4-ANEPPS was chosen as it was one of the most currently used voltage dyes with a good fractional fluorescent change [93], [102], [104]. The di-4-ANEPPS (50 µM; Biotium, California, USA) was stored in 25µl aliquots of 5mg/ml. For each experiment an aliquot was mixed with 1ml of Krebs solution and injected through a bolus port in the Langendorff system over a period of 5 minutes.

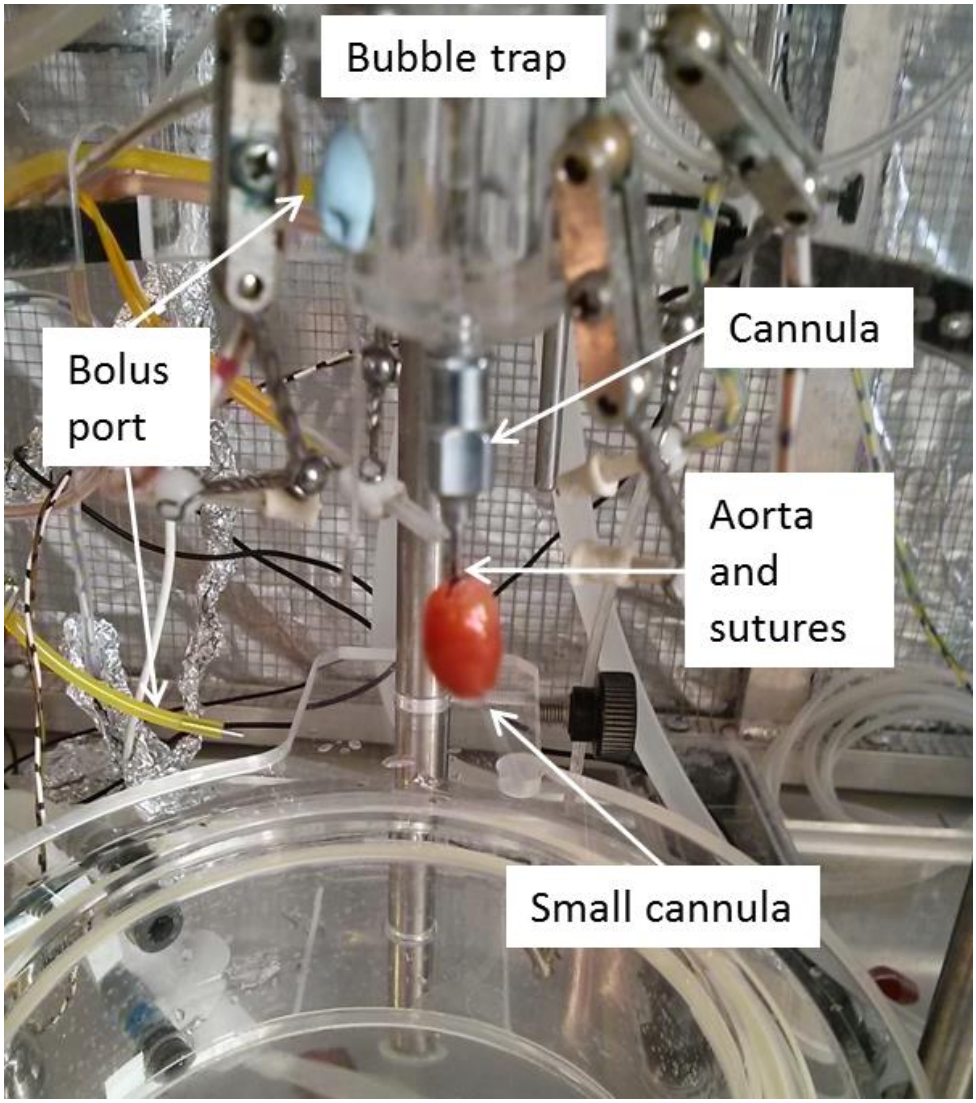

Figure 3.2. Langendorff preparation of the heart.

The heart is shown connected to the aortic cannula by its aorta with sutures. Warm perfusate (37ºC), was pumped to the heart passing a bubble trap at the top. Dye was added via a bolus port at the back of the bubble trap. The bolus port was connected to a piece of tubing as indicated above. The tubing allowed for easy infusion of the dye. A small cannula with an outer diameter of 1mm was inserted at the left ventricular wall near the apex to allow for excess fluid to drain, at the location indicated above.

3.6. Optical mapping

After 5 minute dye infusion on the Langendorff apparatus, the left atrium (LA) was carefully dissected away from the ventricles using fine forceps and scissors. The LA was subsequently transferred to a custom made superfusion chamber, where

the surface was covered in back silicone (Figure 3.3). The silicone aided in removing any background fluorescence. Two fine entomology pins were used to hold the LA in place. The pins were placed on the very edges of the tissue to ensure they did not obstruct the view of the camera. A space was left where the LA were attached to the septal wall to allow space for the stimulus electrodes. Preparations were continuously superfused with oxygenated KHB and the excitation-contraction uncoupler blebbistatin (5 μM; Cayman Chemical, Michigan, USA). The use of blebbistatin was important to inhibit the motion artefacts from contractions [55], [117], [118]. The solution was maintained at 35-37ºC by use of a heating element and a feedback thermometer created by Martyn Preston of Oxford University. The heating element was placed before the inflow of the solution with a bubble trap (Labtech, UK). Bubble traps were put in place so that these would not cause any ripples in the solution. The solution was transported using a peristaltic pump (Minipuls 3, Gilson, UK) providing a rate of 10ml/min. The excess solution was removed using a separate peristaltic pump (R323, Watson Marlow, UK) and returned to its original container for recirculation.

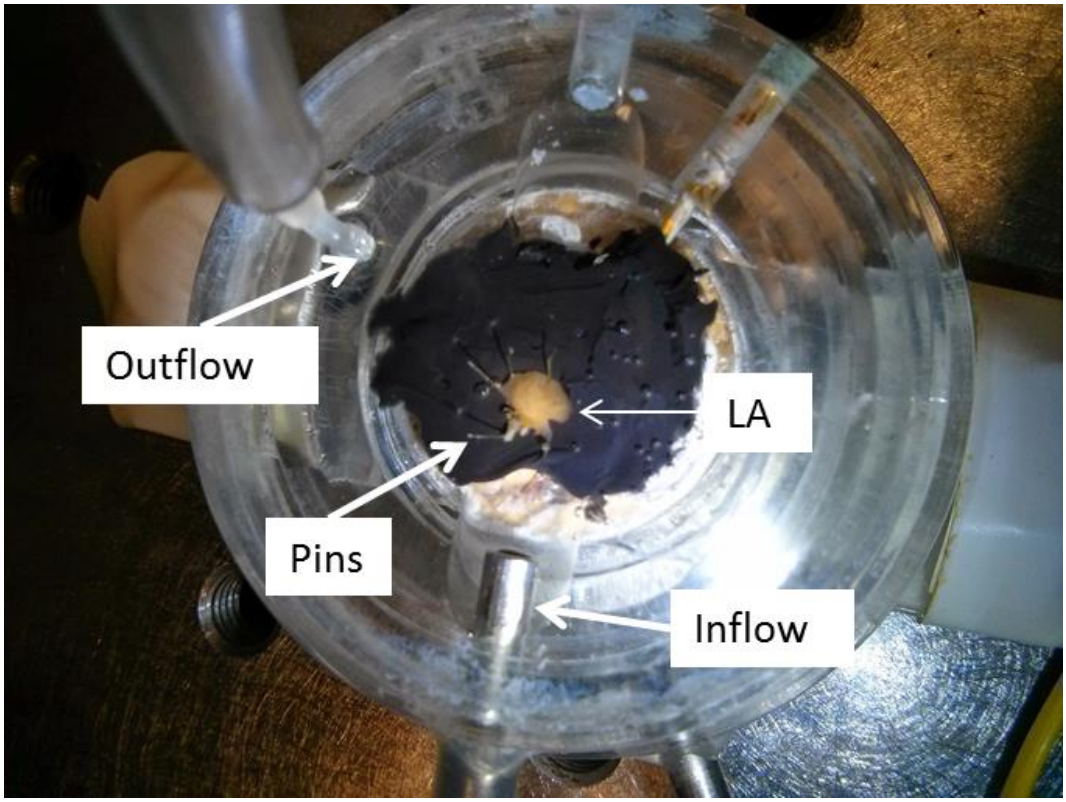

Figure 3.3. The left atrium pinned to the optical imaging chamber.

This shows the LA secured to the imaging chamber by several fine pins. The LA was pinned to a layer of black silicone. Warm buffer solution at 37ºC was pumped into the chamber by the inflow port, as shown above. The outflow was placed towards the opposite side of the inflow and above the solution.

The LA were paced at twice the diastolic threshold and kept stimulated at a rate of 200bpm or a beat every 300ms known as a cycle length (CL) of 300ms for at least 15 minutes to allow for the blebbistatin to inhibit contractions. The LA were then paced using the ramp protocol (300ms to 80ms CL) via platinum electrodes placed in the tissue bath at twice the diastolic voltage threshold at 2ms pulse width. Stimuli were generated using an isolated constant voltage stimulator (Digitimer, Hertfordshire, UK) driven by an analogue to digital converter with spike2 software (Cambridge Electronic Design, UK). The LA was field illuminated by two twin LEDs at 530nm (Cairn Research, Kent, UK). Wide field macroscopic images of emitted

fluorescence (630nm) were captured at a sampling frequency of 1 or 2 kHz using a novel, high speed, high resolution (128 by 2048 pixels, single pixel area: 6.5µm by 6.5µm) camera (ORCA flash 4.0; Hamamatsu, Japan). A schematic of the optical mapping system can be seen in Figure 3.4.

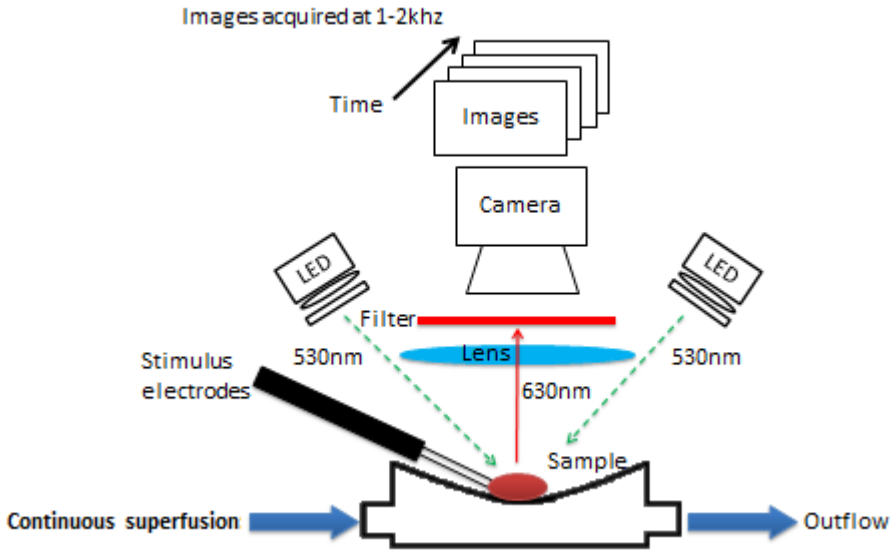

Figure 3.4. Schematic of the optical mapping system.

The LA sample was placed in the superfusion bath and imaged using the custom designed optical mapping system. Blue arrows indicate the inflow and outflow of the buffer solution which was kept at 35-37°C. The electrodes stimulate the sample at set rates and the LEDs illuminate at 530nm. Images were captured by the CMOS camera above the 630nm filter and lens at 1-2 kHz frame rates. Images were exported for offline analysis using automated algorithms.

3.6.1. Stimulation protocol

The stimulus electrodes were carefully placed on the edge of the LA in close proximity to the septal region. The LA was then stimulated at twice the diastolic threshold at a holding frequency of 300ms CL. To determine the diastolic threshold the stimuli were set to 0V and voltage was increased until beats were

seen on the time course window. The voltage was then set to double the minimum required to induce an action potential (AP). The samples were continuously superfused with blebbistatin to reduce the tissue contraction. After 15 minutes of blebbistatin infusion, the images were checked to determine whether there were any contraction artefacts. When the tissue had suitably stopped contractions the ramp protocol was initiated. The ramp consisted of stimulus cycles with decreasing length and as described as follows:

- Holding stimulus rate 300ms CL – 200bpm
- 300 beats at 120ms CL – 500bpm
- 50 beats at 100ms CL – 600bpm
- 50 beats at 80ms CL – 750bpm

After the ramp was executed, the stimulus rate returned to the holding frequency. Figure 3.5 illustrates the APs recorded during a typical protocol. The tissue was constantly stimulated at 300ms CL until the ramp was initiated at 10 seconds after the start of recording. After the 50 stimulations at 80ms CL the LA returned to a stimulated rate of 300ms.

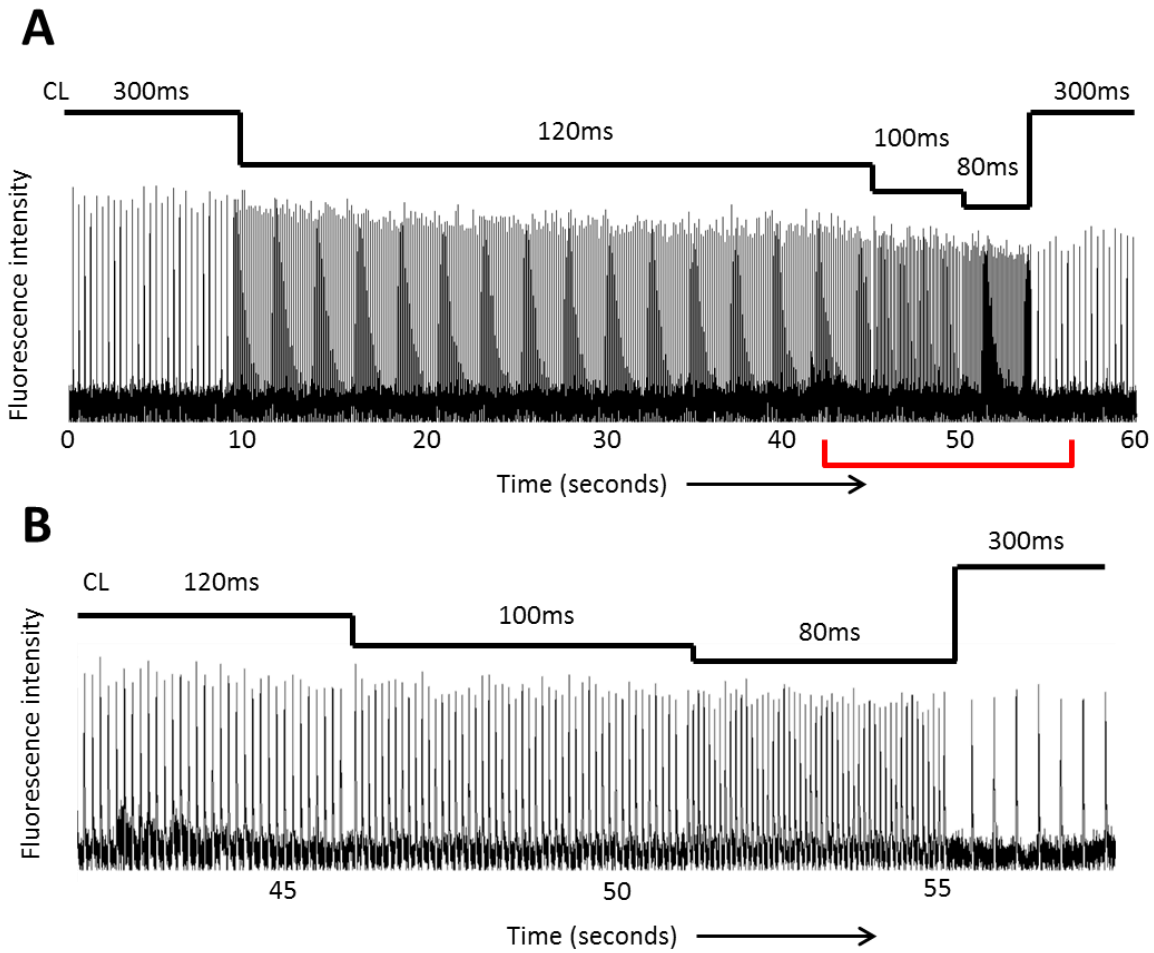

Figure 3.5. Action potentials recorded over ramp protocol for a period of 60 seconds.

A) Shows the optical APs recorded over 60 seconds during the ramp protocol. An initial holding rate of 300ms was used, after which the ramp protocol was selected. The ramp was started after 10 seconds of recording. 200 stimuli were recorded at 120ms CL taking 36 seconds, 50 stimuli at 100ms taking 5 seconds. Finally, the last part of the ramp takes 50 stimulations at 80ms CL taking 4 seconds. After the ramp, the protocol returns to the holding frequency which is shown above at 55 seconds onwards. The red bar highlights the zoomed in area for B).

3.6.2. Image recordings

Images were extracted and collated using WinFluor V3.4.9 (Dr John Dempster, University of Strathclyde, UK) so that the fluorescence intensity from a specific region of interest (ROI) of 4 x 4 pixels was viewed as a single continuous waveform. This permitted the identification and monitoring of a greater number of

optical action potentials (OAPs) across the entire surface of the mouse LA at high spatial resolution. Isochrones are lines which connect points of equal activation time. Isochronal or activation maps are commonly used to depict the activation pattern from a cardiac tissue sample [119]. The image recordings gathered here were exported as uncompressed Tagged Image File Format (TIFF) and were used to generate isochronal activation maps.

3.6.3. Flecainide infusion

For experiments with flecainide, 1 µM of the drug (Flecainide acetate, Tambocor, Meda Pharmaceuticals, Bishop's Stortford, UK) was added to the KHB and superfused for 15 minutes before repeating the stimulus protocol [92]. The time course trace was observed to ensure that there was no loss of capture at any of the CL. If any beats appeared to be missing, the LA was left to be stimulated at the holding frequency for at least a minute before repeating the ramp protocol. If there was a significant loss of capture which was more common at the shorter CLs, the stimulation threshold voltage was determined at the shorter CL. Doubling the threshold voltage, the ramp was repeated. After each experiment it was important to flush the optical mapping system with KHB to remove any remaining flecainide.

3.7. Monophasic action potentials (MAPs)

MAP recordings were obtained in the intact, perfused heart immediately prior to dissecting the LA for optical mapping. Whole hearts were cannulated and mounted on a vertical Langendorff apparatus (Hugo Sachs, Germany) and the aorta was retrogradely perfused with standard bicarbonate KHB solution at 36-

37°C, at constant perfusion pressure (100 ± 5mmHg) and coronary flow (4 ± 0.5ml/min). A 2.0 French octapolar mouse electrophysiological catheter with electrodes sized 0.5mm and spaced at 0.5mm (CIB'ER MOUSE, NuMED, LLC., Hopkinton, N.Y., USA) was inserted into the right atrium (RA) for pacing (120ms to 80ms, 2ms pulse width), see Figure 3.6A and B. Stable LA MAP recordings were obtained using a miniaturised MAP catheter mounted on spring-loaded electrode holders. Figure 3.6A shows how MAP electrodes were placed on the heart for measurements from other chambers such as the right atrium and the left ventricle (LV) as well. This also served to stabilise the heart during contractions for better contact between the LA and the electrode. Figure 3.6B shows the schematic of the heart, octapolar catheter and the location of the MAP recording electrode. Figure 3.6C displays the schematic of the MAP electrode. Voltage signals were amplified, digitised and viewed on a PC loaded with iox2 software (EMKA, France). Measurements of APD and inter-atrial activation times were acquired using algorithms generated in iox2. MAP experiments were performed by Dr Fahima Syeda from the University of Birmingham, UK and not by the author of this thesis.

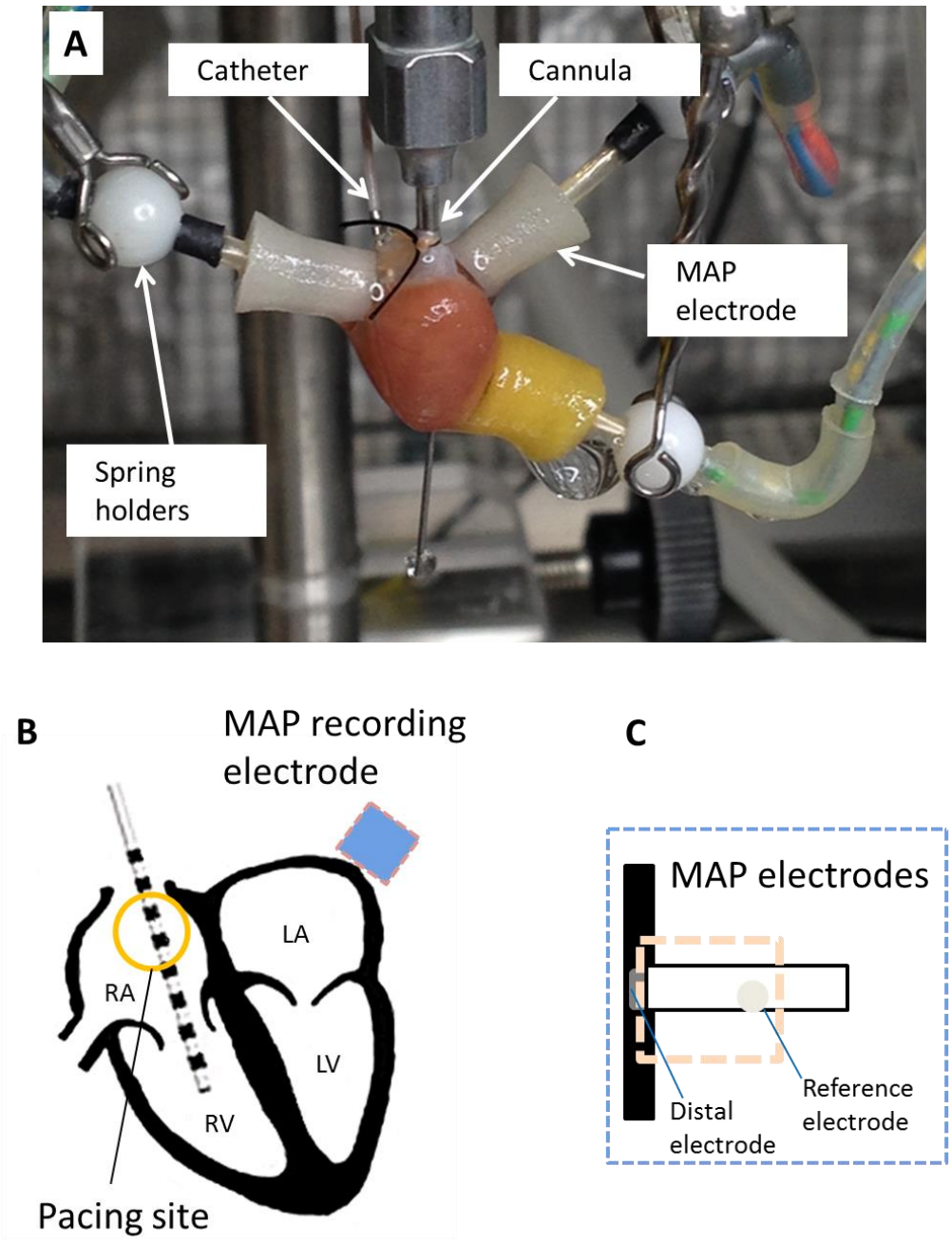

Figure 3.6. Whole heart stimulation and MAP recordings on the Langendorff apparatus.

A) Image taken from a typical Langendorff experiment. The aorta is cannulated and MAP electrodes were placed onto the chambers of the heart. The catheter is inserted to the right atrium (RA) as indicated. MAP electrodes were held in pace by spring loaded holders. B) Illustrates the heart, octapolar catheter and the recording electrode. An octapolar catheter as shown by the black and white rod was inserted through the RA to the right ventricle (RV) for stimulation. The blue square represents the MAP electrode placed onto the left atrium (LA) for measurement. The left ventricle of the heart is chamber labelled LV. C) Schematic of the MAP electrode placed onto the LA. The surface of the tissue is represented by the black vertical block. Figure has been adapted and edited from unpublished work created Dr Fahima Syeda from the University of Birmingham, UK and not by the author of this thesis.

3.8. Transmembrane action potentials (TAPs)

Transmembrane murine atrial action potentials (TAP) were recorded as published [85] immediately before or after the optical mapping procedure. TAPs were recorded from isolated superfused LA samples prepared using the same procedure as optical mapping with borosilicate glass microelectrodes (tip resistance 15-30 MΩ), filled with 3M KCl. Figure 3.7 illustrates how TAPs were recorded, the location of the stimulus site on the LA is located nearest to the septal wall. Voltage signals were amplified (Axoclamp 2B; Molecular Devices, USA), digitised and displayed using spike2 software (Cambridge Electronic Design, UK). The sampling frequency was 20 kHz. Preparations were paced successively using the ramp protocol (300ms to 80ms) with platinum electrodes at twice the diastolic voltage threshold, with a minimum of 50 APs recorded at each CL using an isolated constant voltage stimulator (Digitimer, UK) driven by an analogue to digital converter with Spike2 software (Cambridge Electronic Design, UK). Measurements of APD and intra-atrial activation times were obtained using custom–made spike2 algorithms. Microelectrode recordings were performed by Dr Andrew Holmes from the University of Birmingham, UK and not by the author of this thesis.

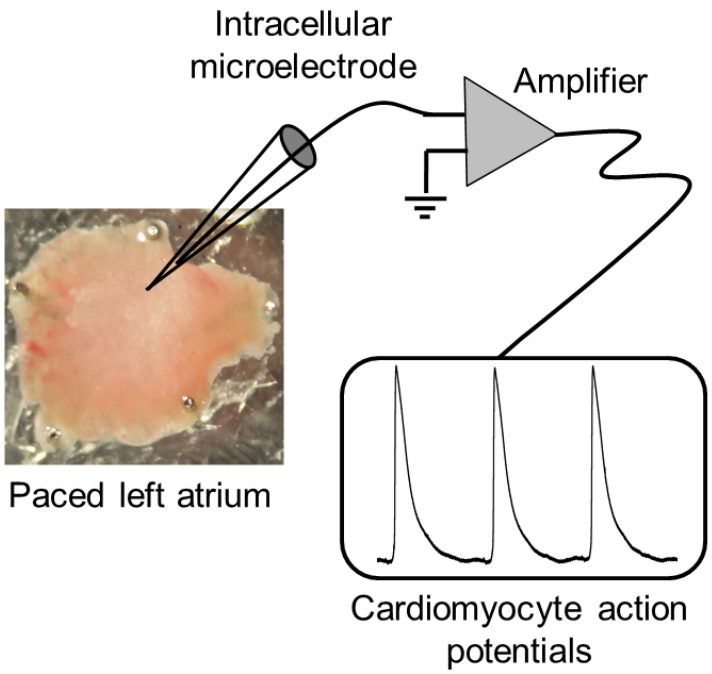

Figure 3.7. Microelectrode recordings from the left atrium.

Atrial samples were continuously superfused with KHB solution at 35-37ºC and pinned to a recording chamber as seen in the photograph portion above. Glass microelectrodes with a tip resistance of 15-30MΩ were used for recoding voltage signals. Signals were amplified and recorded using Spike2 at a sampling rate of 20 kHz. Microelectrode recordings were performed by Dr Andrew Holmes from the University of Birmingham, UK and not by the author of this thesis. Figure has been adapted and edited from unpublished work created Dr Andrew Holmes from the University of Birmingham, UK and not by the author of this thesis.

4. Optical mapping design and development

4.1. Overall design

The main hardware components to the optical mapping system consisted of the imaging chamber or superfusion chamber, illumination light emitting diodes (LEDs), filters and camera which can be seen in Figure 4.1. Each component is described below but also along with the necessary methods for imaging acquisition. Finally, after data collection, the methods used to analyse optical mapping images are described in detail as these were custom made algorithms in MATLAB.

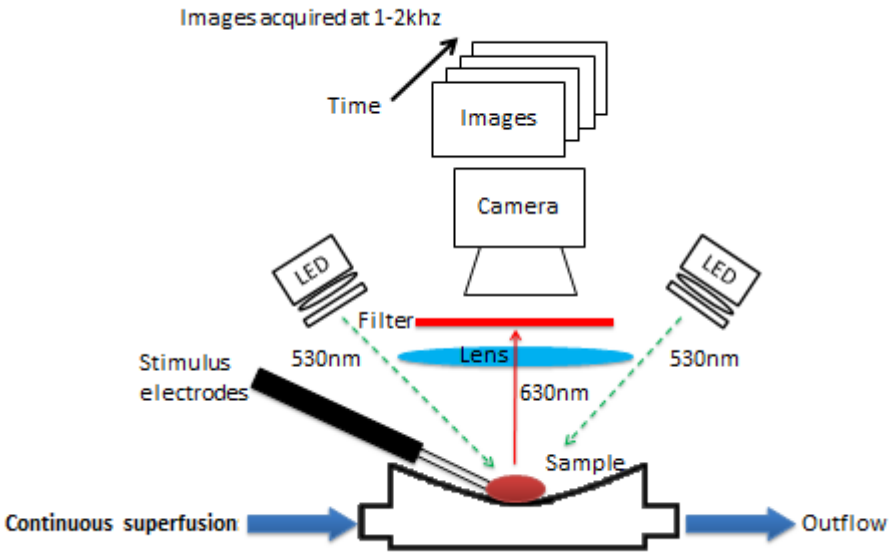

Figure 4.1. Schematic of the optical mapping system.

The left atrial sample was placed in the superfusion bath and imaged using the custom designed optical mapping system. Blue arrows indicate the inflow and outflow of the buffer solution which was kept at 35-37°C. The electrodes stimulate the sample at set rates and the LEDs illuminate at 530nm. Images were captured by the CMOS camera above the 630nm filter and lens at 1-2 kHz frame rates. Images were exported for offline analysis using automated algorithms.

4.2. Superfusion system

During experimentation, the left atrium (LA) was continuously superfused with oxygenated KHB. The LA was pinned down to black silicone (Silcoset 158, ACC Silicones Limited, UK) on a custom made superfusion chamber. 10mm neodymium magnets (Rapid Electronics Ltd, UK) were used to hold the chamber onto an optical bench. The solution was maintained at a temperature of 35-37ºC using a heater module and feedback thermometer which was managed by a control module which indicated the thermometer temperature and the heater temperature. The heating element inside the module consisted of an Aluminium clad wire wound resistor with an embedded thermocouple for temperature control and 4 stainless steel pipes fitted into the housing to transfer heat to the bath solution. The heating module and control unit was constructed by Martyn Preston (Department of Pharmacology, Oxford University, UK). The position of the thermometer was placed between the inflow and the tissue which ensured accurate measurements. Typically, setting the heater to 44ºC allowed the perfusate to cool to the desired temperature by the time it took to reach the chamber through 17cm of tubing. A bubble trap (Labtech Ltd, UK) was placed between the heater and the superfusion chamber to remove any bubbles that would enter the inflow and disrupt the imaging. Figure 4.2 shows how the KHB is heated and bubbles removed before it reaches the chamber for imaging. Black silicone rubber was placed at the centre of the superfusion chamber as this allowed for the pins to be inserted with tissue. Black also limits the amount of reflected light during imaging. The superfusate was transferred to the chamber using a peristaltic pump (Minipuls 3, Gilson, UK) and removed by use of another

peristaltic pump (R323, Watson Marlow, UK). The KHB was returned to its original container for recirculation.

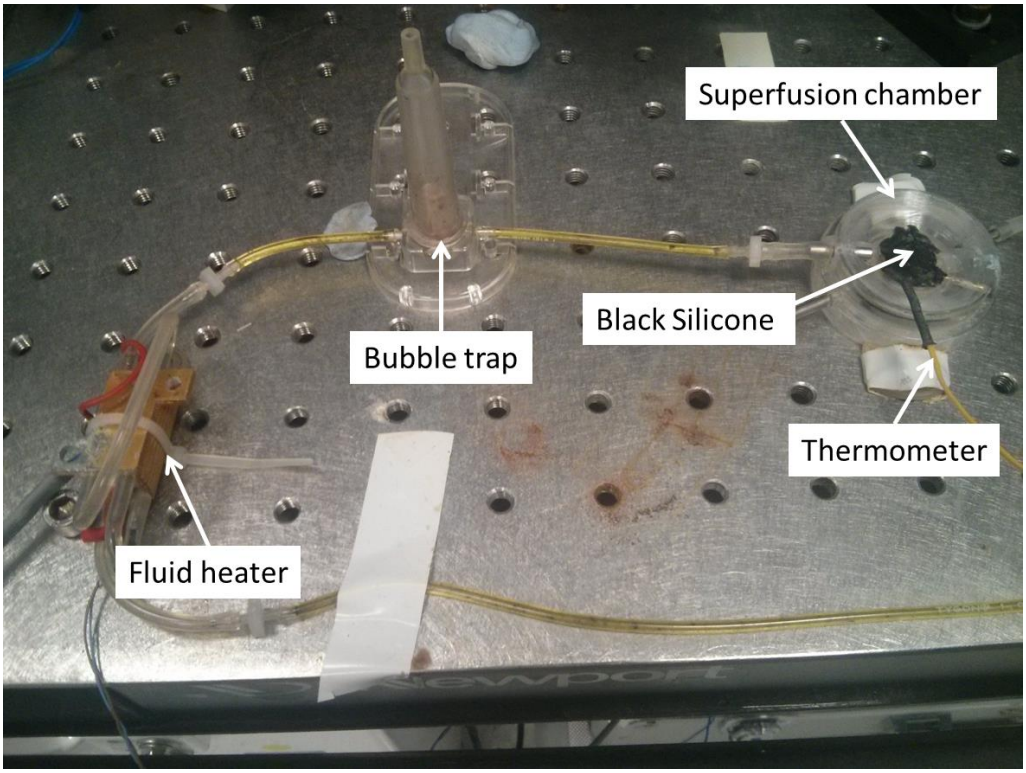

Figure 4.2. Optical mapping superfusion system.

The KHB solution was pumped through the tubing as shown above. The solution was then heated using a custom made heater set to 44ºC. As the buffer travels through to a bubble trap as indicated above. The buffer solution cools from 44ºC to 35-37ºC as it moves through the 17cm of tubing to the superfusion chamber. Black silicone rubber was placed in the centre of the chamber as shown above to allow for tissues to be pinned onto the surface. The black silicone limits the amount of reflected light. A thermometer was placed close to the entrance of the superfusate to regulate the solution temperature.

4.3. Optics

Tissues stained with di-4-ANEPPS were excited by a set of 2 dual LED lamps (OptoLED, Cairn Research, UK). The excitation wavelength for di-4-ANEPPS is 465nm and its peak emission is at 635nm. The power source was set to feedback which allowed for continuous stable luminosity. The LED heads were placed in close proximity surrounding the superfusion chamber and were filtered using 530/40nm filters (Chroma, USA), see Figure 4.3. The emission photons were focused through a C-mounted lens (Schneider-Kreuznach, Germany). This lens has an f-number (N) of 0.95 which equates to a numerical aperture of 0.52 using Equation 1. The outflow nozzle was kept out of the line of sight from the tissue to the lens as shown in Figure 4.3B. The nozzle was placed over the top of the solution to allow for the level of fluid to be maintained at the desired amount.

$$N \approx \frac{1}{2N_A} \quad \textbf{(1)}$$

Equation 1. F-number.

Equation to determine the relation between f-number (N) and numerical aperture (N_A) of a lens.

The lens was mounted onto an image splitter (Optosplit II, Cairn Research, UK) which housed a filter cube with a dichroic mirror (Cairn Research, UK) with 50% transmittance at 546nm. The incoming light was split into two paths where one was filtered using a 630nm long pass filter (Chroma, USA) and the other was blocked though the auxiliary component mount. For future use the secondary mount would be used for other filter ranges and dyes. After filtering the light passed onto the CMOS detector (ORCA Flash 4.0, Hamamatsu, Japan).

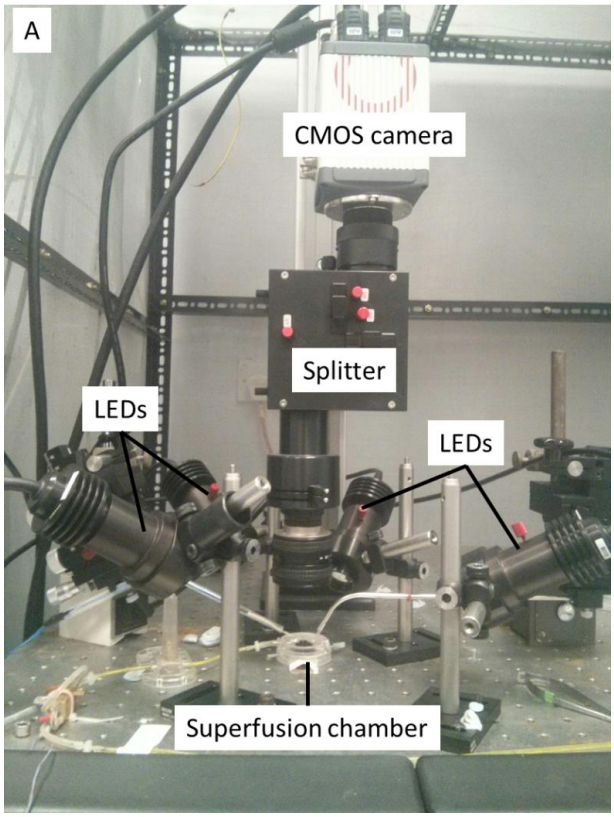

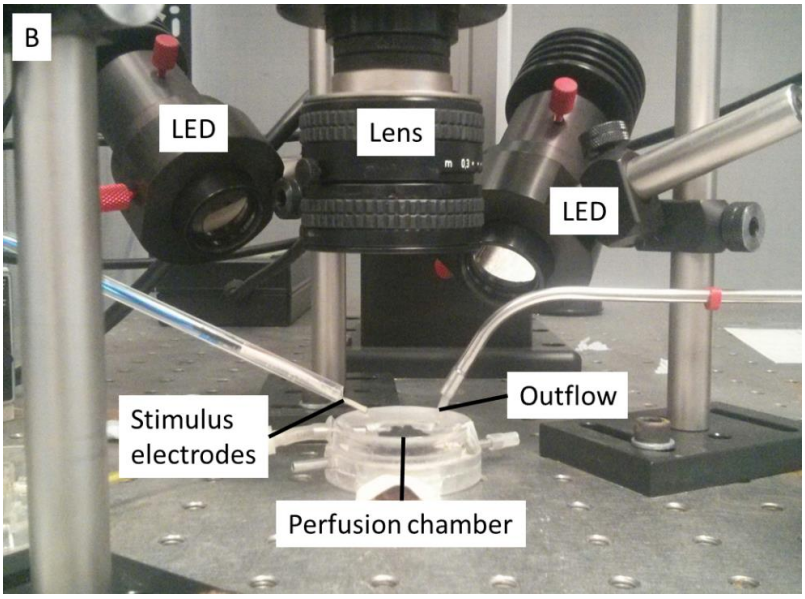

Figure 4.3. Optical mapping set up.

A) Shows the imaging rig which was built on an optical bench. The LA was placed in the superfusion chamber were it was illuminated by the LEDs at 530nm. The emitted light passes through the splitter to the camera at the top. B) Shows a close up of the superfusion area, the outflow tube was placed over the top of the solution on the opposite end of the inflow. Placing the nozzle over the top allowed for the solution to be maintained at a constant level. The stimulus electrodes were placed at an angle to allow for easy reach to the tissue. The LEDs were also placed at an angle and to provide an even illumination.

4.4. Image Acquisition

All imaging data was collected using WinFluor Version 3.4.9, developed by Dr John Dempster of Strathclyde University, UK and not by the author of this thesis. This software was designed for electrophysiology fluorescence imaging. The Flash 4.0 camera has 2048x2048 pixels; this allowed a maximum readout of 100 frames/sec. In order to increase the time resolution, the vertical number of pixels was reduced as the camera utilised a rolling shutter, reading line by line from the centre. To achieve a minimum readout of 1000 frames/sec, a maximum number of 2048 x 204 pixels were used. Relation between frame rate (fr) and number of vertical pixels (Vn) is given by Equation 2. The number of horizontal pixels has no effect on the camera readout time. To achieve the fastest frame rates, the imaging area was taken from the centre of the sensor. The Y-pixel range was selected from 922-1026, this represents 1024 ± 102 pixels from the centre to obtain a vertical pixel length of 204 lines. As the horizontal length did not change the readout time, the X range was chosen anywhere between 0-2048.

$$fr = \frac{1}{\left(\frac{Vn}{2}\right) \times 9.74\mu s} \quad \textbf{(2)}$$

Equation 2. Frame rate calculation.

Equation to determine the frame rate of the camera from the number of vertical pixels used. Where fr is the frame rate and Vn is the number of vertical lines.

At 1000 frames/sec the maximum exposure time was set to approximately 1ms. For high speed recordings such as described here, large volumes of data were generated. In order to decrease the data sizes, the number of horizontal pixels

was reduced so that only the LA was visible in the window. The camera converts photons that reach the sensor to 16 bit data values; therefore the fluorescence has 65,535 shades of grey. A region of interest (ROI) of 4 x 4 pixels was selected from the centre of the LA image; this provided a time course of the fluorescence. To maximise the fractional fluorescent change of the dye, the fluorescent intensity was kept as high as possible by increasing the LED power source during image acquisition. For example, a fluorescent signal of 60,000 units with a 10% ΔF/F would give a 6,000 unit change. A signal at 30,000 with the same ΔF/F yields a 3,000 unit change, showing a lower signal to noise ratio. The LED lamps were switched off during recordings as this reduced the risk of photobleaching. To record the entire stimulus protocol, a 60 second time lapse mode was set.

4.5. Pixel binning and improvement of temporal resolution

To gain a stronger signal to noise ratio of the changes in fluorescence, pixels were binned together using a 4 x 4 region posteriorly. Figure 4.4A shows the effect of varying region size, the trace was exported from the same area. The trace from the 4 x 4 ROI shows 10 optical action potentials (OAPs) over a period of 1 second, whereas the single pixel trace contains large amounts of noise. It was possible to visualise the 10 OAPs from the single pixel trace but analysis proved impossible using the algorithms stated. To gain a higher temporal resolution, the camera acquisition speed was increased to 2000 frames/sec by halving the vertical window size and decreasing the exposure time to 0.5ms. Figure 4.4, demonstrates how the AP shape and length remains largely unchanged as a result of increasing the acquisition speed as seen in the overlaid trace. This limited the size of the

tissues which were recorded but testing the differences in APs showed no changes in morphology. Hence, it was decided to use a frame rate of 1000 per second as this allowed us for greater resolution isochronal maps.

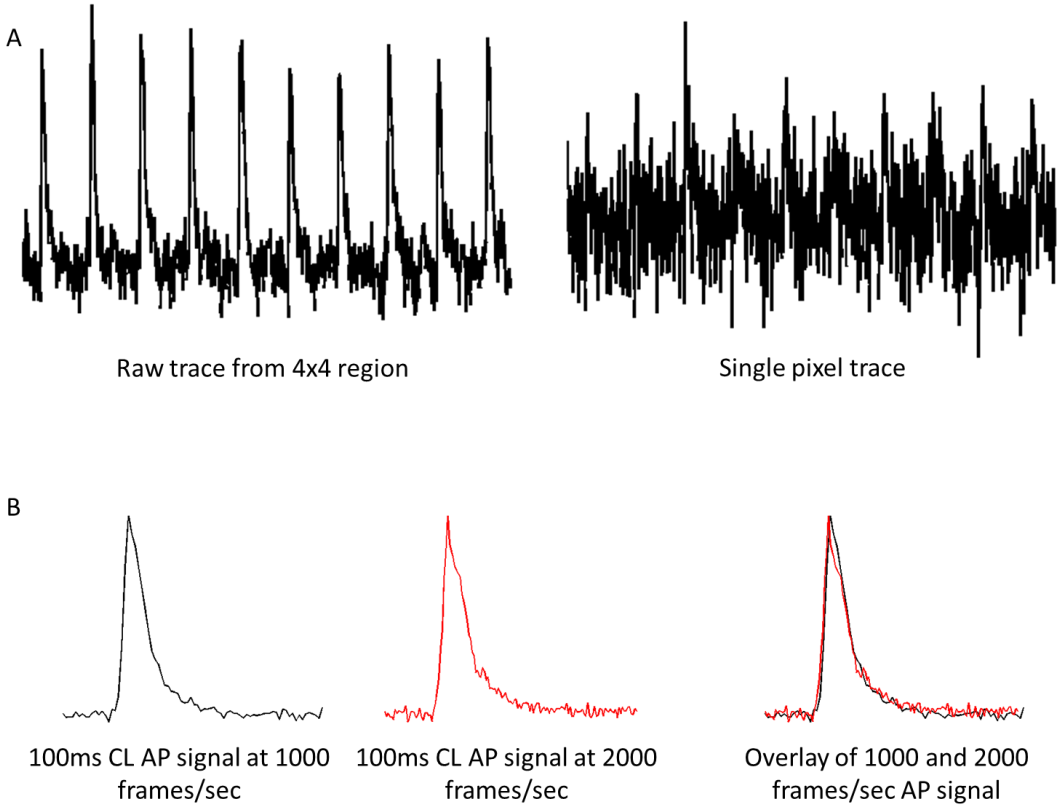

Figure 4.4. Raw data traces from different region sizes and acquisition rates.

A) Represents an optical trace over a period of one second stimulated at 100ms CL. The signal from a 4 x 4 ROI on the right show 10 distinct peaks with the repolarisation clearly visible. The trace displayed on the left was taken at the same region but from a single ROI. The peaks were visible from the single pixel region but contain high levels of noise and the repolarisation cannot be clearly seen and analysed. B) Shows a comparison of an AP signal stimulated at 100ms CL at different recording rates. The signal in black is recorded at 1000 frames/sec and the red trace at 2000 frames/sec. The overlay trace shows that at different recording rates the AP morphology remains the same. It should be noted that the example AP signals shown here were taken at the same region from the same sample.

4.6. Pixel calibration

The size of each pixel on the CMOS detector was listed as 6.5µm. To convert the pixels to physical space, a known length was measured against its image length in pixels. A ruler was placed under the lens of the rig and a single image was taken, the image was then converted to TIFF and analysed in ImageJ (National Institutes of Health, USA). To measure the distance between two known lines on the ruler, the straight line tool was used to draw between the two points. The 'measure' function outputted the line information; from here the distance in pixels was given. To obtain the resolution of the system the physical distance was divided by the length of the drawn line. The distance between 10mm was 140 pixels which results in a resolution of 71.4µm per pixel.

4.7. Data processing

4.7.1. Exporting data

The WinFluor software generated image files in .IDR format, from here the data was either exported to an image series in tagged image file format (TIFF) or a region of interest (ROI) time course as a text file.

In order to generate isochronal or activation maps, an image stack of an individual beat was selected at each of the paced cycle lengths (CL). The last beat of the 300ms section of the protocol was selected. The frames before and after the AP was selected and exported to TIFF format. As each set of data contained all the CL information, the exported files were renamed to add '300ms' in the filename.

This was repeated for the CL at 120ms, 100ms and 80ms and the exported files were renamed as appropriately.

To calculate action potential duration (APD) values, a 4 x 4 pixel (ROI) on the image was selected and exported as plain text. The last 25 beats of each of the stimulus CL were exported. The exported text file was renamed to add the CL in the filename. The text file contains two columns of information, the first column indicates the time in seconds and the second column the fluorescence values. Nine regions were also exported for investigating the LA heterogeneity. The WinFluor software exported all selected regions into a single text file. The first column of data in this text file indicates the time and columns 2-10 represents the fluorescent data for region one onwards. A MATLAB script was used to separate these columns into a separate file containing only one region of data. Firstly, a new text file was created and the time column of data from the original data file was copied to the new file. Subsequently the second column for region one was copied to the new text file. This was repeated so that column one of every new file indicated the time and the second column was the fluorescent data for each subsequent region.

To investigate the heterogeneity of the LA further, APD maps were also generated. This was done by selecting the last 10 beats from the data set at each CL and exporting this as an image series in TIFF format.

4.7.2. Calculating APD values

The algorithms used to calculate the APD values from the fluorescence data were performed using MATLAB version 7.12.0.635 (R2011a) on a 64-bit Intel® Core™ i7-3820 desktop machine running Windows 7 Enterprise (Stone Group, UK).

4.7.2.1. Baseline wander correction

Firstly, the fluorescence data which were exported to text files were loaded into the MATLAB space. The optical APs presented here showed a decrease in fluorescence as the cardiac cells depolarise. In order to convert these signals to traditional APs whereby the voltage increases as cells depolarise, the traces were inverted by using the 'imcomplement' MATLAB function. The obtained traces often exhibit shifts in baseline which was attributed to changes in the surface of the bath solution causing ripples which introduces refraction to the illumination. Photobleaching also causes a decline in fluorescence intensity which can be modelled by an inverse exponential decay [1]. As these recordings were taken over a short period of a few seconds, this contributed minutely to the shift in signal.

The shifting baseline may display linear or non-linear behaviour. Several methods were investigated to correct this artefact so that APD values can be calculated correctly. However, creating a constant baseline becomes difficult when the drift pattern varies per experiment or pixel within the same tissue. The first method tested was using a polynomial fitting algorithm to characterise a signal trace with moderate drift and repeated with a slightly more complex drift.

Figure 4.5 Illustrates the resulting polynomial fitting on a set of two different drift patterns taken at 100ms CL over 3 seconds. It can be seen that the 4^{th} order polynomial in Figure 4.5A show a reasonable fit and Figure 4.5B shows the flattened signal. However, on a slightly complex pattern the 4^{th} fitting breaks down as shown in C and D. To compensate for this, higher order polynomials were used

to test the fit. As a result, the 11^{th} order showed a good sign of flattening of the signal as seen in Figure 4.5E and F. From Figure 4.5F the signal shows signs of tailing off at the end. Whilst this shows a good method for baseline drift correction, changing the polynomial parameters per trace was inefficient.

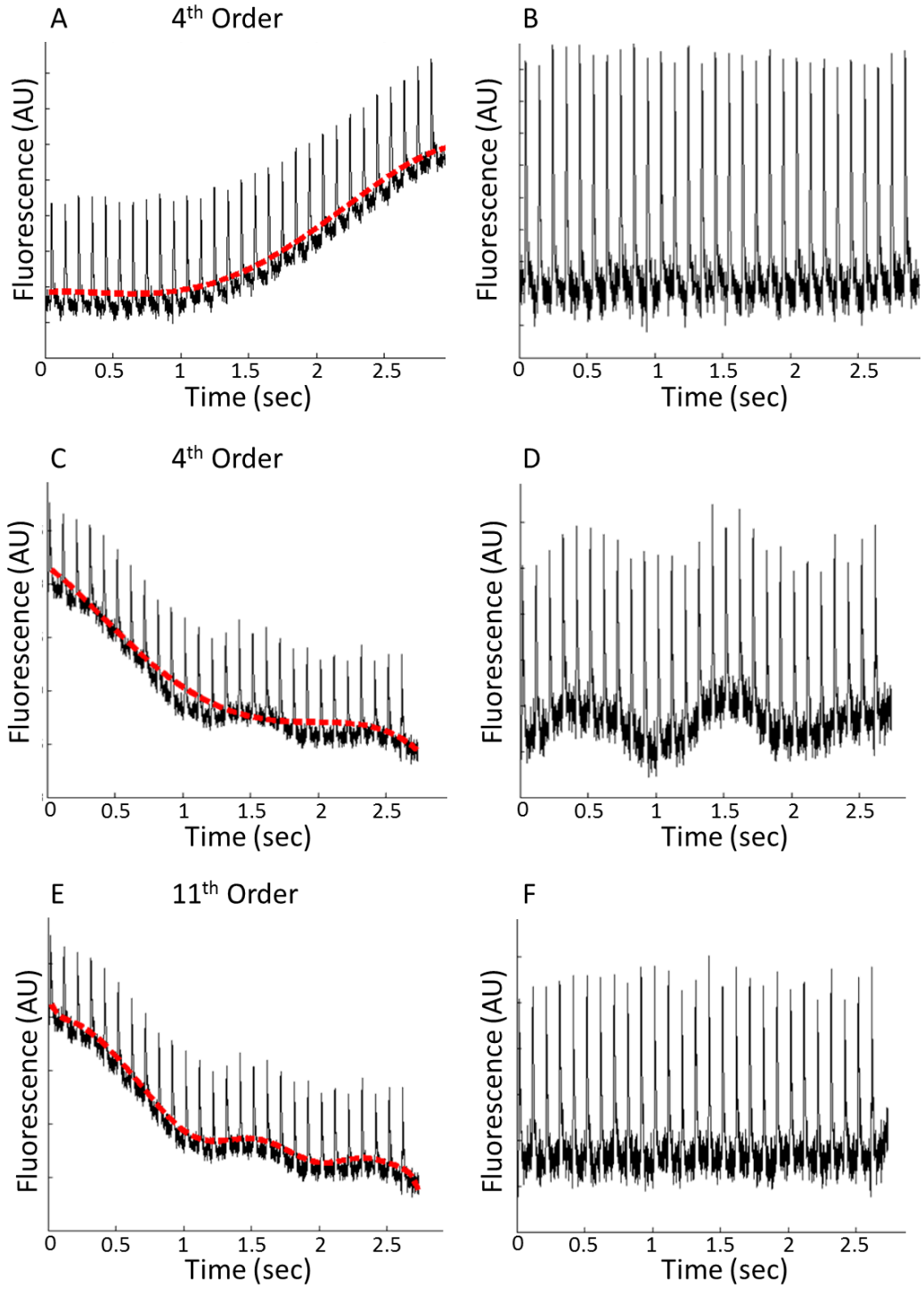

Figure 4.5. Baseline drift removal by polynomial fitting.

Examples taken from a 3 second time course from the LA stimulated at 100ms CL with a varying baseline. A) Shows the fitting for a 4th order polynomial on the red dashed line. B) Shows the corresponding trace with the drift removed by subtracting the polynomial fit from the signal. C) Shows the 4th order polynomial fitting in red on a more complex drift pattern. D) Represents the results from the fitting on the signal, showing that the baseline remained uneven. E) Demonstrates an 11th order polynomial to fit the complex drift pattern showing a good fit. F) Displays the resulting baseline corrected trace but it should be noted that the end of the signal shows an elevated tail.

As the baseline drifts do not appear to follow a predetermined pattern, a method was required which was robust for many signal morphologies. Another method tested was to apply a linear top hat transform to filter the signal. This removes the difference of the signal and its opening by a given structuring element. The MATLAB function ‘imopen’ performs an opening function to an image but applying this to a 1D signal provides a basis for the top hat filter. The structuring element used was linear with a length of 100 points over an angle of 90 degrees. The angle was specified by the desired orientation of the line measured counter clockwise from the horizontal axis. The length is the approximate distance between the centres of the structuring element members at opposite ends of the line. 100 was found to be sufficient for the purpose of correcting baseline drift at all CLs. Small changes in the length yielded little difference in APD value. Figure 4.6 illustrates the efficacy of the top hat filter. It shows the top hat filter applied to the same signals in Figure 4.5. Figure 4.6A shows a signal stimulated at 100ms CL which has a simple drift. Figure 4.6B shows that the baseline has been corrected. Figure 4.6C and D display a complex drift pattern which has been corrected with the same parameter as the previous signal. The lack of changing of the input parameters provides a distinct advantage of the polynomial fitting method that allowed for this process to be automated. Other methods to solve this problem exist, such as retrospective shading methods for images [120]. Further information can be found in the discussion section of this chapter.

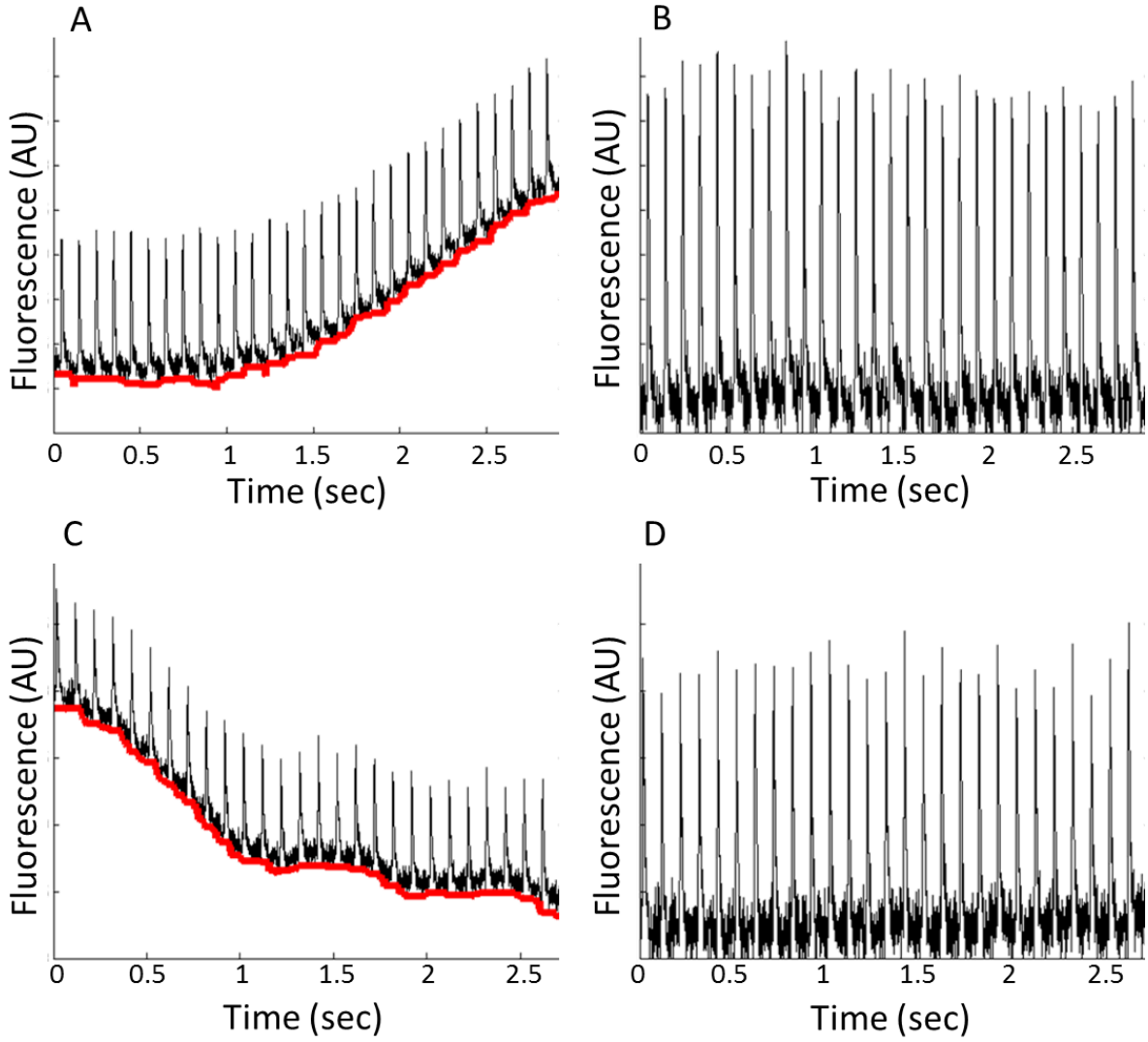

Figure 4.6. Baseline drift removal using a linear top hat filter.

Example signals taken from a 3 second time course from the LA stimulated at 100ms CL with a varying baseline. A top hat function was applied to these signals with a structuring element of 100 points in length with an angle of 90 degrees. The baseline is indicated in red. A) Demonstrates the top hat filter applied to a simple drift which is corrected in B. C) Shows the top hat filter applied to a complex drift pattern with the same parameters as A to yield a flattened baseline signal shown in D.

4.7.2.2. Signal averaging

It is common practice to smooth the signals by using a temporal filter and taking measurements from several APs to provide an average. Extending this idea of smoothing and measuring multiple APs, repeat measurements of consecutive APs were recorded and combined to produce an average AP. This allowed for the SNR to be increased.

The first step was to identify each individual AP in the data set. The ‘findpeaks’ function was used to locate the maxima within the trace. The criteria for defining a peak were given by any values which were over half the height of the maximum value. As the shortest CL in the protocol was 80ms, the minimum peak distance from one to the next was defined as 50ms to ensure that the software did not confuse smaller maxima as APs. Subsequently, after locating the peak of each AP, the whole of the AP was defined as 20 frames before and 60 frames after the peak. Ignoring the first and last peak, the APs were then stored in a 3D matrix (frame x fluorescence value x AP). The fluorescence value for each frame for every AP was averaged which generated an overall mean AP as seen in Figure 4.7. The first and last peaks were neglected as a way to prevent errors as the algorithm was required to look 20 frames before and 60 frames after a peak, this often resulted in exceeding matrix dimensions.

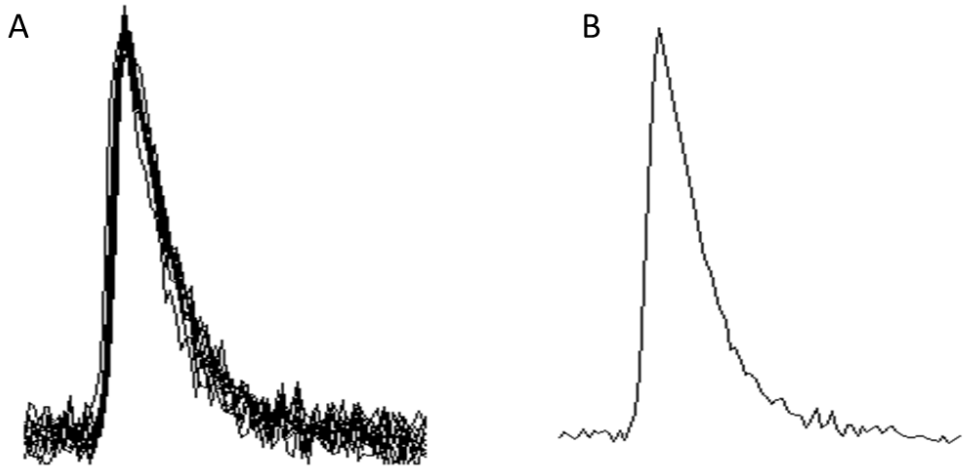

Figure 4.7. Signal averaging.

An optical trace where 10 APs stimulated at 100ms CL from the LA was used to demonstrate how they were averaged to obtain a mean AP. Each peak of the signal was obtained using the 'findpeaks' function in MATLAB. From the peak, 20 points before and 60 points after was deemed as the whole length of the AP. The criteria for determining the peak was set to locate points over half the maximum value in the signal and a minimum distance of 50 points between peaks. A) Shows an overlay of the 10 optical APs which was stored in a separate matrix. B) Shows the result of taking the mean of the selected APs. With this mean signal, it was used to calculate the APD of the LA.

4.7.2.3. APD Calculation

With an averaged signal the APD values were calculated. In order to perform this calculation several parameters were required:

- Baseline value/resting potential or phase 4 of the AP
- Relative AP amplitude
- Activation time

Firstly, to calculate the baseline, the initial values from the first 10 frames were averaged. Secondly, the amplitude was given by the maximum value minus the baseline. The averaged signal was then differentiated with respect to time where

the maximum point corresponded to the activation time. This method is known as the fastest upstroke velocity. The repolarisation at 30%, 50% and 70% were subsequently calculated (APD30, APD50 and APD70, respectively). To determine APD30, the two closest points to 30% of the repolarisation tail was determined as shown in Figure 4.8. The APD value typically falls between two points of data which is illustrated in the magnified section of Figure 4.8. Using a linear interpolation (Equation 3) between these two points allowed for the time value where the 30% repolarisation intersection to be found. This was repeated for APD50 and APD70. A summary of how the AP signals were processed for APD calculation can be seen in Figure 4.9. As this process was all automated it was possible to create a folder containing hundreds of text files from multiple recordings. A script was generated to automatically read through all the text files to calculate the APD values for each mouse at different pacing CL and multiple regions.

$$y = mx + c \quad \textbf{(3)}$$

Equation 3. Linear Interpolation.

Equation of a straight line where m is the gradient, c is the y intercept and x is the time value.

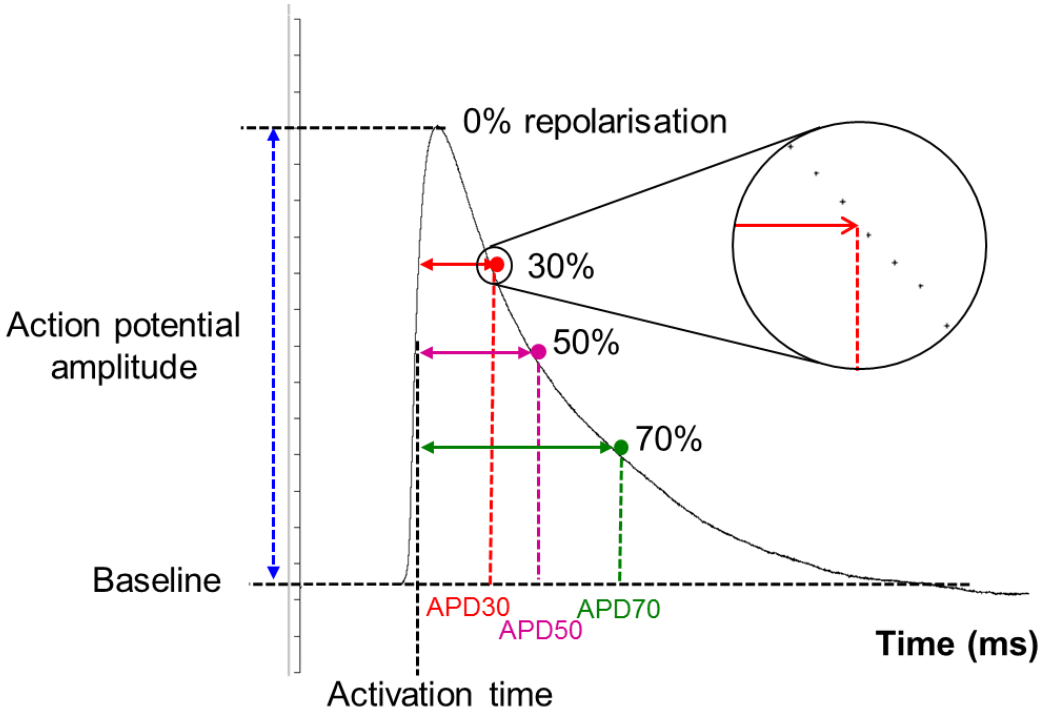

Figure 4.8. APD calculation.

The signal averaged APs were used to calculate the APD. The baseline was determined by taking the mean value of the first 10 points of the signal. The signal was then differentiated with respect to time, where the peak yielded the activation time. With the baseline and the height of the peak, the amplitude of the signal was found. The values of 30%, 50%, and 70% repolarisation from the peak height and baseline were determined. The corresponding times at 30%, 50% and 70% repolarisation represented APD3, APD50 and APD70 respectively. The magnified area shows the duration value at 30% repolarisation falling between two data points. Interpolating between the two points yielded an accurate value; this value was then subtracted from the activation time and provided the APD30 value.

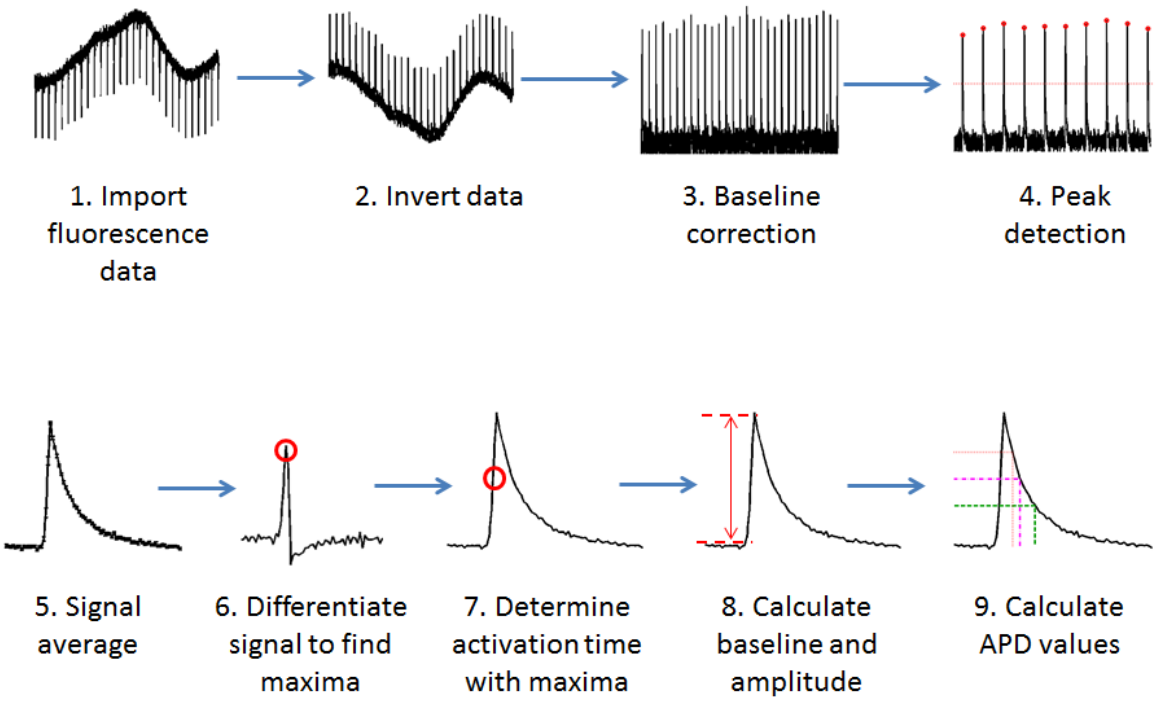

Figure 4.9. Summary algorithms calculating APD values from fluorescence data.

Shown above are the steps in the algorithms used to calculate the APD from the optical mapping data of the LA. 1) The fluorescence information was imported to MATLAB in text format. 2) The APs from the imported data appear upside down compared to traditional signals hence they were inverted. 3) The baseline drift of the signal was removed by using a linear top hat filter with length 100 points and angle 90 degrees. 4) Individual APs were detected using the 'findpeaks' algorithm in MATLAB. The criteria for locating a peak were given by values which were over half the height of the maximum value in the signal and a minimum distance of 50 points between peaks. 5) After each peak was found, they were averaged to yield a mean AP. 6) The mean signal was then differentiated, and the peak of this was found. 7) The peak of the differentiated signal was used to define the activation start time as this was the steepest point in the upstroke. 8) The baseline of the signal was calculated from the mean of the first 10 points in the averaged signal. With the baseline the amplitude of the signal was found. 9) APDs at 30%, 50% and 70% of the repolarisation were found by determining the time where the descending tail of the signal reached 30%, 50% and 70% of the signal amplitude. The values were then subtracted from the activation start time.

4.7.3. Data masking

Each frame within a data set comprised of the tissue and the background. In order to analyse these images accurately, background pixels needed to be distinguished from pixels of the LA as the background contains noise. The noise can interfere with algorithms and produce inaccurate maps. Segmenting the pixels of the LA from the background was performed using an image mask. The mask is essentially a binary image where the 1's represent the LA pixels and 0's for the background. Multiplying the mask with each frame preserves the pixels from the tissue and forces the background pixels to become 0's. To create an image mask, there are automatic and manual methods. Manually defining a mask involves a user to draw the segment they wish to highlight. Manual segmentation is time consuming and can be inconsistent between users but is considered a gold standard. The automated methods investigated were edge detection algorithms and thresholding. Figure 4.10 illustrates the two methods. Edge detection was used to locate pixels where the image brightness changed sharply or had discontinuities. Figure 4.10A is a greyscale fluorescence image of a LA sample. The Canny edge detection algorithm in MATLAB was used resulting in Figure 4.10B. The white lines show the pixels where an edge was considered. The general outline of the shape was similar to the original image. In order to create the mask the lines needed to be connected and any holes filled. The outcome of using the canny edge detection algorithm was dependent on each image and as a result; the process of connecting lines and filling holes varied by each image. Figure 4.10C is the image histogram for the LA. Many of the pixels were within the dark region hence a high pixel count towards the zero value in the histogram. Figure 4.10D is the result of thresholding above a value of 3000 and performing

an image erosion of a two pixel structuring element. This value was chosen as many images were investigated and 3000 fluorescence units proved to be suitable for a range of intensities. Experiments where the LA had many pixels around the 3000 fluorescence value were deemed too low for analysis as this would indicate that the dye had been poorly perfused. Each segmentation technique has limitations, Figure 4.10C shows that there were outlying pixels at the top of the image and around the edge of the atria where the pins were used to hold the LA in place. To test the efficacy of image segmentation, manual selection is considered the gold standard. Ideally, one should perform manual segmentation on a series of images with a range of different users and compare the segmentation methods.

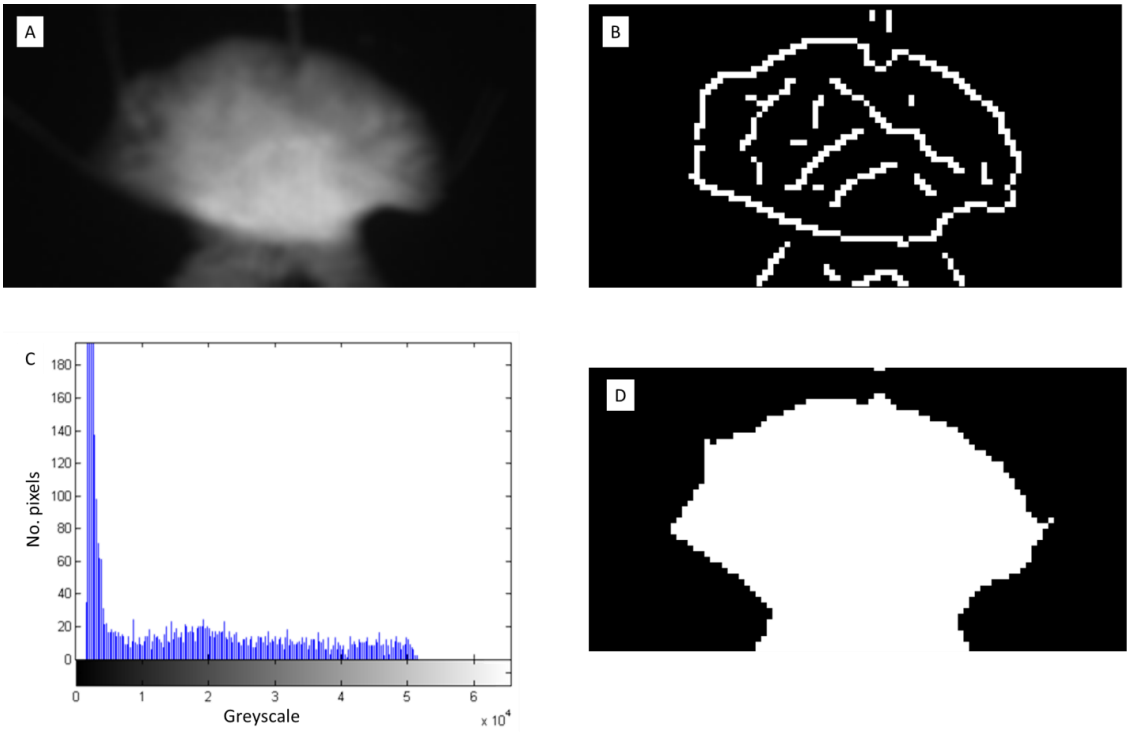

Figure 4.10. Data masking for image segmentation.

A) Shows a raw fluorescence image taken from the optical mapping system of the LA. B) One of the edge detection methods used was the Canny edge detector. Some of the edges were located but it also highlighted some areas within the sample C) An image histogram was used to look at the distribution of 64 bit pixel values. The background pixels were predominantly blacks hence the higher pixel count towards the zero value. D) Shows the mask from thresholding the LA image. A value set above 3000 and values below this were rejected.

4.7.4. Action potential duration maps

To test the heterogeneity of the LA, maps of the APD distribution were generated. Each pixel from these maps represented an APD.

Figure 4.11A illustrates the time course fluorescence from a pixel at the central region as indicated by an asterisk and a region towards the outer edge of the LA indicated by a cross. The corresponding traces show a large proportion of the signal is noise. The trace from the edge region shows a repolarisation passing below the initial baseline value which is not typical shape of a cardiac AP. In order to increase the signal to noise ratio, an image stack of 10 beats were exported to TIFF format. The images were imported to MATLAB where they were averaged to create a smaller image stack with a mean beat. The images were initially cropped to only display the LA and were Gaussian filtered using a 3 x 3 kernel. The average pixel intensity per frame was determined to generate a time course of fluorescence data analogous to the optical traces used to calculate APD values. The difference here was that each value represented the average fluorescence intensity for the entire image rather than just for a small ROI. The signal averaging algorithm was performed on this trace but instead of averaging fluorescent value, the frame from the image stack was averaged. Image thresholding was used to generate a mask to remove the background values. An intensity of 3000 was used for the thresholding. The red dots from Figure 4.11A indicate areas where the tissue was held onto the silicone rubber in the chamber by small pins. The number of pins varied depending on the tissue.

Figure 4.11B Shows an LA fluorescence image that has been averaged from 10 beats. It can be seen that the time course traces for the central and edge pixels

were improved. The smoother signal allowed for the algorithms to determine the repolarisation values as there SNR was increased.

The APD values for every pixel were calculated using the same algorithms as described in the Optical mapping design and development chapter, section 4.7.2.3. In order to generate a map from these values, each APD value for 30%, 50% and 70% repolarisation was stored in a corresponding array which was displayed as an image. As a result three images were generated for APD30, APD50 and APD70 as seen in Figure 4.11C. The areas highlighted in red show that there were outliers or areas where the algorithms to determine APD had not accurately calculated the values. The highlighted regions were in close proximity to the location of the pins, it was assumed that the pins may have caused some localised damage which in turn generated poor quality signals with low SNR.

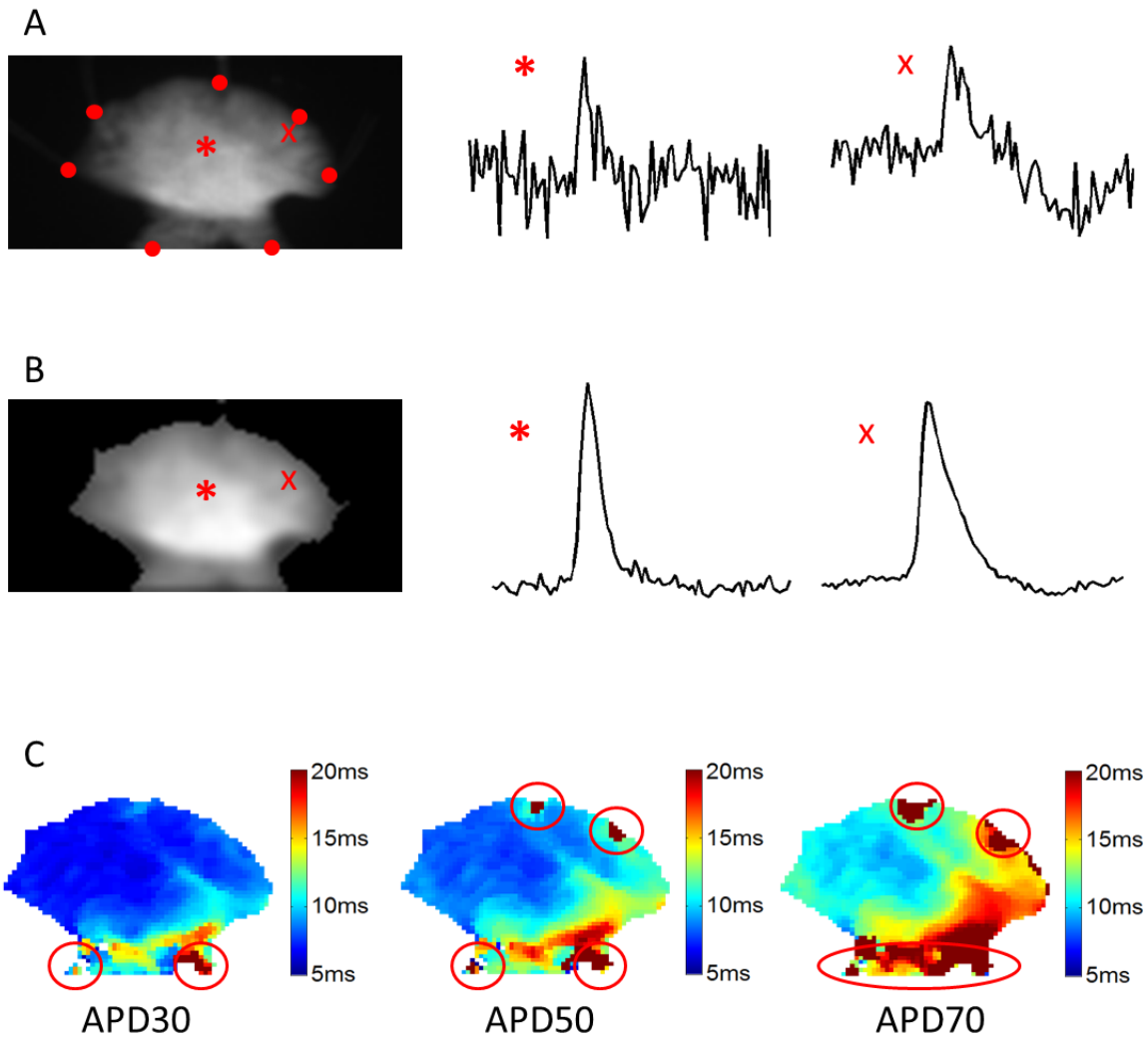

Figure 4.11. Action potential duration maps.

The images depicted above show an example of APs recorded from all pixels to generate a map of the APD distribution. The example used was from a LA preparation stimulated at 100ms CL. A) Shows the original unprocessed LA image with asterisk indicating the central region and the cross indicating the outer edge. The corresponding single pixel traces are shown on the middle and right of the row and display large amounts of noise rendering it unanalysable. The red dots indicate a location of a pin used to hold the LA to the silicone rubber mounted on the chamber. The number of pins varied between tissues. B) Shows the LA image which was generated from averaging 10 consecutive beats. The corresponding single pixel traces from the centre and edge showed a smoother AP hence the APD measurements were easier to perform compared no on averaged images. C) Illustrates the APD measurements for 30, 50 and 70% repolarisation for each pixel represented as a heat map. This shows the heterogeneity of the APD across the whole LA. It should be noted that the areas highlighted in red in C) showed outliers, these were typically regions where a pin was located. These areas were not easily analysed by the algorithms to calculate APD possibly due to weak signals caused by physiological damage from the pins.

4.7.5. Isochronal maps

Isochronal maps are image plots which display the activation times for each pixel within the image by mapping data values to a colour scheme. In the field of cardiac electrophysiology they can also be referred to as activation maps and are a common way to depicting an activation pattern on cardiac tissue [119]. The isochronal maps were generated allowing for quick visualisation of the activation times of the LA. After an image series of a singular beat was imported to MATLAB, it was cropped to show only the LA. In addition to this an image mask was created by thresholding a value of 3000 to remove the background pixels. Subsequently, the images were smoothed spatially using a mean filter with a kernel of 3 x 3. Following this, the activation point was determined for every pixel. In order to perform this step, a moving average filter was applied temporally to each pixel. The filter used was a Savitzky-Golay filter [121] with an 11^{th} order polynomial and a frame size of 3. This reduced the noise amplification during differentiation. The time signal at each pixel was differentiated and the peak was used to find the fastest upstroke; corresponding to the activation time. These steps were repeated for every pixel and each of these values was then stored in a corresponding array which generated an activation image. The repolarisation tail of the signal was ignored by the algorithms as calculating the activation only requires the depolarisation. The depolarisation time was recorded and stored in a matrix where it was represented as an isochronal image. The image was then median filtered to remove outlying pixels using a 3 x 3 kernel.

The start of activation (t=0) occurred at an arbitrary frame within an image series. In order to analyse these automatically, the initial point was calculated. This was

done by determining the sequence of consecutive activation times and subtracting from the first value of the sequence. As the process of determining the activation time was not greatly affected by noise, a single AP was used to generate these isochronal maps. This was useful for looking at arrhythmias where multiple APs cannot be measured to gain an average value and beat to beat changes can be investigated. Figure 4.12 illustrates the steps required to create an activation map from the fluorescent TIFF images. As the parameters were predetermined, the map generation process was automated.

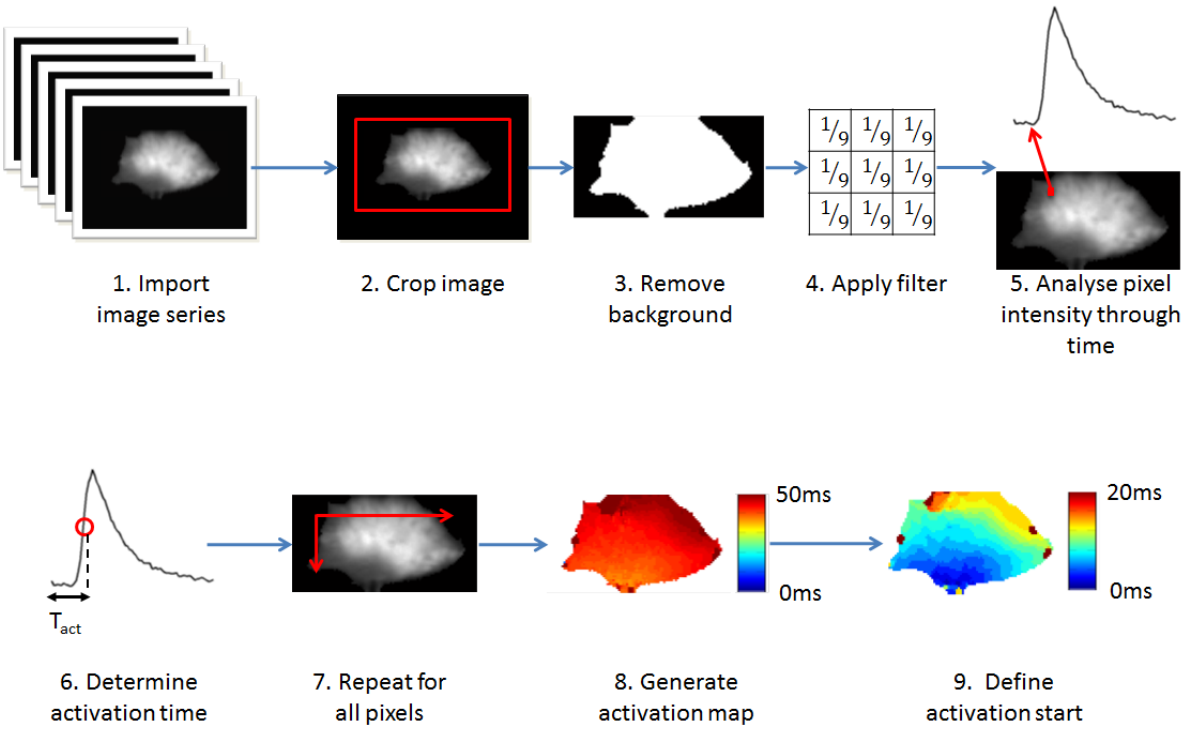

Figure 4.12. Isochronal map generation.

The isochronal maps depict the activation times and pattern from the data generated from the optical mapping system. Shown above are the steps that analyse the raw images to generate the maps. 1) Fluorescence images were imported into the MATLAB space the format of a TIFF image stack. 2) The image was then cropped manually to highlight the desired region. 3) The background of the image was removed by thresholding values above 3000 to create an image mask. 4) A median filter was applied to smooth the image for analysis. 5) The fluorescence intensity was extracted from a single pixel through the time domain. Only pixels from the LA yielded an AP signal. Pixels from the background provided no information as they were removed in the earlier steps. 6) The activation time of the signal was defined as the steepest point on the upstroke of the AP. This was calculated by differentiating the signal with respect to time and using the peak of the differential as the point of activation. 7) The previous steps of (5) and (6) were repeated for all pixels in the image. 8) The activation time for each pixel was stored in a matrix which was used to create the map. Background pixels were also stored as zeros and appeared as white pixels in the activation maps. It shows that the scale was set from 0ms to 50ms but the majority of pixels were in the 30ms to 40ms range. 9) The time in which the LA is activated was determined and used as an offset for the start time of the isochronal map. This now shows the pixels to range from 0ms to 20ms.

4.7.6. Conduction velocity measurements of the LA

The conduction velocity (CV) describes the speed and direction of activity. Several methods were investigated for measuring CV across the LA. The simplest method investigated was to measure the distance between two points. The isochronal map was generated using MATLAB and two points were selected from the image. The distance between the points and the activation was known and as a result the velocity was calculated. There were limitations to this method; the measurements had to be taken from two points which were perpendicular to the wavefront. With complex activation patterns finding a suitable line between two points proved difficult. If the line was not perpendicular the result would be skewed. Figure 4.13A and B show the importance of measuring points perpendicular to the wavefront. Figure 4.13A the points used is perpendicular to the wavefront, dividing the distance between the time difference gives a good estimate of velocity. Figure 4.13B the points used when not perpendicular to the wavefront. To gain a more accurate result, a longer distance which traversed several time zones or contour lines was used to gain an average reading. The slight increase in distance yields a slower estimate of CV. The isochronal maps generated had many regions with the same activation time which posed another problem of where to select the points of measurements. From Figure 4.13C, the two points selected were very close to each other. The difference was that the second point had been selected a single pixel over a different activation time that resulted in a relatively large change in velocity.

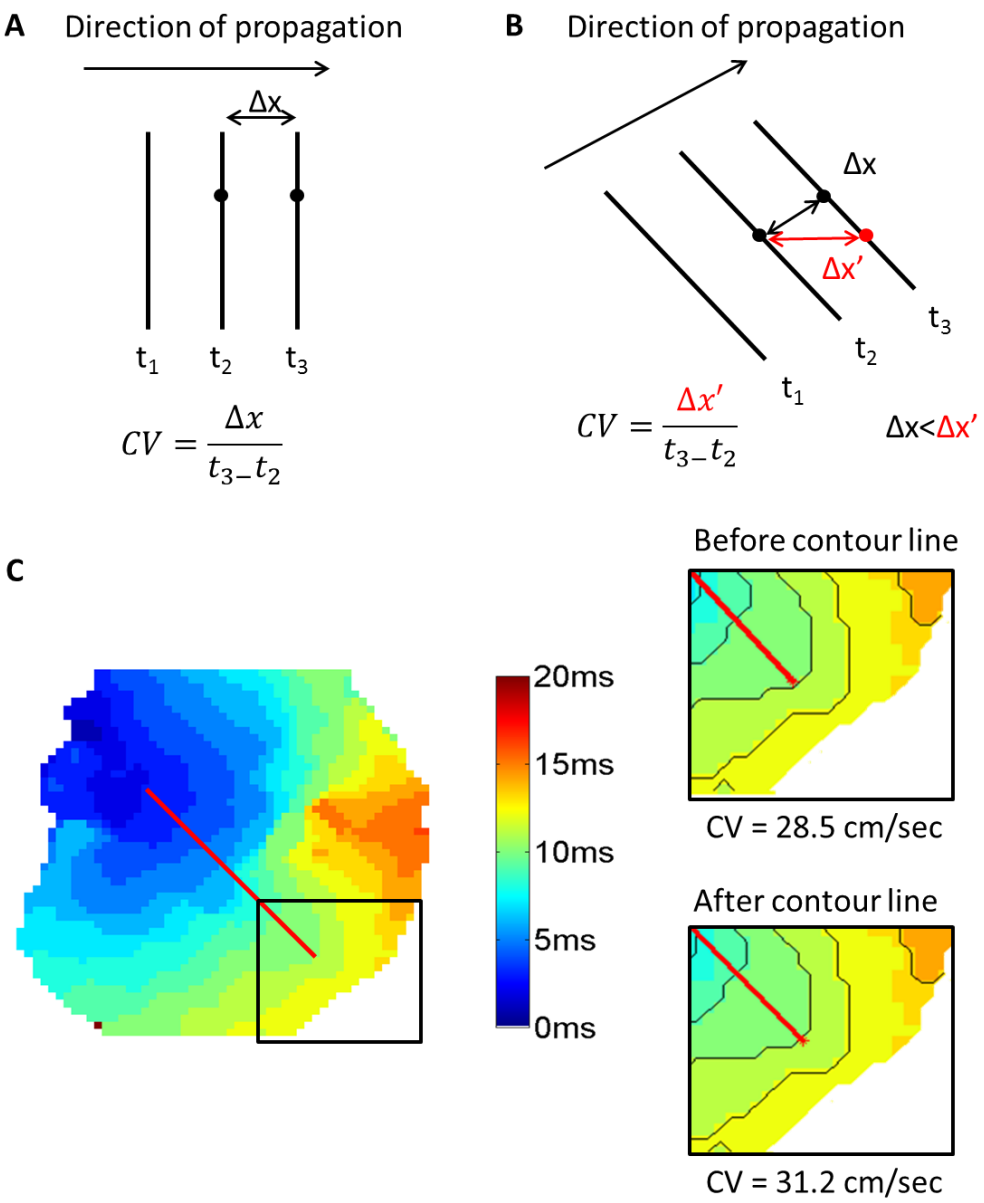

Figure 4.13. Conduction velocity measurements using point to point method.

A) Shows the CV measurements from two activation time points (t_2,t_3) which were taken perpendicularly to the wavefront or in line with the direction of propagation. The distance between the activation points is Δx. The CV was calculated from the distance and time between the two points. B) Shows the CV measurement when made from two points which intersect the wavefront at an angle. The distance between the two activation points was given as Δx'. As the time values for the points have not changed, yet the distance between them had increased, the CV value was higher compared to the measurement taken perpendicular to the wavefront. C) Illustrates the difference in CV value when the points selected were from two pixels in close proximity but differ in activation time. This shows the CV measured from two points on the LA stimulated at 100ms CL. The red line indicates the distance between the two points which were selected manually. The magnified sections show the difference between CV values before (28.5cm/sec) and after (31.2cm/sec) the contour line which separate the different activation times. The difference of 2.7cm/sec is a relatively large change in value indicating that measuring between two points proved to be unreliable.

Another method tested to calculate the CV was quantifying the spatial inhomogeneity in CV using a phase method. Here the phase was defined as the maximal difference between neighbouring activation sites [122]. This method also allowed for its homogeneity to be measured using a phase map and provided a CV value from its median from the distribution of local CV phases. To calculate the phase, the isochronal map was loaded into MATLAB whereby the difference from each neighbouring pixel was calculated. The maximal value between the neighbours was determined and defined as the phase. Figure 4.14A shows an example isochronal map stimulated at 100ms CL from the LA. The phase was calculated to generate a map B). It can be seen that there were many white gaps between the blue phase points; this is a result of many neighbouring pixels containing the same value. Each activation point is limited to the value of the exposure time; as a result a phase difference was only detected when a neighbouring pixel changed value. The phase method proved problematic as the maps generated had many pixels of the same value and hence the phase values were always the same number which can be seen in Figure 4.14B as the majority of pixels were the same colour.

The final method investigated was to use an algorithm to fit a small localised surface to a set of activation points. This surface had a gradient and magnitude which was translated into a local CV. As each point on the isochronal map represents an activation time, each of these points were defined as a wavefront which propagated. The velocity vector for each pixel and its neighbours were determined by looking at a window of 4 pixels in each x-y direction within a maximum time of 16ms. From this window a polynomial surface was fitted using a least-squares algorithm. The x-y window needed to contain enough varying values

to yield solutions to the polynomial coefficients. Each polynomial surface represented a local isochrone or activation contour, from here the gradient vector was found. The gradient vector is always orthogonal to the surface of the local isochrone and hence defined the direction of propagation for this window. Repeating this over each point yielded a set of CVs for x and y directions. With these velocities the magnitude and mean value was calculated. This represented the overall CV for a sample. Figure 4.14C shows the activation points in three dimensions (x, y, time). It was from these active points that a polynomial surface was fitted. As each surface had its own magnitude, this was represented as a set of quiver arrows which was superimposed onto the original isochronal image as seen in Figure 4.14D. The process of generating the isochronal maps and the mathematical operations to calculate CV were performed automatically. A script was written to save the CV values for each mouse in a text data file. The result of this advanced method allowed for complex conduction patterns to be studied. Figure 4.14E shows an isochronal map of the LA stimulated at 100ms CL and the corresponding map with a 1µM infusion of flecainide which has induced a CV slowing to the point the activation becomes re-entrant which is shown in Figure 4.14F. The path of conduction is indicated by the curved black arrow.

The CV measurement method and theory used for calculating CV was developed at Washington University lead by Professor Philip Bayly [123], not by the author of this thesis. This technique was originally designed for measurements from unipolar electrode arrays for epicardial mapping data.

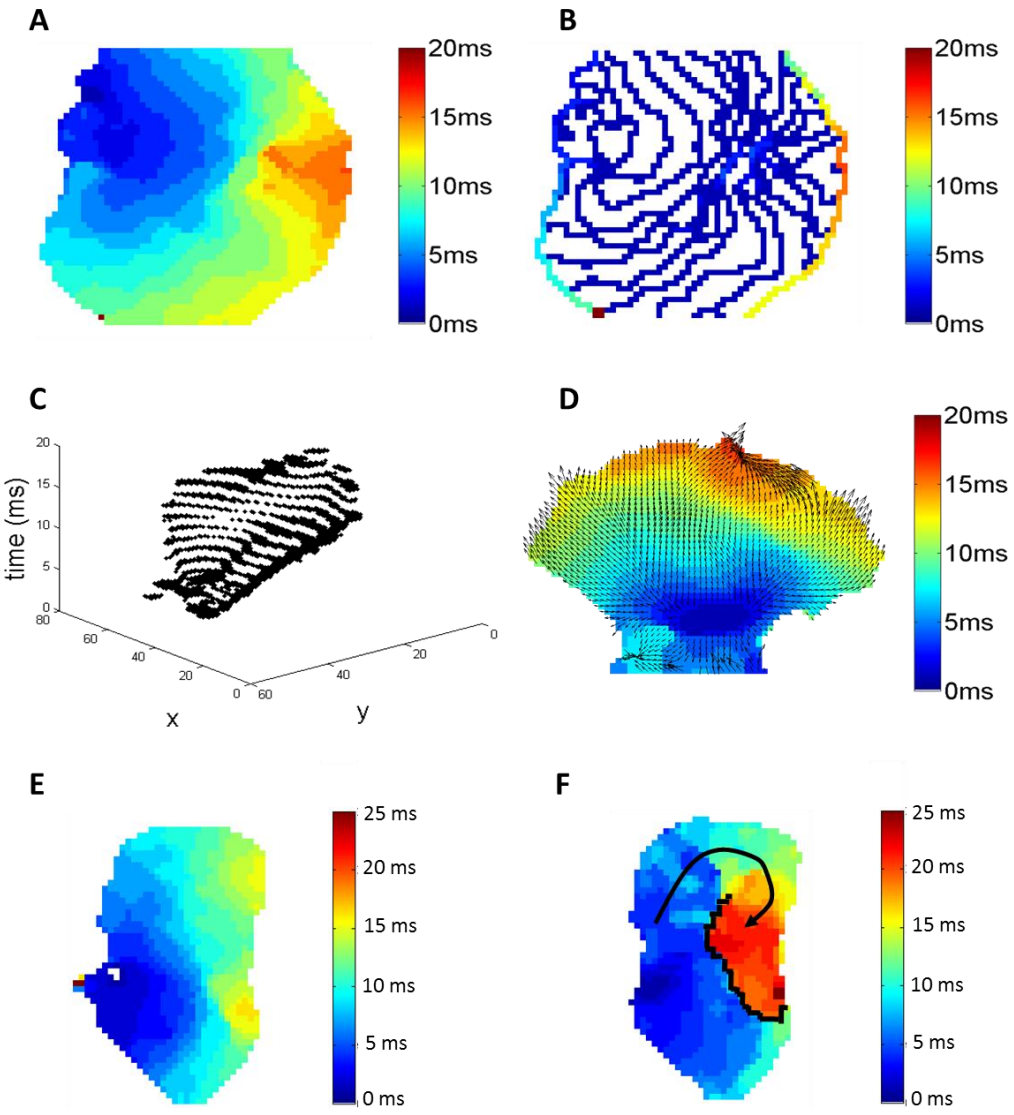

Figure 4.14. Conduction velocity measurements from three isochronal maps.

A) Shows an example of a LA activation map stimulated at 100ms CL. B) Shows the corresponding phase map of A). It was calculated by taking the maximal difference between each of its neighbouring pixels. The maximal difference between neighbouring pixels (i.e. phase difference) was calculated. The median of the distribution of the local conduction phases provided its velocity value. This method was first described by Lammers *et al* [122] but proved to be insufficient for calculating CV for maps which have many neighbouring pixels with the same activation times. This can be seen in the white regions in the image which represent zero values. C) Displays the activation times in 3D (*x,y,time)* – space for an LA sample stimulated at 100ms CL. Surface polynomials were fitted onto the points of the activation sites to yield a local gradient vector. D) Shows the LA with velocity vector arrows for each polynomial surface superimposed onto the isochronal map. Each vector arrow was calculated by fitting a local surface with a 4 x 4 window in each x-y direction with a maximum time of 16ms. Each window was fitted using a least squares algorithm. E) Shows an LA activation map stimulated at 100ms CL. F) Illustrates the corresponding LA sample infused with a sodium channel blocker (1µM Flecainide) resulting in a complex activation pattern. Using the polynomial fitting method the CV was calculated. The black line which separates the blue and red regions represents the direction of block. The arrow indicates the path of activation propagation.

4.8. Validation of optical mapping

To investigate the reliability of the optical mapping system, AP recordings were compared against other known methods such as monophasic action potentials (MAP) and transmembrane action potentials (TAP) which both use direct contact. Measurement of APD using MAP electrodes were performed on a Langendorff apparatus and TAP using glass microelectrodes were performed using isolated LA superfused samples. These techniques are described in the materials and method section. CV measurements were not directly compared but the activation times were recorded from the contact methods. Activation times from MAP and TAP give a rough estimate of the time taken for the tissue to depolarise from the time of the stimulus. The stimulation point can be seen as an artefact from the MAP and TAP methods. The stimulus artefact arises when the measurement electrodes receives a signal caused by the stimulator pulse and not from the tissue. Another method used to validate the optical mapping CV was to add noise to the images and investigate the resulting CV values.

4.8.1. Comparisons between optical action potentials with MAP and TAP recordings

To test the accuracy of the APD measurements made from optical mapping, signals were measured against the MAP and TAP methods. Figure 4.15A shows example traces from the optical mapping system at 300ms and 100ms CL over a period of 0.5 seconds from a 4 x 4 region. Figure 4.15B illustrates TAP measured with glass microelectrodes at 300ms and 100ms CL and Figure 4.15C from MAP electrodes at 100ms CL only. APs measured using this novel method exhibited

similar morphology and duration characteristics when compared with those recorded using more standard electrophysiology techniques.

At 300ms CL OAPs at APD50 were 10.9 ± 0.9ms and APD70 14.7 ± 1.2ms and showed no difference from TAPs at 300ms CLs (10 cells, 5 atria). In another set of experiments, MAPs were recorded from the intact, beating heart just prior to dissection of LA tissue for OAP measurement. The MAP data was gathered on a Langendorff apparatus which did not include 300ms CL pacing as this rate was slower than the inherent natural rate of the whole heart. A significant difference was not detected in APD50 or APD70 between OAPs (9.6 ± 0.9ms and 14.3 ± 1.4ms, respectively), TAPs and MAPs at a more physiological paced CL of 100ms (n = 14). However, there was a trend in shorter OAPs compared to TAPs and MAPs. This degree of uniformity therefore suggests that OAPs obtained using this technique can be used to make accurate and reliable assessments of APDs in the mouse atria.

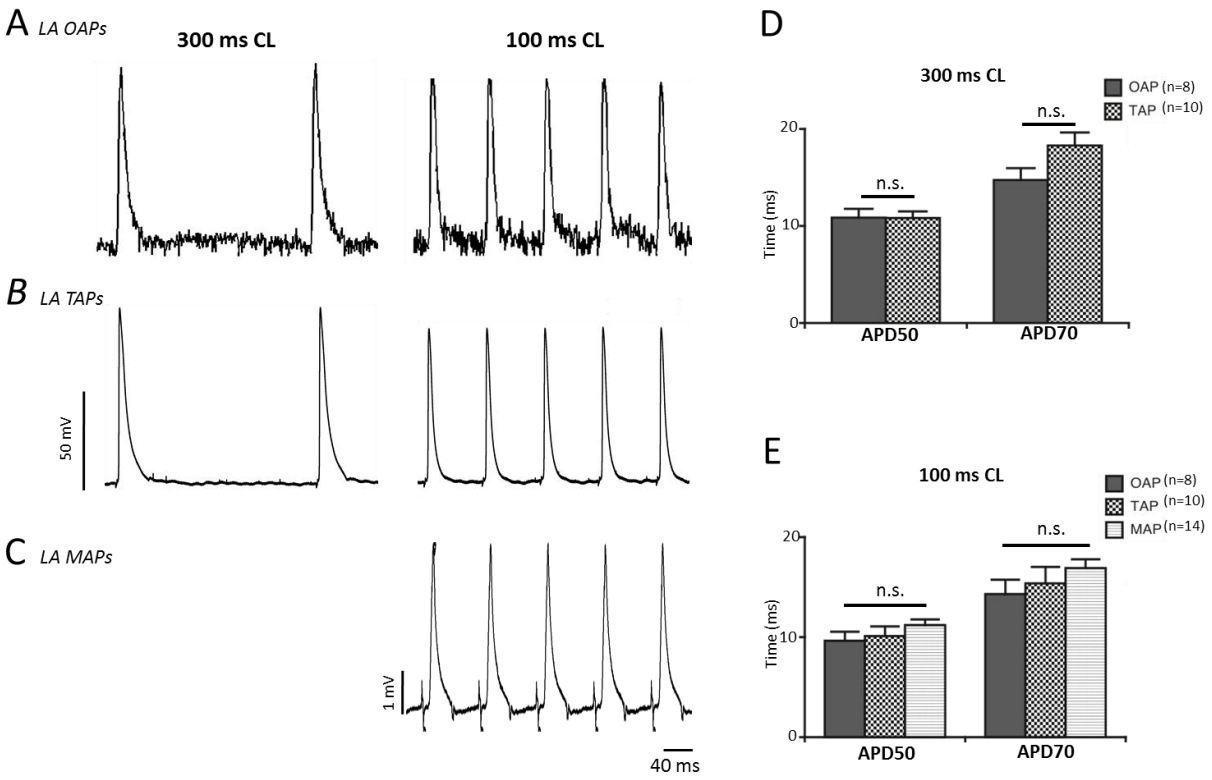

Figure 4.15. Comparison of action potentials obtained using the high resolution optical system with other standard electrophysiological techniques.

This shows the characteristic traces of APs from the LA from different techniques. A) Show the optical action potentials (OAPs) acquired at 1 kHz for 300ms and 100mc CL. B) Show the transmembrane action potentials (TAPs) at 300ms and 100ms CL. C) Show the monophasic action potentials (MAPs) recorded at 100ms CL only. The MAPs were recorded from a whole isolated heart on a Langendorff apparatus, the inherent heart rate of the samples were faster than 300ms CL hence only rates at 100ms were recorded. D) Comparisons between the OAPs and TAPs at 300ms CL were made at APDs at 50% and 70% repolarisation (APD50 and APD70, respectively) which showed no significant difference between the two methods. E) Compared the LA samples at 100ms for all three techniques for APD50 and APD70 showing no significant difference between the techniques. It should be noted that despite no statistical significance optical signals showed a slightly lower value. Error bars indicate SEM. Data presented is from 8 regions of interest (ROI) from 8 LAs (OAPs), 10 cells from 5 LAs (TAPs) and 14 recordings from 14 LAs (MAPs).

4.8.2. Conduction velocity measurements

An increase in activation time indicates a decrease in CV. From an isochronal map, regions with a larger proportion of pixels towards the red end of the spectrum indicate an increase in time across the tissue. The LA showed an increase in activation spread with decreasing stimulation CL as shown in Figure 4.16A, this is indicated by the increase in red pixels. The activation times from TAP and MAP recordings also confirm this. Figure 4.16B and C show that the time from the stimulus artefact to the activation time measured by the fastest upstroke had increased with shorter CL, indicated by the red double arrows. Figure 4.16D provides a mean CV decrease with decreasing CL. The velocity ranged from 31.32 ± 1.27cm/sec to 25.05 ± 1.10cm/sec from 300ms to 80ms, respectively. F) Illustrates the parallel increase in activation times measured by the contact methods. MAP recordings were much higher due to the fact that the whole heart was stimulated from the RA taking more time to conduct to the left. This differs from the isolated LA as this is stimulated directly. Measurements at 300ms CL were not performed on using MAP electrodes as the intrinsic rate of the intact heart which includes the RA and sinus node was much higher than stimulation rate.

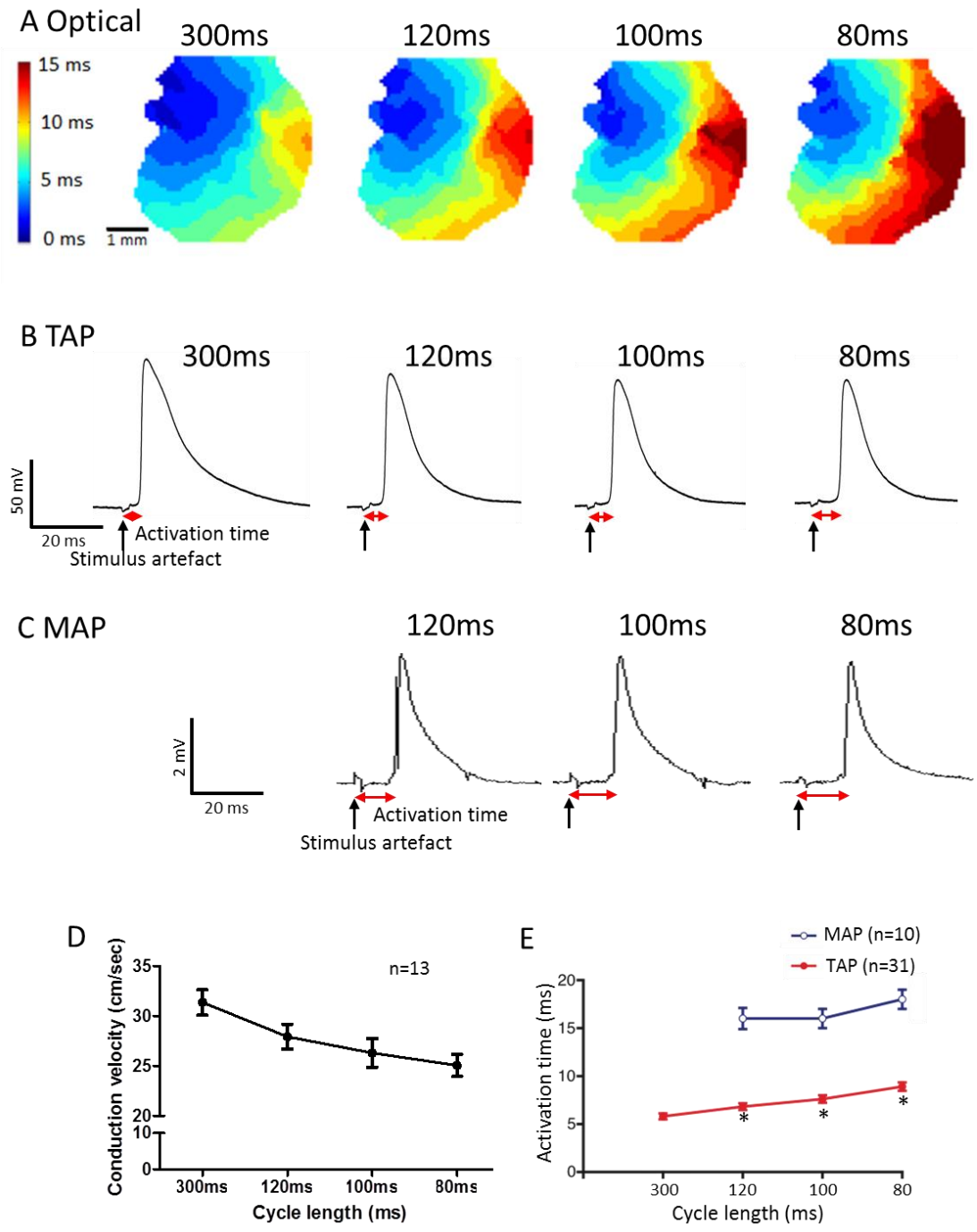

Figure 4.16. Comparison of conduction velocity measurements with activation times at different stimulus cycle lengths.

A) Examples of the activation spread across the same LA at different CLs as recorded by the new optical mapping system at 1000 frames/sec. At shorter CL, the activation times across the whole atrium increased. B) TAP and C) MAP recordings indicated a longer activation time from the stimulus artefact to the point of activation. Mean CV at different CLs, n=13 LA. Error bars indicate ± SEM. F) TAP and MAP activation times at decreasing CL. Data presented is from 10 cells from 5 LAs (TAPs) and 31 recordings from 31 LAs (MAPs). Error bars indicate ± SEM, * denotes P<0.05 compared with activation time at 300ms CL; one way ANOVA with Dunnett's post hoc analysis.

To test the robustness of the CV calculations, measurements were repeated with Gaussian white noise added to each frame of the image series. Bearing in mind the signal to noise ratio is a logarithmic measurement, small changes in SNR is typically a large change in signal quality. An image of high SNR was measured at 50dB with 5dB decrements to 30dB. Table 1 shows the results of increasing the image noise. As shown, the velocity measurements remain relatively unchanged. Sample 2 has the largest variance and standard deviation of 0.71 and 0.84, respectively. Sample 1 has the lowest variance of 0.14 and standard deviation of 0.37.

SNR (dB)	sample 1	sample 2	sample 3	sample 4	sample 5
50	18.44	21.42	35.17	26.17	22.76
45	18.35	21.99	34.88	25.82	22.97
40	18.17	20.72	35.99	24.9	22.86
35	17.87	20.67	34.21	25.79	23.24
30	17.53	19.77	34.42	24.37	21.34
Mean	18.07	20.91	34.93	25.41	22.63
Variance	0.14	0.71	0.49	0.56	0.56
Standard Deviation	0.37	0.84	0.70	0.75	0.75

Table 1. Left atrial conduction velocity measurements stimulated at 100ms cycle length with decreasing signal to noise ratios.

Five sample data measurements were taken from the LA stimulated at 100ms CL to test the effect of noise on CV measurements. Images were distorted by adding Gaussian white noise to each frame in the data stack thus reducing the signal to noise ratio (SNR). Images of high SNR were measured at 50dB with 5dB decrements to 30dB. As noise was increased the CV values remain relatively unchanged as the variance and standard deviation have relatively low values. Values given are in cm/sec unless otherwise stated.

4.9. Video animation

Software was also created to visualise the fluorescent activity in the LA and record them to .AVI video format. Two versions of the video animation software were designed: one version for visualising the isochrones, looking at the times of activation of the LA. The isochrones were overlaid onto the greyscale image to allow for better understanding of the conduction pathway; the second to display the relative fluorescence intensity of the LA whilst stimulated. The difference between the two is that the activation videos show a discretised set of isochrones, whilst the other displays a continuous set of fluorescence ($\Delta F/F$).

4.10. Concluding remarks

This chapter has presented a new optical mapping system capable of imaging isolated murine LA, whereby the APD values were compared against microelectrode and monophasic action potential electrodes. In contrast, the present work mainly focuses on improving the automation of processing the image data by further reducing bias and speeding up analysis. The use of the TIFF image format allowed for more open access for others to develop an imaging system compared to those which often uses proprietary file types. The algorithms used have shown to perform APD calculations autonomously from fluorescence data, increasing signal quality by use of averaging.

The baseline correction was shown to allow for signal averaging to generate higher SNR signals. Other methods such as polynomial fitting have limited use with signals that fluctuate greatly [124]. The isochronal activation maps were generated automatically; the only input was the user cropping the image to

highlight the ROI. However, other methods exist for the removal of uneven baselines. In biomedical imaging, the problem of inhomogeneities that distort the background of an image is commonly known as shading [125]. Applying a solution to shading can be an alternative way to correct the variation in baseline. One solution by Reyes-Aldasoro utilises a method of generating an estimated signal envelop from the input image [120]. This method can be understood as stretching a surface over or under a series of objects. The flexibility in this method was that it made no assumptions whether the foreground signal was greater or lower in intensity than the background. The outcome was that it could develop a shading surface which was not easily described by a polynomial function [120].

The segmentation method of thresholding was shown to be sufficient in removing the background from the fluorescence images. However, to improve upon this, other segmentation methods exist. There are many thresholding techniques for image segmentation which can be subcategorised into methods which use histogram shape, entropy and clustering etc. [126]. One popular thresholding technique, known as Otsu's method is common within image processing [126]. The algorithm assumes the image contains two pixels classes, background and foreground. Otsu's method performs clustering based thresholding by minimising the variance between the background and foreground pixels in an attempt to find the optimal threshold [127]. Each method of thresholding will have its own advantages and limitations. One should ideally compare manual segmentation on a series of images with a range of different users to determine the best method for the specified types of images.

In Figure 4.12, the algorithms used to determine t=0, the activation start point, were automated which saved time and in turn allowed for faster analysis. This

differs from most current methods where manual selection was required, which can introduce subjectivity to results. Whilst it was possible to determine the CV without correcting for the start of the propagating AP, having the offset provided easy comparison between different tissue samples or the same sample with varying CV as seen in Figure 4.16A. This gave a rapid indication of samples which had a faster or slower CV.

CV calculations were automatically performed, which allowed for reproducible results and the elimination of user bias. Methods calculating the distance between two activation points and their time difference proved to yield varying results that were greatly dependent on where the activation points were chosen. Calculating CVs was especially difficult from images that had irregular conduction paths as described in the results with flecainide. These isochronal maps have many neighbouring pixels which show a depolarisation at the same time. This caused problems when measuring the activation between two points as this yielded an unreliable velocity value. It has also been shown that tissues may have many localised CV vectors, the magnitude of these values were dependent on the orientation [128].The advantage of using the gradient method as described here was that it measured multiple polynomial surfaces that were fitted to the entire tissue and yielded an overall CV value. This accounted for the vector components in the x and y directions and takes its magnitude into account. The robustness of the CV algorithms were also tested by increasing the noise of the images, it is shown in Table 1 that there is little variance in the CV with decreasing SNR. As SNR is measured on the decibel scale, decrements of 5dB, indicates relatively large increases in noise. This is particularly true from 50dB to 30dB, thus indicating that the algorithms handle distortions in the image quality very well.

It should be noted that one of the limiting factors of signal averaging arises from measurements of the APD values. Each of these values must be in a steady state as multiple signals were combined. This limited the measurement of arrhythmias such as alternans and extra early beats. Measurements from the isochronal maps required a single signal as only the depolarisation was necessary. The depolarisation and the entirety of the repolarisation were needed to calculate the APD, hence signal averaging provided a way to increase the SNR.

The main achievements for this system was that the APDs measured coincide largely with other methods such as the MAPs and TAPs. The algorithms were automatic and a robust to increased noise levels as shown in Table 1. The resolution of the system is higher than others [52] and the images generated was in TIFF format making them easy to distribute and analyse. Other imaging systems are limited by their proprietary formats.

5. Optical imaging of the Pitx2c deficient mouse left atrium

5.1. Introduction and overview

Atrial fibrillation (AF) is the most common sustained arrhythmia in human and a common cause of stroke and cardiac deaths. Although much progress has been made in the characterisation of factors that cause AF [29], [46], [129], the mechanisms involved remain elusive [130], [131]. Genome-wide association studies have found that common gene variants or single nucleotide polymorphisms (SNP) on chromosomes 4q25, close to the PITX2 gene are strongly associated with AF [48], [49]. These variants are associated with altered mRNA expression of the transcription factor Pitx2 [132] and show an increased risk of AF by up to 1.72 times [49].

Pitx2 is a homeobox transcription factor which is responsible for the body's left-right asymmetry [133], [134]. Four isoforms of Pitx2 are found (a-d), isoform-c mRNA levels are expressed in the adult left atrium (LA) in mice and humans [55], [135]. Pitx2c expression levels can be found up to 100 fold higher in the LA compared to the other three chambers of the heart [54], [55]. Furthermore, evidence is found that Pitx2c regulates ion channel expression within the atria [53]. A complete lack of Pitx2 in the atrium is thought to downregulate sodium (I_{Na}) and potassium (I_{K1}) channels expressions which can lead to electrophysiological remodelling and atrial arrhythmias [53]. It has been shown from previous studies using Pitx2c$^{+/-}$ mouse models that there is a shortening of the action potential duration (APD) at the fast paced stimulations [55].

One therapy for controlling arrhythmias is by use of antiarrhythmic drugs (AAD). AADs have only been shown to be moderately effective [45], [136] but we lack the understanding of the mechanisms affecting their efficacy [47], [136]. Therefore it is advantageous to limit therapies to patients that will show an increased benefit. Understanding the reasons behind altered individual responses to AADs allow for a personalised approach to prescribing antiarrhythmic therapies. A study has shown that approximately every third to fourth AF patient who receives AADs caries the SNP closest to the 4q25 chromosome. The 4q25 chromosome lies close to the PITX2 gene and is strongly associated with AF. Some SNP variants respond well to sodium channel inhibitors such as flecainide [137].

It was hypothesised that Pitx2c$^{+/-}$ littermates show electrophysiological changes such as shortened APD compared to wild-type (WT) and that flecainide shows a preferential affect to Pitx2c$^{+/-}$. In addition to this, regular activation patterns were expected in both genotypes at baseline as no overt structural changes have been witnessed in previous studies [55]. However, it was expected that the use of flecainide reduces the conduction velocity (CV) in both genotypes. It was postulated that flecainide has a functional role in reducing the presence of AF in those with the Pitx2 downregulated mRNA by increasing the APD and by its differential ion channel expression. This can lead to a modification of the efficacy of AADs to maintain sinus rhythm in Pitx2 downregulation.

Here the high resolution optical mapping system was used to measure the APD values from WT and Pitx2c$^{+/-}$ littermates along with comparing baseline values before and after the addition of flecainide acetate. The conduction properties were to study the structural variations between the genotypes with flecainide.

5.2. Methods

The study was performed on WT and Pitx2c$^{+/-}$ heterozygous mouse littermates bred on an MF1 background. Mice were of adult age of 12-20 weeks old. Pitx2c$^{+/-}$ mice were generated by removal of the isoform-c specific exon as seen in Figure 5.1. Mice were first generated and previously described by Lui *et al. 2002* [115], not by the author of this thesis.

Experimental protocols for animal dissection and optical mapping are described in the materials and methods chapter 3 on page 46.

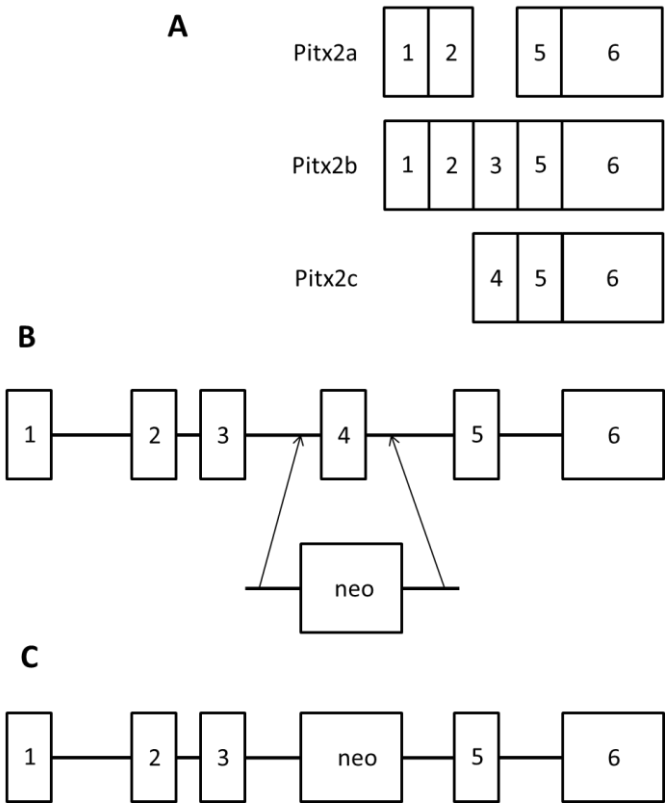

Figure 5.1. Gene targeting strategy for Pitx2.

A) Summarises the exons in the Pitx2 isoforms. Exon 4 is present in Pitx2c only. B) Illustrates the Pitx2 genomic structure. Boxes represent the exons and lines represent introns. The box indicated by neo represents the neomycin gene cassette which is specific to Pitx2c. C) Illustrates the genomic structure with exon 4 now replaced with neomycin, thus removing the expression of Pitx2c. This strategy was first described by Lui *et al. 2002* [115].

5.3. Results

5.3.1. Atrial electrophysiological properties in Pitx2c deficiency

To investigate whether a downregulation of Pitx2c leads to functional changes in the mouse LA, WT and Pitx2c$^{+/-}$ littermates were tested. In this study the APD) and CV values were recorded during pacing.

The activation patterns for each genotype were not shown to be different or irregular as shown in Figure 5.2. However, outlying pixels were observed which can be seen above in dark red which did not follow the colour gradient from blue to red. These points were likely to be caused by pins which were used to hold the tissue to the imaging chamber. The pins can block the view from the camera but also can cause localise damage to the tissue. The CVs calculated from the isochronal maps showed that there were no changes between genotypes (WT: n = 8, Pitx2c$^{+/-}$: n = 12) at all cycle lengths (CL) which can be seen in Figure 5.3.

Figure 5.4 show atrial APD values were significantly shorter in Pitx2c$^{+/-}$ (n=12) atria compared to WT littermates (n=12). Figure 5.4A shows that at 100ms CL mean values at AP30 were 6.39 ± 0.75ms for WT and 4.63 ± 0.37ms for Pitx2c$^{+/-}$ showing a reduction by almost 2ms. Figure 5.4B shows the mean values at 100ms CL at APD50 were 8.88 ± 1.08ms for WT and 6.61 ± 0.37ms again a reduction of approximately 2ms. Figure 5.4C shows the mean values for APD70 at 100ms were found to be 12.48 ± 1.55ms for WT and 9.40 ± 0.58ms for Pitx2c$^{+/-}$, a reduction of almost 3ms. Significance was measured across the board between genotypes. Performing Bonferroni post hoc analysis revealed that the significance

arose from the shorter CLs (APD30: 100ms, 80ms; APD50: 120ms, 100ms, 80ms; APD70: 100ms). This suggests that the genotype differences were more pronounced when the LA were stimulated faster.

Taken together, this data shows that the rate of conduction is no different between the genotypes. However, there is a reduced APD in the Pitx2c$^{+/-}$ LA compared to the WT LA. With this information, it can be tested to see whether the effects of flecainide have a greater effect on the Pitx2c$^{+/-}$ model compared to the WT LA.

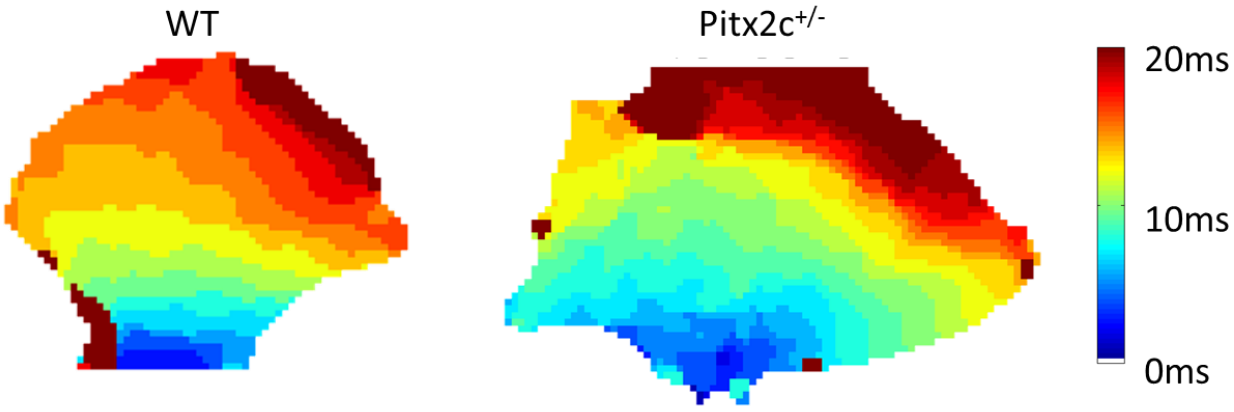

Figure 5.2. Activation patterns for WT and Pitx2c$^{+/-}$ left atrial samples.

LA samples between WT (n=8) and Pitx2c$^{+/-}$ (n=12) were compared. This shows representative examples of the LA stimulated at 100ms CL. The blue regions indicate the start of activation with it propagating upwards. No irregular activation patterns were found between the genotypes. The CV for the samples shown above were 29.3cm/sec and 22.8cm/sec for the WT and Pitx2c$^{+/-}$, respectively. From the 8 WT and 12 Pitx2c$^{+/-}$ samples, the mean CV values showed no significant difference between the genotypes. Outlying pixels were observed which can be seen above in dark red which did not follow the colour gradient from blue to red. These points were likely to be caused by pins which were used to hold the tissue to the imaging chamber. The pins may incur some damage to the local area of the tissue affecting the activation time of the sample.

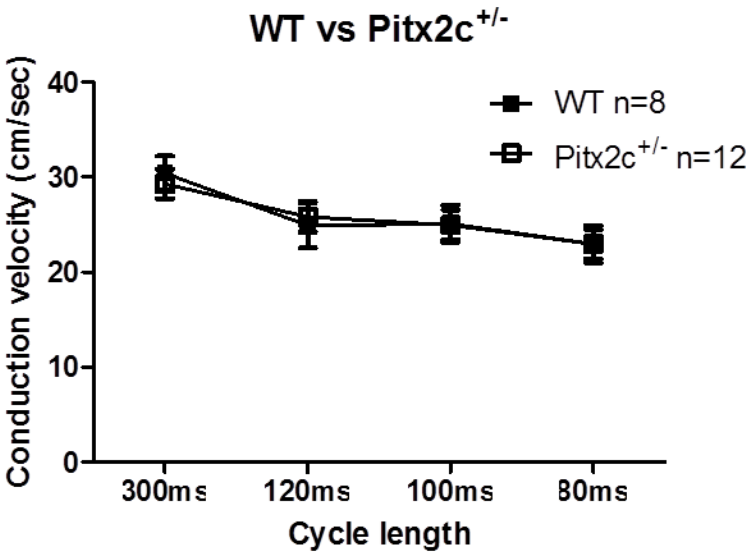

Figure 5.3. Cycle length dependent conduction velocity measurements between WT Pitx2c$^{+/-}$ littermates.

The CV of the WT and Pitx2c$^{+/-}$ LA were measured. The decrease in CL stimulations showed a reduction in CV in both genotypes. No differences in CV were found between genotypes for all CLs. This suggests that Pitx2c deficient LA samples do not show a change in CV compared to WT samples. Points indicate mean values with error bars representing SEM. Statistical analysis was performed using two way repeated measures ANOVA.

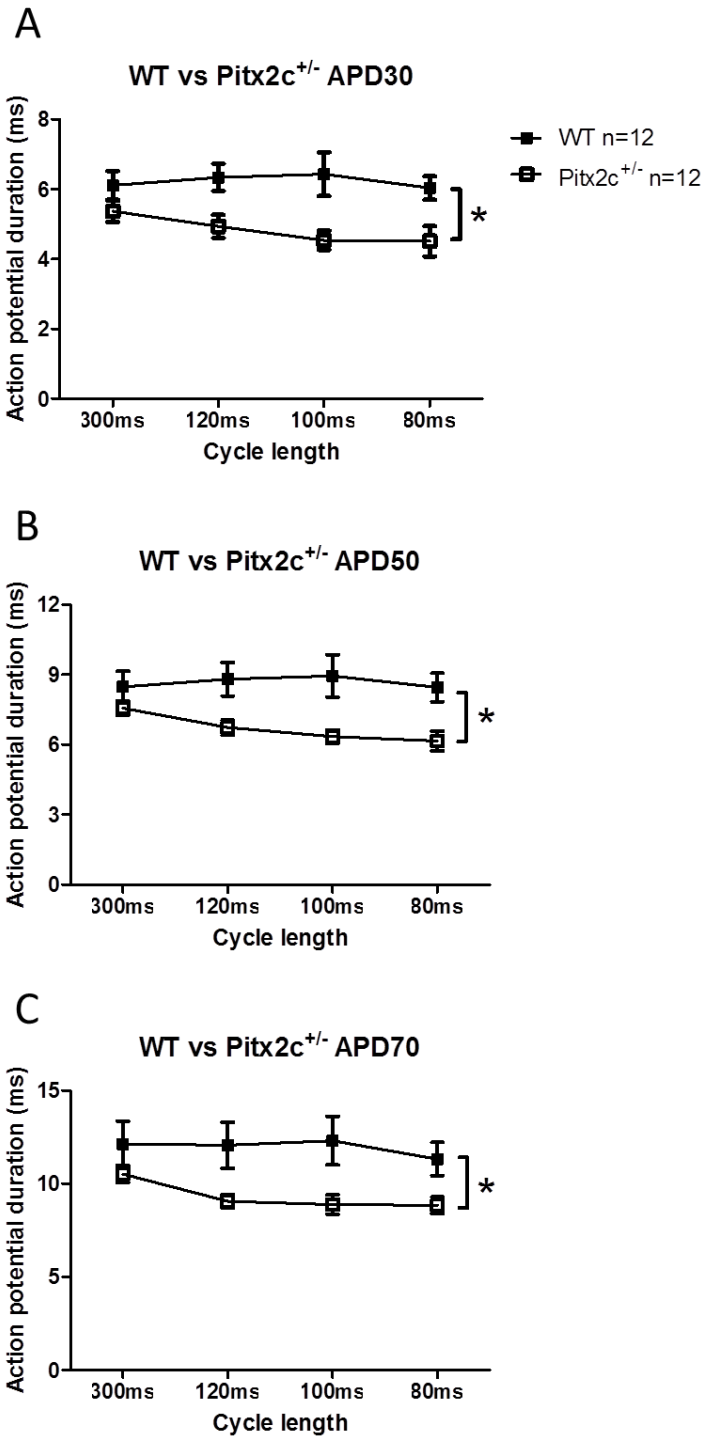

Figure 5.4. Pitx2c$^{+/-}$ deficient mice indicate a lower APD value in the left atrium.

WT and Pitx2c$^{+/-}$ littermates were stimulated at multiple CLs and action potentials recorded and analysed. Samples from Pitx2c deficient mice showed a significantly lower APD value when compared to WT littermates. Significance across the board is denoted by * $P<0.05$. Bonferonni post hoc analysis revealed that significance arose from the shorter CLs (APD30: 100ms, 80ms; APD50: 120ms, 100ms, 80ms; APD70: 100ms). Statistical analysis was performed using two way repeated measures ANOVA. Error bars represent SEM.

5.3.2. Flecainide reduces conduction velocity in the left atrium

Figure 5.5 shows isochronal maps of WT and Pitx2c$^{+/-}$ LA samples before and after the infusion of flecainide. The atrial samples in the Figure 5.5 were stimulated at 100ms CL. Following the infusion of flecainide the activation times increase substantially, as indicated by the large areas of red in the lower row of Figure 5.5. Figure 5.6 shows the CV values from 5 WT and Pitx2x$^{+/-}$ samples both showing a slowed conduction as a result of the flecainide. Mean CV at baseline for WT mice 24.92 ± 3.05cm/sec compared to 17.54 ± 1.06cm/sec after 15 minutes of flecainide infusion and stimulated at 100ms CL. Mean CV values for Pitx2c$^{+/-}$ before and after flecainide were 25.76 ± 2.17cm/sec and 20.36 ± 1.29cm/sec, respectively at 100ms stimulation CL. Significance was measured across the board for the WT and Pitx2c$^{+/-}$ LA. Performing Bonferroni post tests revealed that the significance in the WT were at 300ms, 100ms and 80ms. For the Pitx2c$^{+/-}$, the post test showed that the significance was due to 120ms, 100ms and 80ms. Figure 5.6C compares the difference in conduction between the genotypes after flecainide infusion showing no significant changes between the WT and Pitx2c$^{+/-}$ littermates. This data suggests that the flecainide does not have a preferential effect on CV between the genotypes.

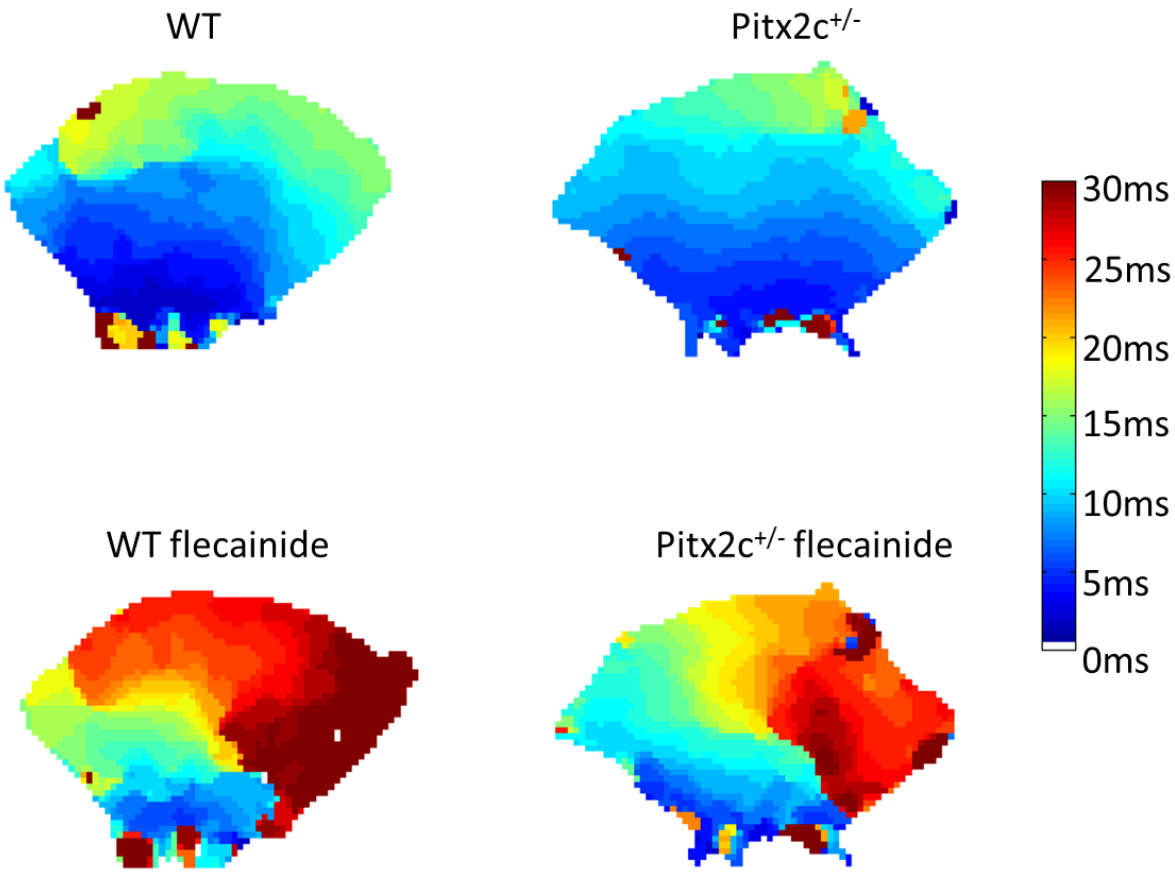

Figure 5.5. Activation maps at baseline and 1μM flecainide for WT and Pitx2c$^{+/-}$.

This shows LA samples from both WT (n=5) and Pitx2c$^{+/-}$ (n=5) stimulated at 100ms CL at baseline (top row) and flecainide infusion (bottom row). The flecainide was infused for 15 minutes at a concentration of 1μM. CV values for the WT atrium in this sample were calculated to be 22.1cm/sec at baseline and 17.3cm/sec with flecainide. CV values for the Pitx2c$^{+/-}$ sample was 27.8cm/sec at baseline and 17.0cm/sec with flecainide. The slow in CV due to flecainide can be seen with the large number of red pixels indicating later activation times compared to baseline levels.

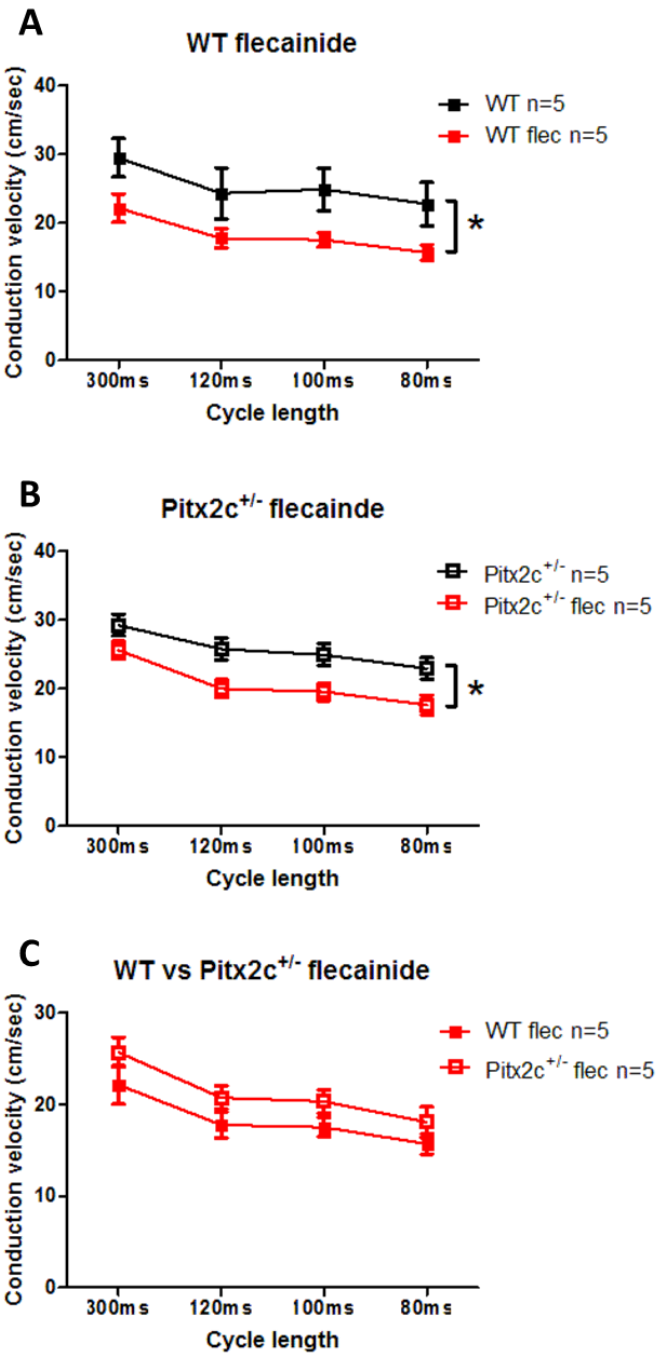

Figure 5.6. Conduction velocity reduction in left atrial WT and Pitx2c$^{+/-}$ littermates in response to 1µM flecainide.

The CV of the WT and Pitx2c$^{+/-}$ LA were measured at baseline and after 1µM flecainide infusion. A) Shows a significant reduction in CV with flecainide compared to baseline levels for WT LA samples. B) Indicates a reduction in CV after flecainide for Pitx2c$^{+/-}$ littermates. C) Shows the comparison between genotypes with flecainide indicating no difference between the CV. This suggests that the flecainide does not have a preferential effect on CV between the genotypes. Significance across the board is denoted by * P<0.05. Bonferroni post tests revealed that the significance in the WT were at 300ms, 100ms and 80ms. Pitx2c$^{+/-}$ post test showed that the significance was due to 120ms, 100ms and 80ms. Error bars represent SEM. Statistical analysis was performed using two way repeated measures ANOVA.

5.3.3. Flecainide prolongs the APD in Pitx2c$^{+/-}$

The addition of flecainide following baseline measurements showed a prolongation in APD. Figure 5.7 shows effect of the addition of 1µM flecainide compared to baseline measurements for both genotypes. Figure 5.7A to Figure 5.7C shows that there was a trend in prolongation at all APD and stimulation pacing cycles for WT (n=5) littermates but was not statistically significant. Baseline values were calculated as 10.95 ± 0.85ms compared to 13.70 ± 1.81ms with flecainide at APD70 and 100ms CL. Figure 5.7D to Figure 5.7F showed a significant prolongation in APD after the infusion of flecainide in Pitx2c$^{+/-}$ (n=5). At APD70 and 100ms baseline values were 8.58 ± 0.61ms compared to 14.46 ± 1.95ms after flecainide. The greatest difference was seen in the shorter CL stimulations. Performing Bonferroni post hoc tests revealed that the significance was due to 100ms and 80ms in AP50 and APD70. This coincides with the nature of flecainide's use dependence; the effect is increased with as heart rate increases.

The differences in APD values previously witnessed between WT and Pitx2c$^{+/-}$ in Figure 5.4 appear to be abolished with 1µM flecainide as seen in Figure 5.8. The values at baseline showed a decreasing APD with shorter stimulation CLs which were also abolished with flecainide.

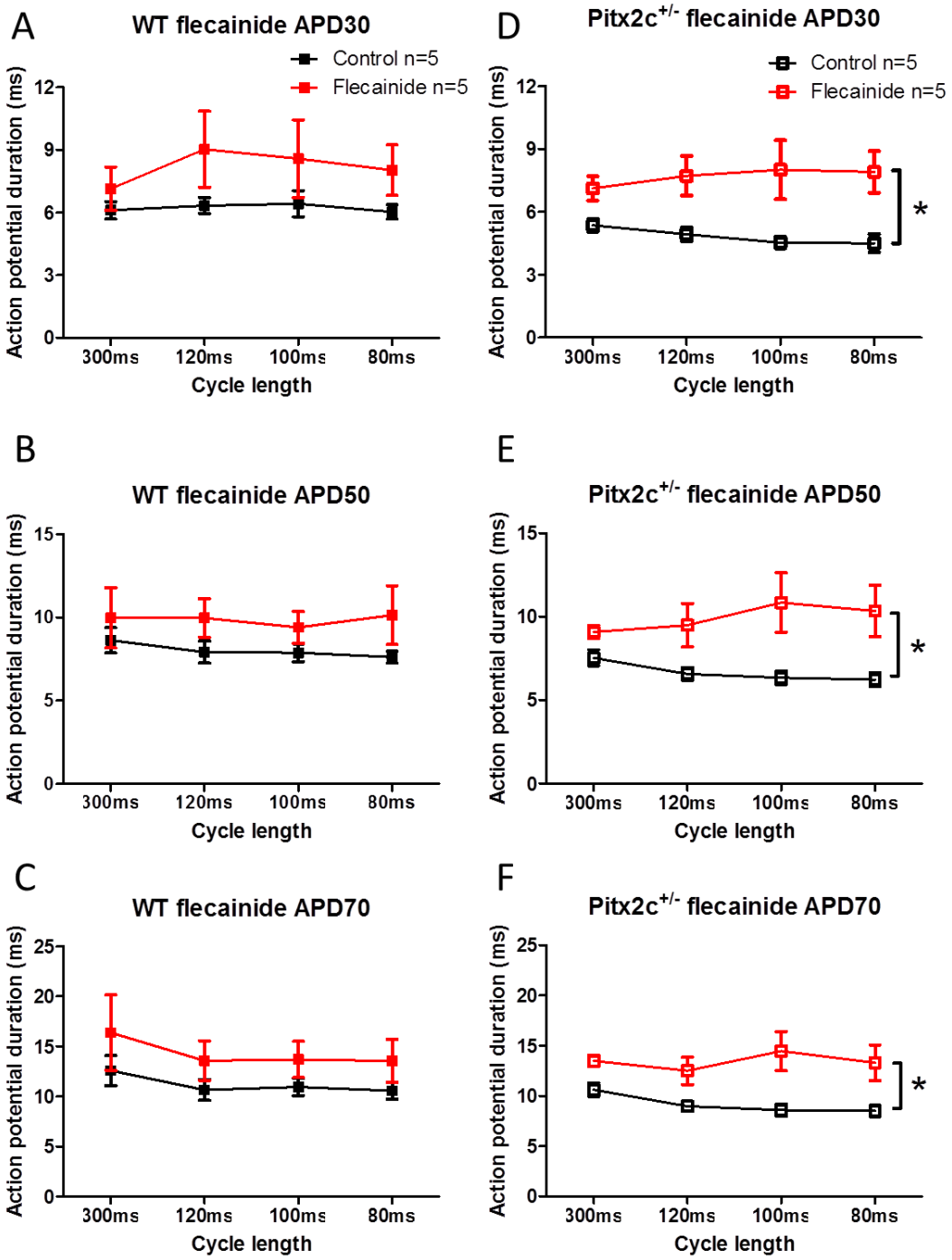

Figure 5.7. Action potential duration prolongation in response to 1μM flecainide infusion in WT and Pitx2c$^{+/-}$ littermates.

APD measurements were made on the LA at baseline and with 1M flecainide. A) to C) Shows the change in APD for WT littermates from baseline to flecainide had no significant differences. However, the data suggests that there is a trend in increased APD value with flecainide. D) to F) Shows a significant increase for all APD measurements in Pitx2c$^{+/-}$ samples with flecainide. Significance is denoted by across the board is denoted by * $P<0.05$. Bonferroni post hoc tests revealed that the significance was due to 100ms and 80ms in AP50 and APD70. Points indicate mean values with error bars representing SEM. Statistical analysis was performed using two way repeated measures ANOVA.

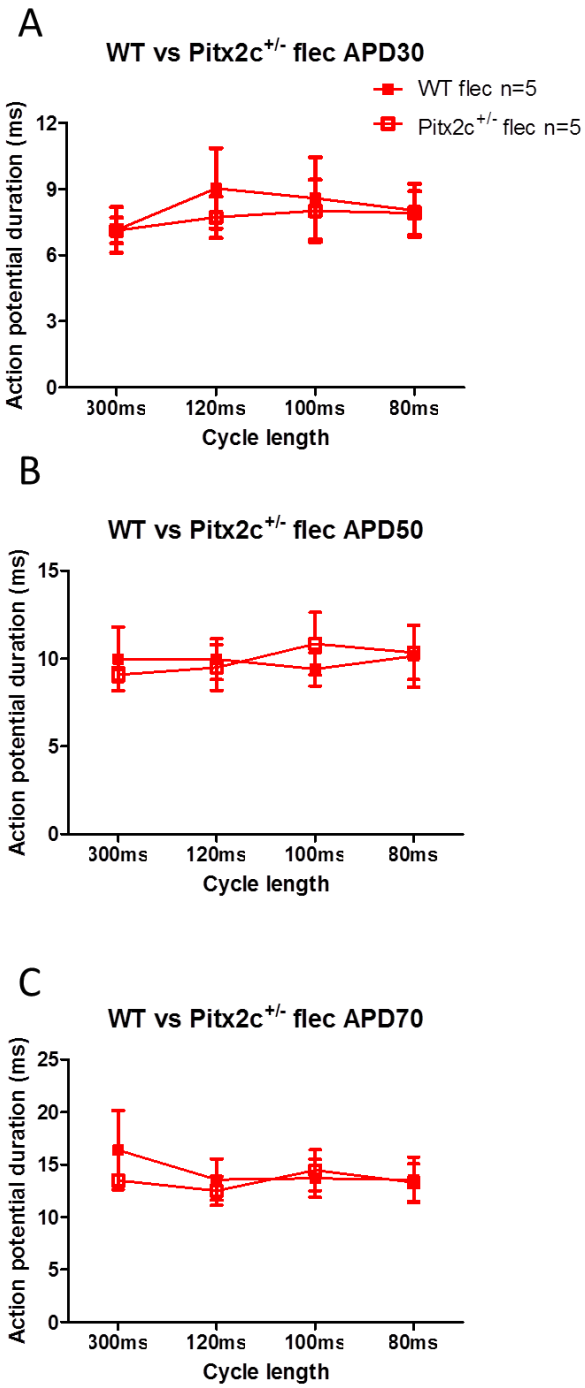

Figure 5.8. Action potential duration differences between WT and Pitx2c$^{+/-}$ littermates after 1μM flecainide infusion.

This shows the APD measurements at 30%, 50% and 70% repolarisation for both genotypes after the addition of flecainide. The comparisons show no change in APD between genotypes, which suggests that the differences previously seen at baseline were absolved. Points indicate mean values with error bars representing SEM. Statistical analysis was performed using two way repeated measures ANOVA.

5.4. Discussion

In this study, no changes affecting the activation spread and CV of the LA samples between WT and Pitx2c$^{+/-}$ were witnessed. This data supports previous findings by Kirchhof *et al* (2011) whereby the isochronal maps showed no irregular activation patterns and activation times as measured by contact and optical mapping but with cruder spatial resolution of the optical signal. Activation times give an indication of CV by measuring the duration between a stimulus artefact and the fastest upstroke [138], [32]. As this method only measures in theory two points, the conduction pathway may be non-linear and complex [123] as discussed in the method development chapter. The CV measurements made by the optical mapping system gives a more reliable result as this can measure complex activation patterns.

These findings also showed that there was a significant reduction in APD value for the atrial samples which were Pitx2c$^{+/-}$ deficient compared to WT littermates (Figure 5.4). Kirchhof *et al* also showed reduced APD at short paced CL stimulations in Pitx2c$^{+/-}$ compared to WT littermates. Figure 5.4 shows that the difference between the genotypes is seen at the shorter stimulation CLs, whereas the previous study [55] showed a reduction at the short CLs only (80ms CL for APD50 and APD70).

The CV and activation patterns were not different between genotypes which suggest that shortening of the APD is responsible for the wavelength reduction in Pitx2c$^{+/-}$ mice.

5.4.1. Flecainide and Pitx2c deficiency

It has been shown that a lack of Pitx2c in the atrium impairs the sodium channel expression [53]. Flecainide is a sodium channel blocker which may enhance its effects with the lower sodium channel expression in Pitx2c$^{+/-}$ mice. The results shown corroborate with this enhanced effect as hypothesised. Figure 5.7 showed that the APD had increased significantly only for the Pitx2c$^{+/-}$ mice and not for the WT littermates. In addition to this, flecainide abolished the difference in APD in the LA between the genotypes. One explanation for the APD values reaching similar levels between the genotypes after flecainide may be that flecainide non-selectively binds to potassium channels [139], [140]. The potassium current plays a major role in repolarising the cardiac AP and it would be interesting to see whether the expression of potassium channels is affected by Pitx2c$^{+/-}$ which could explain the APD shortening compared to WT. Flecainide was also shown to significantly reduce the CV in both genotypes of the LA. The CV slowing was apparent from the isochronal maps shown in Figure 5.5, whereby both genotypes were affected to the same degree. As discussed earlier, a reduced repolarisation in Pitx2c$^{+/-}$ with a static CV value may increase inducible AF.

A limitation of the optical mapping system was that the changes in fluorescent intensities which give rise to optical action potentials were not absolute voltage values. Hence other techniques as such microelectrode and patch clamp aid in supporting our findings. Current unpublished data from the group have shown a significant difference between resting membrane potential between the WT and Pitx2c$^{+/-}$ littermates. Using microelectrode measurements atrial cardiomyocytes with reduced Pitx2 mRNA expression showed a higher positive resting membrane

potential in different experimental conditions. Patch clamp studies showed a small difference in holding potential and have reproduced the observed differences in sodium channel blockade by flecainide found in Pitx2-deficient cardiomyocytes. Controlling the holding potential abolished any difference in Pitx2 deficient and WT isolated atrial cardiomyocytes. Our unpublished data suggest that such a difference could explain the effectiveness of sodium channel blockers in patients with a common gene variants on chromosome 4q25 (see Syeda *et al.* Appendix 5 - PITX2 modulates atrial membrane potential and reduced PITX2 potentiates the antiarrhythmic effects of sodium-channel blockers.).

The key finding here was that flecainide shows an enhanced antiarrhythmic effect in Pitx2c$^{+/-}$ LA. From a clinical perspective, sodium channel blockers may be an attractive therapy for AF patients with reduced Pitx2c expression.

6. Optical imaging of the plakoglobin deficient mouse left atrium

6.1. Introduction and overview

Arrhythmogenic right ventricular cardiomyopathy (ARVC) is an inherited heart disease which is a significant cause of sudden death in young athletes. ARVC is caused by genetic defects in genes coding proteins in the “area composita” i.e. of the desmosomal region of the myocardium. Mutations in the proteins which encode the cell-cell junction play a central role in ARVC [114], [141].

Previous studies have shown that the chromosomes near the 17q21 locus encodes the gene for plakoglobin [69]–[71]. Plakoglobin is a protein which is a key constituent for the adherent junctions and is responsible for the tight adhesion between cardiomyocytes [69], [71]. It is involved in the area composita of adhering junctions, which consists of adherent fascia molecules in the intercalated disk of vertebrates [67], [68] and anchorage of cytoskeleton filaments to specific cadherins [72].

Genetically altered murine models have verified the roles of junctional protein dysfunction in ARVC. Homozygous deletion of plakoglobin ($plako^{-/-}$) is lethal during gestation [72]. However, heterozygous deletion ($plako^{+/-}$) in murine models is sufficient to provoke the ARVC phenotype which consists of enlarged right ventricle (RV) and inducible ventricular tachycardia [64]. Kirchhof *et al* have also shown that the RV enlargement and ventricular tachycardia was inducible without fibro-fatty infiltration of the cardiac muscle. Other studies have characterised ARVC by the fibro-fatty replacement of cardiomyocytes primarily in the RV [58],

[142], but also show biventricular infiltration and abnormalities in conduction and repolarisation [143]. This cardiac remodelling due to the fibrosis and enlargement of the RV can act as a substrate for arrhythmias.

It has been shown that patients with ARVC have not only a greater prevalence of ventricular arrhythmias, mostly generating from the RV, but also more atrial arrhythmias [65], [144], [145]. Studies of atrial pathology in ARVC are still only recent. Other studies have shown a reduction in sodium channel availability in some cases of human ARVC [146], [147]. As the cardiac sodium channel ($Na_v1.5$) is responsible for the upstroke phase of the action potential, a reduction in availability can lead to reduced sodium current and conduction velocity (CV) which in turn increases arrhythmia susceptibility. Other desmosomal proteins such as Plakophillin-2 have been shown to decrease sodium current and CV [148], [149]. Therefore, optical mapping was used to investigate potential changes in CV across the whole left atrium (LA). Functional changes were also investigated using the optical mapping system to study action potential variations between wild-type (WT) and plako$^{+/-}$ littermates. It was hypothesised that there may be changes between the plako$^{+/-}$ atrial CVs and APDs due to potential functional and structural differences compared to WT samples.

6.1.1. Flecainide and plakoglobin deficiency

Flecainide is antiarrhythmic drug (AAD) which is a sodium channel blocker. In the desmosomal macromolecular complex, $Na_v1.5$ channels are preferentially expressed at the intercalated disc [150]. As discussed previously, the ARVC model may lead to sodium channel dysfunction [146], [147] and increased arrhythmia susceptibility. One of flecainide's effects is prolonging the inactivated

state of the sodium channel [151] increasing the time between the next possible action potential, known as the effective refractory period (ERP). As sodium is responsible for the depolarisation of an action potential, a blockade in the channel reduces the sodium current density causing a decrease in CV. Subtle sodium channel effects may be enhanced by flecainide as it causes sodium channel blockade. This may give insight into the differences between effects of the sodium channel block on the atrial plakoglobin deficient model.

It was hypothesised that as some patients with ARVC are predisposed to sodium channel irregularities, the effect of flecainide on atrial CV might be enhanced in plakoglobin deficiency.

6.1.2. Effect of endurance training

There is an increasing body of evidence for those who are predisposed to ARVC, which suggests to avoid excessive exercise [152], [153]. An estimated 22% of young athletes who suffer from sudden cardiac death do so as a result of ARVC [152]. Previous studies have shown that older age groups of endurance trained plako$^{+/-}$ mice developed ventricular arrhythmias and conduction slowing in the RV [64]. Another study performed in rat models showed significant increase in cardiac fibrosis due to intensive training for 16 weeks which were reversed after 8 weeks post training [154]. Human studies have found that intense exercise may cause acute dysfunction in the RV along with structural remodelling [155]. Rigorous physical activity has also shown to increase the incidence of AF in older adults (>=65 years) [156] and younger men [157]. Early stage dysfunction can be reversed by halting training and evidence shows that preload reducing therapy,

protecting the RV from stress during exercise, can prevent ARVC in mouse models [158].

Structural and functional changes which may give rise to atrial arrhythmias in ARVC models have not been well described. Here, findings where the atrial APD and CV were measured along with the addition of flecainide which may exacerbate small changes in sodium activity are presented.

6.1.3. Effect of dihydrotestosterone

Androgenic anabolic steroids (AAS) are synthetic derivatives of the male sex hormone testosterone and can enhance an athlete's performance. In animal studies, observations have shown AAS to produce hazardous effects on heart structure and function [159]. Dihydrotestosterone (DHT) is a metabolite of testosterone which has often been abused as an AAS and can be detected in the plasma by mass spectrometry. One study showed hypertrophic effects in that the weight of the right ventricular wall and atria to body weight ratio increased significantly in rats given elevated doses of DHT [160]. In general, there exists a higher prevalence of cardiovascular disease in males [161], [162].

These cardiovascular effects of AAS on atria of mice genetically predisposed to vulnerable cell-cell connections could exacerbate small changes in cardiac function. Hypertrophic effects have been shown in the ventricles [160] but little work has been published on the effects of ARVC on the mouse atria. It was suspected that there may be small changes in atrial morphology causing conduction differences between plako$^{+/-}$ and WT littermates that may increase with DHT. DHT treatment may result in APD changes. With the development of the high resolution optical mapping system these hypotheses were investigated.

6.2. Methods

This study was performed on atria of WT and Plakoglobin deficient littermates (plako$^{+/-}$) [64], [114]. Mice were of adult age of 12-20 weeks old. Plako$^{+/-}$ mice were generated by removal of the plakoglobin specific exon as seen in Figure 6.1. Mice were first generated and previously described by Ruiz *et al. 1996* [72], not by the author of this thesis.

Experimental protocols and procedures are described in the material and methods on page 46. Other procedures specific to this study are as follows.

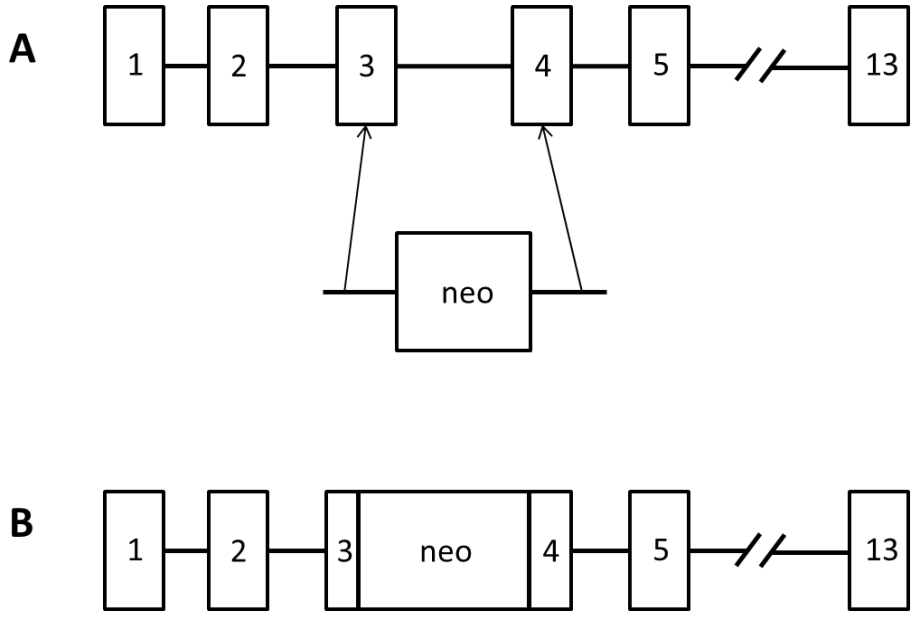

Figure 6.1. Gene targeting strategy for plakoglobin.

A) Shows the genomic structure of plakoglobin. Boxes represent the exons and lines represent introns. The neomycin gene cassette is represented by the box labelled neo. The cassette targets a part portion of exon 3, the following intron sequence, and a portion of exon 4. B) Illustrates the genomic structure with the inserted neomycin cassette with portions of exon 3 and exon 4 removed. The result of the exon removal stops the expression of plakoglobin. This strategy was described by Ruiz *et al. 1996* [72].

6.2.1. Controlled exercise intervention

To test the effects of exercise as a mode of exacerbating ARVC like phenotype, plako$^{+/-}$ mice were endurance trained by swimming. Cohorts of mice were placed in 30x50x30cm containers (Home Bargains, UK) with lukewarm tap water for training. To ensure a suitable temperature, floating bath thermometers (Philips, NL) were used to maintain the water at 28°C. Swimming sessions were performed over 6 weeks, 6 days a week at 2 sessions per day. Each session was performed in the morning and late afternoon. The mice were originally trained for 2 minutes per session to acclimatise them to the water. The duration was increased by 1 minute per day until they reached 24 minutes and then 2 minutes per day until 45 minutes was reached. For cages with fewer than 3 mice, multiple cages were combined but no more than 7 were placed into each container. To distinguish the mice, white marks were drawn on their tail. Only mice of the same sex were allowed to share a single container. To ensure the mice were swimming adequately, an activity score was used for each mouse:

- 0 = floating
- 1 = moderate intensity
- 2 = actively swimming

After the end of each swimming session, mice were dried and returned to their respective cages. Any signs of distress during the training session, the mice were quickly removed from the container and dried.

The swim training was carried out at the Biomedical Services Unit (BMSU) at the University of Birmingham by the author and at least another licensed individual or a qualified staff member of the BMSU for every session.

6.2.2. Effective refractory period measurements

Programmed stimulation was used to determine the ERP of the LA and recorded using optical mapping. The electrodes were attached to a constant voltage isolation unit (Grass Technologies, USA) which was connected to a Grass s88x stimulator (Grass Technologies, USA). The voltage used was twice the diastolic threshold that was determined using the same method as described in section 3.6. The recording time was increased to 100 seconds as this allowed ample time to determine the ERP. A train of eight stimuli (S1) was produced at a rate of 120ms CL with an early ninth stimulus (S2). This procedure was repeated with the S2 stimulus reducing in 1ms decrements until a response was not produced. The ERP was determined by the time between the last S1 beat and when the S2 failed to produce an action potential as seen in Figure 6.2.

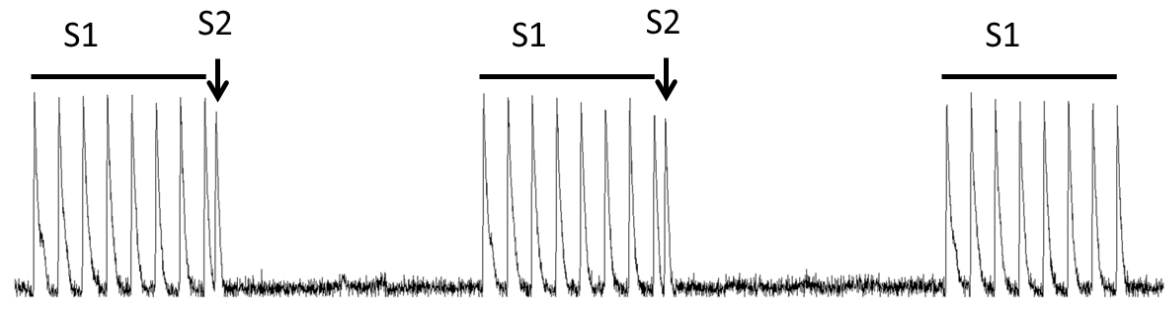

Figure 6.2. Effective refractory period determination using S2 stimulus at 120ms.

The ERP was determined using optical mapping by providing a train of eight stimuli (S1) at 120ms CL and a ninth premature stimulus (S2). From above, the middle train's S2 beat comes 1ms earlier than the previous train shown on the left. The S1-S2 train is repeated with 1ms decrements until the ninth stimulus fails to illicit a response as seen from the train on the right.

6.2.3. Dihydrotestosterone pump implantation

To test the effects of doping, mice were surgically implanted with osmotic pumps (Alzet, USA) which released 5α-Dihydrotestosterone (DHT) (Sigma-Aldrich, USA) over a period of 42 days at a rate of 0.15µl per hour. The osmotic pumps were prepared by Dr Genna Riley from the University of Birmingham and surgical implantation by Ian Ricketts (Named Animal Care and Welfare Officer, Biomedical Services Unit, University of Birmingham, UK) not by the author of this thesis. A 200µl solution of 62.5mg/ml of DHT-ethanol solution was filled into each pump. The pumps each contained a flow moderator which was initially removed, so that a filling tube could be inserted. The pumps were held upright and the DHT-ethanol solution was injected through the aperture. The pumps were filled when a small volume of solution would begin to overflow. The flow moderator was replaced and the pumps were stored in centrifuge tubes for a minimum of 48 hours before implantation. The 48 hour period was necessary as the DHT-ethanol solution required time to diffuse out of the pump.

Mice were anaesthetised by inhalation with isoflurane, (Abbott Laboratories, USA). A small incision was made on the back skin of the mouse, approximately 2cm above the base of the tail. A blunt dissection was performed using surgical scissors until a space was suitable for the pump. Forceps held the incision open whilst the pump was slowly inserted. The wounds were then closed with surgical clips.

6.3. Results

6.3.1. Atrial electrophysiological properties in plakoglobin deficiency

In order to investigate if plakoglobin heterozygous deficiency leads to changes in atrial CV and atrial action potential, the LA from plako$^{+/-}$ mice and their WT littermates were examined using optical mapping. Example activation maps are shown in Figure 6.3 depicting a typical activation spread starting from the bottom to the top in atria from young sedentary mice. There were no signs of irregular activation patterns in either young sedentary plako$^{+/-}$ or WT mice. In Figure 6.3 CV values were calculated to be 29.3cm/sec and 25.7cm/sec for WT and plako$^{+/-}$, respectively.

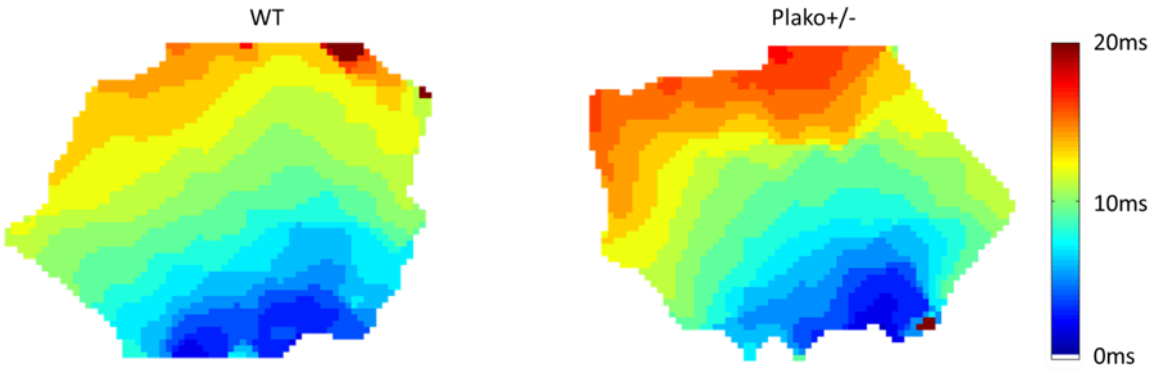

Figure 6.3. Sedentary WT and plako$^{+/-}$ littermate activation maps.

Sednetary LA samples from WT (n=13) and plako$^{+/-}$(n=11) littermates were compared. Representative examples of the LA stimulated at 100ms CL are shown above. CV values were calculated to be 29.3cm/sec and 25.7cm/sec for WT and plako$^{+/-}$, respectively. The mean values from both genotypes suggested that plako$^{+/-}$ LA had no significant CV slowing compared to WT. No irregular activation patterns were found between the samples. The blue regions indicate the start of activation propagating upwards to the red and orange regions. The LA samples were pinned to the imaging chamber which may have caused irregularities in certain pixels which can be seen on the edges of the activation maps.

Furthermore, CV changes at various cycle lengths (CLs) were investigated. Figure 6.4 shows the comparison of CV plako$^{+/-}$ vs WT all CLs from 300-80ms. The mean CV values from 300ms to 80ms CL were calculated to be 31.35 ± 1.27cm/sec, 27.93 ± 1.24cm/sec, 26.29 ± 1.44cm/sec and 25.05 ± 1.11cm/sec, respectively for the WT littermates (n = 13). For the plako$^{+/-}$ samples (n=12) the CV calculations were 30.89 ± 1.04cm/sec, 28.90 ± 1.41cm/sec, 27.68 ± 1.11cm/sec and 25.38 ± 1.12cm/sec for 300ms to 80ms, respectively. CV decreased with decreasing CL as expected in both genotypes.

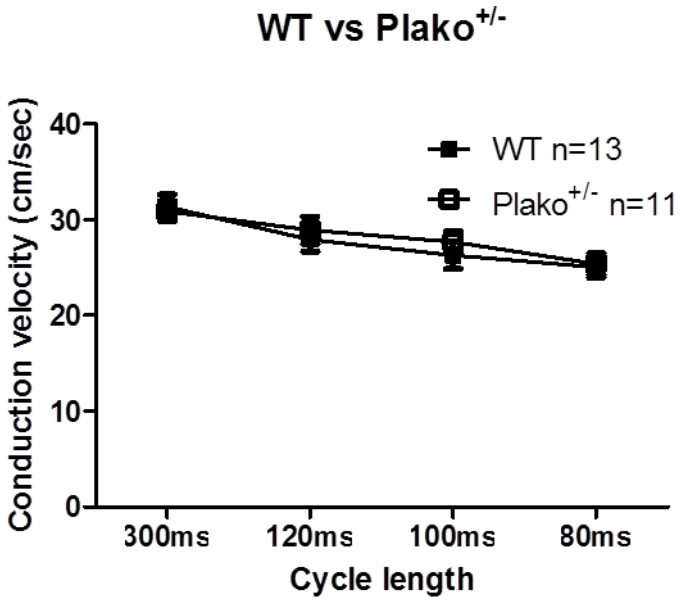

Figure 6.4. Conduction velocity measurements from sedentary WT and plako$^{+/-}$ LA samples.

The CV of the WT and plako$^{+/-}$ LA were measured. The decrease in CL stimulations showed a reduction in CV in both genotypes. No differences in CV were found between genotypes for all CLs. This suggests that plako deficient LA samples do not show a change in CV compared to WT samples. Points indicate mean values with error bars representing SEM. Statistical analysis was performed using two way repeated measures ANOVA.

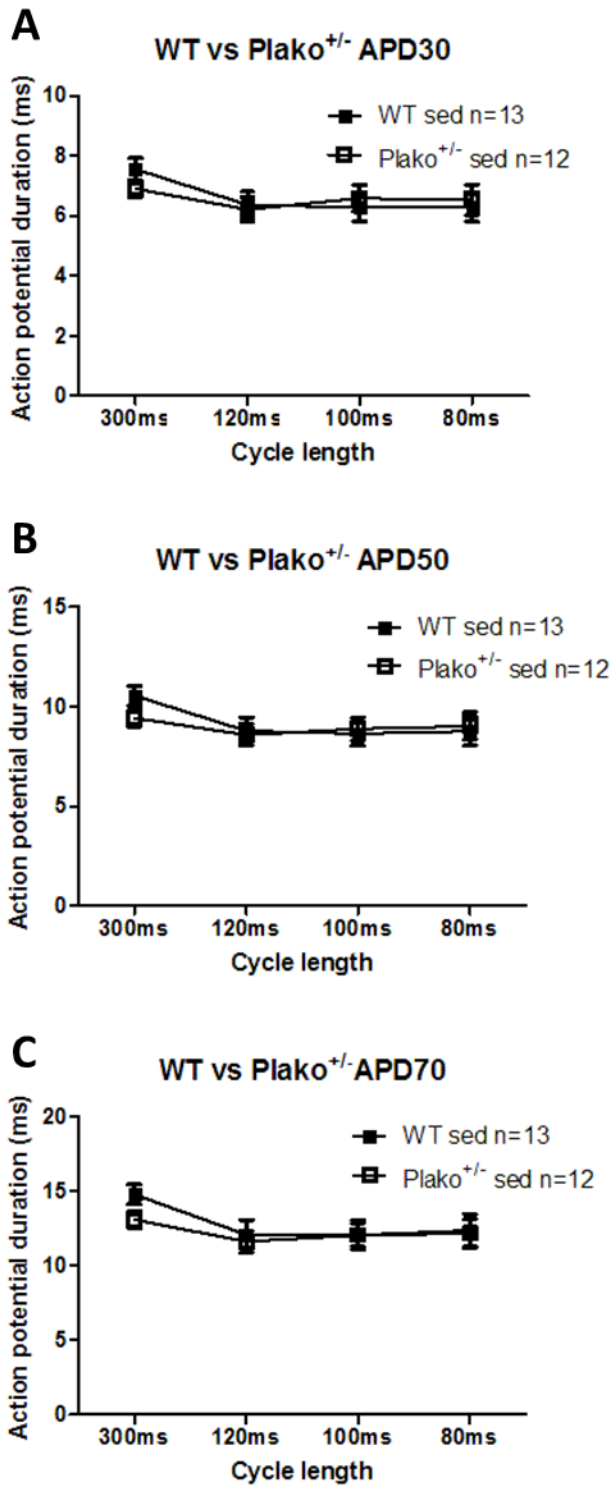

Figure 6.5. Atrial action potential duration measurements from WT and plako$^{+/-}$ sedentary mice.

APD measurements were taken from the LA of 13 WT and 12 plako$^{+/-}$ mice at decreasing CLs. A), B), C) represent APD measurements at 30%, 50% and 70% repolarisation, respectively. No significant changes were observed between genotypes. Points indicate mean values with error bars representing SEM. Statistical analysis was performed using two way repeated measures ANOVA.

Both genotypes exhibit decreases in APD70 with decreasing stimulation CLs (Figure 6.5). There was however, no significant difference in APD70 in plako$^{+/-}$ and WT littermates seen. Measurements were also performed at APD50 and 30 showing no statistical difference between the genotypes.

6.3.1.1. Flecainide prolongs APDs in WT and plako$^{+/-}$ atria

In order to investigate alterations in physiological parameters with the addition of a sodium channel blocker known to slow CV, 1µM of flecainide acetate was added to the tissue samples. A significant prolongation in APDs was found in WT mice at all APD30, APD50 and APD70 with flecainide, this is shown on the left column of Figure 6.6. Significance was seen across the board and performing Bonferroni post hoc test revealed that at all CLs significance was found. A prolongation was also found in the plako$^{+/-}$ mice at APD30 and APD70 (Figure 6.6) APD50 showed a strong trend that durations were increased with flecainide. ($p=0.054$), a reason for the lack of significance was due to outliers in the dataset. Performing Bonferroni post hoc test revealed that only 300ms CL was significant at APD30 and APD70. The APD values at 120ms and 100ms CL for the plako$^{+/-}$ show a large deviation in the standard errors. Looking at the individual APD values, the variation is caused by strong outliers. The data presented here were from a mean of 9 APDs from 5 WT and 4 plako$^{+/-}$.

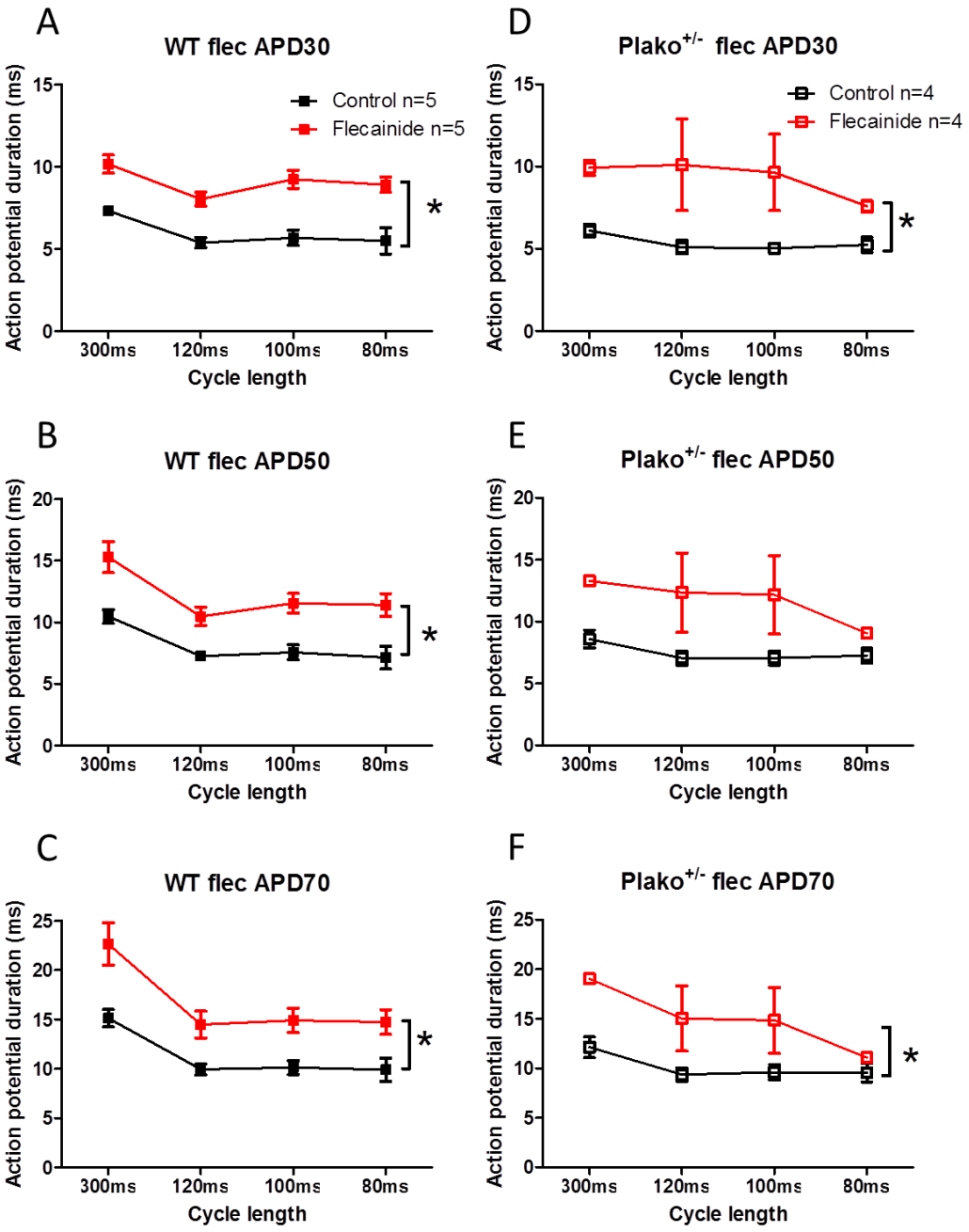

Figure 6.6. Flecainide prolongation of action potential duration in the WT and plako$^{+/-}$ left atrium.

APD measurements were recorded at baseline and then repeated with 1µM flecainide with decreasing stimulation CL for both WT and plako$^{+/-}$ littermates. A) to C) Shows WT data from 5 samples at APD30, APD50 and APD70. The WT APD measurements show a significant increase in mean values with flecainide. Bonferroni post hoc test revealed that at all CLs significance was found. D) to F) Shows plako$^{+/-}$ data from 4 LA samples at baseline and with flecainide. A significant increase in APD value was seen at APD30 and APD70. From D) to F) large SEM values can be seen at 120ms and 100ms CL, this was due to outlying measurements. Bonferroni post hoc test revealed that only 300ms CL was significant at APD30 and APD70. Significance across the board is denoted by * $P<0.05$ between control and flecainide. Points indicate mean values with error bars representing SEM. Statistical analysis was performed using two way repeated measures ANOVA.

6.3.1.2. Flecainide slows conduction in WT and plako$^{+/-}$ murine atria

The CV measurements were recorded from sedentary WT and plako+/- LA samples. Recordings were made at baseline and repeated with 1um flecainide infused after 15 minutes. Flecainide reduced CV in both WT and plako$^{+/-}$ littermates as shown in Figure 6.7. Significance was witnessed across the board with flecainide. Performing Bonferroni post test showed that the results were significant at 120ms and 80ms WT and at 100ms for the plako$^{+/-}$ LA.

Of the original cohort of 13 WT and 12 plako$^{+/-}$ LA, 5 WT and 4 plako$^{+/-}$pairs were used for the flecainide experiments. The remainder of the atrial preparations suffered from lack of stimulus capture with the flecainide infusion. Flecainide increases the threshold potential required to invoke a depolarisation [163]. As a result of the increased potential, stimuli were often not evoked by the stimulator in some of the experiments. CV slowing was consistent at all CLs of the stimulation protocol. Figure 6.8 (bottom row) illustrates the activation spread of WT and plako$^{+/-}$ littermates with flecainide paced at 100ms CL. These maps indicate the activation time has prolonged compared to those in Figure 6.8 (top row), as the samples with flecainide have a high proportion of red pixels indicating 30ms activation time. These maps show the irregularity of activation spread across the atrium on samples of both genotypes with flecainide. The irregularity of the activation is due to the CV slowing to an extent that the activation travels via an alternate route, hence the discontinuity from blue to red regions.

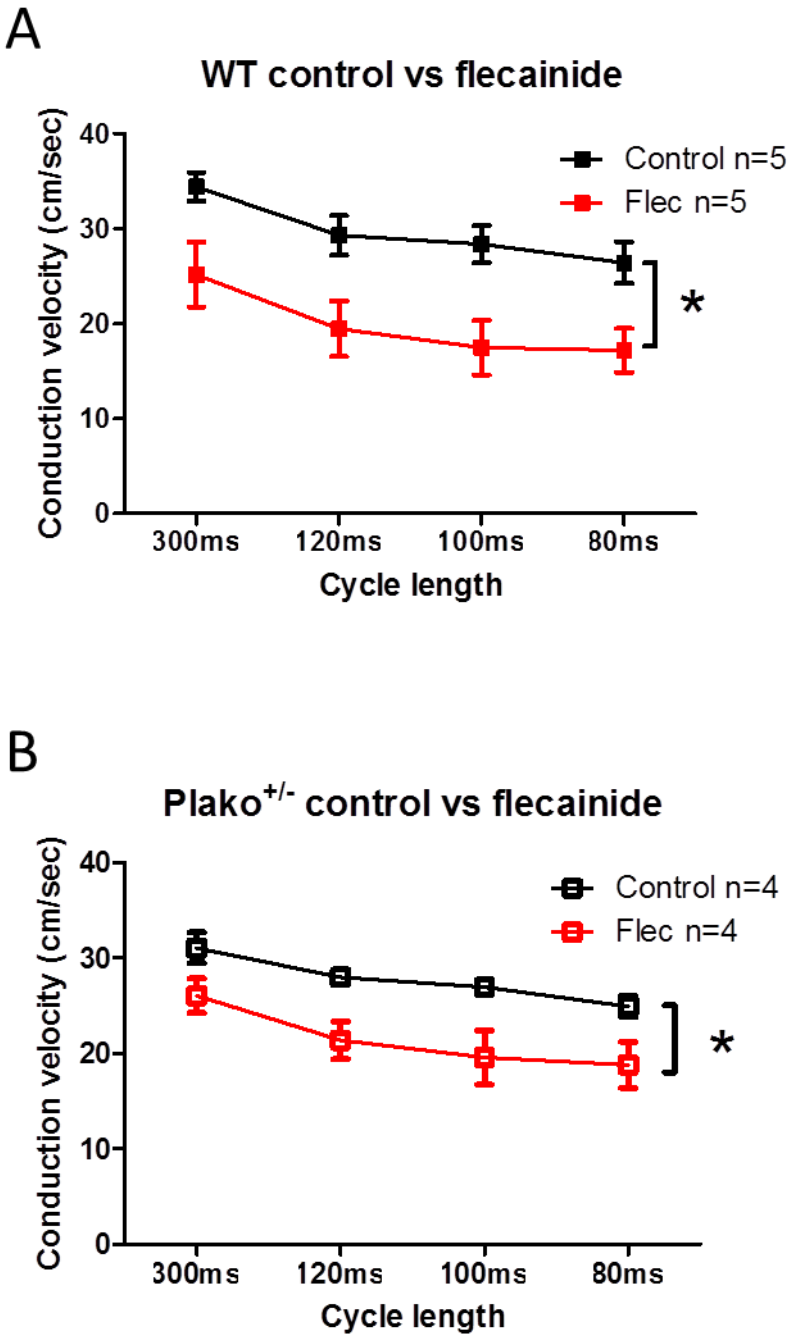

Figure 6.7. Conduction velocity reduction with flecainide infusion.

The CV measurements were recorded from sedentary WT and plako$^{+/-}$ LA samples. Recordings were made at baseline and repeated with 1um flecainide infused after 15 minutes. A) Shows a significant decrease in CV with flecainide compared to baseline levels in WT LA. B) Shows CV measurements for plako$^{+/-}$ samples significantly decreased after flecainide. Significance across the board is denoted by * P<0.05 when compared to control and flecainide samples. Performing Bonferroni post test showed that the results were significant at 120ms and 80ms WT and at 100ms for the plako+/- LA. Points indicate mean values with error bars representing SEM. Statistical analysis was performed using two way repeated measures ANOVA.

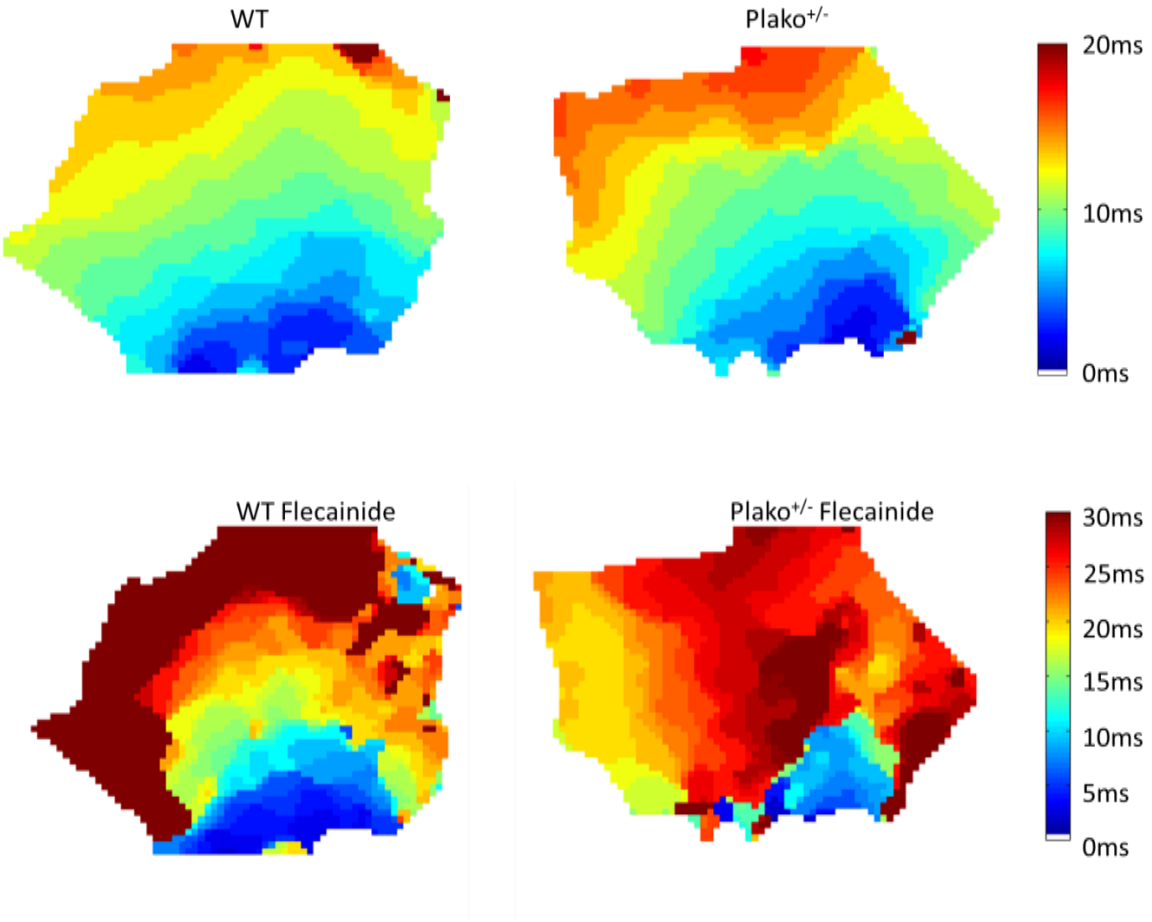

Figure 6.8. Activation maps of left atrial preparations from WT and young sedentary plakoglobin deficient mice with 1µm flecainide stimulated at 100ms CL.

The maps shown above are activation patterns of WT and plako$^{+/-}$ LA samples stimulated at 100ms CL. The measurements were taken at baseline and after 15 minutes of 1µM flecainide infusion. The top row indicates control samples from WT and plako$^{+/-}$ with their activation spreading upwards from the blue to the red regions. The bottom row illustrates activation patterns after flecainide infusion for both genotypes. After the addition of flecainide, the activation times increased which can be seen from the large red regions in the maps. The irregularity of the activation is due to the CV slowing to an extent that the activation travels via an alternate route, hence the discontinuity from blue to red regions. The CV values for WT LA shown above were calculated to be 29.3cm/sec at control and 11.7cm/sec with flecainide. The Plako$^{+/-}$ CV values were measured at 25.7cm/sec at control and 17.32cm/sec with flecainide.

6.3.1.3. Cardiac refractoriness

In order to investigate the LA refractoriness in atria from sedentary WT and the plako$^{+/-}$ LA (n=3), the ERP was measured by an extra early stimulus (S2) as described in section 6.2.2. Measurements were performed before and after the infusion of 1µm flecainide at 120ms CL. Figure 6.9 shows that the atrial ERP was significantly prolonged with the addition of flecainide for plako$^{+/-}$ from 29.3 ± 0.9ms to 43.0 ± 3.0ms after infusion. Statistical significance was calculated by paired Student's t-test at $P<0.05$. In the WT mice the mean ERP values increased from 43.6 ± 4.7ms to 51.6 ± 6.6ms with flecainide but were not statistically significant. It should be noted that the WT LA had a significantly longer ERP that the plako$^{+/-}$ samples at baseline. A longer ERP indicates that it may be protective against atrial arrhythmias as it limits the time that the cardiomyocytes can re-excite. However, greater sample sizes are required for more conclusive results.

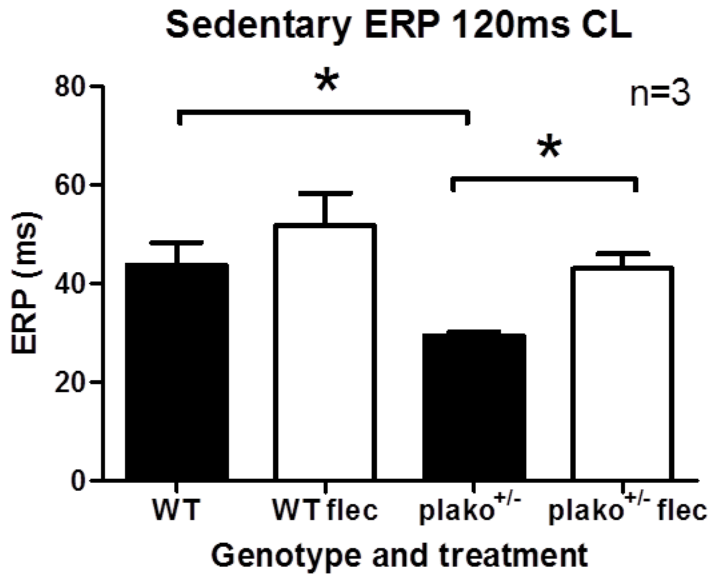

Figure 6.9. Effective refractory measurements in sedentary WT and plako$^{+/-}$ littermates before and after flecainide.

The ERP of sedentary WT and plako$^{+/-}$ littermates (n=3) were measured from the LA at 120ms CL. Measurements were taken at baseline and repeated after 1µM flecainide infusion. In the WT mice, mean ERP values increased from 43.6 ± 4.7ms to 51.6 ± 6.6ms with flecainide. In the plako$^{+/-}$ samples, the mean values significantly increased from 29.3 ± 0.9ms to 43.0 ± 3.0ms. The plako$^{+/-}$ LA had a significantly shorter ERP than the WT samples. Significance is denoted by * (P<0.05). Statistical significance was calculated by paired Student's t-test. Error bars indicate SEM.

6.3.2. Effect of endurance training on left atrial electrophysiological parameters function

6.3.2.1. Effects on left atrial conduction velocity

Initial experiments investigated the potential of moderate swim training induced cardiac remodelling. The majority of samples showed normal activation patterns as seen in Figure 6.10. A sample of 14 WT and 10 plako$^{+/-}$ mice were used in the training cohort. No changes in CV were observed between WT and plako$^{+/-}$ LA preparations from sedentary or trained young mice from activation maps. The CV

from the activation maps are presented in Figure 6.10C. The mean values for WT trained LA were 29.78 ± 1.34cm/sec, 24.44 ± 1.36cm/sec, 24.48 ± 1.36 cm/sec, and 22.87 ± 1.61cm/sec for stimulation CLs from 300ms to 80ms, respectively. The mean values for plako$^{+/-}$ trained samples were 29.50 ± 1.37cm/sec, 25.37 ± 1.62cm/sec, 24.28 ± 1.69cm/sec, and 23.34±1.70cm/sec for 300ms to 80ms, respectively. In addition to this, no atrial changes in CV were detected from the swim training itself when compared to atria from sedentary mice. From Figure 6.11 no significant changes in CV were determined from either the WT or plako$^{+/-}$ littermates post training. At certain CLs such as 120ms in both WT and plako$^{+/-}$ appear to have lower CV values, however, there was no statistical significance in this cohort.

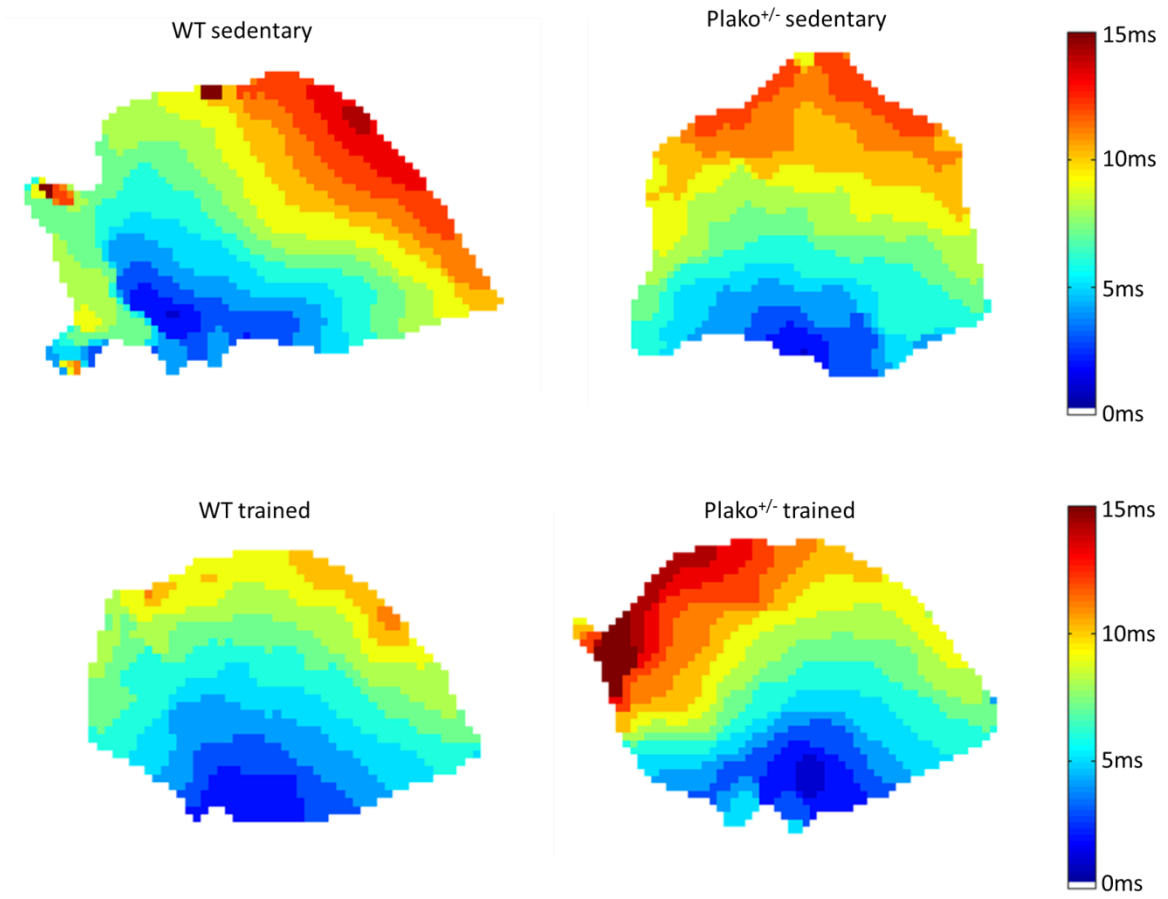

Figure 6.10. Sedentary and swim trained activation maps. WT and plako$^{+/-}$ littermate left atrial maps stimulated at 100ms CL.

Activation maps were generated from the LA of WT and plako$^{+/-}$ mice from both sedentary and swim trained cohorts. The top row shows samples which were sedentary for both genotypes and measured at 100ms CL. The sedentary CV values for WT and plako$^{+/-}$ were 23.68cm/sec and 26.44cm/sec, respectively. The bottom row shows samples which were swim trained for both genotypes measured at 100ms CL. The CV values for trained mice were 25.13cm/sec and 20.99cm/sec for WT and plako$^{+/-}$, respectively. However, the measurements from the cohort of 13 WT sedentary, 14 WT trained, 11 plako$^{+/-}$ sedentary and 10 plako$^{+/-}$ trained LA showed that the training showed no significant effect on CV in both genotypes. The activation pattern of the LA showed no effects from the swim training in this cohort

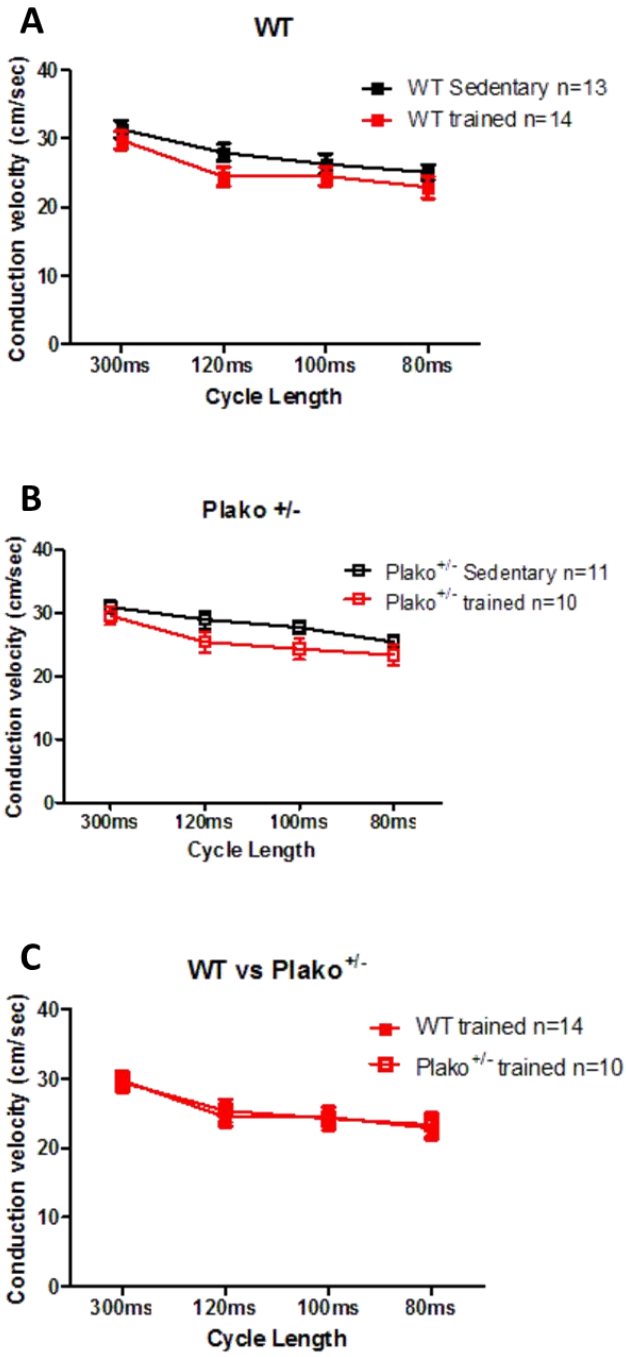

Figure 6.11. Conduction velocity values in response to swim training in WT and plako$^{+/-}$ littermates.

The data presented here compares the CV of the LA in a sedentary cohort to a trained group in both WT and plako$^{+/-}$. A) Shows the mean CV values for the WT LA for sedentary and trained mice. B) Shows the mean CV values plako$^{+/-}$ LA for sedentary and trained mice. C) Compares the genotype differences as a result of swim training. The effect of training has shown no change in CV for LA measurements for both genotypes. Points indicate mean values with error bars representing SEM. Statistical analysis was performed using two way repeated measures ANOVA.

6.3.3. Effects on APD

To test the effect of swim training further atrial AP changes in the LA were investigated. Comparisons between sedentary cohorts and trained cohorts were made as seen in Figure 6.12. The mean value for APD70 in WT sedentary mice at 100ms CL was 12.04 ± 0.96ms compared to the trained value of 12.63 ± 0.61ms. For the plako$^{+/-}$ samples the values for APD70 were 12.04 ± 0.77ms for sedentary versus 13.06 ± 1.40ms trained at 100ms CL. All results showed a pattern of decreasing APD value with decreasing CL.

Figure 6.12 shows the APD values for the sedentary and trained cohorts did not detect statistically significant changes for neither WT nor plako$^{+/-}$ at APD50 and 70 in the LA. However, there was a significant increase in APD30 in WT mice due to training but not in plako$^{+/-}$. Performing a Bonferroni post hoc analysis revealed that there were no statistical changes at specific CLs. Results show a slight trend in increased APD value due to training, but this showed no statistical significance.

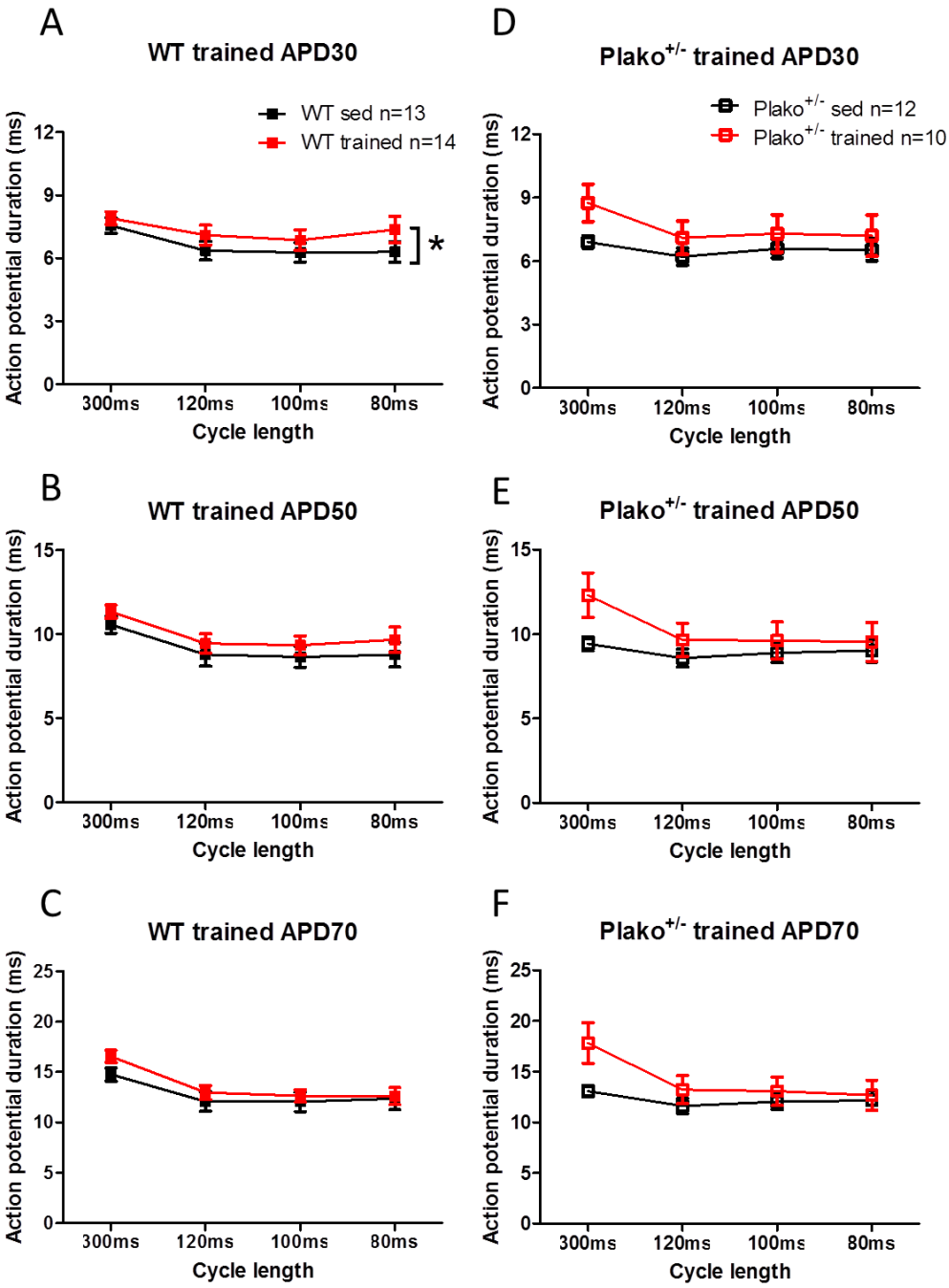

Figure 6.12. Action potential duration differences in response to swim training in WT and plako$^{+/-}$ littermates.

Data presented here compares the APD of the LA in a sedentary cohort of mice to a trained group. A) to C) Compares the effect of swim trained and sedentary mice at APD30, APD50 and APD70 in WT mice. D) to F) Compares the plako$^{+/-}$ genotype. The effect of training has shown no significant changes in APD for both genotypes with the exception of WT LA at APD30. Performing a Bonferroni post hoc test revealed that at there were no significant changes at individual CLs measurements for the WT mice at APD30. Significance is denoted by * $P<0.05$ comparing the sedentary samples to the swim trained. Points indicate mean values with error bars representing SEM. Statistical analysis was performed using two way repeated measures ANOVA.

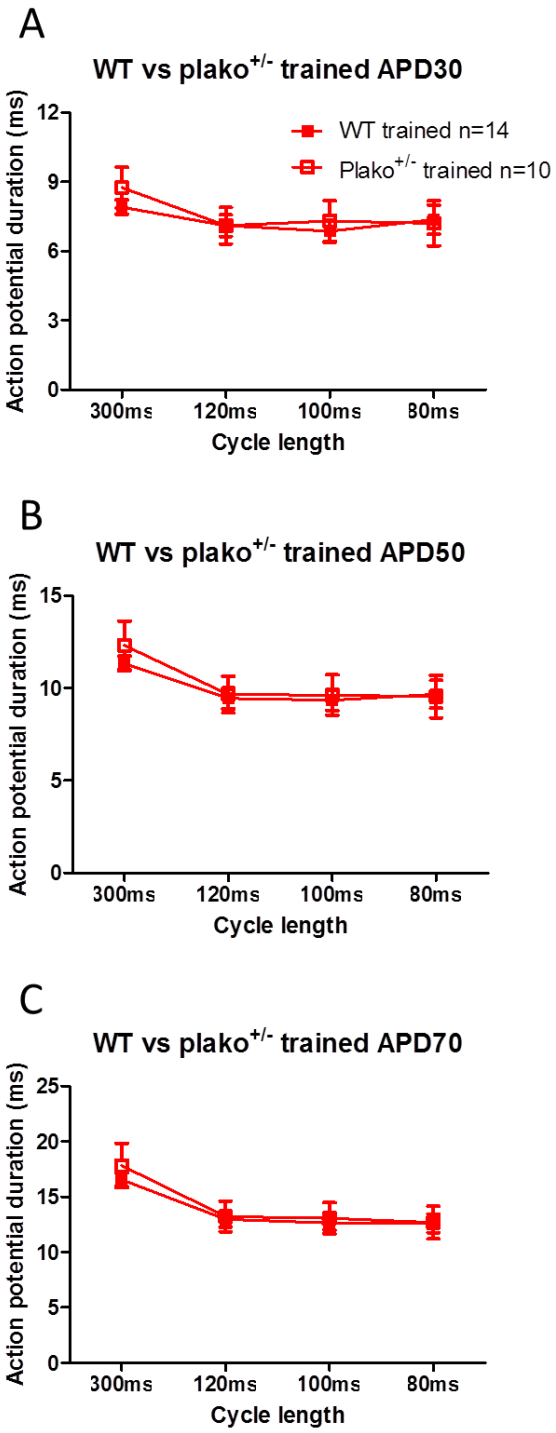

Figure 6.13. Action potential duration differences between WT and plako$^{+/-}$ littermates after swim training.

The effect of training was compared between WT and plako$^{+/-}$ samples. The APDs were measured at APD30, APD50 and APD70. Any changes across APD due to the effect of swim training were not witnessed. Points indicate mean values with error bars representing SEM. Statistical analysis was performed using two way repeated measures ANOVA.

6.3.4. Flecainide prolongs APD left atria after endurance training

To determine the effects of reducing sodium channel activity in the LA. 1µM flecainide was added to WT and plako$^{+/-}$ littermates as described in the methods. The effect of flecainide has shown to prolong the APD significantly for WT pairs (n=7) as shown in Figure 6.14. Significance was calculated by performing repeated measures two way ANOVA. Bonferroni post test revealed that significance was found at all values bar APD30 at 300ms in the WT LA, suggesting the flecainide had a strong affect. The average increase after flecainide in WT at APD70 was 36%, 41%, 47% and 60% for CLs of 300ms, 120ms, 100ms and 80ms, respectively. A trend in APD prolongation in the trained plako$^{+/-}$ was seen which did not reach significance in this cohort of 6 samples. The average increase in duration for the plako$^{+/-}$ atrial samples was 17%, 17%, 18%, and 16% for stimulation CLs of 300ms to 80ms, respectively. This percentage increase was much lower in the plako$^{+/-}$ than compared to WT. The smaller percentage change in plako$^{+/-}$ suggests that there may be less of a compounded effect from the flecainide and the swim training compared to WT samples. This raises further questions regarding sodium channels in the plakoglobin deficient model but investigations into this is beyond the scope of this study.

6.3.5. Reduction in conduction velocity in the left atrium due to flecainide

To investigate the effect of flecainide on the LA further, CV values were measured from WT and plako$^{+/-}$ pairs. The results show that there is a significant CV slowing

in the trained WT mice but not present in the plako$^{+/-}$ group. Significance was measured by repeated measures two way ANOVA, Bonferroni post hoc tests were also performed. The post hoc test revealed that the significance in the WT LA was at 100ms. On average the CV values dropped from 18 to 26% in the WT mice (n=6) and 13 to 22% in the plako$^{+/-}$ (n=7). The CV slowing due to flecainide can be seen in Figure 6.15.

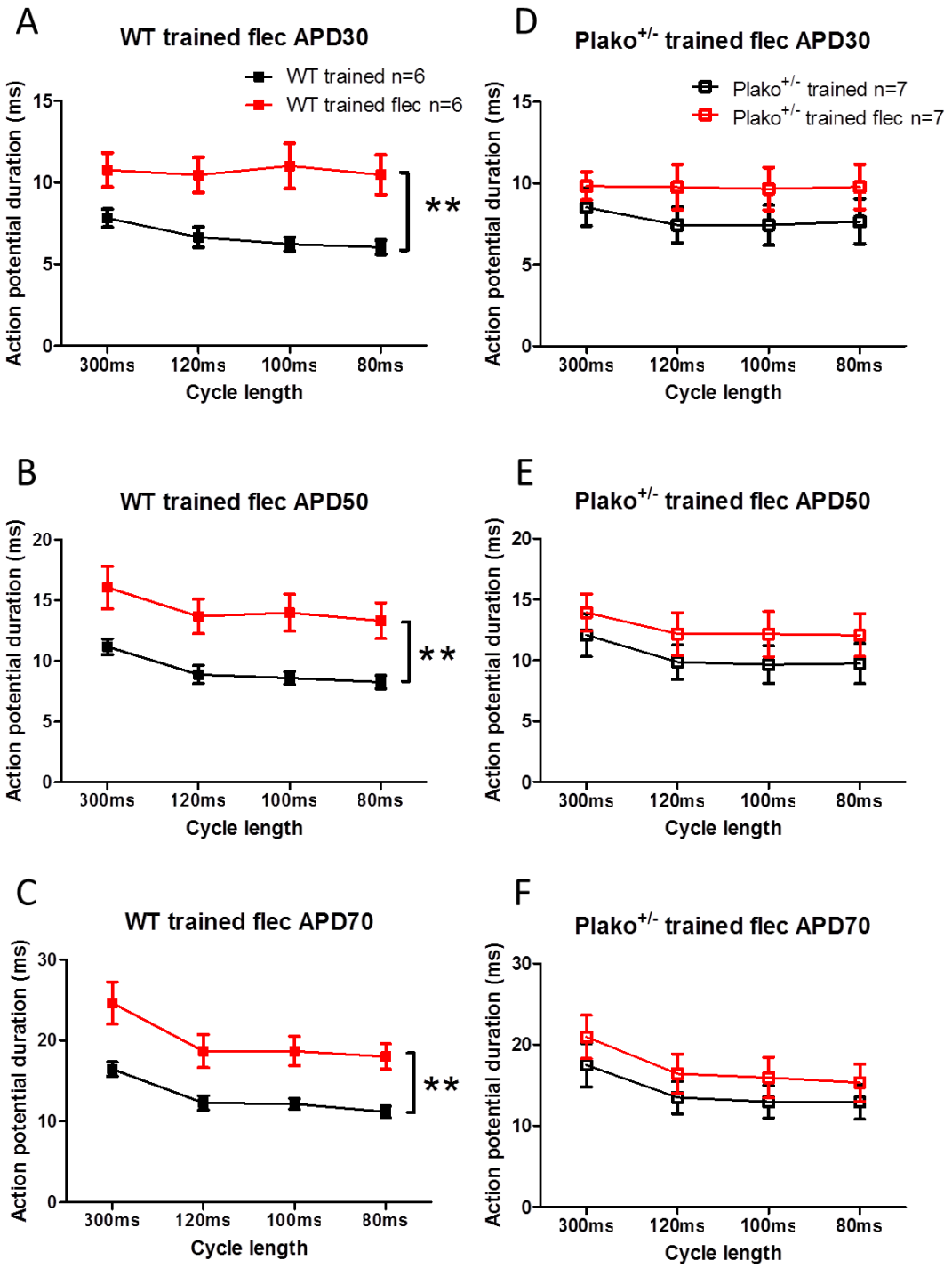

Figure 6.14. Action potential duration increases in response to flecainide in swim trained mice.

Paired data from WT and plako$^{+/-}$ sedentary and swim trained littermates were stimulated at decreasing CLs at baseline values and repeated with 1µM flecainide. A) to C) Shows a significant increase in APD in response to flecainide for WT trained LA samples. Bonferroni post test revealed that significance was found at all values bar APD30 at 300ms in the WT LA. D) to F) Show a trend in increased APD with flecainide compared to control values. The effects of flecainide appeared to have a greater effect on the WT swim trained than the plako$^{+/-}$ mice. Significance is denoted by ** P<0.01 compared with the baseline and flecainide mean values.

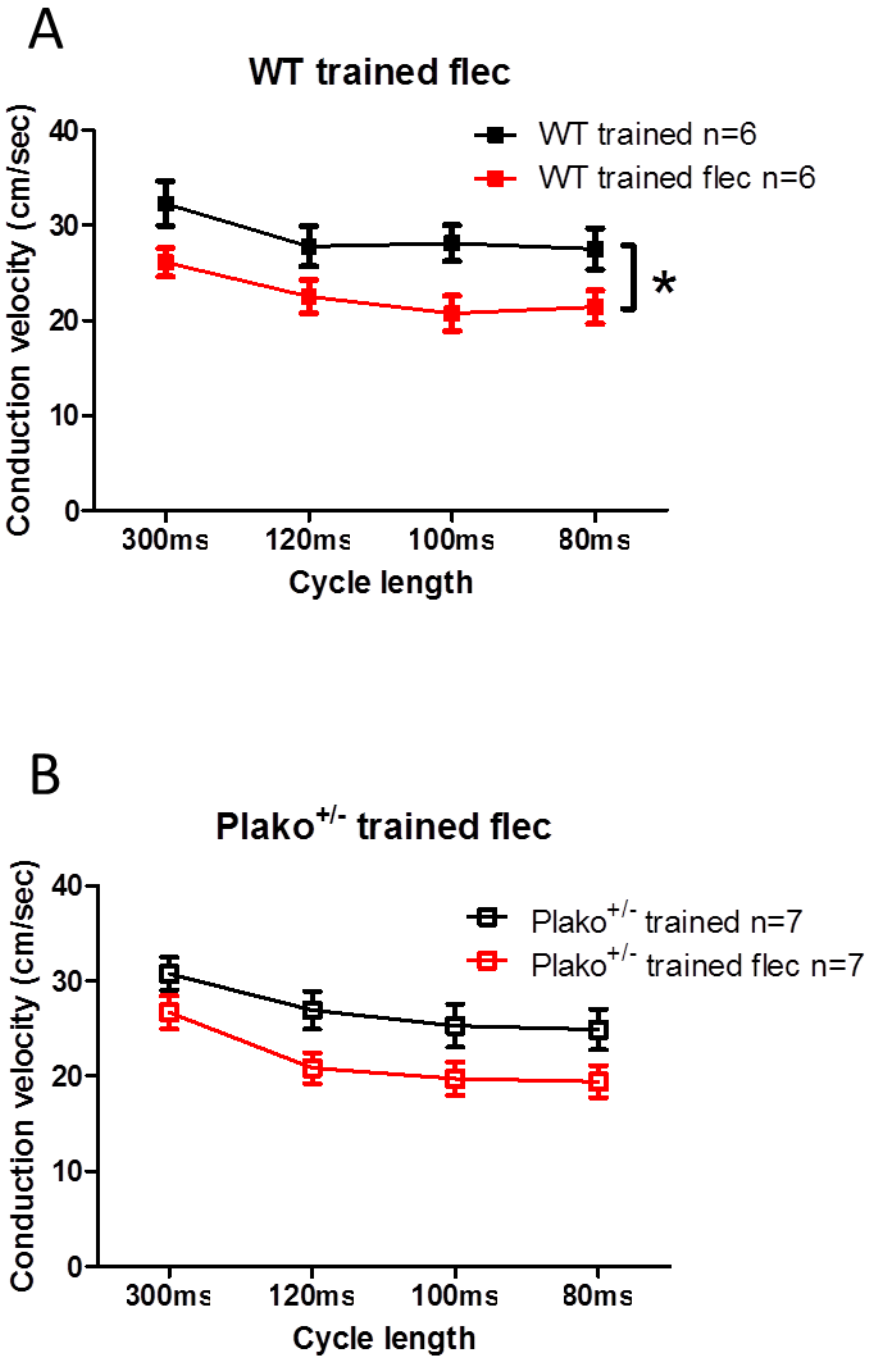

Figure 6.15. Flecainide reduces conduction velocity measurements from left atrial swim trained mice.

CV values were measured at baseline stimulation CLs and repeated with 1µM flecainide infusion. A) Shows a significant decrease in CV in WT trained mice after the addition of flecainide compared to at baseline. B) Shows a trend in decreased CV but this not statistically significant in plako$^{+/-}$. Significance is denoted by * P<0.05. Performing Bonferroni post hoc test revealed that the significance in the WT LA was at 100ms. Points indicate mean values with error bars representing SEM. Statistical analysis was performed using two way repeated measures ANOVA.

6.3.6. Flecainide and refractoriness after endurance training

To investigate the refractoriness effect of flecainide on the LA after swim training, WT and plako$^{+/-}$ littermates were stimulated with an extra early beat after a train of 8 stimulations as described in the methods. The S2 protocol was performed at 120ms CL at baseline and repeated after 15 minutes of 1µM flecainide infusion. Figure 6.16 shows that both the WT and plako$^{+/-}$ atria ERP were prolonged due to flecainide. WT (n=7) measurements were found to be 36.14 ± 3.60ms at baseline versus 48.71 ± 4.45ms flecainide. Plako$^{+/-}$ (n=5) ERP values were 43.20 ± 6.76ms at baseline compared to 54.00 ± 5.10ms with flecainide. Statistical analysis was performed using non parametric paired t-test (Wilcoxon matched pairs test) and significance was deemed at $P<0.05$. The plako$^{+/-}$ post training showed a longer ERP compared to LA plako$^{+/-}$ non trained (29.3 ± 0.9ms). The shorter ERP values in the sedentary plako$^{+/-}$ LA suggests that they may be more susceptible to atrial arrhythmias as there is a shorter time before the cardiomyocytes can be re-excited. However, from unpublished data from the lab show that swim training increases its arrhythmia inducibility. This is an interesting find and warrants further investigation.

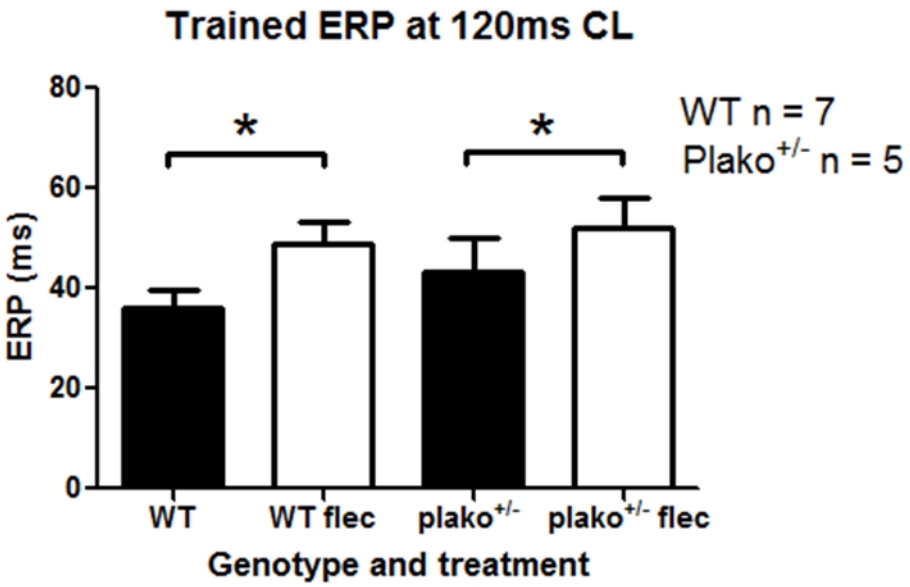

Figure 6.16. Effective refractory measurements in swim trained WT and plako$^{+/-}$ littermates before and after flecainide.

The ERP of swim trained WT (n=7) and plako$^{+/-}$ (n=5) littermates were measured from the LA at 120ms CL. Measurements were taken at baseline and repeated after 1μM flecainide infusion. In the WT mice, mean ERP values increased from 36.14 ± 3.60ms to 48.71 ± 4.45ms with flecainide. In the plako$^{+/-}$ samples, the mean values significantly increased from 43.20 ± 6.76ms to 54.00 ± 5.10ms. Significance is denoted by * ($P<0.05$). Statistical significance was calculated by paired Student's t-test. Error bars indicate SEM.

6.3.7. The effect of dihydrotestosterone on left atrium in sedentary models

An application for the optical mapping was to investigate the effects of DHT in WT and plako$^{+/-}$ littermates. The use of DHT as a doping agent may cause structural remodelling such as fibrosis and atria of the plako$^{+/-}$ model may be more susceptible to adverse effects. The mice were implanted with osmotic pumps as described in the method chapter. Optical mapping experiments were performed on isolated LA littermate pairs to measure CV and APD values. Figure 6.17 illustrates the isochronal maps for both WT and plako$^{+/-}$ LA samples with DHT.

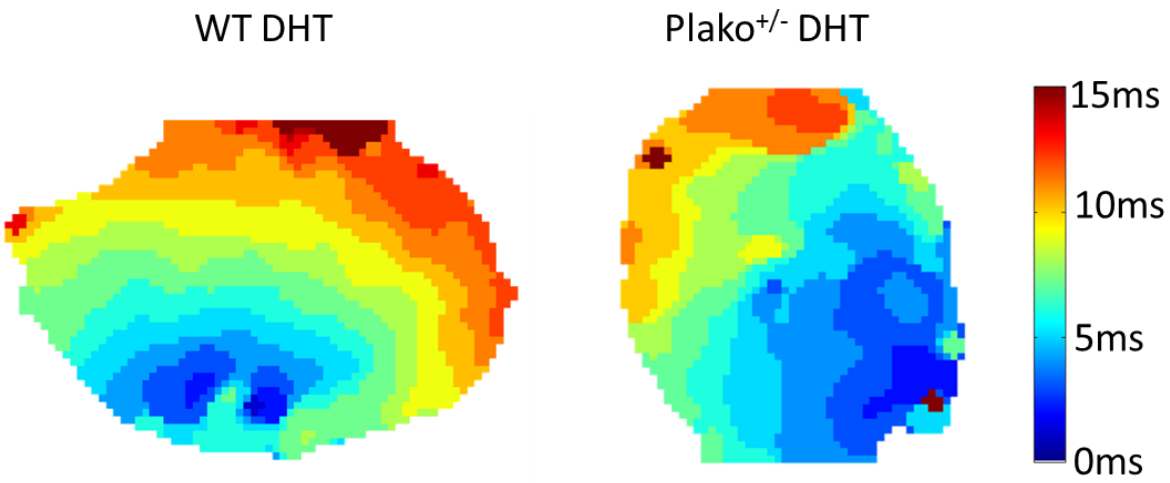

Figure 6.17. Sedentary DHT left atrial activation maps.

LA activation maps were generated from samples stimulated at 100ms CL from WT and plako$^{+/-}$ littermates. Osmotic pumps were filled with DHT and implanted in the mice over a period of 42 days. The atrial CV from both genotypes showed no significant differences between genotypes. Samples were measured from 5 WT and 3 plako$^{+/-}$ mice LA with DHT. However, due to the low sample size, the results presented here were not conclusive and warrant more experimentation.

6.3.8. Conduction velocity differences in murine models exposed to DHT

The atrial CV values as assessed with optical mapping were unchanged when comparing samples with DHT exposure to sedentary samples. The data presented is from 5 WT DHT treated mice and 3 plako$^{+/-}$ DHT samples. Figure 6.18 illustrate the CV values and show no significant change in mean values between DHT and sedentary and genotype differences with the DHT pumps implanted. The mean values for the CV values for the WT DHT littermates were 32.65 ± 0.99cm/sec, 28.05 ± 1.98cm/sec and 25.14 ± 1.84cm/sec and 23.08 ± 2.3cm/sec. For the plako$^{+/-}$ DHT mean values: 29.72 ± 2.94cm/sec, 27.19 ± 2.11cm/sec, 24.48 ±

2.3cm/sec and 22.88 ± 1.92cm/sec for CLs of 300ms, 120ms, 100ms and 80ms, respectively.

6.3.9. APD prolongation in the left atrium with DHT

Figure 6.19 shows a comparison between the sedentary cohorts of mice with and without DHT pumps implanted. The mean values for APD values for the plako$^{+/-}$ LA samples showed a prolongation. At 70% repolarisation mean values for plako$^{+/-}$ sedentary mice without DHT (n=11) stimulated at 100ms CL was 15.85 ± 1.94ms compared to 12.04 ± 0.77ms with DHT (n=3). Significance was calculated by two way repeated measures ANOVA. Performing Bonferroni post hoc test revealed that the main contributor of significance between the DHT and control were due to the 300ms CL at all APD values in plako$^{+/-}$ and at 120ms at APD30. The post hoc test suggests that the DHT mainly affect the LA during slower stimulations. However, more experiments should be repeated for higher statistical power due to the small sample size (n=3) and variability in experiments.

A change was seen at APD30 in the WT cohorts (n=13) from 6.28 ± 0.45ms to 8.97 ± 0.86ms with DHT (n=5), but no statistical differences were found at other APD values. Post hoc analysis revealed that the point of greatest significance was measured at 100ms in APD30 in the WT. Figure 6.20 show the changes in APD values seen with the addition of DHT were not significantly different between the WT and plako$^{+/-}$ genotypes.

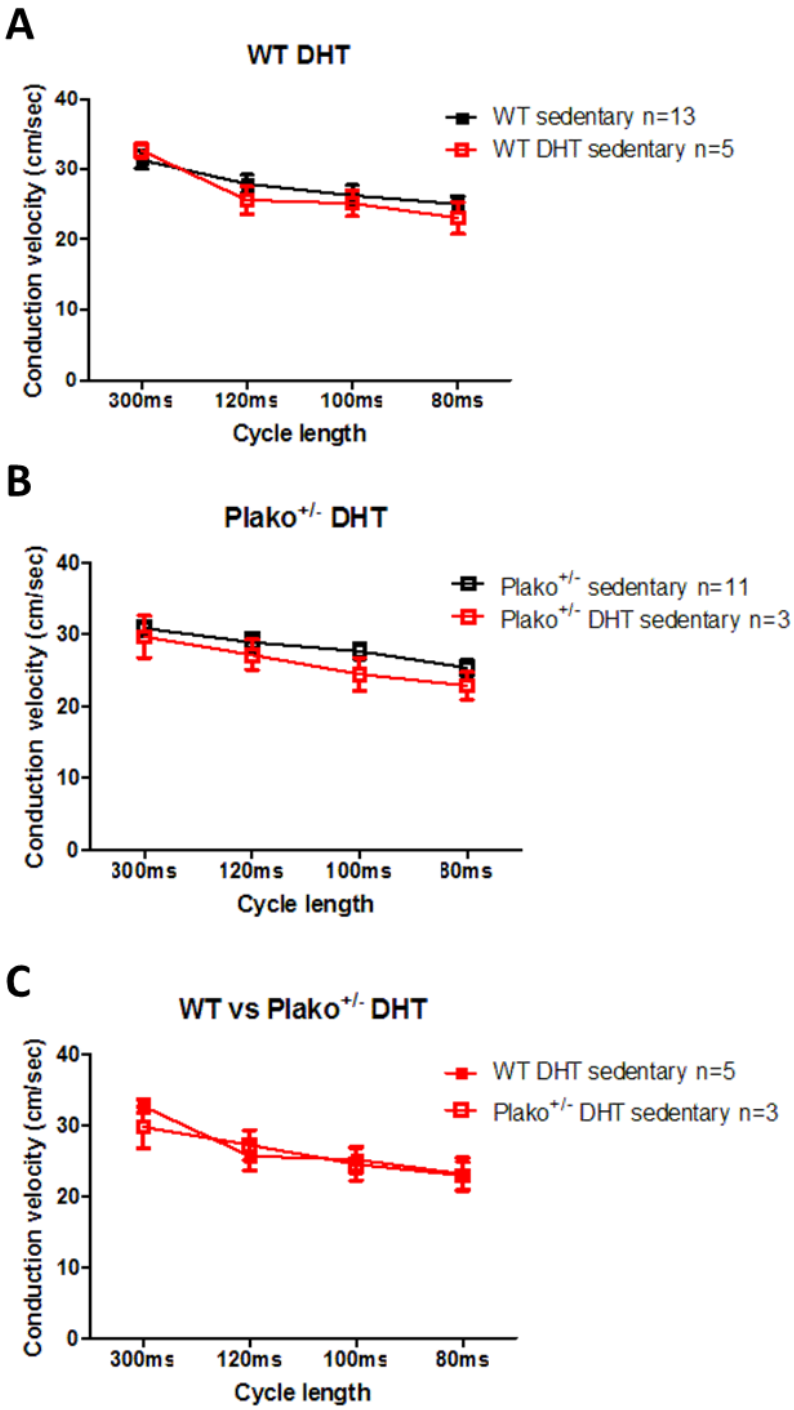

Figure 6.18. Atrial conduction velocity values remain unchanged in response to DHT.

The data here compares WT and plako$^{+/-}$ littermates with DHT osmotic pumps implanted to sedentary WT and plako$^{+/-}$ littermates. A) Shows the effect on CV in WT mice. B) The effect of DHT implanted plako$^{+/-}$ mice is compared to plako$^{+/-}$ sedentary LA samples. C) Comparisons between the WT and plako$^{+/-}$ LA CV show no difference between genotypes with DHT. Due to the low sample size with DHT, the results were not conclusive and warrant more experimentation. Points indicate mean values with error bars representing SEM. Statistical analysis was performed using two way repeated measures ANOVA.

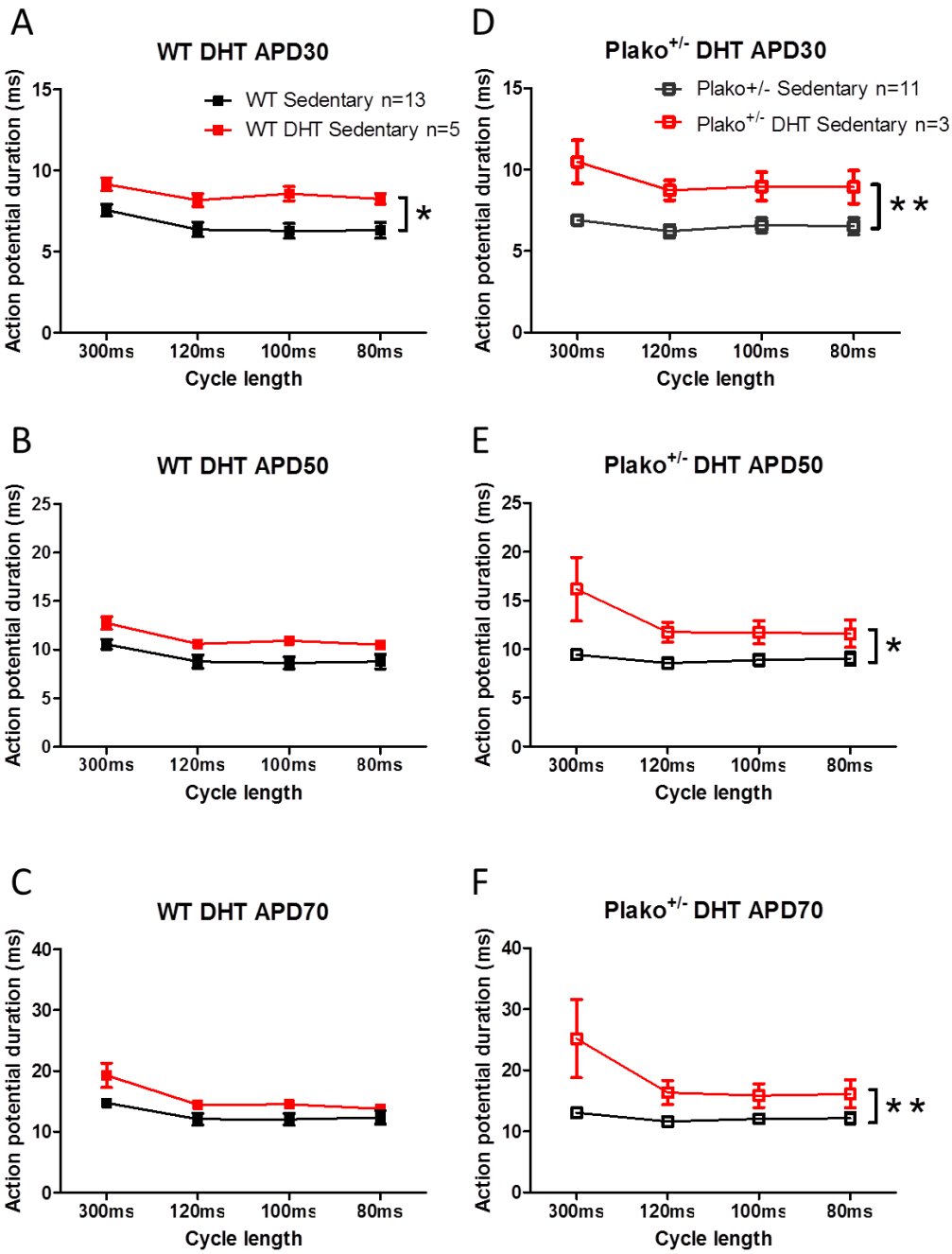

Figure 6.19. Atrial action potential duration changes compared between sedentary control and sedentary DHT mice.

The data presented here show sedentary WT and plako$^{+/-}$ littermate cohorts compared to littermates with DHT osmotic pumps implanted. A) to C) shows comparisons between WT mice with a trend in APD at APD50 and APD70. APD30 shows a significant increase in duration. Post hoc analysis revealed that the point of greatest significance was measured at 100ms in APD30 in the WT. D) to F) Presents the comparison between control groups and DHT samples. Significant increases was seen for all APD values. Performing Bonferroni post hoc test revealed that the main contributor of significance between the DHT and control were due to the 300ms CL at all APD values in plako+/- and at 120ms at APD30. Significance across the board is denoted by * $P<0.05$ when comparing mean values of sedentary and DHT littermates. Points indicate mean values with error bars representing SEM. Statistical analysis was performed using two way repeated measures ANOVA.

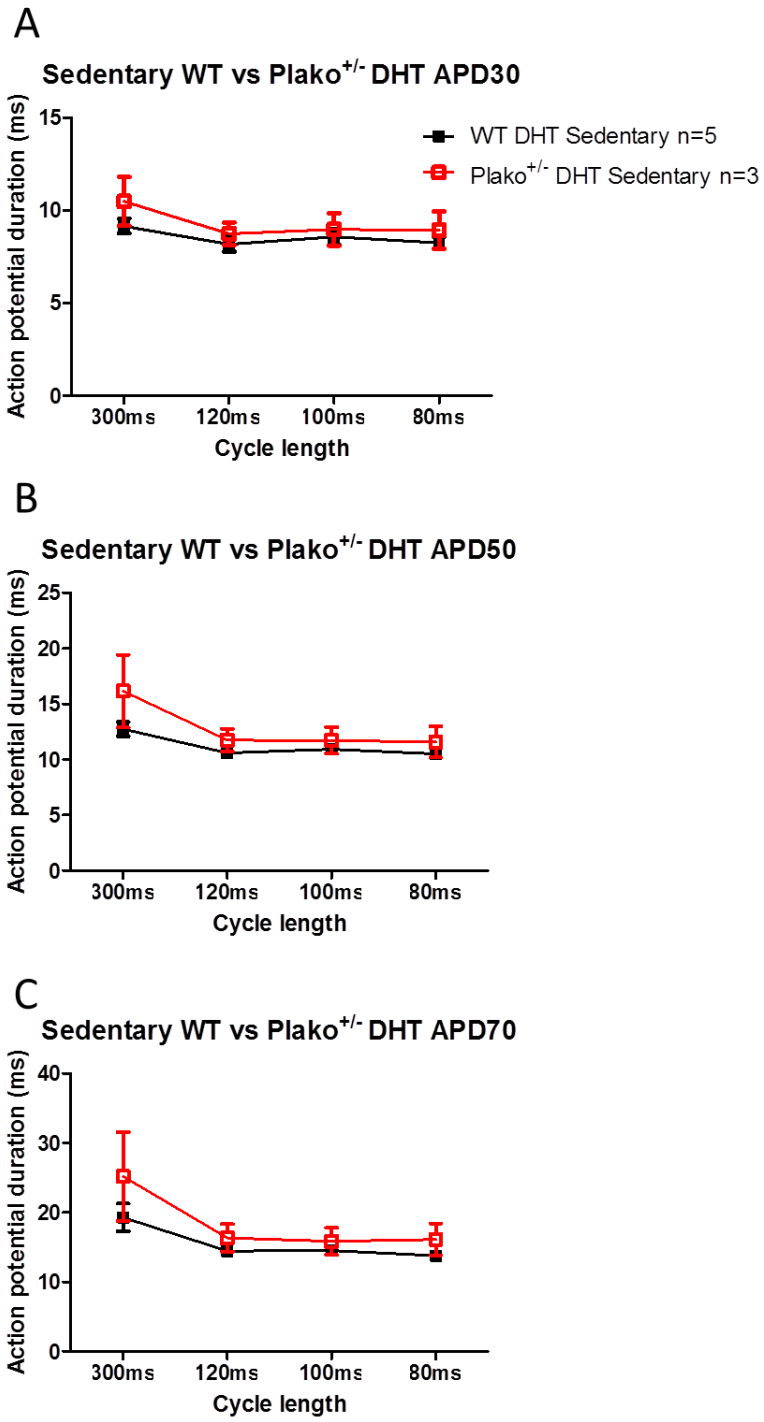

Figure 6.20. Action potential duration in the left atrium of WT and plako$^{+/-}$ littermates in mice with DHT osmotic pumps implanted.

The data presented here compares the APD of the LA from both WT and plako$^{+/-}$ that have been implanted with osmotic mini pumps. The pumps were filled with DHT for the duration of 42 days. A) to C) Compares the APD values at APD30, APD50 and APD70, respectively. The effect of DHT showed no significant changes on APD value. Due to the low sample size with DHT, the results were not conclusive and warrant more experimentation. Points indicate mean values with error bars representing SEM. Statistical analysis was performed using two way repeated measures ANOVA.

6.4. Discussion and conclusion

The aim of this chapter was to apply the high resolution optical mapping system and the analysis algorithms to characterise LA electrophysiology of a genetically altered mouse model. Optical mapping was used to investigate the functional and structural differences between WT and plako$^{+/-}$ LA physiology. The effects of endurance training on the LA and the use of acute flecainide and chronic DHT were also tested.

6.4.1. Effects of plakoglobin deficiency

Optical mapping of the LA of the WT and plako$^{+/-}$ sedentary littermates did not reveal any measurable changes in activation pattern, CV and APD. ARVC mainly affects the RV giving rise to its name, but it has been shown that the left ventricle can also be affected [143]. As such it was suspected that there may be atrial fibro-fatty replacement or atrial dilation due to the heterozygous deficiency of the plakoglobin protein which could cause conduction defects. A study has shown that the electrophysiological abnormalities precede structural changes in ARVC in desmoplakin deficient mouse models [164]. This was also shown to be true in human ARVC [165]. The sodium current is responsible for the upstroke phase of the action potential. The maximum upstroke velocity is used here to calculate the start of the action potential (starting time point for the APD measurements). A small change may be undetectable using the current optical mapping system.

6.4.1.1. Effect of flecainide

Flecainide was used to establish whether CV and APD were altered preferentially in atria isolated from plako$^{+/-}$ mice. Some ARVC phenotypes have been shown to have lower Nav1.5 channel expression [146]. It was expected that flecainide would show an enhanced selectivity in plako$^{+/-}$ atrium compared to WT. Figure 6.6 shows that the APD is prolonged in both genotypes. The use of 1µM flecainide caused some difficulty in obtaining analysable images from the optical mapping system as it also caused the atrial myocardium to occasionally ignore stimulus events. As a result, the number of analysable experiments was reduced and hence more experiments are required in the future. Figure 6.7 shows that the CV is reduced for the LA of both genotypes during flecainide with no selectivity to plakoglobin. It was hypothesised that with the possible dysfunction in the sodium channels in ARVC hearts and possible desmosomal damage, the effect of flecainide could be greater in the plako$^{+/-}$ atrium. The activation maps in Figure 6.8 show a large change in pattern with flecainide compared to control samples. There were many areas of late activation due to the slow CV but no indications that specific patterns arise from genotype related incidences.

The ERP was measured at one CL of 120ms for a sample size of 3 from each genotype (Figure 6.9). It revealed that flecainide did not significantly increase the ERP in WT mice. This result was surprising as flecainide prolongs the time for sodium channels to re-open after the blockade [151] and thus increases the ERP. There was a significant increase in ERP in the plako$^{+/-}$ mice compared to the WT mice with the presence of flecainide. As genetic alterations in the desmosomal macromolecular complex were shown to cause dysfunction in the sodium

channels, it is possible that the addition of flecainide significantly increases the threshold voltage leading to an increase in ERP [163]. The increase in ERP is likely to be protective against any atrial arrhythmias as this limits the opportunity for cardiomyocytes to be re-excited. However, concrete conclusions from the low sample size cannot be drawn. Performing power calculations will be warranted to determine the necessary sample size required for statistical significance for future experiments.

6.4.2. Effects of controlled endurance training

Assessment of the effect of training in WT and plako$^{+/-}$ littermates was made using optical mapping. There were no changes between the activation patterns (Figure 6.10) or any obvious irregularities in the LA. CV measurements showed no change as a result of swim training in the LA of either genotype (Figure 6.11). A previous study [64], [114] showed plako$^{+/-}$ trained mice developed arrhythmias and CV slowing in the RV. It was hypothesised that these effects may have been witnessed in the LA as a recent study showed an increase in protein expression of fibrotic markers in the ventricles and atrium in trained rats [154].

The atrial APD vales were not significantly different as a result of training. Arrhythmias have been shown to be increased in trained humans [156] and mouse models [64]. It appears that the swim training had little effect on atrial electrophysiology as described by optical mapping in this study. One limitation of this study was possibly the only mild to moderate intensity of the swim training. However, the activity scores were reviewed to ensure that the mice were swimming sufficiently and mice that were floating were encouraged to swim. The study performed by Benito *et al* had rats trained using treadmills for up to 5 days a

week for 16 weeks. In the study by Benito *et al*, treadmills provided an electric stimulus on a grid which was placed at the end of the lane to ensure the rats were running at speeds up to 60cm/sec for 60 minutes. This speed and duration is a considerable amount for a rodent. In our study, it could be argued that intensity of training was milder compared to the training performed by Benito *et* al. The swimming sessions also ran for a shorter period of time (6 weeks) which may not have been long enough for any hypertrophic or cardiac dysfunctions to be observed. It is therefore possible that a longer and more intense swim training protocol may reveal underlying differences in electrophysiological properties. Swim training was the preferred method in this study as equipment was easily obtainable but running may be more intense and likely to reveal cardiac dysfunctions. It should be noted that the severity of endurance training is limited by regulations of the biomedical services unit and that the welfare of the mice were not caused excessive stress during the swim training. Histological techniques are the gold standard for measuring fibrosis and hypertrophy but it has been shown that electrophysiological changes can occur before any histological ones [164], [165]. Therefore the use of techniques such as optical mapping may provide earlier insight into disease characteristics before they are measurable in histology.

6.4.2.1. Effects of flecainide

As no changes in baseline electrophysiology were shown in the LA of trained mice compared to sedentary mice, it was hypothesised that flecainide coupled with the swim training could highlight any subtle electrophysiological changes between the two genotypes. Indeed, some ARVC patients have been shown to have a reduced

sodium channel expression [146]. Figure 6.14 shows that with the addition of flecainide, the APD was significantly prolonged ($p<0.01$) in the WT trained atria and displayed a trend in APD prolongation in the plako$^{+/-}$ samples. It was expected that flecainide may show a more pronounced effect in the plako$^{+/-}$ atria especially compounded with any effects of swim training. The addition of flecainide should cause a sodium channel block, prolonging the depolarisation, increasing the refractory period and reducing CV [151]. Whilst these results were unexpected, there were biological variations within the samples and the training as discussed earlier. However, using these results for preliminary data allows for planning of future experiments such as statistical power to determine the number of samples required.

Our experiments also found that using a total of 24 LA samples (14 WT and 10 plako$^{+/-}$), only 13 flecainide experiments were successful (6 WT and 7 plako$^{+/-}$) in the trained mice. In the sedentary cohort, there was a total of 25 samples (13 WT and 12 plako$^{+/-}$), where 9 experiments with flecainide were successful (5 WT and 4 plako$^{+/-}$). Flecainide increases the threshold potential required to invoke a depolarisation [163]. As a result of the increased potential, stimuli were often not evoked by the stimulator in some of the experiments. The effect of flecainide on the sodium channels increases with the heart rate, known as use-dependence [44], [166]. As a result of the use-dependence, action potentials at the shorter CL (100ms and 80ms) were difficult to stimulate. If no action potentials were evoked, the protocol was repeated but failure to do so after several attempts lead to experimental loss. Different concentrations of flecainide may be investigated in future to find the optimal dosage.

ERP measurements (Figure 6.16) were collected and showed an increase in both genotypes after training at 120ms CL. These results were expected as flecainide causes a reduction in sodium channel activity, thus lengthening refractoriness of the atrial tissue. As the CV was not significantly lengthened, it appeared that flecainide may prove to be protective against arrhythmias by increasing the wavelength [167]. As wavelength is the product of CV and ERP, an increase in either of these values increases the wavelength value. Re-entry is favoured by shorter wavelengths as a travelling impulse has a greater window of opportunity to re-excite another cell which can cause an arrhythmia [32]. The ERP results showed no significant change in the WT LA after flecainide, however, there was an increase in ERP with the plako$^{+/-}$ with flecainide. A greater change in the plako$^{+/-}$ atrium was expected as it was thought to have fewer sodium channels [146] which may cause flecainide to saturate the number of available channels. Atrial ERP in plako$^{+/-}$ samples for the sedentary LA were shown to be lower compared to the trained samples. A longer ERP is believed to be protective against arrhythmias as it limits the time a cardiomyocyte can re-excite. The longer ERP in the trained plako$^{+/-}$ compared to WT suggests that the swim training had a protective effect, however, there exists variability within the plako$^{+/-}$ LA samples post training and the sample size of the plako$^{+/-}$ LA sedentary was only 3.

6.4.3. The effect of DHT and plakoglobin deficiency

APD and CV values were measured from sedentary mice with DHT osmotic pumps implanted from both WT and plako$^{+/-}$. These mice were compared against sedentary mice without DHT. CV values showed no change in the presence of DHT. This is surprising as previous studies have shown that DHT administration

induces hypertrophy [160], [168], [169]. As a result, the propagation of an action potential can be reduced.

When comparing the APD values, the plako$^{+/-}$ LA shows a slight but significant prolongation in with DHT treated atria. Bearing in mind the experimental number was low (n=3), this cannot be considered confirming evidence. A prolongation was also seen in the WT at APD30, but neither at APD50 nor APD70 which may be due to statistical chance. The dosage of 62.5mg/ml of DHT and ethanol was used as it was deemed sufficient to yield a supraphysiological dose used in literature [170]. It should be noted that mice will have a baseline value of testosterone and any addition of DHT may act as a surplus. Nevertheless, no alterations in cardiac electrophysiological parameters were observed in our studies. However, bearing in mind the low experimental numbers (n=3), further experiments are required in order to reach statistically meaningful conclusions. The low sample size was due to time and resource limitations.

The future work for investigating DHT in plako$^{+/-}$ LA will include: repeating the experiments with larger sample groups, administering placebo pumps with no DHT and finally, a cohort of littermates which have been endurance trained. The endurance training and DHT may prove relevant to athletes doping.

6.4.4. Overall conclusions on plako$^{+/-}$ mouse studies

- APD and CV measurements in the LA showed no significant change between WT and plako$^{+/-}$ mice without training.
    - It was hypothesised a reduced CV in the plako$^{+/-}$ but electrophysiological changes may have been too small to detect.

- Untrained mice showed an increase in APD and a reduced CV in the LA after treatment with flecainide for both genotypes.
    - Flecainide had not shown a preferential treatment in either genotype, however, the plako$^{+/-}$ LA data shows greater variability within the APD values. If differences between the genotypes are small, the biological variation between samples may greater and hence not detectable.
- Flecainide prolongs the ERP in plako$^{+/-}$ sedentary LA samples.
    - The prolongation of the ERP indicates a protective effect against arrhythmia inducibility after flecainide.
- APD and CV measurements show no significant change in the LA of swim trained mice.
    - It was hypothesised that the effect of training would exacerbate the ARVC like phenotype but previous studies have shown strong effects of endurance training in the form of running. It is likely that the swim training involved required increased intensity to witness these effects.
- Flecainide prolongs APD in WT LA samples after training
    - The prolongation was expected to be seen in the plako$^{+/-}$ LA also, but biological variations exist between each mouse and the efficacy of training severity may have contributed to this finding.
- Flecainide prolongs the ERP in WT and plako$^{+/-}$ LA samples after training.
    - A short ERP is seen to be favourable to arrhythmic activity hence flecainide may protect against this.
- ERP in plako$^{+/-}$ trained (n=5) LA is greater than untrained (n=3).

    - This was unexpected as training was assumed to enhance arrhythmia inducibility. However, variations in training and low sample sizes warrant further study. These results may be used to determine the sample sizes necessary for power calculation statistics.
- Untrained mice treated with DHT show a slight increase in APD for plako$^{+/-}$ LA but no changes in CV were observed in either genotype.
    - Low sample sizes (n=5 and 3 for WT and plako$^{+/-}$, respectively) limit conclusive results. Further studies should include placebo vehicle pumps but also cohorts after training to mimic athletic steroid doping.

Overall, the effect of training did not yield significant changes as expected which has led to question the efficacy of the training regime compared to other studies. The effect of flecainide on the plakoglobin deficient model yielded some unexpected results. This raises further questions regarding sodium channels in the plakoglobin deficiency model but investigations into this is beyond the scope of this study.

7. Discussion

7.1. General Outcomes

The main aim of this thesis was to develop an optical mapping system which could be used to investigate the electrophysiological properties of mouse models. These investigations were performed using an off the shelf camera with a high spatial resolution to study isolated left atrial (LA) samples from genetically altered murine models of heart disease. The outcomes of this thesis were:

- The high spatial property of the camera has led to further studies on the electrophysiological heterogeneity of the LA (see Appendix 1) along with regional differences in ion channel expression which has led to a publication – see Appendix 2.
- Development and automated analysis of optical mapping data. The algorithms implemented allowed for analysis without user bias. Action potential duration (APD) values were automatically determined from fluorescence data from pre-selected regions. Conduction velocity (CV) values were calculated automatically from isochronal maps derived from time series images. This has led to publications in Appendix 3 and Appendix 4.
- $Pitx2c^{+/-}$ mice showed a shorter APD value than their wild-type (WT) littermates. This data confirms previous findings of a shorter APD in the $Pitx2c^{+/-}$ LA with respect to WT [55].

- The use of flecainide indicated a more pronounced effect to Pitx2c$^{+/-}$ mice LA, showing a possible reason for its efficacy for certain patients. This work contributed to a publication which is currently under review – Appendix 5.
- Optical mapping was applied to a Plakoglobin$^{+/-}$ deficient model to characterise CV and APD after chronic and with acute interventions.
    - No significant changes were witnessed in LA of untrained cohorts at baseline and with flecainide treatment.
    - The effect of swim training showed limited changes between genotypes in APD and CV but a prolongation in atrial ERP after flecainide treatment.
    - Plako$^{+/-}$ untrained mice treated with DHT showed a prolongation in atrial APD. These findings were preliminary as larger sample sizes were required and cohorts of trained and placebo pumps need to be studied.

7.2. Optical mapping applications on cardiac electrophysiology

The system makes use of new imaging technology, namely a high-resolution 2nd generation CMOS camera, to achieve high temporal and spatial resolution of electrical activation and repolarisation in the murine atrium. It was demonstrated that recording was feasible using the system and shown that the measurements yield comparable action potential waveforms and action potential durations when compared to monophasic and transmembrane atrial action potentials. Furthermore, it was shown that the system was capable of detecting changes in conduction velocity and functional conduction block. In our hands, the oversampling of recordings allowed us to maximise the information collected in each experiment, as a higher spatial resolution is conducive to the detection of small activation changes. Larger sampling areas needed for the assessment of atrial repolarisation, as a higher signal to noise ratio may be needed to accurately determine the APD. In addition to this, the algorithms used were useful in reducing the time needed for a user to analyse APD measurements and produce activation maps. For example, to correct for baseline shifts, it is common to fit a linear or polynomial equation to the signal [124]. In the experiments, these baseline shifts were extremely variable. Therefore, a different approach to existing correction methods was used. Here a common top hat filter which was normally applied to 2D images but was used on a 1D signal on our action potentials. Another example was the detection of t=0 on the isochronal maps. It proved to be a useful tool for speeding up analysis and for limiting user bias.

Assessment of murine atrial electrophysiology is an essential tool to understand the functional consequences of defined genetic modifications, including complex gene expression changes e.g. secondary to altered function of transcription factors [55], [74], [135] or the effects of inhibitory or regulatory RNA molecules. Environmental factors such as the effect of training, interventions and chronic or acute drug treatment [114], [171] can be assessed with the increased number of pixels in this system in the future, including larger and irregular specimens. The increased spatial resolution in this system also allowed for the identification of heterogeneities within the tissue. Imaging of murine embryos should also be possible with this system [172].

By building an optical mapping system around a novel 2nd generation oversampling high-resolution CMOS camera with high light sensitivity, the system was able to record electrical activation and repolarisation with high accuracy and reliability, yielding information that reflects murine atrial biology. The ORCA camera has recently been used and shown to capture action potentials in spontaneously spiking human embryonic kidney (HEK) cells [173]. Signals from HEK cells occur at approximately 3 APs per second. The pacing rate applied in our experiments in live intact organ tissue was much higher and represented a higher challenge to the camera resolution. The validation data suggested that the system reliably recorded atrial repolarisation, making it attractive for the study of arrhythmia mechanisms in genetically altered murine models that mimic inherited arrhythmogenic diseases and/or replicate common gene expression changes associated with common cardiac diseases.

7.3. Technical aspects of optical mapping

Optical mapping of mouse hearts has been used to characterise arrhythmia mechanisms since the beginning of this century. Initially, systems were developed to measure ventricular activation and repolarisation [174], [175], and more recently expanded to atrial preparations [55], [176], [177]. One of the most commonly used systems is the custom-made SCIMEDIA system that provides a 100x100 pixel field at high temporal resolution (Bezzina et al., 2013; Kirchhof et al., 2011). Especially at high sampling rates, the relatively low signal strength generated by the thin murine atrial tissue proved to be challenging. The system developed and validated here used an emerging technology, namely the 2nd generation CMOS detector. The camera was capable of detecting low amplitude light signals at superior spatial resolution (128x2048 pixels) and good temporal resolution (1-2 kHz). A higher temporal resolution was needed when capturing quick cellular changes, such as AP depolarisation. A higher spatial resolution was desirable when trying to precisely locate phenomena changing at a lower rate. With this resolution span, each individual pixel provided a signal with a relatively low SNR, due to the limited number of light emitting events of the recorded tissue. The spatial oversampling of the signals during data acquisition allowed for the post-processing of signals to optimise the information per pixel. Specifically, a high spatial resolution was used to assess atrial activation with optimal accuracy and an acceptable SNR. The employed algorithm for correcting the baseline fluctuation was robust to all types of – sometimes random – changes in baseline fluorescence, thus increased the reliability of the measurements and the yield of analysable experiments. Reliable assessment of repolarisation, in contrast, was possible using combination of individual signals in the analysis phase, thereby

sacrificing some of the spatial resolution, and by signal averaging during steady state pacing. Thus, the proposed new, versatile system allowed for the adjustment of image parameters after the end of the experiment to suit specific analysis needs, therefore increasing the information yield from each experiment.

This system was capable of recording valid action potential waveforms over a wide range of paced cycle lengths (CLs), and with simultaneous recording of APDs from all regions of the LA. Using the post-processing methods described above, this system will provide detailed insights into the regional differences in atrial action potential duration, and their change in genetically modified models.

The preparation used here was stable over experimental protocols of 1 to 1.5 hours duration, demonstrating that superfusion of the murine atrium is adequate to maintain the integrity of the superfused atrium during acute interventions such as antiarrhythmic drugs at bradycardic and physiological CLs. Automated analysis of APD and activation patterns was another important feature of the present system. The stage where user input was required for cropping of the images could have been automated as the LA was the only object within the field of view, but was left as manual cropping as it allowed for flexibility in future applications. The camera acquisition rate was not dependent on the larger horizontal pixel size, so multiple samples or filters can be simultaneously imaged, hence cropping different regions may prove advantageous for these types of experiments.

7.4. Limitations and future developments

7.4.1. Experimental limitations

The optical mapping system makes use of voltage sensitive dyes. These dyes have many advantages over other electrophysiology techniques and are an important tool, but little is known about their effects on cardiac tissue. In order for dyes to function, there is always an interaction on the cellular level. Di-4-ANEPPS is one of the most used dyes, but there have been studies to show electrophysiological changes associated with the dye such as decreased APD value and slowed conduction velocity [102], [179]. Di-4-ANEPPS show some level of internalisation [100] which at increased illuminations showed an increase in temperature and phototoxicity [89], [179]. The effect of heat has been shown to significantly affect the characteristics of atrial myocytes [180]. These should be considered when attempting optical mapping experiments. The use of electro-mechanical uncouplers such as blebbistatin may have an effect on the outcome of results. A recent study showed that blebbistatin has the ability to precipitate and accumulate in the vasculature [181], although this may have proved to be less significant in a superfusion system and proves to be an important tool in optical imaging [117].

7.4.2. Future Work

Due to the multidisciplinary aspects of this project, it can be lead into multiple avenues which include:

- Combined calcium imaging – The optical mapping system has already been modified for it to be used for calcium imaging using Rhod-2 acetoxymethyl ester derivative including software changes. As the Hamamatsu Flash4.0 camera has the ability of imaging with a 2048 pixel width, the system can be modified to image both voltage and calcium simultaneously including the software generation for analysing both types of images (see appendix for submission by Holmes *et al*).
- Improved experimental numbers for DHT investigation – the sample size for the plako$^{+/-}$ models was low which limited statistical reliability. Repeating these experiments with a larger cohort and placebo control groups will be necessary for both sedentary and swim trained.
- Increased number flecainide samples – for both Pitx2c$^{+/-}$ and plako$^{+/-}$ cohorts the sample size with flecainide decreased. Techniques to avoid experimental loss need to be investigated such as varying dosage of flecainide. Another aspect may be to develop a method of stimulation to increase voltage at short CLs as the rates at 100ms and 80ms often missed stimulations.

References

[1] R. J. Levick, *An Introduction to Cardiovascular Physiology*, 1st ed. Butterworth and Co. Ltd., 1991.

[2] E. Marbán, “Cardiac channelopathies,” *Nature*, vol. 415, no. 6868, pp. 213–218, Jan. 2002.

[3] P. A. Iaizzo, “Part I. Introduction. General Features of the Cardiovascular System,” in *Handbook of Cardiac Anatomy, Physiology, and Devices*, 1st ed., P. A. Iaizzo, Ed. Humana Press Inc., 2005, pp. 3 – 14.

[4] D. E. Newby, N. R. Grubb, and A. Bradbury, “Cardiovascular disease,” in *Davidson’s principles and practice of medicine*, 22nd ed., N. R. Colledge, B. R. Walker, S. Ralston, and I. D. Penman, Eds. Elsevier, 2014, pp. 525–642.

[5] P. A. Iaizzo, “Part II. Anatomy. Anatomy of the Human Heart,” in *Handbook of Cardiac Anatomy, Physiology, and Devices*, 3rd ed., P. A. Iaizzo, Ed. Cham: Springer International Publishing, 2015, pp. 61 – 88.

[6] T. G. Laske, M. Shrivastav, and P. A. Iaizzo, “Part III. Physiology and Assessment. The Cardiac Conduction System,” in *Handbook of Cardiac Anatomy, Physiology, and Devices*, P. A. Iaizzo, Ed. Springer International Publishing, 2015, pp. 215 – 234.

[7] J. Renwick, C. Kerr, R. McTaggart, and J. Yeung, “Cardiac electrophysiology and conduction pathway ablation,” *Can. J. Anaesth.*, vol. 40, no. 11, pp. 1053–1064, 1993.

[8] B. Hille, “Ionic channels in excitable membranes. Current problems and biophysical approaches,” *Biophys. J.*, vol. 22, no. 2, pp. 283–294, May 1978.

[9] A. O. Grant, “Cardiac Ion Channels,” *Circ. Arrhythmia Electrophysiol.*, vol. 2, no. 2, pp. 185–194, Apr. 2009.

[10] J. M. Nerbonne and R. S. Kass, “Molecular physiology of cardiac repolarization,” *Physiol Rev*, vol. 85, no. 4, p. 1205, 2005.

[11] J. W. Cain and D. G. Schaeffer, “Shortening of cardiac action potential duration near an insulating boundary.,” *Math. Med. Biol.*, vol. 25, no. 1, pp. 21–36, Mar. 2008.

[12] P. Attuel, R. Childers, B. Cauchemez, J. Poveda, J. Mugica, and P. Coumel, “Failure in the rate adaptation of the atrial refractory period: its relationship to vulnerability,” *Int. J. Cardiol.*, vol. 2, no. 2, pp. 179–197, Jan. 1982.

[13] A. R. Pérez Riera, C. Ferreira, C. Ferreira Filho, M. Ferreira, A. Meneghini, A. H. Uchida, E. Schapachnik, S. Dubner, and L. Zhang, “The enigmatic sixth wave of the electrocardiogram: The U wave,” *Cardiol. J.*, vol. 15, no. 5, pp. 408–421, 2008.

[14] P. J. Schwartz, L. Crotti, and R. Insolia, “Long-QT syndrome from genetics to management,” *Circ. Arrhythmia Electrophysiol.*, vol. 5, no. 4, pp. 868–877, 2012.

[15] A. C. Guyton, “Electrocardiographic Interpretation in Cardiac Myopathies -

Vectorial Analysis," in *Textbook of Medical Physiology*, 6th ed., 1981, pp. 182 – 197.

[16] V. N. Batchvarov, M. Malik, and A. J. Camm, "Incorrect electrode cable connection during electrocardiographic recording," *Europace*, vol. 9, no. 11, pp. 1081–1090, 2007.

[17] J. Malmivuo and R. Plonsey, *Bioelectromagnetism - Principles and Applications of Bioelectric and Biomagnetic Fields*. Oxford University Press, 1995.

[18] G. 2013 M. and C. of D. Collaborators, "Global, regional, and national age–sex specific all-cause and cause-specific mortality for 240 causes of death, 1990–2013: a systematic analysis for the Global Burden of Disease Study 2013," *Lancet*, vol. 385, no. 9963, pp. 117–171, Dec. 2014.

[19] P. Bhatnagar, K. Wickramasinghe, J. Williams, M. Rayner, and N. Townsend, "The epidemiology of cardiovascular disease in the UK 2014.," *Heart*, pp. heartjnl–2015–307516–, 2015.

[20] N. Townsend, P. Bhatnagar, E. Wilkins, K. Wickramasinghe, and M. Rayner, *Cardiovascular Disease Statistics 2015*. British Heart Foundation, 2015.

[21] P. Poirier, T. D. Giles, G. A. Bray, Y. Hong, J. S. Stern, F. X. Pi-Sunyer, and R. H. Eckel, "Obesity and cardiovascular disease: pathophysiology, evaluation, and effect of weight loss: an update of the 1997 American Heart Association Scientific Statement on Obesity and Heart Disease from the Obesity Committee of the Council on Nutrition, Physical," *Circulation*, vol. 113, no. 6, pp. 898–918, Feb. 2006.

[22] I. S. Ockene and N. H. Miller, "Cigarette Smoking, Cardiovascular Disease, and Stroke : A Statement for Healthcare Professionals From the American Heart Association," *Circulation*, vol. 96, no. 9, pp. 3243–3247, Nov. 1997.

[23] S. Kathiresan and D. Srivastava, "Genetics of human cardiovascular disease.," *Cell*, vol. 148, no. 6, pp. 1242–57, Mar. 2012.

[24] G. A. Donnan, M. Fisher, M. Macleod, and S. M. Davis, "Stroke.," *Lancet*, vol. 371, no. 9624, pp. 1612–23, May 2008.

[25] H. Roukoz, F. Lu, and S. Sakaguchi, "Catheter Ablation of Cardiac Arrhythmias," in *Handbook of Cardiac Anatomy, Physiology, and Devices*, 3rd ed., Springer, 2015, pp. 493 – 520.

[26] E. Braunwald, *Braunwald's Heart Disease. A Textbook of Cardiovascular Medicine.*, 9th. ed. Elsevier, 2011.

[27] J. Pellman and F. Sheikh, "Atrial Fibrillation: Mechanisms, Therapeutics, and Future Directions," *Compr. Physiol.*, vol. 5, no. April, pp. 649–665, 2015.

[28] C. Antzelevitch and A. Burashnikov, "Overview of Basic Mechanisms of Cardiac Arrhythmia.," *Card. Electrophysiol. Clin.*, vol. 3, no. 1, pp. 23–45, Mar. 2011.

[29] U. Schotten, S. Verheule, P. Kirchhof, and A. Goette, "Pathophysiological mechanisms of atrial fibrillation: a translational appraisal," *Physiol Rev*, vol. 91, no. 1, pp. 265–325, 2011.

[30] J. Miller and D. P. Zipes, "Therapy for Cardiac Arrhythmias," in *Braunwald's Heart Diesease. A Textbook of Cardiovascular medicine.*, 9th ed., E.

Braunwald, Ed. Elsevier, 2011.

[31] G. Breithardt, M. Borggrefe, A. J. Camm, and M. Shenasa, *Antiarrhythmic Drugs. Mechanisms of Antiarrhythmic and Proarrhythmic Actions*. Springer, 1995.

[32] P. F. Kirchhof, C. L. Fabritz, and M. R. Franz, “Postrepolarization refractoriness versus conduction slowing caused by class I antiarrhythmic drugs: antiarrhythmic and proarrhythmic effects.,” *Circulation*, vol. 97, no. 25, pp. 2567–2574, 1998.

[33] D. Dang, R. Arimie, and L. J. Haywood, “A review of atrial fibrillation.,” *J. Natl. Med. Assoc.*, vol. 94, no. 12, pp. 1036–48, Dec. 2002.

[34] J. M. Hudak, E. H. Banitt, and J. R. Schmid, “Discovery and development of flecainide.,” *Am. J. Cardiol.*, vol. 53, no. 5, p. 17B–20B, Feb. 1984.

[35] E. Aliot, A. Capucci, H. J. Crijns, A. Goette, and J. Tamargo, “Twenty-five years in the making: flecainide is safe and effective for the management of atrial fibrillation.,” *Europace*, vol. 13, no. 2, pp. 161–73, Feb. 2011.

[36] S. Apostolakis, M. Oeff, U. Tebbe, L. Fabritz, G. Breithardt, and P. Kirchhof, “Flecainide acetate for the treatment of atrial and ventricular arrhythmias.,” *Expert Opin. Pharmacother.*, vol. 14, no. 3, pp. 347–57, 2013.

[37] Z. Wang, B. Fermini, and S. Nattel, “Mechanism of flecainide’s rate-dependent actions on action potential duration in canine atrial tissue.,” *J. Pharmacol. Exp. Ther.*, vol. 267, no. 2, pp. 575–581, 1993.

[38] J. A. Wang, C. P. Lau, Y. T. Tai, and B. Z. Wu, “Effects of flecainide on exercise hemodynamics and electrocardiography in patients without structural heart disease.,” *Clin. Cardiol.*, vol. 18, no. 3, pp. 140–4, 1995.

[39] J. E. Krebs, E. S. Goldstein, and S. T. Kilpatrick, *Genes X*, 10th ed. Jones and Bartlett Publishers, 2011.

[40] Y. K. Iwasaki, K. Nishida, T. Kato, and S. Nattel, “Atrial fibrillation pathophysiology: Implications for management,” *Circulation*, vol. 124, pp. 2264–2274, 2011.

[41] S. Nattel, “New ideas about atrial fibrillation 50 years on.,” *Nature*, vol. 415, no. 6868, pp. 219–226, 2002.

[42] S. Nattel, B. Burstein, and D. Dobrev, “Atrial remodeling and atrial fibrillation: mechanisms and implications.,” *Circ. Arrhythm. Electrophysiol.*, vol. 1, no. 1, pp. 62–73, 2008.

[43] E. K. Heist, M. Mansour, and J. N. Ruskin, “Rate control in atrial fibrillation: Targets, methods, resynchronization considerations,” *Circulation*, vol. 124, no. 24, pp. 2746–2755, 2011.

[44] Z. Wang, P. Pagé, and S. Nattel, “Mechanism of flecainide’s antiarrhythmic action in experimental atrial fibrillation.,” *Circ. Res.*, vol. 71, no. 2, pp. 271–87, Aug. 1992.

[45] A. J. Camm, G. Y. H. Lip, R. De Caterina, I. Savelieva, D. Atar, S. H. Hohnloser, G. Hindricks, and P. Kirchhof, “2012 focused update of the ESC Guidelines for the management of atrial fibrillation: an update of the 2010 ESC Guidelines for the management of atrial fibrillation. Developed with the special contribution of the European Heart Rhythm Association.,” *Eur. Heart*

J., vol. 33, no. 21, pp. 2719–47, Nov. 2012.

[46] R. Wakili, N. Voigt, S. Kääb, D. Dobrev, and S. Nattel, “Recent advances in the molecular pathophysiology of atrial fibrillation.,” *J. Clin. Invest.*, vol. 121, no. 8, pp. 2955–68, Aug. 2011.

[47] P. Kirchhof, G. Breithardt, E. Aliot, S. Al Khatib, S. Apostolakis, A. Auricchio, et al. “Personalized management of atrial fibrillation: Proceedings from the fourth Atrial Fibrillation competence NETwork/European Heart Rhythm Association consensus conference.,” *Europace*, vol. 15, no. 11, pp. 1540–56, Nov. 2013.

[48] P. T. Ellinor, K. L. Lunetta, C. M. Albert, N. L. Glazer, M. D. Ritchie, A. V Smith, et al. “Meta-analysis identifies six new susceptibility loci for atrial fibrillation.,” *Nat. Genet.*, vol. 44, no. 6, pp. 670–5, Jun. 2012.

[49] D. F. Gudbjartsson, D. O. Arnar, A. Helgadottir, S. Gretarsdottir, H. Holm, A. Sigurdsson, A. Jonasdottir, A. Baker, G. Thorleifsson, K. Kristjansson, A. Palsson, T. Blondal, P. Sulem, V. M. Backman, G. a Hardarson, E. Palsdottir, A. Helgason, R. Sigurjonsdottir, J. T. Sverrisson, K. Kostulas, M. C. Y. Ng, L. Baum, W. Y. So, K. S. Wong, J. C. N. Chan, K. L. Furie, S. M. Greenberg, M. Sale, P. Kelly, C. a MacRae, E. E. Smith, J. Rosand, J. Hillert, R. C. W. Ma, P. T. Ellinor, G. Thorgeirsson, J. R. Gulcher, A. Kong, U. Thorsteinsdottir, and K. Stefansson, “Variants conferring risk of atrial fibrillation on chromosome 4q25.,” *Nature*, vol. 448, no. 7151, pp. 353–7, Jul. 2007.

[50] J. Wang, Y. Bai, N. Li, W. Ye, M. Zhang, S. B. Greene, Y. Tao, Y. Chen, X. H. T. Wehrens, and J. F. Martin, “Pitx2-microRNA pathway that delimits sinoatrial node development and inhibits predisposition to atrial fibrillation.,” *Proc. Natl. Acad. Sci. U. S. A.*, vol. 111, no. 25, pp. 9181–6, Jun. 2014.

[51] K. Kitamura, H. Miura, S. Miyagawa-Tomita, M. Yanazawa, Y. Katoh-Fukui, R. Suzuki, H. Ohuchi, a Suehiro, Y. Motegi, Y. Nakahara, S. Kondo, and M. Yokoyama, “Mouse Pitx2 deficiency leads to anomalies of the ventral body wall, heart, extra- and periocular mesoderm and right pulmonary isomerism.,” *Development*, vol. 126, no. 24, pp. 5749–5758, 1999.

[52] P. Kirchhof, E. Marijon, L. Fabritz, N. Li, W. Wang, T. Wang, K. Schulte, J. Hanstein, J. S. Schulte, M. Vogel, N. Mougenot, S. Laakmann, L. Fortmueller, J. Eckstein, S. Verheule, S. Kaese, A. Staab, S. Grote-Wessels, U. Schotten, G. Moubarak, X. H. Wehrens, W. Schmitz, S. Hatem, and F. U. Muller, “Overexpression of cAMP-response element modulator causes abnormal growth and development of the atrial myocardium resulting in a substrate for sustained atrial fibrillation in mice,” *Int J Cardiol*, 2011.

[53] A. Chinchilla, H. Daimi, E. Lozano-Velasco, J. N. Dominguez, R. Caballero, E. Delpón, J. Tamargo, J. Cinca, L. Hove-Madsen, A. E. Aranega, and D. Franco, “PITX2 insufficiency leads to atrial electrical and structural remodeling linked to arrhythmogenesis.,” *Circ. Cardiovasc. Genet.*, vol. 4, no. 3, pp. 269–79, Jun. 2011.

[54] P. C. Kahr, I. Piccini, L. Fabritz, B. Greber, H. Schöler, H. H. Scheld, A. Hoffmeier, N. a Brown, and P. Kirchhof, “Systematic analysis of gene expression differences between left and right atria in different mouse strains and in human atrial tissue.,” *PLoS One*, vol. 6, no. 10, p. e26389, Jan. 2011.

[55] P. Kirchhof, P. Kahr, and S. Kaese, “PITX2c is expressed in the adult left atrium, and reducing Pitx2c expression promotes atrial fibrillation inducibility and complex changes in gene expression,” *Circ. Cardiovasc. Genet.*, 2011.

[56] D. Corrado, C. Basso, A. Pavei, P. Michieli, M. Schiavon, and G. Thiene, “Trends in Sudden Cardiovascular Death in Young Competitive Athletes After Implementation of a Preparticipation Screening Program,” *JAMA*, vol. 296, no. 13, p. 1593, Oct. 2006.

[57] D. Corrado, “Arrhythmogenic Right Ventricular Cardiomyopathy/Dysplasia: Clinical Impact of Molecular Genetic Studies,” *Circulation*, vol. 113, no. 13, pp. 1634–1637, Apr. 2006.

[58] C. Gemayel, A. Pelliccia, and P. D. Thompson, “Arrhythmogenic right ventricular cardiomyopathy,” *J. Am. Coll. Cardiol.*, vol. 38, no. 7, pp. 1773–1781, Dec. 2001.

[59] C. Basso, D. Corrado, F. I. Marcus, A. Nava, and G. Thiene, “Arrhythmogenic right ventricular cardiomyopathy.,” *Lancet (London, England)*, vol. 373, no. 9671, pp. 1289–300, Apr. 2009.

[60] L. Daliento, G. Rizzoli, G. Thiene, A. Nava, M. Rinuncini, R. Chioin, and S. Dalla Volta, “Diagnostic accuracy of right ventriculography in arrhythmogenic right ventricular cardiomyopathy.,” *Am. J. Cardiol.*, vol. 66, no. 7, pp. 741–5, Sep. 1990.

[61] B. Bauce, G. Frigo, G. Benini, P. Michieli, C. Basso, A. F. Folino, I. Rigato, E. Mazzotti, L. Daliento, G. Thiene, and A. Nava, “Differences and similarities between arrhythmogenic right ventricular cardiomyopathy and athlete’s heart adaptations.,” *Br. J. Sports Med.*, vol. 44, no. 2, pp. 148–54, Mar. 2010.

[62] G. Fontaine, J. Umemura, P. Di Donna, R. Tsezana, J. J. Cannat, and R. Frank, “[Duration of QRS complexes in arrhythmogenic right ventricular dysplasia. A new non-invasive diagnostic marker].,” *Ann. Cardiol. Angeiol. (Paris).*, vol. 42, no. 8, pp. 399–405, Oct. 1993.

[63] C. D. Ainsworth, A. C. Skanes, G. J. Klein, L. J. Gula, R. Yee, and A. D. Krahn, “Differentiating arrhythmogenic right ventricular cardiomyopathy from right ventricular outflow tract ventricular tachycardia using multilead QRS duration and axis.,” *Heart Rhythm*, vol. 3, no. 4, pp. 416–23, Apr. 2006.

[64] P. Kirchhof, L. Fabritz, M. Zwiener, H. Witt, M. Schäfers, S. Zellerhoff, M. Paul, T. Athai, K. H. Hiller, H. a. Baba, G. Breithardt, P. Ruiz, T. Wichter, and B. Levkau, “Age- and training-dependent development of arrhythmogenic right ventricular cardiomyopathy in heterozygous plakoglobin-deficient mice,” *Circulation*, vol. 114, no. 17, pp. 1799–1806, 2006.

[65] B. Brembilla-Perrot, L. Jacquemin, P. Houplon, P. Houriez, D. Beurrier, V. Berder, A. Terrier de la Chaise, and P. Louis, “Increased atrial vulnerability in arrhythmogenic right ventricular disease,” *Am. Heart J.*, vol. 135, no. 5, pp. 748–754, May 1998.

[66] D. Garrod and M. Chidgey, “Desmosome structure, composition and function.,” *Biochim. Biophys. Acta*, vol. 1778, no. 3, pp. 572–87, Mar. 2008.

[67] W. W. Franke, C. M. Borrmann, C. Grund, and S. Pieperhoff, “The area

composita of adhering junctions connecting heart muscle cells of vertebrates. I. Molecular definition in intercalated disks of cardiomyocytes by immunoelectron microscopy of desmosomal proteins," *Eur. J. Cell Biol.*, vol. 85, no. 2, pp. 69–82, 2006.

[68] C. M. Borrmann, C. Grund, C. Kuhn, I. Hofmann, S. Pieperhoff, and W. W. Franke, "The area composita of adhering junctions connecting heart muscle cells of vertebrates. II. Colocalizations of desmosomal and fascia adhaerens molecules in the intercalated disk.," *Eur. J. Cell Biol.*, vol. 85, no. 6, pp. 469–85, Jun. 2006.

[69] G. McKoy, N. Protonotarios, A. Crosby, A. Tsatsopoulou, A. Anastasakis, A. Coonar, M. Norman, C. Baboonian, S. Jeffery, and W. J. McKenna, "Identification of a deletion in plakoglobin in arrhythmogenic right ventricular cardiomyopathy with palmoplantar keratoderma and woolly hair (Naxos disease).," *Lancet (London, England)*, vol. 355, no. 9221, pp. 2119–24, Jun. 2000.

[70] H. Aberle, C. Bierkamp, D. Torchard, O. Serova, T. Wagner, E. Natt, J. Wirsching, C. Heidkämper, M. Montagna, and H. T. Lynch, "The human plakoglobin gene localizes on chromosome 17q21 and is subjected to loss of heterozygosity in breast and ovarian cancers.," *Proc. Natl. Acad. Sci. U. S. A.*, vol. 92, no. 14, pp. 6384–8, Jul. 1995.

[71] a S. Coonar, N. Protonotarios, a Tsatsopoulou, E. W. Needham, R. S. Houlston, S. Cliff, M. I. Otter, V. a Murday, R. K. Mattu, and W. J. McKenna, "Gene for arrhythmogenic right ventricular cardiomyopathy with diffuse nonepidermolytic palmoplantar keratoderma and woolly hair (Naxos disease) maps to 17q21.," *Circulation*, vol. 97, no. 20, pp. 2049–2058, 1998.

[72] P. Ruiz, V. Brinkmann, B. Ledermann, M. Behrend, C. Grund, C. Thalhammer, F. Vogel, C. Birchmeier, U. Günthert, W. W. Franke, and W. Birchmeier, "Targeted mutation of plakoglobin in mice reveals essential functions of desmosomes in the embryonic heart.," *J. Cell Biol.*, vol. 135, no. 1, pp. 215–25, Oct. 1996.

[73] J. M. Nerbonne, "Studying cardiac arrhythmias in the mouse--a reasonable model for probing mechanisms?," *Trends Cardiovasc. Med.*, vol. 14, no. 3, pp. 83–93, Apr. 2004.

[74] G. Riley, F. Syeda, P. Kirchhof, and L. Fabritz, "An introduction to murine models of atrial fibrillation," *Front. Physiol.*, vol. 3, p. 296, 2012.

[75] B. C. Knollmann, A. N. Katchman, and M. R. Franz, "Monophasic action potential recordings from intact mouse heart: validation, regional heterogeneity, and relation to refractoriness.," *J. Cardiovasc. Electrophysiol.*, vol. 12, no. 11, pp. 1286–94, Nov. 2001.

[76] B. C. Knollmann, T. Schober, A. O. Petersen, S. G. Sirenko, and M. R. Franz, "Action potential characterization in intact mouse heart: steady-state cycle length dependence and electrical restitution.," *Am. J. Physiol. Heart Circ. Physiol.*, vol. 292, no. 1, pp. H614–H621, 2007.

[77] M. C. Sanguinetti and N. K. Jurkiewicz, "Two components of cardiac delayed rectifier K+ current. Differential sensitivity to block by class III antiarrhythmic agents.," *J. Gen. Physiol.*, vol. 96, no. 1, pp. 195–215, 1990.

[78] J. Guo, T. Wang, T. Yang, J. Xu, W. Li, M. D. Fridman, J. T. Fisher, and S. Zhang, “Interaction between the cardiac rapidly (IKr) and slowly (IKs) activating delayed rectifier potassium channels revealed by low K+-induced hERG endocytic degradation.,” *J. Biol. Chem.*, vol. 286, no. 40, pp. 34664–74, Oct. 2011.

[79] B. London, A. Jeron, J. Zhou, P. Buckett, X. Han, G. F. Mitchell, and G. Koren, “Long QT and ventricular arrhythmias in transgenic mice expressing the N terminus and first transmembrane segment of a voltage-gated potassium channel.,” *Proc. Natl. Acad. Sci. U. S. A.*, vol. 95, no. 6, pp. 2926–31, Mar. 1998.

[80] H. Li, W. Guo, K. a Yamada, and J. M. Nerbonne, “Selective elimination of I(K,slow1) in mouse ventricular myocytes expressing a dominant negative Kv1.5alpha subunit.,” *Am. J. Physiol. Heart Circ. Physiol.*, vol. 286, no. 1, pp. H319–H328, 2004.

[81] M. R. Franz, “Long-term recording of monophasic action potentials from human endocardium.,” *Am. J. Cardiol.*, vol. 51, no. 10, pp. 1629–34, Jun. 1983.

[82] J. V Tranquillo, M. R. Franz, C. Knollmann, A. P. Henriquez, D. a Taylor, C. S. Henriquez, V. Joseph, and C. S. Hen-, “Genesis of the monophasic action potential: role of interstitial resistance and boundary gradients,” vol. 0281, pp. 1370–1381, 2004.

[83] R. M. Bell, M. M. Mocanu, and D. M. Yellon, “Retrograde heart perfusion: the Langendorff technique of isolated heart perfusion.,” *J. Mol. Cell. Cardiol.*, vol. 50, no. 6, pp. 940–50, Jun. 2011.

[84] B. F. Hoffman, P. F. Cranefield, E. Lepeschkin, B. Surawicz, and H. C. Herrlich, “Comparison of cardiac monophasic action potentials recorded by intracellular and suction electrodes,” *Am J Physiol -- Leg. Content*, vol. 196, no. 6, pp. 1297–1301, Jun. 1959.

[85] M. D. Lemoine, J. E. Duverger, P. Naud, D. Chartier, X. Y. Qi, P. Comtois, L. Fabritz, P. Kirchhof, and S. Nattel, “Arrhythmogenic left atrial cellular electrophysiology in a murine genetic long QT syndrome model,” *Cardiovasc. Res.*, vol. 92, no. 1, pp. 67–74, Jun. 2011.

[86] J. H. King, C. Wickramarachchi, K. Kua, Y. Du, K. Jeevaratnam, H. R. Matthews, A. A. Grace, C. L.-H. Huang, and J. A. Fraser, “Loss of Nav1.5 expression and function in murine atria containing the RyR2-P2328S gain-of-function mutation.,” *Cardiovasc. Res.*, vol. 99, no. 4, pp. 751–9, Sep. 2013.

[87] C.-J. Chang, C.-C. Cheng, T.-F. Yang, Y.-C. Chen, Y.-K. Lin, S.-A. Chen, and Y.-J. Chen, “Selective and non-selective non-steroidal anti-inflammatory drugs differentially regulate pulmonary vein and atrial arrhythmogenesis.,” *Int. J. Cardiol.*, vol. 184, pp. 559–67, Apr. 2015.

[88] F. L. Burton and S. M. Cobbe, “Effect of sustained stretch on dispersion of ventricular fibrillation intervals in normal rabbit hearts,” *Cardiovasc. Res.*, vol. 39, no. 2, pp. 351–359, 1998.

[89] P. Lee, F. Taghavi, P. Yan, P. Ewart, E. A. Ashley, L. M. Loew, P. Kohl, C. Bollensdorff, and C. E. Woods, “In situ optical mapping of voltage and

calcium in the heart," *PLoS One*, vol. 7, no. 8, p. e42562, 2012.

[90] T. Y. Yu, F. Syeda, A. P. Holmes, B. Osborne, H. Dehghani, K. L. Brain, P. Kirchhof, and L. Fabritz, "An automated system using spatial oversampling for optical mapping in murine atria. Development and validation with monophasic and transmembrane action potentials.," *Prog. Biophys. Mol. Biol.*, vol. 115, no. 2–3, pp. 340–348, Aug. 2014.

[91] R. Arora, M. K. Das, D. P. Zipes, and J. Wu, "Optical mapping of cardiac arrhythmias.," *Indian Pacing Electrophysiol. J.*, vol. 3, no. 4, pp. 187–96, Jan. 2003.

[92] A. Blana, S. Kaese, L. Fortmuller, S. Laakmann, D. Damke, K. van Bragt, J. Eckstein, I. Piccini, U. Kirchhefer, S. Nattel, G. Breithardt, P. Carmeliet, E. Carmeliet, U. Schotten, S. Verheule, P. Kirchhof, and L. Fabritz, "Knock-in gain-of-function sodium channel mutation prolongs atrial action potentials and alters atrial vulnerability," *Hear. Rhythm*, vol. 7, no. 12, pp. 1862–1869, 2010.

[93] M. Attin and W. T. Clusin, "Basic concepts of optical mapping techniques in cardiac electrophysiology.," *Biol. Res. Nurs.*, vol. 11, no. 2, pp. 195–207, Oct. 2009.

[94] T. J. Herron, P. Lee, and J. Jalife, "Optical imaging of voltage and calcium in cardiac cells & tissues.," *Circ. Res.*, vol. 110, no. 4, pp. 609–23, Feb. 2012.

[95] R. Arora, S. Verheule, L. Scott, A. Navarrete, V. Katari, E. Wilson, D. Vaz, and J. E. Olgin, "Arrhythmogenic substrate of the pulmonary veins assessed by high-resolution optical mapping," *Circulation*, vol. 107, no. 13, pp. 1816–1821, 2003.

[96] I. R. Efimov, V. P. Nikolski, and G. Salama, "Optical imaging of the heart," *Circ Res*, vol. 95, no. 1, pp. 21–33, 2004.

[97] I. R. Efimov, D. T. Huang, J. M. Rendt, and G. Salama, "Optical mapping of repolarization and refractoriness from intact hearts," *Circulation*, vol. 90, no. 3, pp. 1469–1480, 1994.

[98] G. Salama, R. Lombardi, and J. Elson, "Maps of optical action potentials and NADH fluorescence in intact working hearts," *Am J Physiol*, vol. 252, no. 2 Pt 2, pp. H384–94, 1987.

[99] M. Morad and G. Salama, "Optical probes of membrane potential in heart muscle.," *J. Physiol.*, vol. 292, no. 1, pp. 267–295, Jul. 1979.

[100] L. M. Loew, "Potentiometric dyes: Imaging electrical activity of cell membranes," *Pure Appl. Chem.*, vol. 68, no. 7, pp. 1405–1409, 1996.

[101] M. Zochowski, M. Wachowiak, C. X. Falk, L. B. Cohen, Y. W. Lam, S. Antic, and D. Zecevic, "Imaging membrane potential with voltage-sensitive dyes," *Biol Bull*, vol. 198, no. 1, pp. 1–21, 2000.

[102] A. P. Larsen, K. J. Sciuto, A. P. Moreno, and S. Poelzing, "The voltage-sensitive dye di-4-ANEPPS slows conduction velocity in isolated guinea pig hearts.," *Heart Rhythm*, vol. 9, no. 9, pp. 1493–500, Sep. 2012.

[103] L. M. Loew, G. W. Bonneville, and J. Surow, "Charge shift optical probes of membrane potential. Theory," *Biochemistry*, vol. 17, no. 19, pp. 4065–4071, Sep. 1978.

[104] L. M. Loew, “Design and Use of Organic Voltage Sensitive Dyes,” in *Membrane Potential Imaging in the Nervous System: Methods and Applications*, 1st ed., M. Canepari and D. Zecevic, Eds. New York: Springer, 2011, pp. 139–145.

[105] E. Fluhler, V. G. Burnham, and L. M. Loew, “Spectra, membrane binding, and potentiometric responses of new charge shift probes,” *Biochemistry*, vol. 24, no. 21, pp. 5749–5755, Oct. 1985.

[106] L. Loew, L. Cohen, J. Dix, E. Fluhler, V. Montana, G. Salama, and W. Jian-young, “A naphthyl analog of the aminostyryl pyridinium class of potentiometric membrane dyes shows consistent sensitivity in a variety of tissue, cell, and model membrane preparations,” *J. Membr. Biol.*, vol. 130, no. 1, Oct. 1992.

[107] A. Bullen and P. Saggau, “High-speed, random-access fluorescence microscopy: II. Fast quantitative measurements with voltage-sensitive dyes.,” *Biophys. J.*, vol. 76, no. 4, pp. 2272–87, Apr. 1999.

[108] V. G. Fast, “Recording Action Potentials Using Voltage-Sensitive Dyes,” in *Practical Methods in Cardiovascular Research*, S. Dhein, F. W. Mohr, and M. Delmar, Eds. Springer Berlin Heidelberg, 2005, pp. 233–255.

[109] S. Rohr, “Optical mapping of microscopic impulse propagation,” in *Quantitive Cardiac Electrophysiology*, C. Cabo and D. S. Rosenbaum, Eds. Marcel Dekker, 2002, pp. 507–555.

[110] W. Jian-young, L. B. Cohen, and C. X. Falk, “Fast Multisite Optical Measurement of Memebrane Potential, with Two Examples,” in *Fluorescent and Luminescent Probes for Biological Activity: A Practical Guide to Technology for Quantitative Real-Time Analysis*, W. Mason, Ed. Academic Press, 1999, p. 647.

[111] A. E. Moe, S. Marx, N. Banani, M. Liu, B. Marquardt, and D. M. Wilson, “Improvements in LED-based fluorescence analysis systems,” *Sensors Actuators B Chem.*, vol. 111–112, pp. 230–241, Nov. 2005.

[112] H. A. Tritthart, “Optical Techniques for the Recording of Action Potentials,” in *Practical Methods in Cardiovascular Research*, 1st ed., S. Dhein, F. W. Mohr, and M. Delmar, Eds. Berlin, Heidelberg: Springer Berlin Heidelberg, 2005, pp. 215–232.

[113] I. Efimov and G. Salama, “The future of optical mapping is bright: RE: review on: ‘Optical Imaging of Voltage and Calcium in Cardiac Cells and Tissues’ by Herron, Lee, and Jalife.,” *Circ. Res.*, vol. 110, no. 10, pp. e70–1, May 2012.

[114] L. Fabritz, M. G. Hoogendijk, B. P. Scicluna, S. C. van Amersfoorth, L. Fortmueller, S. Wolf, S. Laakmann, N. Kreienkamp, I. Piccini, G. Breithardt, P. R. Noppinger, H. Witt, K. Ebnet, T. Wichter, B. Levkau, W. W. Franke, S. Pieperhoff, J. M. de Bakker, R. Coronel, and P. Kirchhof, “Load-reducing therapy prevents development of arrhythmogenic right ventricular cardiomyopathy in plakoglobin-deficient mice,” *J Am Coll Cardiol*, vol. 57, no. 6, pp. 740–750, 2011.

[115] C. Liu, W. Liu, J. Palie, M. F. Lu, N. a Brown, and J. F. Martin, “Pitx2c patterns anterior myocardium and aortic arch vessels and is required for

local cell movement into atrioventricular cushions.," *Development*, vol. 129, no. 21, pp. 5081–5091, 2002.

[116] J. M. Di Diego, S. Sicouri, R. C. Myles, F. L. Burton, G. L. Smith, and C. Antzelevitch, "Optical and electrical recordings from isolated coronary-perfused ventricular wedge preparations.," *J. Mol. Cell. Cardiol.*, vol. 54, pp. 53–64, Jan. 2013.

[117] V. V Fedorov, I. T. Lozinsky, E. A. Sosunov, E. P. Anyukhovsky, M. R. Rosen, C. W. Balke, and I. R. Efimov, "Application of blebbistatin as an excitation-contraction uncoupler for electrophysiologic study of rat and rabbit hearts.," *Heart Rhythm*, vol. 4, no. 5, pp. 619–26, May 2007.

[118] Y. Dou, P. Arlock, and A. Arner, "Blebbistatin specifically inhibits actin-myosin interaction in mouse cardiac muscle," *Am. J. Physiol. Cell Physiol.*, pp. 1148–1153, 2007.

[119] M. Potse, A. C. Linnenbank, and C. A. Grimbergen, "Automated generation of isochronal maps in the presence of activation block," vol. 4, Jan. 2002.

[120] C. C. Reyes-Aldasoro, "Retrospective shading correction algorithm based on signal envelope estimation," *Electron Lett*, vol. 45, no. 9, p. 454, 2009.

[121] A. Savitzky and M. J. E. Golay, "Smoothing and Differentiation of Data by Simplified Least Squares Procedures.," *Anal. Chem.*, vol. 36, no. 8, pp. 1627–1639, Jul. 1964.

[122] W. J. Lammers, M. J. Schalij, C. J. Kirchhof, and M. a Allessie, "Quantification of spatial inhomogeneity in conduction and initiation of reentrant atrial arrhythmias.," *Am. J. Physiol.*, vol. 259, no. 4 Pt 2, pp. H1254–H1263, 1990.

[123] P. V Bayly, B. H. KenKnight, J. M. Rogers, R. E. Hillsley, R. E. Ideker, and W. M. Smith, "Estimation of conduction velocity vector fields from epicardial mapping data.," *IEEE Trans. Biomed. Eng.*, vol. 45, no. 5, pp. 563–71, May 1998.

[124] J. I. Laughner, F. S. Ng, M. S. Sulkin, R. M. Arthur, and I. R. Efimov, "Processing and analysis of cardiac optical mapping data obtained with potentiometric dyes.," *Am. J. Physiol. Heart Circ. Physiol.*, vol. 303, no. 7, pp. H753–65, Oct. 2012.

[125] B. Likar, J. B. a Maintz, and M. a Viergever, "Retrospective shading correction based on entropy minimisation," *J. Microsc.*, vol. 197, no. July 1999, pp. 285–295, 2000.

[126] S. Mehmet and B. Sankur, "Survey over image thresholding techniques and quantitative performance evaluation," *J. Electron. Imaging*, vol. 13, no. 1, p. 220, Jan. 2004.

[127] N. Otsu, "A threshold selection method from gray-level histograms," *IEEE Trans. Syst. Man. Cybern.*, vol. 9, no. 1, pp. 62–66, 1979.

[128] G. E. Morley, D. Vaidya, and J. Jalife, "Characterization of conduction in the ventricles of normal and heterozygous Cx43 knockout mice using optical mapping.," *J. Cardiovasc. Electrophysiol.*, vol. 11, no. 3, pp. 375–7, Mar. 2000.

[129] A. J. Camm, S. M. Al-Khatib, H. Calkins, J. L. Halperin, P. Kirchhof, G. Y. H.

Lip, S. Nattel, J. Ruskin, A. Banerjee, D. Blendea, E. Guasch, M. Needleman, I. Savelieva, J. Viles-Gonzalez, and E. S. Williams, “A proposal for new clinical concepts in the management of atrial fibrillation.,” *Am. Heart J.*, vol. 164, no. 3, pp. 292–302.e1, Sep. 2012.

[130] A. V Postma, L. R. C. Dekker, A. T. Soufan, and A. F. M. Moorman, “Developmental and genetic aspects of atrial fibrillation.,” *Trends Cardiovasc. Med.*, vol. 19, no. 4, pp. 123–30, May 2009.

[131] O. Campuzano and R. Brugada, “Genetics of familial atrial fibrillation,” *Europace*, vol. 11, no. 10, pp. 1267–1271, 2009.

[132] R. I. R. Martin, M. S. Babaei, M.-K. Choy, W. A. Owens, T. J. A. Chico, D. Keenan, N. Yonan, M. S. Koref, and B. D. Keavney, “Genetic variants associated with risk of atrial fibrillation regulate expression of PITX2, CAV1, MYOZ1, C9orf3 and FANCC.,” *J. Mol. Cell. Cardiol.*, vol. 85, pp. 207–14, Aug. 2015.

[133] a K. Ryan, B. Blumberg, C. Rodriguez-Esteban, S. Yonei-Tamura, K. Tamura, T. Tsukui, J. de la Peña, W. Sabbagh, J. Greenwald, S. Choe, D. P. Norris, E. J. Robertson, R. M. Evans, M. G. Rosenfeld, and J. C. Izpisúa Belmonte, “Pitx2 determines left-right asymmetry of internal organs in vertebrates.,” *Nature*, vol. 394, no. 6693, pp. 545–551, 1998.

[134] M. Logan, S. M. Pagán-Westphal, D. M. Smith, L. Paganessi, and C. J. Tabin, “The Transcription Factor Pitx2 Mediates Situs-Specific Morphogenesis in Response to Left-Right Asymmetric Signals,” *Cell*, vol. 94, no. 3, pp. 307–317, Aug. 1998.

[135] J. Wang, E. Klysik, and S. Sood, “Pitx2 prevents susceptibility to atrial arrhythmias by inhibiting left-sided pacemaker specification,” *Proc. Natl. Acad. Sci.*, pp. 1–6, 2010.

[136] P. Kirchhof, D. Andresen, R. Bosch, M. Borggrefe, T. Meinertz, U. Parade, U. Ravens, A. Samol, G. Steinbeck, A. Treszl, K. Wegscheider, and G. Breithardt, “Short-term versus long-term antiarrhythmic drug treatment after cardioversion of atrial fibrillation (Flec-SL): A prospective, randomised, open-label, blinded endpoint assessment trial,” *Lancet*, vol. 380, no. 9838, pp. 238–246, 2012.

[137] B. Parvez, J. Vaglio, S. Rowan, R. Muhammad, G. Kucera, T. Stubblefield, S. Carter, D. Roden, and D. Darbar, “Symptomatic response to antiarrhythmic drug therapy is modulated by a common single nucleotide polymorphism in atrial fibrillation.,” *J. Am. Coll. Cardiol.*, vol. 60, no. 6, pp. 539–45, Aug. 2012.

[138] L. Fabritz, P. Kirchhof, M. R. Franz, L. Eckhardt, G. Moennig, and P. Milberg, “Prolonged action potential durations, increased dispersion of repolarization, and polymorphic ventricular tachycardia in a mouse model of proarrhythmia,” vol. 32, pp. 25–32, 2003.

[139] C. H. Follmer and T. J. Colatsky, “Block of delayed rectifier potassium current, IK, by flecainide and E-4031 in cat ventricular myocytes.,” *Circulation*, vol. 82, no. 1, pp. 289–93, 1990.

[140] A. A. Paul, H. J. Witchel, and J. C. Hancox, “Inhibition of the current of heterologously expressed HERG potassium channels by flecainide and

comparison with quinidine, propafenone and lignocaine.," *Br. J. Pharmacol.*, vol. 136, no. 5, pp. 717–29, Jul. 2002.

[141] Z. Yang, N. E. Bowles, S. E. Scherer, M. D. Taylor, D. L. Kearney, S. Ge, V. V. Nadvoretskiy, G. DeFreitas, B. Carabello, L. I. Brandon, L. M. Godsel, K. J. Green, J. E. Saffitz, H. Li, G. A. Danieli, H. Calkins, F. Marcus, and J. A. Towbin, "Desmosomal dysfunction due to mutations in desmoplakin causes arrhythmogenic right ventricular dysplasia/cardiomyopathy," *Circ. Res.*, vol. 99, no. 6, pp. 646–655, 2006.

[142] C. Basso, G. Thiene, D. Corrado, A. Angelini, A. Nava, and M. Valente, "Arrhythmogenic Right Ventricular Cardiomyopathy: Dysplasia, Dystrophy, or Myocarditis?," *Circulation*, vol. 94, no. 5, pp. 983–991, Sep. 1996.

[143] a P. Burke, a Farb, G. Tashko, and R. Virmani, "Arrhythmogenic right ventricular cardiomyopathy and fatty replacement of the right ventricular myocardium: are they different diseases?," *Circulation*, vol. 97, no. 16, pp. 1571–1580, 1998.

[144] C. F. Camm, C. A. James, C. Tichnell, B. Murray, A. Bhonsale, A. S. J. M. te Riele, D. P. Judge, H. Tandri, and H. Calkins, "Prevalence of atrial arrhythmias in arrhythmogenic right ventricular dysplasia/cardiomyopathy," *Hear. Rhythm*, vol. 10, no. 11, pp. 1661–1668, Nov. 2013.

[145] A. F. Chu, E. Zado, and F. E. Marchlinski, "Atrial arrhythmias in patients with arrhythmogenic right ventricular cardiomyopathy/dysplasia and ventricular tachycardia.," *Am. J. Cardiol.*, vol. 106, no. 5, pp. 720–2, Sep. 2010.

[146] M. Noorman, S. Hakim, E. Kessler, J. A. Groeneweg, M. G. P. J. Cox, A. Asimaki, H. V. M. van Rijen, L. van Stuijvenberg, H. Chkourko, M. A. G. van der Heyden, M. A. Vos, N. de Jonge, J. J. van der Smagt, D. Dooijes, A. Vink, R. A. de Weger, A. Varro, J. M. T. de Bakker, J. E. Saffitz, T. J. Hund, P. J. Mohler, M. Delmar, R. N. W. Hauer, and T. A. B. van Veen, "Remodeling of the cardiac sodium channel, connexin43, and plakoglobin at the intercalated disk in patients with arrhythmogenic cardiomyopathy," *Hear. Rhythm*, vol. 10, no. 3, pp. 412–419, Mar. 2013.

[147] R. M. Shaw, "Reduced sodium channels in human ARVC.," *Heart Rhythm*, vol. 10, no. 3, pp. 420–1, Mar. 2013.

[148] S. Rizzo, E. M. Lodder, A. O. Verkerk, R. Wolswinkel, L. Beekman, K. Pilichou, C. Basso, C. A. Remme, G. Thiene, and C. R. Bezzina, "Intercalated disc abnormalities, reduced Na(+) current density, and conduction slowing in desmoglein-2 mutant mice prior to cardiomyopathic changes.," *Cardiovasc. Res.*, vol. 95, no. 4, pp. 409–18, Sep. 2012.

[149] P. Y. Sato, H. Musa, W. Coombs, G. Guerrero-Serna, G. A. Patiño, S. M. Taffet, L. L. Isom, and M. Delmar, "Loss of plakophilin-2 expression leads to decreased sodium current and slower conduction velocity in cultured cardiac myocytes.," *Circ. Res.*, vol. 105, no. 6, pp. 523–6, Sep. 2009.

[150] J. P. Kucera, S. Rohr, and Y. Rudy, "Localization of sodium channels in intercalated disks modulates cardiac conduction.," *Circ. Res.*, vol. 91, no. 12, pp. 1176–82, Dec. 2002.

[151] E. Ramos and M. E. O'leary, "State-dependent trapping of flecainide in the cardiac sodium channel.," *J. Physiol.*, vol. 560, no. Pt 1, pp. 37–49, Oct.

2004.

[152] D. Corrado, C. Basso, M. Schiavon, and G. Thiene, “Screening for hypertrophic cardiomyopathy in young athletes.,” *N. Engl. J. Med.*, vol. 339, no. 6, pp. 364–369, 1998.

[153] B. J. Maron, B. R. Chaitman, M. J. Ackerman, A. B. De Luna, D. Corrado, J. E. Crosson, B. J. Deal, D. J. Driscoll, N. a M. Estes, C. G. S. Araújo, D. H. Liang, M. J. Mitten, R. J. Myerburg, A. Pelliccia, P. D. Thompson, J. a. Towbin, and S. P. Van Camp, “Recommendations for physical activity and recreational sports participation for young patients with genetic cardiovascular diseases,” *Circulation*, vol. 109, no. 22, pp. 2807–2816, 2004.

[154] B. Benito, G. Gay-Jordi, A. Serrano-Mollar, E. Guasch, Y. Shi, J. C. Tardif, J. Brugada, S. Nattel, and L. Mont, “Cardiac arrhythmogenic remodeling in a rat model of long-term intensive exercise training,” *Circulation*, vol. 123, no. 1, pp. 13–22, 2011.

[155] A. La Gerche, A. T. Burns, D. J. Mooney, W. J. Inder, A. J. Taylor, J. Bogaert, A. I. MacIsaac, H. Heidbüchel, and D. L. Prior, “Exercise-induced right ventricular dysfunction and structural remodelling in endurance athletes,” *Eur. Heart J.*, vol. 33, no. 8, pp. 998–1006, 2012.

[156] D. Mozaffarian, C. D. Furberg, B. M. Psaty, and D. Siscovick, “Physical activity and incidence of atrial fibrillation in older adults: the cardiovascular health study.,” *Circulation*, vol. 118, no. 8, pp. 800–7, Aug. 2008.

[157] A. Aizer, J. M. Gaziano, N. R. Cook, J. E. Manson, J. E. Buring, and C. M. Albert, “Relation of vigorous exercise to risk of atrial fibrillation.,” *Am. J. Cardiol.*, vol. 103, no. 11, pp. 1572–7, Jun. 2009.

[158] L. Fabritz, L. Fortmuller, T. Y. Yu, M. Paul, and P. Kirchhof, “Can preload-reducing therapy prevent disease progression in arrhythmogenic right ventricular cardiomyopathy? Experimental evidence and concept for a clinical trial,” *Prog. Biophys. Mol. Biol.*, vol. 110, no. 2–3, pp. 340–346, 2012.

[159] F. Hartgens and H. Kuipers, “Effects of androgenic-anabolic steroids in athletes.,” *Sports Med.*, vol. 34, no. 8, pp. 513–54, Jan. 2004.

[160] K. Tsunoda, Y. Yamaguchi, T. Taguchi, K. Doge, Y. Kato, A. Sato, and S. Keizo, “Cardiovascular effects of dihydrotestosterone in rats,” *Leg. Med.*, vol. 1, no. 2, pp. 95–104, Apr. 1999.

[161] L. Mosca, E. Barrett-Connor, and N. Kass Wenger, “Sex/gender differences in cardiovascular disease prevention: What a difference a decade makes,” *Circulation*, vol. 124, no. 19, pp. 2145–2154, 2011.

[162] D. J. Lerner and W. B. Kannel, “Patterns of coronary heart disease morbidity and mortality in the sexes: a 26-year follow-up of the Framingham population.,” *Am. Heart J.*, vol. 111, no. 2, pp. 383–90, Feb. 1986.

[163] K. J. Hellestrand, P. J. Burnett, J. R. Milne, R. S. Bexton, A. W. Nathan, and A. J. Camm, “Effect of the antiarrhythmic agent flecainide acetate on acute and chronic pacing thresholds.,” *Pacing Clin. Electrophysiol.*, vol. 6, no. 5 Pt 1, pp. 892–9, Sep. 1983.

[164] J. Gomes, M. Finlay, A. K. Ahmed, E. J. Ciaccio, A. Asimaki, J. E. Saffitz, G.

Quarta, M. Nobles, P. Syrris, S. Chaubey, W. J. McKenna, A. Tinker, and P. D. Lambiase, “Electrophysiological abnormalities precede overt structural changes in arrhythmogenic right ventricular cardiomyopathy due to mutations in desmoplakin-A combined murine and human study.,” *Eur. Heart J.*, vol. 33, no. 15, pp. 1942–53, Aug. 2012.

[165] M. C. Finlay, A. K. Ahmed, A. Sugrue, J. Bhar-Amato, G. Quarta, A. Pantazis, E. J. Ciaccio, P. Syrris, S. Sen-Chowdhry, R. Ben-Simon, A. W. Chow, M. D. Lowe, O. R. Segal, W. J. McKenna, and P. D. Lambiase, “Dynamic conduction and repolarisation changes in early arrhythmogenic right ventricular cardiomyopathy versus benign outflow tract ectopy demonstrated by high density mapping & paced surface ECG analysis.,” *PLoS One*, vol. 9, no. 7, p. e99125, Jan. 2014.

[166] G. O’Hara, C. Villemaire, M. Talajic, and S. Nattel, “Effects of flecainide on the rate dependence of atrial refractoriness, atrial repolarization and atrioventricular node conduction in anesthetized dogs,” *J. Am. Coll. Cardiol.*, vol. 19, no. 6, pp. 1335–1342, May 1992.

[167] A. Costard-J$\ddot{u}$_zckle and M. R. Franz, “Frequency-dependent antiarrhythmic drug effects on postrepolarization refractoriness and ventricular conduction time in canine ventricular myocardium in vivo,” *J. Pharmacol. Exp. Ther.*, vol. 251, pp. 39–46, 1989.

[168] Y. Ikeda, K. I. Aihara, T. Sato, M. Akaike, M. Yoshizumi, Y. Suzaki, Y. Izawa, M. Fujimura, S. Hashizume, M. Kato, S. Yagi, T. Tamaki, H. Kawano, T. Matsumoto, H. Azuma, S. Kato, and T. Matsumoto, “Androgen receptor gene knockout male mice exhibit impaired cardiac growth and exacerbation of angiotensin II-induced cardiac fibrosis,” *J. Biol. Chem.*, vol. 280, no. 33, pp. 29661–29666, 2005.

[169] J. D. Marsh, M. H. Lehmann, R. H. Ritchie, J. K. Gwathmey, G. E. Green, and R. J. Schiebinger, “Androgen receptors mediate hypertrophy in cardiac myocytes.,” *Circulation*, vol. 98, no. 3, pp. 256–261, 1998.

[170] J. Brouillette, K. Rivard, E. Lizotte, and C. Fiset, “Sex and strain differences in adult mouse cardiac repolarization: Importance of androgens,” *Cardiovasc. Res.*, vol. 65, no. 1, pp. 148–157, 2005.

[171] L. Fabritz, D. Damke, M. Emmerich, S. G. Kaufmann, K. Theis, A. Blana, L. Fortmüller, S. Laakmann, S. Hermann, E. Aleynichenko, J. Steinfurt, D. Volkery, B. Riemann, U. Kirchhefer, M. R. Franz, G. Breithardt, E. Carmeliet, M. Schäfers, S. K. G. Maier, P. Carmeliet, and P. Kirchhof, “Autonomic modulation and antiarrhythmic therapy in a model of long QT syndrome type 3.,” *Cardiovasc. Res.*, vol. 87, no. 1, pp. 60–72, Jul. 2010.

[172] J. Benes, G. Ammirabile, B. Sankova, M. Campione, E. Krejci, A. Kvasilova, and D. Sedmera, “The role of connexin40 in developing atrial conduction.,” *Fed. Eur. Biochem. Sci. Lett.*, vol. 588, no. 8, pp. 1465–9, Apr. 2014.

[173] J. Park, C. A. Werley, V. Venkatachalam, J. M. Kralj, S. D. Dib-Hajj, S. G. Waxman, and A. E. Cohen, “Screening fluorescent voltage indicators with spontaneously spiking HEK cells.,” *PLoS One*, vol. 8, no. 12, p. e85221, Jan. 2013.

[174] M. Brunner and S. Kodirov, “In vivo gene transfer of Kv1. 5 normalizes

action potential duration and shortens QT interval in mice with long QT phenotype," *Am. J. Physiol. Heart Circ. Physiol.*, vol. 02115, pp. 194–203, 2003.

[175] L. C. Baker, B. London, B.-R. Choi, G. Koren, and G. Salama, "Enhanced Dispersion of Repolarization and Refractoriness in Transgenic Mouse Hearts Promotes Reentrant Ventricular Tachycardia," *Circ. Res.*, vol. 86, no. 4, pp. 396–407, Mar. 2000.

[176] A. V Glukhov, V. V Fedorov, M. E. Anderson, P. J. Mohler, and I. R. Efimov, "Functional anatomy of the murine sinus node: high-resolution optical mapping of ankyrin-B heterozygous mice.," *Am. J. Physiol. Heart Circ. Physiol.*, vol. 299, no. 2, pp. H482–H491, 2010.

[177] S. Verheule, T. Sato, T. Everett, S. K. Engle, D. Otten, M. Rubart-von der Lohe, H. O. Nakajima, H. Nakajima, L. J. Field, and J. E. Olgin, "Increased vulnerability to atrial fibrillation in transgenic mice with selective atrial fibrosis caused by overexpression of TGF-beta1.," *Circ. Res.*, vol. 94, no. 11, pp. 1458–65, Jun. 2004.

[178] C. R. Bezzina, J. Barc, Y. Mizusawa, C. A. Remme, J.-B. Gourraud, F. Simonet, et al. "Common variants at SCN5A-SCN10A and HEY2 are associated with Brugada syndrome, a rare disease with high risk of sudden cardiac death.," *Nat. Genet.*, vol. 45, no. 9, pp. 1044–9, Sep. 2013.

[179] G. Kanaporis, I. Martišienė, J. Jurevičius, R. Vosyliūtė, A. Navalinskas, R. Treinys, A. Matiukas, and A. M. Pertsov, "Optical mapping at increased illumination intensities.," *J. Biomed. Opt.*, vol. 17, no. 9, pp. 96007–1, Sep. 2012.

[180] Y.-C. Chen, Y.-H. Kao, C.-F. Huang, C.-C. Cheng, Y.-J. Chen, and S.-A. Chen, "Heat stress responses modulate calcium regulations and electrophysiological characteristics in atrial myocytes.," *J. Mol. Cell. Cardiol.*, vol. 48, no. 4, pp. 781–8, Apr. 2010.

[181] L. M. Swift, H. Asfour, N. G. Posnack, A. Arutunyan, M. W. Kay, and N. Sarvazyan, "Properties of blebbistatin for cardiac optical mapping and other imaging applications," *Pflugers Arch. J. Physiol.*, vol. 464, no. 5, pp. 503–512, 2012.

[182] J. Jalife, O. Berenfeld, and M. Mansour, "Mother rotors and fibrillatory conduction: A mechanism of atrial fibrillation," *Cardiovasc. Res.*, vol. 54, pp. 204–216, 2002.

[183] T. J. Wu, J. J. Ong, C. M. Chang, R. N. Doshi, M. Yashima, H. L. Huang, M. C. Fishbein, C. T. Ting, H. S. Karagueuzian, and P. S. Chen, "Pulmonary veins and ligament of Marshall as sources of rapid activations in a canine model of sustained atrial fibrillation.," *Circulation*, vol. 103, no. 8, pp. 1157–1163, 2001.

[184] M.-E. Ridler, M. Lee, D. McQueen, C. Peskin, and E. Vigmond, "Arrhythmogenic consequences of action potential duration gradients in the atria.," *Can. J. Cardiol.*, vol. 27, no. 1, pp. 112–9, Jan. 2011.

[185] P. Sanders, O. Berenfeld, M. Hocini, P. Jaïs, R. Vaidyanathan, L. F. Hsu, S. Garrigue, Y. Takahashi, M. Rotter, F. Sacher, C. Scavée, R. Ploutz-Snyder, J. Jalife, and M. Haïssaguerre, "Spectral analysis identifies sites of high-

frequency activity maintaining atrial fibrillation in humans," *Circulation*, vol. 112, no. 6, pp. 789–797, 2005.

[186] R. A. Gray, A. M. Pertsov, and J. Jalife, "Incomplete Reentry and Epicardial Breakthrough Patterns During Atrial Fibrillation in the Sheep Heart," *Circulation*, vol. 94, no. 10, pp. 2649–2661, Nov. 1996.

[187] R. Arora, J. Ng, J. Ulphani, I. Mylonas, H. Subacius, G. Shade, D. Gordon, A. Morris, X. He, Y. Lu, R. Belin, J. J. Goldberger, and A. H. Kadish, "Unique Autonomic Profile of the Pulmonary Veins and Posterior Left Atrium," *J. Am. Coll. Cardiol.*, vol. 49, no. 12, pp. 1340–1348, 2007.

[188] N. M. Al-Saady, O. A. Obel, and A. J. Camm, "Left atrial appendage: structure, function, and role in thromboembolism.," *Heart*, vol. 82, no. 5, pp. 547–54, Nov. 1999.

[189] J. N. Dominguez, S. M. Meilhac, Y. S. Bland, M. E. Buckingham, and N. a. Brown, "Asymmetric Fate of the Posterior Part of the Second Heart Field Results in Unexpected Left/Right Contributions to Both Poles of the Heart," *Circ. Res.*, vol. 111, no. 10, pp. 1323–1335, 2012.

[190] S. Y. Ho, R. H. Anderson, and D. Sánchez-Quintana, "Atrial structure and fibres: morphologic bases of atrial conduction.," *Cardiovasc Res*, vol. 54, no. 2, pp. 325–36, 2002.

[191] J. Feng, L. Yue, Z. Wang, and S. Nattel, "Ionic mechanisms of regional action potential heterogeneity in the canine right atrium.," *Circ. Res.*, vol. 83, no. 5, pp. 541–551, 1998.

[192] A. Burashnikov, S. Mannava, and C. Antzelevitch, "Transmembrane action potential heterogeneity in the canine isolated arterially perfused right atrium: effect of IKr and IKur/Ito block.," *Am. J. Physiol. Heart Circ. Physiol.*, vol. 286, no. 6, pp. H2393–400, 2004.

[193] D. Gong, Y. Zhang, B. Cai, Q. Meng, S. Jiang, X. Li, L. Shan, Y. Liu, G. Qiao, Y. Lu, and B. Yang, "Characterization and comparison of Na+, K+ and Ca2+ currents between myocytes from human atrial right appendage and atrial septum.," *Cell. Physiol. Biochem.*, vol. 21, no. 5–6, pp. 385–94, Jan. 2008.

[194] N. J. Chandler, I. D. Greener, J. O. Tellez, S. Inada, H. Musa, P. Molenaar, D. DiFrancesco, M. Baruscotti, R. Longhi, R. H. Anderson, R. Billeter, V. Sharma, D. C. Sigg, M. R. Boyett, and H. Dobrzynski, "Molecular architecture of the human sinus node insights into the function of the cardiac pacemaker," *Circulation*, vol. 119, no. 12, pp. 1562–1575, 2009.

[195] J. Li, S. Inada, J. E. Schneider, H. Zhang, H. Dobrzynski, and M. R. Boyett, "Three-dimensional computer model of the right atrium including the sinoatrial and atrioventricular nodes predicts classical nodal behaviours.," *PLoS One*, vol. 9, no. 11, p. e112547, Jan. 2014.

[196] M. Haissaguerre, P. Jais, D. C. Shah, A. Takahashi, M. Hocini, G. Quiniou, S. Garrigue, A. Le Mouroux, P. Le Metayer, and J. Clementy, "Spontaneous Initiation of Atrial Fibrillation by Ectopic Beats Originating in the Pulmonary Veins," *N Engl J Med*, vol. 339, no. 10, pp. 659–666, 1998.

[197] S. Webb, M. Kanani, R. H. Anderson, M. K. Richardson, and N. a Brown, "Development of the human pulmonary vein and its incorporation in the

morphologically left atrium," *Cardiol. Young*, vol. 11, no. 6, pp. 632–642, 2001.

[198] W. -j. Li, Y. -y. Bai, H. -y. Zhang, R. -b. Tang, C. -l. Miao, C. -h. Sang, X. -d. Yin, J. -z. Dong, and C. -s. Ma, "Additional Ablation of Complex Fractionated Atrial Electrograms After Pulmonary Vein Isolation in Patients With Atrial Fibrillation: A Meta-Analysis," *Circ. Arrhythmia Electrophysiol.*, vol. 4, no. 2, pp. 143–148, 2011.

[199] H. Calkins, K. H. Kuck, R. Cappato, J. Brugada, a. J. Camm, et al. "2012 HRS/EHRA/ECAS Expert Consensus Statement on Catheter and Surgical Ablation of Atrial Fibrillation: Recommendations for Patient Selection, Procedural Techniques, Patient Management and Follow-up, Definitions, Endpoints, and Research Trial Design: A re," *Europace*, vol. 14, no. 4, pp. 528–606, 2012.

Appendices

Appendix 1 - Ectopic activity and arrhythmias due to left atrial APD heterogeneity.

Introduction

This chapter discusses an additional application of the optical mapping system applied to investigate the heterogeneity of action potentials across the whole left atrium (LA). The investigations of this chapter have led onto further developments of the optical mapping system to analyse calcium transient heterogeneity. In addition to this, channel expressions were measured from multiple sections of the LA. Calcium imaging and ion channel expression measurements were performed by other research lab members and not the author of this thesis. The main advantage of the optical mapping system presented here is its high spatial resolution. Other advantages over contact methods such as microelectrode and MAP electrodes include the ability to measure multiple regions of interest from a single image acquisition hence it is an ideal method for investigation of action potential duration (APD) variation. The optical mapping system was used to calculate APDs for each pixel and to generate a map, representing the distribution of APD value.

The heterogeneity of the LA is of interest as the pulmonary vein region has been proposed as a key anchorage point for re-entrant activity in atrial fibrillation (AF) [182], [183]. Other studies have shown that a gradient or heterogeneity and high frequency activity in the atria contribute or help maintain AF [184], [185]. Mapping

studies have shown that the complicated 3D nature of the atrium is a key component of the activation patterns during AF [186]. It is also hypothesised that the activation and repolarisation of characteristics of the left atrial pulmonary vein (LA-PV) region differs from the rest of the LA [187], which indicates a susceptibility to conduction slowing.

The development of the pulmonary vein area in the LA is subtly different to the left atrial appendage (LAA). The LAA forms an outfacing pouch of the primary heart field and the LA-PV develops from the left posterior second heart field [188], [189]. Structurally, the two regions are also distinct with the LAA exhibiting clear pectinations compared with the relatively smooth walled LA-PV, relating functionally to differences in contraction [190]. It is becoming apparent that a heterogeneous electrical arrangement may act a substrate for arrhythmic activity. Regional cellular electrical differences in the right atrium have been characterised in both animals [191], [192] and humans [193], including detailed analysis of the sinoatrial node, the atrioventricular node region and the conduction system [194], [195] but few studies have been performed on small tissues such as murine LA. Here we investigate the APD heterogeneity of the LA to identify electrophysiological variations within tissues.

We have used optical mapping to contribute to a larger study whereby microelectrodes were also used to measure APD variations across the different regions of the LA. In addition to this, ion channel expressions were measured to study the profile in multiple regions of the LA. The results and findings for these were compiled in a research paper titled “A Regional Reduction in I_{to} and I_{KACh} in the Murine Posterior Left Atrial Myocardium Is Associated with Action Potential

Prolongation and Increased Ectopic Activity" (see Appendix - 2) but only the optical mapping techniques and results are discussed in this chapter.

Methods

Mouse LA samples were collected as described in the materials and methods chapter. The samples were then stimulated as described in material and methods: Stimulation protocol along with the optical mapping technique. 18 mice from an MF-1 background were used in this cohort. Images were analysed using MATLAB algorithms as described in Optical mapping design and development: Action potential duration maps.

Results

Using the high-spatial resolution optical mapping system we were then able to characterise the regional changes in AP repolarisation across the whole LA in greater detail. For these experiments, images were recorded from LAs isolated from male MF-1 mice (n=18 LA). An example raw fluorescent image is shown in Figure 1A and the corresponding isochronal APD70 and APD50 distribution maps for this LA, paced at 10Hz, were presented in Figure 1B. Characteristic example OAPs recorded from each of the 9 regions within a single LA are shown in Figure 1C. The most obvious finding was that OAPs in the LA-PV (regions 1-3) were significantly longer than other LA regions (Figure 1D). In addition, APD70 times were significantly different between segments 1 and 3 (Figure 1D), suggestive of considerable APD heterogeneity within the LA-PV region that was not apparent in the mid or lateral LAA. A summary of the mean 9 region APD70 spatial distribution is presented in Figure 1E.

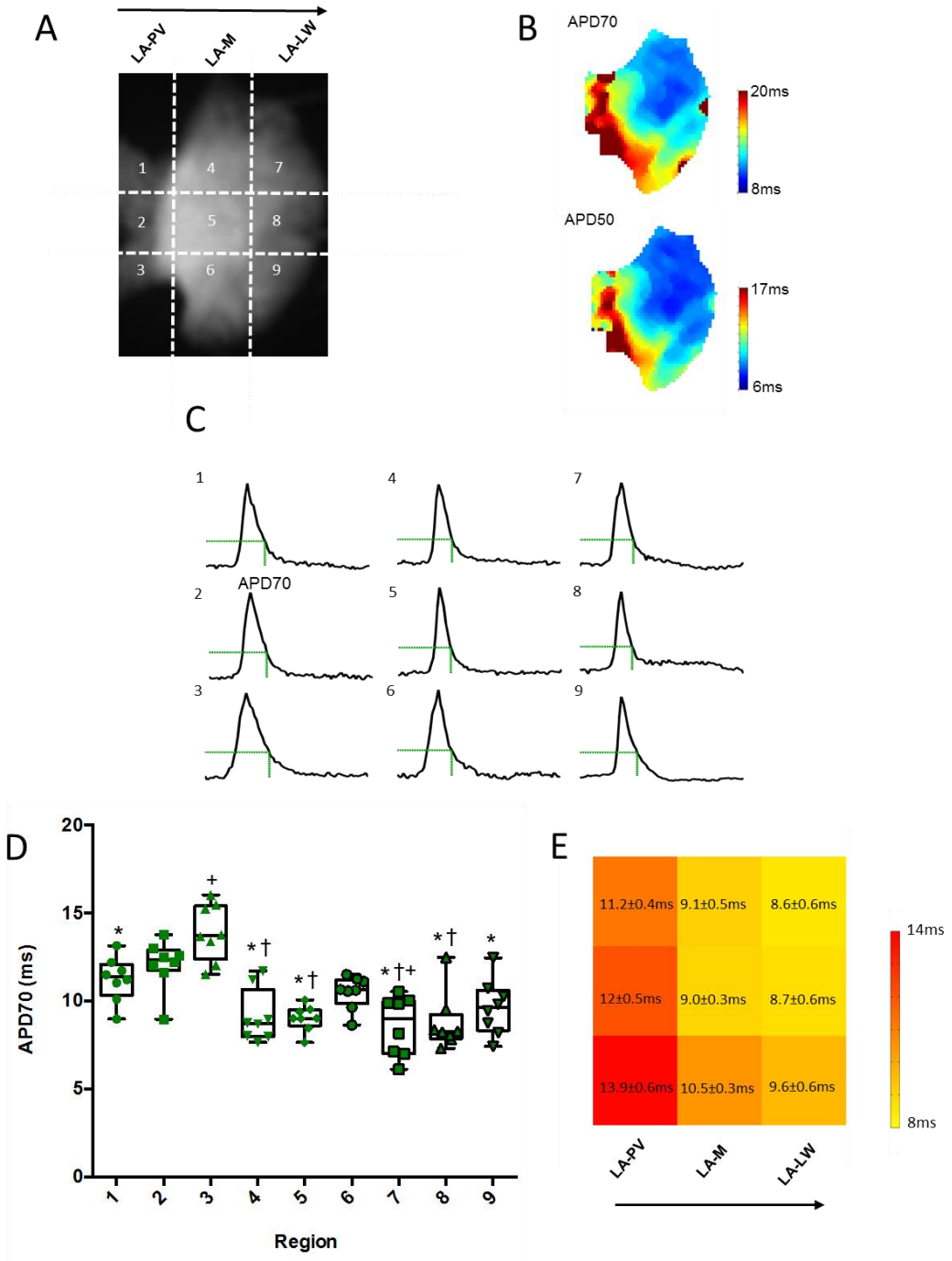

Figure 1. High spatial resolution action potential duration distribution patterns in the murine left atrium

A) Raw fluorescence image of a LA loaded with di-4-ANEPPS, along with the 9 region grid used for regional analysis. B) Corresponding high spatial resolution isochronal action potential duration (APD70) distribution map. C) Example action potentials recorded from the 9 different LA regions during 10Hz pacing. Green dotted line indicates APD70. D) Box and whisker plot of APD70 values measured in each LA region. +, † and * denote P<0.05 vs region 1,2 and 3, respectively, one way repeated measures ANOVA with Bonferroni post hoc analysis. (N=18 LA). (E) 9 region map depicting mean APD70 values, ± SEM, in the 9 regions of the LA.

Discussion

Here we demonstrate an important application of the high resolution mapping system which other techniques fall short. We show that the regions 1-3, the PV area may be an important source of ectopic activity in the mouse LA. The PV region shows unique characteristics of a prolonged APD. Additional data gathered from the research group also shows increased action potential amplitude and upstroke velocity. Using the optical mapping system, we display APD distribution maps of the murine LA in high detail and identify that in addition to APs being longer, the LA-PV also exhibits increased intra-regional APD heterogeneity. As a result of these findings, this led onto further research investigating calcium handling and ion channel expression. The expression profile for the ion channels proved to be significantly different between the LA-PV and lateral wall of the LAA regions. Calcium relaxation time distribution maps were also analysed in an intact murine LA and identified that calcium clearance is protracted in the LA-PV. In addition, the LA-PV has a slower rate of calcium release. These findings may provide some insight into the possible causes of the heightened susceptibility to ectopy and the altered electrical properties and calcium handling.

Our findings were consistent with the idea that the atrial LA-PV myocardium is a source of focal ectopic activity in the LA, given that all measured ectopic activity was abolished after LA-PV resection. In our experiments, the pulmonary vein, a common source of ectopic activity [196] was removed before experimentation, in order to evaluate specifically the electrical properties of the atrial myocardium. Nevertheless, it is possible that some elements of LA-PV myocardium were derived from the dorsal mesocardium and developing pulmonary vein sleeve, as it

infiltrates to fuse and form the posterior LA wall [197]. Thus, some spontaneous activity that we observed may be a consequence of localised regions of pulmonary vein-like myocardium that has been incorporated into the LA-PV atrial myocardium. Importantly, since most, but not all atrial fibrillation is terminated in patients following pulmonary vein isolation [198], [199], it is conceivable that this region gives rise to the ectopic activity accounting for some cases of atrial fibrillation recurrence.

Despite a number of important studies reporting APD variation in the right atrium in animals [191], [192] and humans [193], little is known about APD variation in the LA. Recordings of TAPs and OAPs were used in this study to observe regional differences in LA APD. The high resolution optical mapping system allowed us to develop and observe APD distribution maps of the murine LA in detail. The APD70 distribution maps show that APs in the LA-PV region were prolonged in comparison to the rest of the LA. The prolonged APD in the LA-PV could promote the development of focal ectopic activity in this area of atrial myocardium most likely by increasing the probability of calcium channel recovery and reactivation thereby provoking calcium mediated early-after depolarisations [46]. OAP analysis also revealed significant APD heterogeneity within the LA-PV. This possibly correlates with a previous investigation where changes in effective refractory periods in response to vagal stimulation were most variable in the LA-PV region [187]. The increase in APD heterogeneity in this region could contribute to the heightened susceptibility of the LA-PV to develop and establish re-entrant circuits following the emergence of triggered activity [46], [55].

Appendix 2 - A Regional Reduction in I_{to} and I_{KACh} in the Murine Posterior Left Atrial Myocardium Is Associated with Action Potential Prolongation and Increased Ectopic Activity.

PLOS | ONE

RESEARCH ARTICLE

A Regional Reduction in I_{to} and I_{KACh} in the Murine Posterior Left Atrial Myocardium Is Associated with Action Potential Prolongation and Increased Ectopic Activity

Andrew P. Holmes[1☯], Ting Y. Yu[1,2☯], Samantha Tull[1], Fahima Syeda[1], Stefan M. Kuhlmann[1], Sian-Marie O'Brien[1], Pushpa Patel[1], Keith L. Brain[1], Davor Pavlovic[1], Nigel A. Brown[3], Larissa Fabritz[1,4,5*], Paulus Kirchhof[1,4,5,6]

1 Institute of Cardiovascular Science, University of Birmingham, Birmingham, United Kingdom, **2** Physical Sciences of Imaging in the Biomedical Sciences, School of Chemistry, College of Engineering Physical Sciences, University of Birmingham, Birmingham, United Kingdom, **3** St George's, University of London, London, United Kingdom, **4** Department of Cardiovascular Medicine, Hospital of the University of Münster, Münster, Germany, **5** University Hospitals Birmingham NHS Foundation Trust, Birmingham, United Kingdom, **6** Sandwell and West Birmingham Hospitals NHS Trust, Birmingham, United Kingdom

☯ These authors contributed equally to this work.
* l.fabritz@bham.ac.uk

OPEN ACCESS

Citation: Holmes AP, Yu TY, Tull S, Syeda F, Kuhlmann SM, O'Brien S-M, et al. (2016) A Regional Reduction in I_{to} and I_{KACh} in the Murine Posterior Left Atrial Myocardium Is Associated with Action Potential Prolongation and Increased Ectopic Activity. PLoS ONE 11(5): e0154077. doi:10.1371/journal.pone.0154077

Editor: Vladimir E. Bondarenko, Georgia State University, UNITED STATES

Received: March 21, 2016

Accepted: April 10, 2016

Published: May 5, 2016

Data Availability Statement: All relevant data are within the paper.

Funding: This work was supported by European Union (EUTRAF 251057), (CATCH ME 633193), British Heart Foundation (FS/13/43/30324), and Leducq Foundation. S.K. was supported by a Boehringer Ingelheim Fonds MD student fellowship. The funders had no role in study design, data collection and analysis, decision to publish, or preparation of the manuscript.

Abstract

Background

The left atrial posterior wall (LAPW) is potentially an important area for the development and maintenance of atrial fibrillation. We assessed whether there are regional electrical differences throughout the murine left atrial myocardium that could underlie regional differences in arrhythmia susceptibility.

Methods

We used high-resolution optical mapping and sharp microelectrode recordings to quantify regional differences in electrical activation and repolarisation within the intact, superfused murine left atrium and quantified regional ion channel mRNA expression by Taqman Low Density Array. We also performed selected cellular electrophysiology experiments to validate regional differences in ion channel function.

Results

Spontaneous ectopic activity was observed during sustained 1Hz pacing in 10/19 intact LA and this was abolished following resection of LAPW (0/19 resected LA, P<0.001). The source of the ectopic activity was the LAPW myocardium, distinct from the pulmonary vein sleeve and LAA, determined by optical mapping. Overall, LAPW action potentials (APs) were *ca*. 40% longer than the LAA and this region displayed more APD heterogeneity. mRNA expression of *Kcna4*, *Kcnj3* and *Kcnj5* was lower in the LAPW myocardium than in

Competing Interests: The authors have declared that no competing interests exist.

the LAA. Cardiomyocytes isolated from the LAPW had decreased I_{to} and a reduced I_{KACh} current density at both positive and negative test potentials.

Conclusions

The murine LAPW myocardium has a different electrical phenotype and ion channel mRNA expression profile compared with other regions of the LA, and this is associated with increased ectopic activity. If similar regional electrical differences are present in the human LA, then the LAPW may be a potential future target for treatment of atrial fibrillation.

Introduction

The human left atrial posterior wall (LAPW) has been proposed as a key anchor point for atrial re-entrant activity in atrial fibrillation (AF) [1–3]. The LAPW myocardium has a different embryonic origin to the left atrial appendage (LAA) and pulmonary veins (PVs) [4,5]. Furthermore, in animals, the LAPW exhibits a heterogeneous response to autonomic vagal stimulation [6] and has an increased susceptibility to stretch induced conduction slowing [7], potentially indicative of a unique region-specific electrical identity. Precisely how the electrical phenotype of the LAPW differs from other areas of the LA myocardium is however, currently unresolved. Furthermore, it is unclear whether this area of myocardium (different from the PVs) can generate ectopic action potentials. Here, we therefore compared the electrical properties and ion channel mRNA expression profile of the LAPW with the LAA, to more clearly characterise the regional electrical differences that exist throughout the murine LA myocardium.

We analysed transmembrane action potentials (TAPs) and used optical mapping [8] of the LAA and LAPW to systematically characterise the regional AP properties and to reveal the origins of any spontaneously developing ectopic electrical activity within the LA myocardium. Regional differences in ion channel mRNA expression and I_{to}, I_{K1} and I_{KACh} current densities were also assessed.

These experiments show that a significant amount of spontaneous LA ectopy originates from the LAPW myocardium. In addition, the LAPW exhibits prolonged action potential durations (APDs), displays more intra-regional APD heterogeneity and has a distinct ion channel mRNA expression profile. Isolated cells from the LAPW have a significantly reduced I_{to} and I_{KACh} current densities, likely to contribute to the prolonged APD. Thus, the LAPW has a different electrical phenotype compared to other parts of the LA and is more vulnerable to developing spontaneous APs that could promote arrhythmogenesis. If similar findings are validated in humans, antiarrhythmic agents or ablation strategies targeted against LAPW driven ectopy could be a future treatment for AF.

Methods

Ethical Statement

All procedures were conducted in accordance with all rules and regulations for experiments with animals and approved by the UK Home Office (PPL number 30/2967) and by the institutional review board of University of Birmingham. Experiments were conducted on male and female adult mice (12–18 week), bred on the MF1 background. Mice were housed in individually ventilated cages, with sex-matched littermates (2–7 mice/ cage), under standard conditions: 12 h light/dark circle, 22°C and 55% humidity. Food and water were available *ad libitum*.

The general health status of all mice (bearing, grooming, behavior, body weight) used in the study was monitored daily and immediately prior to surgery. Mouse hearts were extracted by thoracotomy under deep terminal isoflurane anaesthesia (4% isoflurane in O_2, 1.5L/min), death by exsanguination.

Left atrial transmembrane action potentials

Following isolation the whole mouse heart was immediately transferred into a dissecting chamber and continuously superfused with a bicarbonate buffered Krebs-Henseleit (KH) solution containing in mM: NaCl 118; $NaHCO_3$ 24.88; KH_2PO_4 1.18; Glucose 5.55; Na-Pyruvate 5; $MgSO_4$ 0.83; $CaCl_2$ 1.8; KCl 3.52, equilibrated with 95%O_2/5% CO_2, pH 7.4. Micro-dissection of the LA was performed using a dissection microscope (Stemi SV 11, Zeiss, Germany). The posterior surfaces of the atria were identified, the PV was removed and then the entire intact LA (including the LAA and LAPW) was dissected free by cutting at the junction between the LAPW and the PV orifice.

The LA was transferred into a recording chamber, and pinned onto a Sylgard-coated surface, carefully ensuring not to stretch either the LAA or LAPW. The LA was continuously superfused (KH buffer solution, pH 7.4, 36–37°C, equilibrated with 95% O_2, 5% CO_2) and paced at 1–10 Hz via bipolar platinum electrodes. TAPs were recorded from freely contracting LA using custom made glass floating microelectrodes containing 3M KCl, (resistance 15–30 MΩ). Voltage signals were amplified and digitised at 20 kHz and were unfiltered (Axoclamp 2B; Molecular Devices, California, USA; *Spike2* software Cambridge Electronic Design, Cambridge, UK). Measured parameters included the resting membrane potential (RMP), action potential amplitude (APA), peak depolarisation rate (Vmax) and action potential duration (APD) at 30–90% repolarisation. APs were only analysed following sufficient rate adaptation.

To assess for ectopy, TAPs were recorded from the left atrial appendage and LA was stimulated at 1Hz for 3–5 minutes. Ectopic preparations were defined as having more than 2% ectopic APs during 1Hz pacing. All experiments were performed after 15 minutes equilibration and were completed within 2 hours of isolation.

Optical mapping of activation and action potential duration

Following isolation, murine hearts were mounted on a vertical Langendorff apparatus (Hugo Sachs, March-Hugstetten, Germany). The aorta was retrogradely perfused at 36–37°C, pH 7.4 and loaded with Di-4-ANEPPS (5μM; Biotium, California, USA) for 10–15 minutes. The entire LA was isolated and the PV, inter-atrial septum and coronary sinus were removed from the preparation. The posterior LA surface was exposed in a recording chamber. The uncoupler blebbistatin (10μM; Cayman Chemical, Michigan, USA) was added to the superfusate to minimise contraction artefacts. Following 15 minutes equilibration, the LA was paced (2ms duration pulses, twice diastolic voltage threshold) at 1-10Hz via bipolar platinum electrodes using an isolated constant voltage stimulator (Digitimer, Welwyn Garden City, UK). APs used for analysis were obtained following sufficient rate adaptation [8].

Di-4-ANEPPS was excited at 530nm by four LEDs (Cairn Research, Kent, UK) and emitted fluorescence was captured using a second generation, high spatial resolution (2048 by 2048 pixels, single pixel area: 6.5μm by 6.5μm) ORCA flash 4.0 camera (Hamamatsu Photonics, Japan). Images were recorded and organised using WinFluor V3.4.9 (Dr John Dempster, University of Strathclyde, UK). OAPs (recorded from an ROI of 4x4 pixels) were analysed using custom made algorithms produced in MATLAB [8]. Activation maps were generated as described previously [8].

Taqman Low Density Array (TLDA) mRNA expression analysis

LA were harvested and dissected into the specific LA regions (LAPW and LAA) before being snap frozen. RNA was isolated from the regional tissue using RNeasy micro kit (Qiagen, Hilden, Germany) with the Precellys Lysis kit containing ceramic beads CK28 (Bertin Technologies, Montigny-le-Bretonneux, France). cDNA was produced using the SuperScript® VILO™ cDNA Synthesis kit (Life Technologies, Paisley, UK). 350ng of RNA was used per TLDA reservoir. Ion channel gene expression levels were quantified using custom-designed and preloaded 96-well TLDA (Life Technologies, Paisley, UK). PCRs were performed using an ABI Real Time PCR 7900HT (Life Technologies, Paisley, UK). Data was acquired using AB SDS 2.4 and RQ manager software (Life Technologies, Paisley, UK). The CT cut off value was 32.

Left atrial cardiomyocyte cell isolation

Hearts were removed under deep terminal inhalation anaesthesia (4% isoflurane in O_2, 1.5L/min) and perfused at 4ml.min^{-1} at 37°C on a vertical Langendorff apparatus with the following solutions, equilibrated with 100% O_2: (i) HEPES-buffered modified Tyrode's solution containing in mM: NaCl 145, KCl 5.4, $CaCl_2$ 1.8, $MgSO_4$ 0.83, Na_2HPO_4 0.33, HEPES 5, and glucose 11 (pH 7.4, NaOH) x 5min; (ii) Ca^{2+}-free Tyrode's solution × 5min; (iii) Tyrode's enzyme solution containing 20μg/mL Liberase™ (Roche, Indianapolis, IN), 0.1% bovine serum albumin (BSA, Sigma), 20mM taurine and 30μM $CaCl_2$ × 20-23min. The heart was removed from the Langendorff and perfused with 5ml of modified Kraft-Bruhe (KB) solution containing in mM: DL-potassium aspartate 10, L-potassium glutamate 100, KCl 25, KH_2PO_4 10, $MgSO_4$ 2, taurine 20, creatine 5, EGTA 0.5, HEPES 5, 0.1% BSA, and glucose 20 (pH 7.2, KOH). The entire LA was dissected free, separated into LAA and LAPW regions, and cardiomyocytes were dissociated by gentle trituration with fire-polished glass pipettes (2 to 1mm diameter in sequence). Cells were filtered through 100μm nylon gauze and the suspension was centrifuged for 5min at 500–1000 rpm. The remaining pellet was re-suspended in 2ml KB buffer and Ca^{2+} was gradually reintroduced to the cell suspension incrementally over a period of 2 hours to reach a final concentration of 1.8mM. All experiments were performed within 12 hours of isolation.

Whole cell patch clamp electrophysiology

Dissociated mouse LA cardiomyocytes were transferred to an initially static bath recording chamber and allowed to adhere to laminin-coated coverslips (10mm diameter). Cells were then continually superfused at 3 ml/min, with an external solution containing in mM; NaCl 140, KCl 5.4, $CaCl_2$ 1, $MgCl_2$ 1, HEPES 10 and glucose 5.5 (pH 7.4 with NaOH). To block L-type Ca^{2+} currents, 300μM $CdCl_2$ was added to the superfusate. Experiments were performed at 22 ±0.5°C. Whole cell patch clamp recordings were obtained in voltage clamp mode using borosilicate glass pipettes (tip resistances 1.5–3 MΩ). For recordings of all K^+ currents, the pipette solution contained in mM: KCl 135, NaCl 4, EGTA 10, HEPES 10, MgATP 3, Na_3GTP, 0.5 and glucose 5 (pH 7.2, KOH). Voltage dependent, Ca^{2+} independent K^+ currents were evoked by 10mV step depolarisations (500ms) from a holding potential of -70mV (close to physiological RMP), at 1Hz. I_{to} was calculated as the difference between peak outward and steady state K^+ current as described previously [9,10], as I_{Kur} hardly inactivates at 22°C [11]. I_{K1} current was isolated by addition of 50μM $BaCl_2$ and applying 10mV step depolarisations (500ms) from -120mV to +50mV from a holding potential of -60mV. Addition of 10μM Carbachol (CCh) to the superfusate in the presence of 50μM $BaCl_2$ (that blocks I_{K1} without affecting I_{KACh}) was used to maximally activate muscarinic receptors [12]. The CCh dependent current was calculated and used to estimate I_{KACh} as previously described [13]. All recordings and analysis protocols were performed using an Axopatch 1D amplifier (Molecular Devices, USA) and a CED

micro1401 driven by Signal v6 software (CED, UK). During experimentation the liquid junction potential (LJP) varied between +3 and +14mV. Best fit I_{K1} and I_{KACh} I/V curves with corrected LJP were calculated post experimentation and were plotted alongside uncorrected values for comparison. The capacitance of each cardiomyocyte was measured by integrating the capacitance current evoked by 10mV depolarising steps from a holding potential of -70mV. The mean cell capacitance was not significantly different between LAA (73±4pF, N = 41) and LAPW (77±3pF, N = 29) cells. Data was only analysed from cells where the input resistance remained above 500MΩ throughout. Series resistance was not compensated, however, voltage errors were assumed to be low given that peak currents were usually less than 2nA.

Data analysis

Values in text are expressed as mean ± standard error of mean unless otherwise stated. For boxplots, boxes and box limits indicate the median and inter quartile range. All individual measurements are shown in the boxplots as points. Statistical analysis was performed using 1) a Fisher's exact test 2) a paired 2-tailed student's t-test, 3) one way repeated measures Analysis of Variance (ANOVA) or 4) two way repeated measures ANOVA with Bonferroni post hoc analysis where appropriate (Prism6, GraphPad, Cal, USA). Significance was taken as two tailed, $P<0.05$.

Results

The LAPW displays intrinsic ectopic activity at low frequency stimulation

Initial experiments aimed to investigate the vulnerability of different LA regions in generating ectopic activity. To do this, intact LAs were paced at 10Hz followed by a more prolonged (up to 5minutes) 1Hz frequency (Fig 1A & 1B). Using this protocol, ectopic activity developed in 10/19 LA preparations (Fig 1B & 1C). The type of ectopic activity varied between preparations and consisted of single isolated ectopic APs, multiple clustered irregular APs and short regular AP bursts that developed into more prolonged pacemaker-like activity (Fig 1D). Interestingly, in these same preparations, all the ectopic activity was abolished after resection of the LAPW (Fig 1B & 1C). In a further 4 ectopic LA preparations, TAP recordings made directly from the resected LAPW tissue showed that it continued to sustain intrinsic ectopic/pacemaker like activity (N = 4/4), whilst the LAA did not (N = 0/4, Fig 1E & 1F). This suggested that the LAPW was the source of the observed ectopy.

To more clearly define the precise origin of the ectopic activity, we generated isochronal activation maps of the entire intact LA. In these experiments, ectopic activity was found in 5/14 LA. Importantly, in all 5 instances, the source of the ectopic activity was the LAPW myocardium (Fig 2A–2C). To control for the LAPW ectopic activity being a consequence of a close proximity to the stimulus electrode, these experiments were performed with the stimulus electrode positioned at several different sites on the LA surface. Fig 2B demonstrates a stimulated AP originating from the stimulation site in the LAA, whilst the ectopic AP originates in the LAPW, and in this example, it generates a more disorganised propagation wave. Thus, LAPW ectopic activity appears to be independent of the position relative to the stimulus electrode.

Action potential prolongation and heterogeneity in the LAPW

The ability of the LAPW but not the LAA to generate spontaneous APs implies that there may be fundamental electrical differences between the two regions. To examine potential regional electrical differences in AP morphology, we compared TAPs from the LAA and LAPW using an incremental ramp stimulation protocol consisting of 300 APs at 8.5Hz, 50APs at 10Hz and

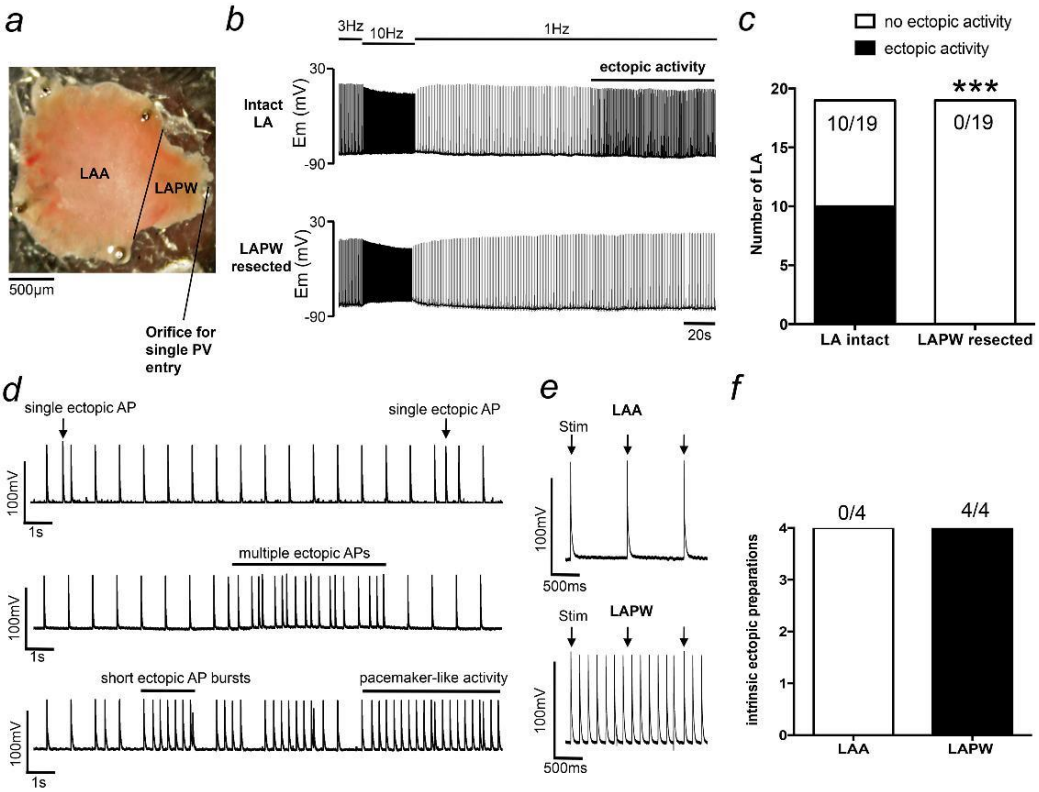

Fig 1. Spontaneous left atrial (LA) ectopy is dependent on intrinsic triggered activity generated in the left atrial posterior wall (LAPW). (a) Light field image of the murine LA showing the anatomical position of the left atrial appendage (LAA) and the LAPW. (b) Example intracellular recordings taken from the same LA with the LAPW attached (intact LA) and after the LAPW has been removed (resected). Ectopic action potentials are abolished following LAPW resection. (c) Number of LA that developed spontaneous ectopic activity before and after LAPW resection. ***denotes P<0.001, Fisher's exact test, N = 19 LA. (d) Example traces demonstrating different types of ectopic activity. (e) Direct recordings made from the LAA (upper) and LAPW (lower) following LAPW resection. Only the LAPW displays intrinsic ectopic activity. (f) Number of isolated LAA and LAPW preparations that display intrinsic ectopic activity.

doi:10.1371/journal.pone.0154077.g001

50APs at 12.5Hz (Fig 3A). This method allowed for sufficient AP rate adaptation and stabilisation of the AP waveform. At 10Hz, the APD was prolonged (*ca* 40%) in cells from the LAPW compared with cells from the LAA at 50, 70 and 90% repolarisation (Fig 3B & 3D). APD was also longer at 30% repolarisation measuring 4.4±0.2ms for LAA and 5.5±0.3 for LAPW cells ($P<0.01$, N = 20 LA). Furthermore, the APA and Vmax were significantly greater in LAPW cells by *ca* 10% and 20–25% respectively (Fig 3E & 3F). At 10Hz, the RMP was not different between the LAA and LAPW (Fig 3C). Interestingly, in cells from both regions the RMP did significantly depolarise during high frequency pacing (as exemplified in Fig 3A). This depolarisation was fully reversible (I.E. the RMP returned to the same value after the period of higher frequency pacing as observed before). Importantly, the magnitude of this depolarisation was

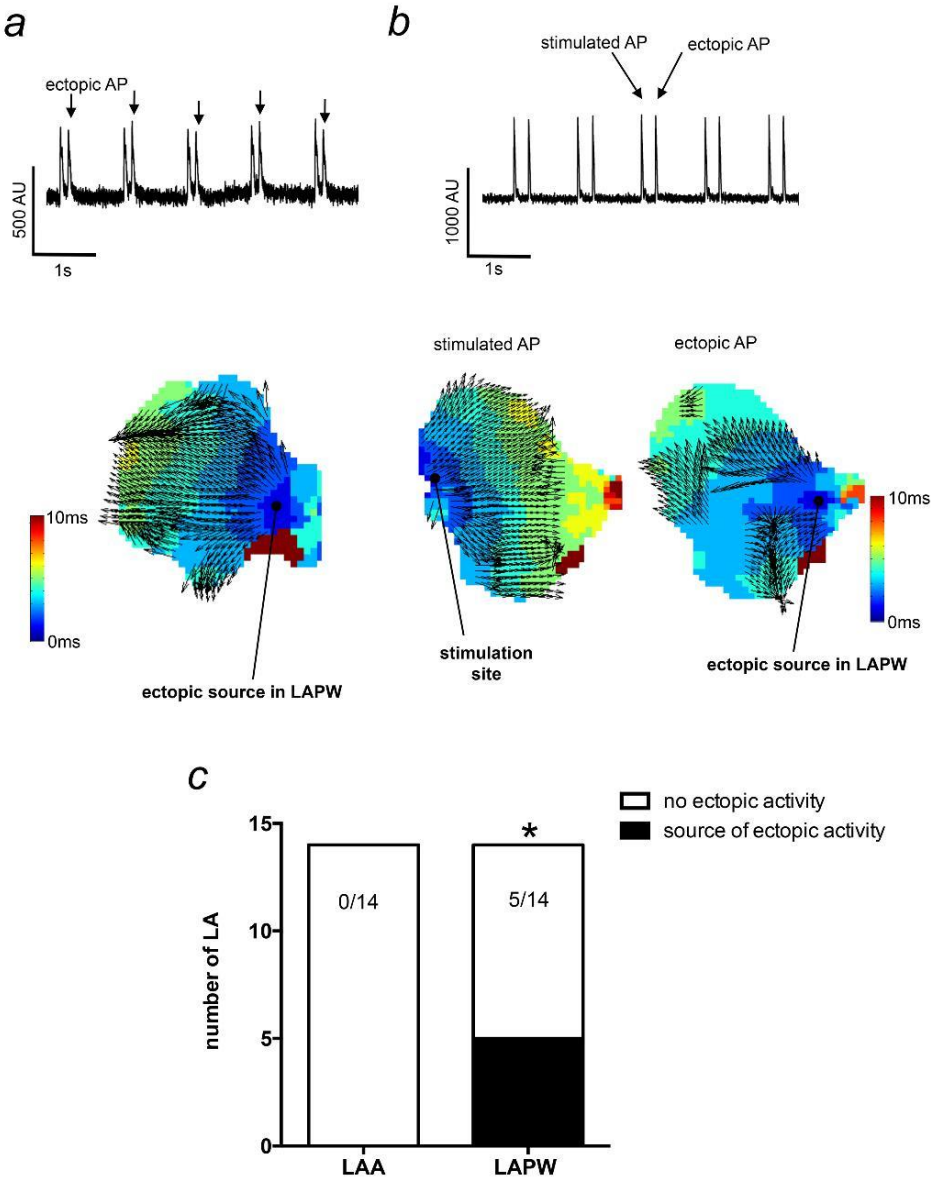
a
ectopic AP
500 AU
1s
b
stimulated AP
ectopic AP
1000 AU
1s
10ms
0ms
ectopic source in LAPW
stimulated AP
ectopic AP
stimulation site
10ms
0ms
ectopic source in LAPW
c
no ectopic activity
source of ectopic activity
number of LA
15
10
5
0
0/14
5/14
*
LAA
LAPW

Fig 2. Activation mapping of ectopic action potentials (APs) originating in the left atrial posterior wall (LAPW). (a) Raw voltage sensitive fluorescence trace demonstrating ectopic APs in the LA (upper). The corresponding activation map for the ectopic APs is shown (lower) and illustrates the source of the ectopic AP originating in the LAPW. (b) A raw voltage sensitive fluorescence trace (upper) taken from another preparation that was stimulated in the left atrial appendage (LAA). The stimulated AP activation map originates from the LAA stimulation site (lower left), whilst the ectopic AP originates in the LAPW (lower right). Thus, ectopy is not dependent on close proximity to the stimulus electrode. (c) Number of LA that developed spontaneous ectopic activity with the source in the LAA or LAPW. *denotes P<0.05, Fisher's exact test, N = 14 LA.

doi:10.1371/journal.pone.0154077.g002

the same for each region, when calculated as the RMP difference between 3 and 10Hz (LAPW +5±0.5 & LAA +7±1mV, P>0.05, paired 2-tailed student's t-test). Thus, the enhanced ectopic activity in the LAPW observed in the earlier experiments was probably not the consequence of

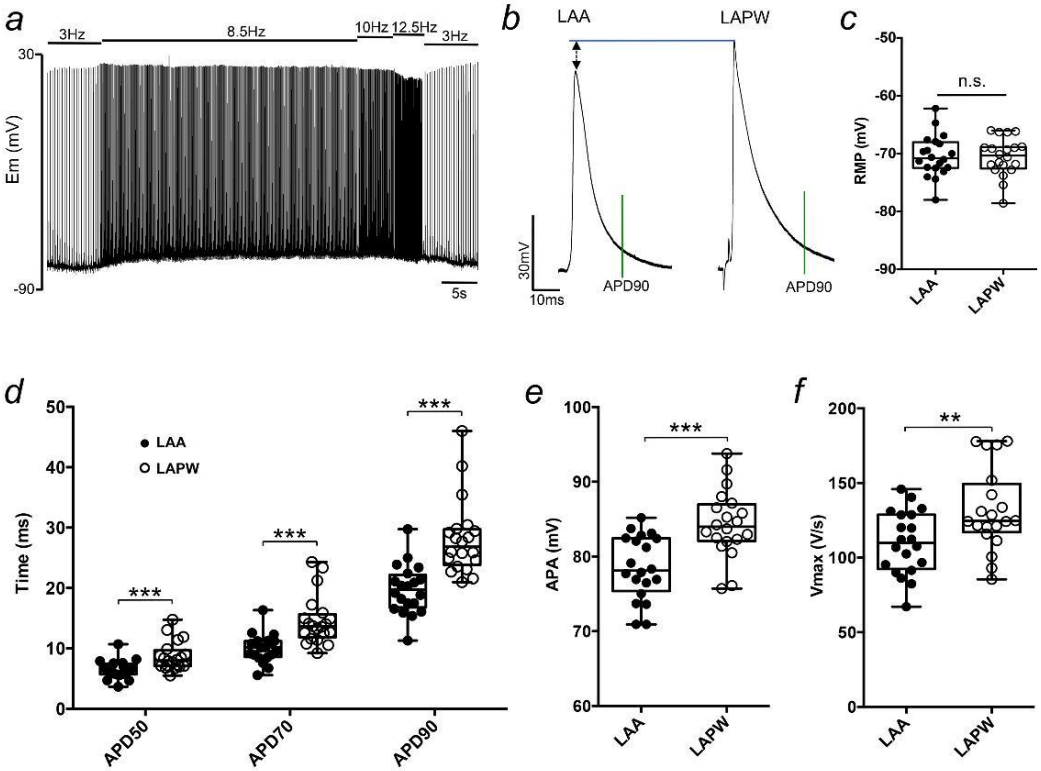

Fig 3. Action potential differences between cardiomyocytes in the left atrial posterior wall (LAPW) and left atrial appendage (LAA). (a) Example intracellular recording trace demonstrating the stimulation protocol used to achieve sufficient action potential rate adaptation. (b) Example transmembrane action potentials (TAPs) taken from the LAA and LAPW of the same left atrium. TAPs are aligned at the resting membrane potential (RMP). The green vertical line indicates action potential duration at 90% repolarisation (APD90). (c-f) Box and whisker plots and individual values comparing the RMP, APD50-90, action potential amplitude (APA) and dV/dt (Vmax), of the LAA and LAPW, at 10Hz pacing frequency. **, *** denotes P<0.01 and P<0.001, LAA v LAPW, one way repeated measures Analysis of Variance (ANOVA) with Bonferroni post hoc analysis, or paired t-test; N = 20 LA.

doi:10.1371/journal.pone.0154077.g003

a build up in extracellular K^+ brought about during the periods of higher frequency pacing. Overall however, these data do identify electrical differences between LAA and LAPW cells.

We next wanted to investigate whether the regional LA APD variation was simply confined to a single difference between LAA and LAPW cells, or if there was any further APD variation existing within these two regions. To do this, we used optical mapping to generate APD distribution maps of the entire murine LA (Fig 4A). Two example maps each for APD30 and APD70 (recorded at 10Hz) are shown in Fig 4A and demonstrate not only longer but also a more heterogeneous APD distribution within the LAPW region. To quantify this, optical action potentials (OAPs) were compared between 9 equally spaced quadratic regions covering

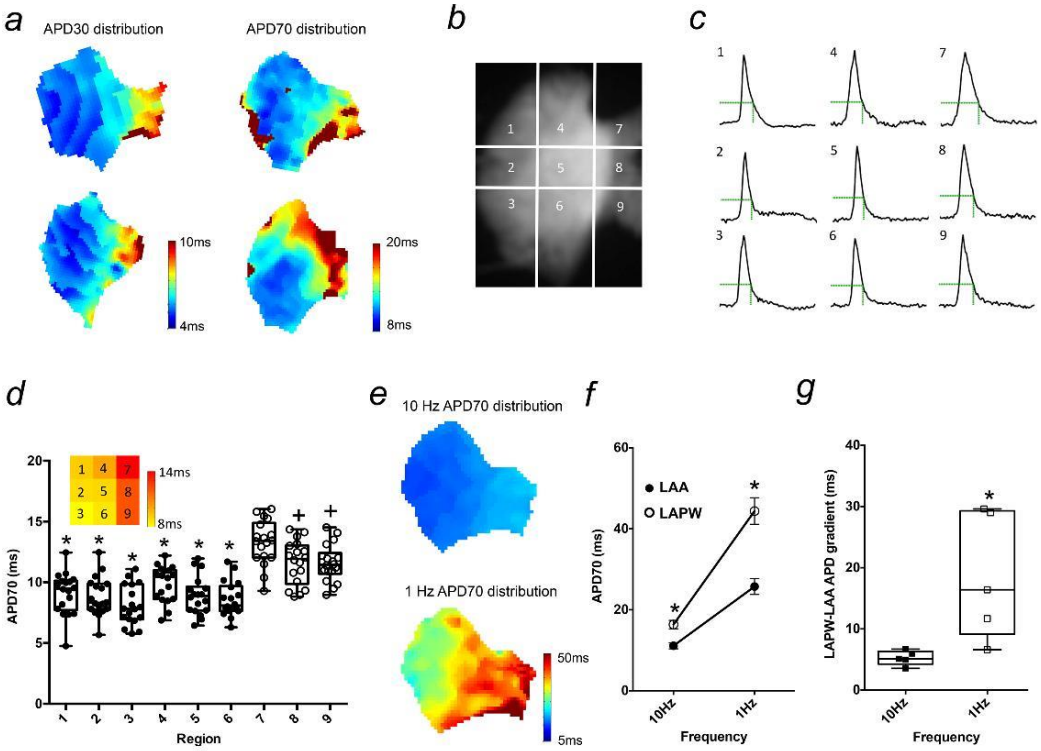

Fig 4. Action potential (AP) prolongation and heterogeneity in the left atrial posterior wall (LAPW). (a) Examples of left atrial (LA) isochronal action potential duration (APD) distribution maps at 30 and 70% repolarisation. (b) A raw fluorescence image of an LA loaded with Di-4-ANEPPS, along with the 9 region grid used for quantitative regional analysis. (c) Example optical action potentials (OAPs) recorded from the 9 different LA regions during 10Hz pacing. The green dotted line indicates APD70. (d) Box and whisker plot of APD70 values measured in each LA region. * denotes P<0.05 vs regions 7,8,9 inclusive, + P<0.05 vs region 7 only, one way repeated measures Analysis of Variance (ANOVA) with Bonferroni post hoc analysis, N = 18 LA. Inset: Heat map depicting mean APD70 values of the 9 LA regions of the LA. (e) Example isochronal APD70 distribution maps of the same LA at 10 and 1Hz (same scale). (f) Mean APD70 at 10 and 1Hz for the left atrial appendage (LAA) and left atrial posterior wall (LAPW). * denotes P<0.05 LAA v LAPW, one way repeated measures Analysis of Variance (ANOVA) with Bonferroni post hoc analysis, N = 5 LA. (g) LA gradients at 10 and 1Hz. * denotes P<0.05 LAA v LAPW, paired t-test, N = 5 LA.

doi:10.1371/journal.pone.0154077.g004

the entire superficial LA surface (Fig 4B). OAPs in the LAPW (regions 7–9) were longer than all other LA regions (1–6; Fig 4C & 4D). In addition, APD70 was significantly longer in region 7 compared with regions 8 and 9, demonstrating APD heterogeneity within the LAPW that was not apparent in the 6 regions of the LAA (Fig 4C & 4D). Thus, APs in the LAPW were longer than the LAA but also showed a more heterogeneous arrangement of APD.

Since the observed ectopic activity in previous experiments emerged at 1Hz, it was also important to evaluate the regional difference in APD at this slower pacing frequency. As expected, we observed APD lengthening in both the LAA and LAPW with a shift from 10 to 1Hz (Fig 4F). Importantly, the magnitude of rate dependent APD increase was greatly exaggerated in the LAPW (Fig 4F), such that, rather than it being diminished, the overall APD difference between the LAA and LAPW regions was markedly increased at slower pacing (Fig 4E & 4G). Collectively therefore, these data suggest that the emergence of ectopic activity in the LAPW at 1Hz was linked with a more prominent increase in APD in the cells in this region and an exaggeration of the LAA to LAPW APD difference.

Differences in ion channel gene expression between the LAA and LAPW

To gain insight into the potential molecular causes of the regional variations in AP characteristics we compared the mRNA expression of a panel of 21 ion channel using TLDA (N = 9 LA) in tissue isolated from the LAA and LAPW. Of the K^+ channel related genes, *Kcna4*, *Kcnj2*, *Kcnj3* and *Kcnj5*, that code for (K_v1.4, Kir2.1, Kir3.1 and Kir3.4 respectively) were reduced in the LAPW (Fig 5A). *Scn5a*, the most abundant Na^+ channel alpha subunit gene in the heart, showed no regional differences, while *Scn1b* and *Scn7a* mRNA expression was higher in the LAPW (Fig 5B). In addition, *Kcnk5* mRNA expression; coding for a background/leak channel TASK2 was increased in the LAPW (Fig 5C).

I_{to} and I_{KACh} are reduced in LAPW cardiomyocytes

To examine a potential cause of APD prolongation in the LAPW, measurements of whole cell voltage dependent, Ca^{2+} independent, K^+ currents were obtained from isolated LAPW and LAA cells (Fig 6A). Peak outward K^+ current density was significantly reduced in LAPW cells

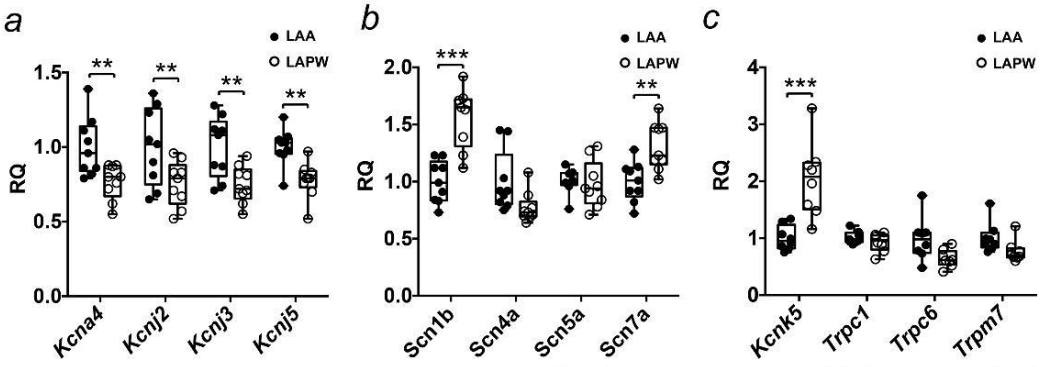

Fig 5. Ion channel expression differences between the left atrial posterior wall (LAPW) and left atrial appendage (LAA). (a-c) Comparisons of K^+, Na^+ and background/leak channel gene expression, between the LAPW and LAA, measured using Taqman Low Density Array (TDLA). Control sample was the LAA. ** and *** denote P<0.01 and P<0.001 respectively, LAA v LAPW, paired t-test, N = 9 LA.

doi:10.1371/journal.pone.0154077.g005

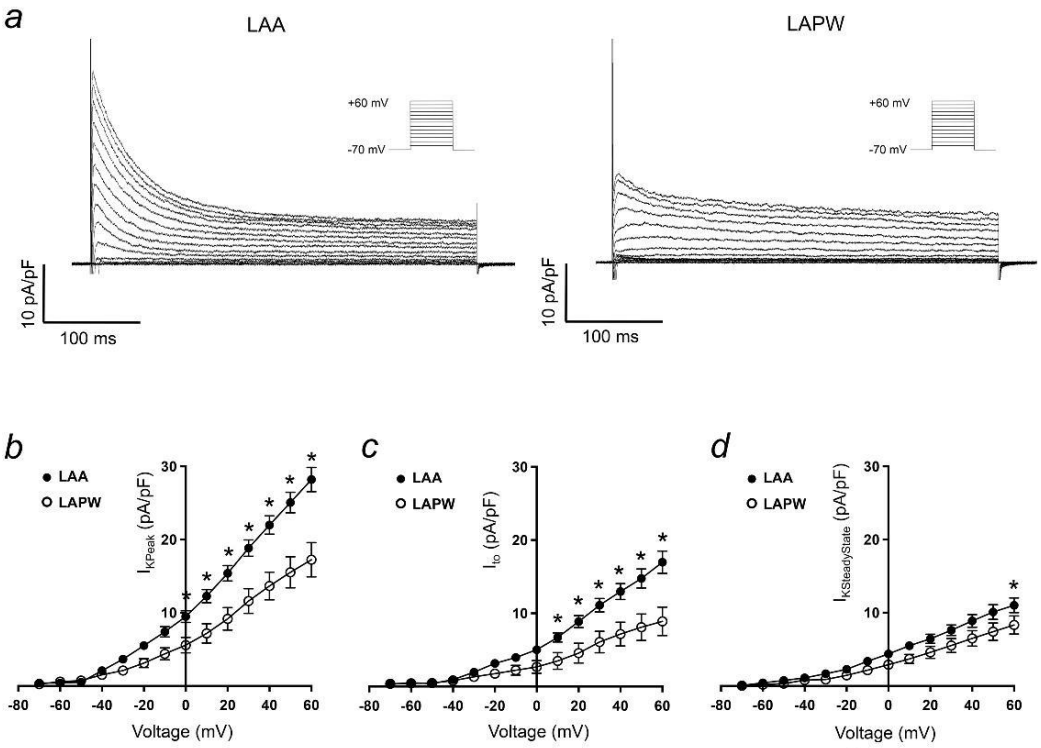

Fig 6. I_{to} reduction in cardiomyocytes isolated from the left atrial poisterior wall (LAPW). (a) Example voltage-sensitive, Ca^{2+} independent, macroscopic K^+ currents evoked in cardiomyocytes isolated from the left atrial appendage (LAA, left) and LAPW (right). Voltage protocol is shown inset. (b-d) LAA and LAPW I/V relationships for the peak outward K^+ current, I_{to} and steady state K^+ current. Data presented as mean ± SEM. * denotes P<0.05 LAA (N = 16 cells) v LAPW (N = 12 cells), two way repeated measures Analysis of Variance (ANOVA) with Bonferroni post hoc analysis.

doi:10.1371/journal.pone.0154077.g006

at all voltages positive to 0mV, for example at +20mV; LAA 15±1pA/pF (N = 16 cells) v LAPW 9±1.5pA/pF (N = 12 cells, P<0.05, Fig 6B). I_{to}, calculated as the difference between peak and steady state K^+ at 22±0.5°C [9,10], was reduced in LAPW cells, at all voltages positive to +10mV (Fig 6C). Since I_{to}, is an important determinant of atrial repolarisation rate, a marked reduction in the LAPW cells is a good candidate for the observed increase in APD and is consistent with the reduction in *Kcna4* expression. The slowly inactivating/steady state K^+ current was more similar between the two cell populations, but did show a consistent decrease in LAPW cells, although this was only statistically significant at +60mV (LAA 11±1pA/pF, N = 16 cells v LAPW 8±1pA/pF, N = 12 cells, P<0.05, Fig 6C).

Given that there were observed regional differences in *Kncj2*, *Kcnj3* and *Kcnj5* expression, I_{K1} and I_{KACh} current densities were also compared between the two regions (Fig 7A). I_{K1} current density was equivalent in both LAA and LAPW (Fig 7B), consistent with there being no

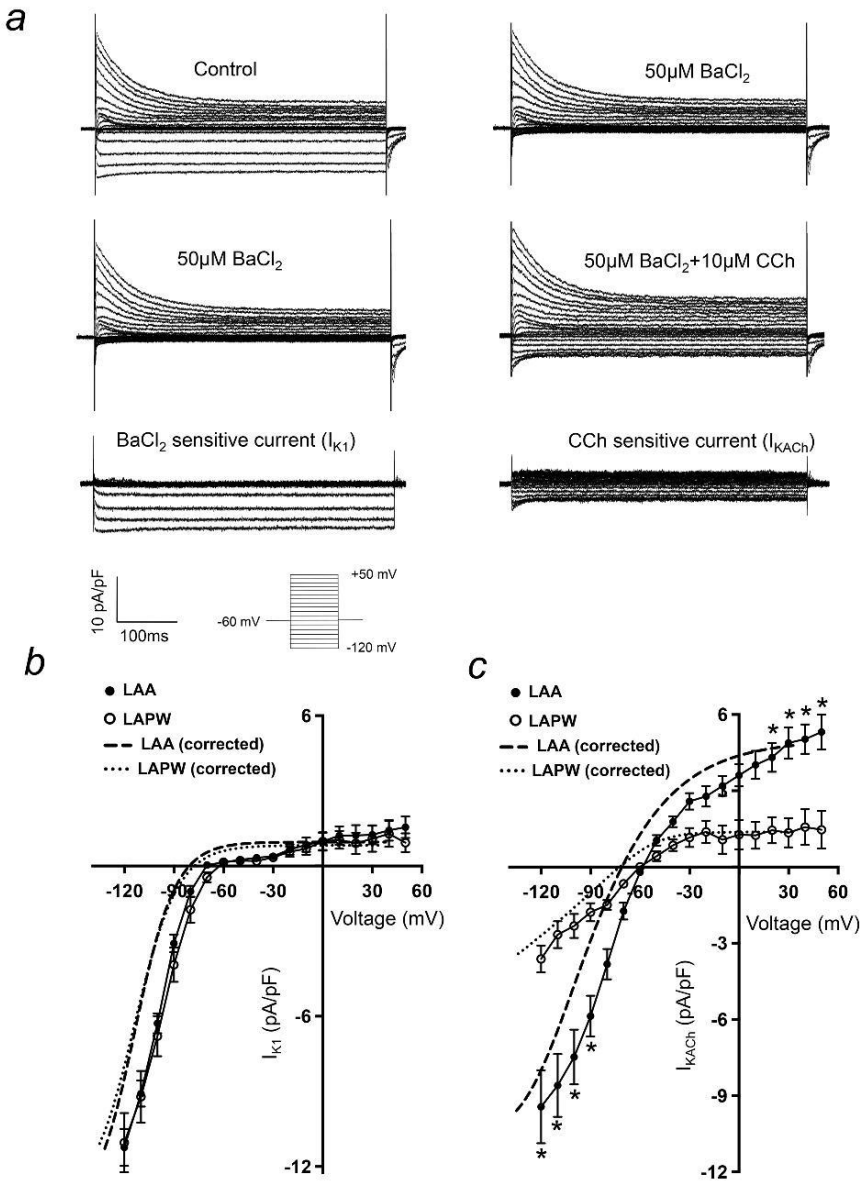
a
Control
50μM BaCl2
50μM BaCl2
50μM BaCl2+10μM CCh
BaCl2 sensitive current (IK1)
CCh sensitive current (IKACh)
10 pA/pF
100ms
+50 mV
-60 mV
-120 mV
b
LAA
LAPW
LAA (corrected)
LAPW (corrected)
Voltage (mV)
IK1 (pA/pF)
c
LAA
LAPW
LAA (corrected)
LAPW (corrected)
Voltage (mV)
IKACh (pA/pF)

Fig 7. I_{KACh} is depleted in left atrial posterior wall (LAPW) cardiomyocytes. (a) Current traces demonstrating isolation of $BaCl_2$ sensitive (I_{K1}) and CCh induced (I_{KACh}) currents in a single left atrial cardiomyocyte. Voltage protocol is shown inset. (b & c) Comparison of LAA and LAPW I/V relationships for I_{K1} and I_{KACh}. The dashed lines indicate mean best fit I_{K1} and I_{KACh} I/V curves with liquid junction potential correction, for both LAA and LAPW. Data presented as mean ± SEM. * denotes P<0.05 LAA (N = 25 cells) v LAPW (N = 17 cells), two way repeated measures Analysis of Variance (ANOVA) with Bonferroni post hoc analysis.

doi:10.1371/journal.pone.0154077.g007

change in the RMP (see Fig 3C). In contrast, I_{KACh} was significantly depressed in the LAPW, at both negative (-120 to -90mV) and positive (+20 to +60mV) test potentials (Fig 7C).

Discussion

Main findings

These data identify some regional electrical differences in the murine left atrium. The LAPW has longer atrial APDs and displays an increased APD heterogeneity compared with the LAA. Furthermore, several key ion channels genes associated with LA repolarisation are decreased in the LAPW including *Kcna4*, *Kcnj3* and *Kcnj5*, and the corresponding ion currents (I_{to} and I_{KACh}) are reduced in LAPW cardiomyocytes. The LAPW is also capable of generating spontaneous APs. These findings therefore reveal molecular and functional differences between these two regions of LA myocardium and support the idea that in addition to the pulmonary veins, the LAPW myocardium could be a source of ectopic activity.

The LAPW has distinct electrophysiological properties

Whilst regional AP variation in the right atrium has been reported in animals [10,14–16] and humans [17], little is known about regional AP variation in the LA, except for a number of studies focusing on the different electrophysiology of PV sleeve [18–21]. More clearly defining the regional electrical differences throughout the LA myocardium may be important in better understanding the different origins and mechanisms of atrial arrhythmia. Here, we demonstrate that cells in the LAPW exhibit larger APA and Vmax than the LAA, consistent with an increased rate of Na^+ influx. Since the magnitude of depolarising current is an important factor in determining conduction velocity, these findings suggest an accelerated electrical activation spread in the LAPW, consistent with previous studies reporting a fast conduction velocity through this area of myocardium [22]. The observed up-regulation in *Scn1b*, coding for the $Na_v1.5$ beta-accessory subunit, is a possible explanation for the increase in Vmax and APA. Whether the change in *Scn1b* expression is causative of the increase in arrhythmia susceptibility observed in the LAPW warrants further consideration. It has been shown that in addition to enhancing peak sodium current density, co-expression of $Na_V1.5$ with the beta 1 accessory subunit is also sufficient to cause negative voltage shifts of both activation and steady state inactivation curves [23]. It is also recognised that *Scn1b* modulates the TTX-sensitive sodium current and Ca^{2+} homeostasis in ventricular myocytes [24]. Furthermore, a higher rate of Na^+ influx may potentially confer the LAPW more susceptible to Na^+ loading (and thus Ca^{2+} loading). Thus, a detailed comparison of Na^+ and Ca^{2+} handling between the two regions could provide further insight into better understanding the increased arrhythmia susceptibility of the LAPW region.

We also found prolonged APD in the LAPW. This regional difference correlates with the lower mRNA expression level of *Kcna4* (coding for $K_v1.4$) and the significant reduction in I_{to}. Although the depressed expression of *Kcna4* is likely to cause a decrease in the slow component of I_{to}, we did not attempt to discriminate between $I_{to,fast}$ and $I_{to,slow}$. The finding of APD prolongation in the LAPW at 30% repolarisation, that was subsequently maintained throughout to 90% repolarisation, suggests at least an alteration in a current responsible for early phase

repolarisation, for which I_{to} is the best characterised. That said, there may be other currents that are altered in the LAPW and contribute significantly to APD lengthening in addition to those identified here, including I_{Kur}, I_{CaL} and I_{NaL}.

I_{to} and the fast inactivating component of I_{Kur} have some overlapping time constants, especially at 37°C [11]. Thus, voltage clamp experiments were performed at 22±0.5°C to reduce almost all fast inactivating I_{Kur} thereby allowing for I_{to} to be calculated [11]. There was also a significant reduction in the steady state outward K^+ current in the LAPW, potentially causing some additional prolongation of the APD.

Despite there being a significant decline in *Kcnj2* expression in the in LAPW, I_{K1} was preserved at all test potentials. This explains the consistency in RMP observed in the 2 regions. The reduction in expression of *Kcnj3* and *Kcnj5*, coding for Kir3.1 and Kir3.4 did associate with a marked depression in I_{KACh}. This could account for some further APD prolongation at late phase repolarisation, but whether or not I_{KACh} is constitutively active in the rodent LA remains to be clarified [25,26]. However, regional changes in Kir3.1 and Kir3.4 expression and I_{KACh} do provide a potential explanation for the regional heterogeneous responsiveness of the LA to vagal stimulation previously reported by others [6].

The prolonged APD in the LAPW is an interesting candidate for initiating the observed focal ectopic activity. The APD prolongation was consistent at both early and late phase repolarisation. It is therefore conceivable that APD prolongation could promote some L-type Ca^{2+} channel recovery during late repolarisation thereby leading to Ca^{2+} mediated after depolarisations [27] and extra-systolic activity. Interestingly, the increase in APD in response to the slower rate pacing was greatly exaggerated in LAPW cells, such that the relative APD difference between the LAA and LAPW was increased at 1Hz. This more pronounced delay in repolarisation at 1Hz would further increase the likelihood of any time dependent Ca^{2+} channel recovery and thus it is perhaps not surprising that it was at this frequency that we observed the emergence of ectopic activity within the LAPW myocardium.

Our finding of increased APD heterogeneity in the LAPW region is consistent with higher variability in effective refractory periods in the LAPW region found by others [6]. The increase in APD heterogeneity in this region may also contribute to susceptibility of the LAPW to develop and establish re-entrant circuits following the emergence of triggered activity [27,28]. Overall, our observations suggest that the LAPW, in addition to the PV sleeve, has intrinsic arrhythmogenic properties that may be amenable to specific therapy.

Embryonic origin of the LAPW–a possible explanation for the distinct electrical properties?

The development of the LAPW myocardium is subtly different to that of the LAA; the LAA forms from an out-pouching of the primary heart field, whereas the LAPW develops from the left posterior second heart field [4,5,22,29,30]. The embryological origin of the LAPW is also different to that of the PVs [4]. However, given the nature by which the PVs are incorporated into the LA [31], it is possible that some LAPW myocardium may also be derived from pulmonary myocardium, the extent of which is unknown. Given our electrophysiology findings and in view of the contrasting embryological origins, it is plausible to suggest that the cells in the LAA and LAPW may also have some different structural properties. Evaluation of the microanatomy at the two sites with emphasis on transverse tubule density or the relative density of caveolae should be considered in future investigations.

This study was done in murine LA, and confirmation of our observations in larger animals is needed. The different electrical phenotype of the LAPW cells we observed is likely to be related to its embryological derivation. In terms of the difference in LA morphology between

human and mouse, the human LA contains four separate PV connections with a significant smooth walled region between them, whilst there is only a single PV connection in the murine LA [31]. Developmentally however, the two species are relatively similar, in that the early human heart has a solitary PV connection, which is only later remodelled to "draw in" the four PVs into the LAPW [31].

Implications for initiation of AF

The current findings illustrate that the LAPW myocardium (outside of the PVs) is susceptible to developing spontaneous ectopic activity. Importantly, these findings were observed following removal of the PVs and coronary sinus from the preparation, as both have been previously been shown to generate triggered activity [32–34]. Optical mapping confirmed an origin of the observed ectopy in the LAPW. Our data suggest that the LAPW has distinct electrical properties. If confirmed in larger animals and patients, our findings provide a reasonable basis to develop antiarrhythmic drugs targeting the ion channels responsible for APD prolongation in the LAPW surrounding the PVs.

Conclusion

We show that the LAPW myocardium has an intrinsic capability for the generation of ectopic APs. In addition, there are important electrophysiological differences between the LAPW, originating from the second heart field, and LAA originating from the primary heart field. Prolonged APD, increased APD heterogeneity, reductions in I_{to} and I_{KACh} and differential mRNA expression of ion channel genes associated with AF are possible contributors to the arrhythmogenicity of the LAPW. Our findings will inform further studies characterising the specific role of the LAPW for the genesis, recurrence, and future treatment of AF.

Acknowledgments

We thank Nashitha Kabir for excellent technical assistance. T.Y.Y. held a PSIBS studentship. This work was supported by European Union (EUTRAF 251057), (CATCH ME 633193), British Heart Foundation (FS/13/43/30324), and Leducq Foundation.S.K. was supported by a Boehringer Ingelheim Fonds MD student fellowship.

Author Contributions

Conceived and designed the experiments: APH TYY LF PK. Performed the experiments: APH TYY ST PP SO. Analyzed the data: APH TYY ST PP SK. Contributed reagents/materials/analysis tools: PK LF NAB. Wrote the paper: APH TYY ST FS KLB DP NAB LF PK.

References

1. Sanders P, Berenfeld O, Hocini MZ, Jais P, Vaidyanathan R, et al. (2005) Spectral analysis identifies sites of high-frequency activity maintaining atrial fibrillation in humans. Circulation 112: 789–797. PMID: 16061740
2. Jalife J, Berenfeld O, Mansour M (2002) Mother rotors and fibrillatory conduction: a mechanism of atrial fibrillation. Cardiovascular Research 54: 204–216. PMID: 12062327
3. Ridler ME, Lee M, McQueen D, Peskin C, Vigmond E (2011) Arrhythmogenic Consequences of Action Potential Duration Gradients in the Atria. Canadian Journal of Cardiology 27: 112–119. doi: 10.1016/j.cjca.2010.12.002 PMID: 21329870
4. Dominguez JN, Meilhac SM, Bland YS, Buckingham ME, Brown NA (2012) Asymmetric fate of the posterior part of the second heart field results in unexpected left/right contributions to both poles of the heart. Circ Res 111: 1323–1335. doi: 10.1161/CIRCRESAHA.112.271247 PMID: 22955731

5. Mosimann C, Panakova D, Werdich AA, Musso G, Burger A, et al. (2015) Chamber identity programs drive early functional partitioning of the heart. Nat Commun 6: 8146. doi: 10.1038/ncomms9146 PMID: 26306682
6. Arora R, Ng J, Ulphani J, Mylonas I, Subacius H, et al. (2007) Unique autonomic profile of the pulmonary veins and posterior left atrium. Journal of the American College of Cardiology 49: 1340–1348. PMID: 17394967
7. Walters TE, Lee G, Spence S, Larobina M, Atkinson V, et al. (2014) Acute Atrial Stretch Results in Conduction Slowing and Complex Signals at the Pulmonary Vein to Left Atrial Junction Insights Into the Mechanism of Pulmonary Vein Arrhythmogenesis. Circulation-Arrhythmia and Electrophysiology 7: 1189–U1317. doi: 10.1161/CIRCEP.114.001894 PMID: 25516579
8. Yu TY, Syeda F, Holmes AP, Osborne B, Dehghani H, et al. (2014) An automated system using spatial oversampling for optical mapping in murine atria. Development and validation with monophasic and transmembrane action potentials. Progress in Biophysics & Molecular Biology 115: 340–348.
9. Li DS, Zhang LM, Kneller J, Nattel S (2001) Potential ionic mechanism for repolarization differences between canine right and left atrium. Circulation Research 88: 1168–1175. PMID: 11397783
10. Feng JL, Yue LX, Wang ZG, Nattel S (1998) Ionic mechanisms of regional action potential heterogeneity in the canine right atrium. Circulation Research 83: 541–551. PMID: 9734477
11. Ravens U, Wettwer E (2011) Ultra-rapid delayed rectifier channels: molecular basis and therapeutic implications. Cardiovascular Research 89: 776–785. doi: 10.1093/cvr/cvq398 PMID: 21159668
12. Yamada M (2002) The role of muscarinic K+ channels in the negative chronotropic effect of a muscarinic agonist. Journal of Pharmacology and Experimental Therapeutics 300: 681–687. PMID: 11805233
13. Lomax AE, Rose RA, Giles WR (2003) Electrophysiological evidence for a gradient of G protein-gated K+ current in adult mouse atria. British Journal of Pharmacology 140: 576–584. PMID: 14522844
14. Spach MS, Dolber PC, Heidlage JF (1989) Interaction of inhomogeneities of repolarization with anisotropic propagation in dog atria—a mechanism for both preventing and initiating reentry. Circulation Research 65: 1612–1631. PMID: 2582593
15. Burashnikov A, Mannava S, Antzelevitch C (2004) Transmembrane action potential heterogeneity in the canine isolated arterially perfused right atrium: effect of I-Kr and I-Kur/I-to block. American Journal of Physiology-Heart and Circulatory Physiology 286: H2393–H2400. PMID: 15148061
16. Nygren A, Lomax AE, Giles WR (2004) Heterogeneity of action potential durations in isolated mouse left and right atria recorded using voltage-sensitive dye mapping. American Journal of Physiology-Heart and Circulatory Physiology 287: H2634–H2643. PMID: 15271666
17. Gong DM, Zhang Y, Cai BZ, Meng QX, Jiang SL, et al. (2008) Characterization and comparison of Na+, K+ and Ca2+ currents between myocytes from human atrial right appendage and atrial septum. Cellular Physiology and Biochemistry 21: 385–394. doi: 10.1159/000129631 PMID: 18453746
18. Egorov YV, Kuz'min VS, Glukhov AV, Rosenshtraukh LV (2015) Electrophysiological Characteristics, Rhythm, Disturbances and Conduction Discontinuities Under Autonomic Stimulation in the Rat Pulmonary Vein Myocardium. Journal of Cardiovascular Electrophysiology 26: 1130–1139. doi: 10.1111/jce.12738 PMID: 26086390
19. Miyauchi Y, Hayashi H, Miyauchi M, Okuyama Y, Mandel WJ, et al. (2005) Heterogeneous pulmonary vein myocardial cell repolarization implications for reentry and triggered activity. Heart Rhythm 2: 1339–1345. PMID: 16360087
20. Kumagai K, Ogawa M, Noguchi H, Yasuda T, Nakashima H, et al. (2004) Electrophysiologic properties of pulmonary veins assessed using a multielectrode basket catheter. Journal of the American College of Cardiology 43: 2281–2289. PMID: 15193694
21. Patterson E, Lazzara R, Szabo B, Liu H, Tang D, et al. (2006) Sodium-calcium exchange initiated by the Ca2+ transient—An arrhythmia trigger within pulmonary veins. Journal of the American College of Cardiology 47: 1196–1206. PMID: 16545652
22. Mommersteeg MT, Brown NA, Prall OW, de Gier-de Vries C, Harvey RP, et al. (2007) Pitx2c and Nkx2-5 are required for the formation and identity of the pulmonary myocardium. Circ Res 101: 902–909. PMID: 17823370
23. Yuan L, Koivumaki JT, Liang B, Lorentzen LG, Tang CY, et al. (2014) Investigations of the Na-v beta 1b sodium channel subunit in human ventricle; functional characterization of the H162P Brugada syndrome mutant. American Journal of Physiology-Heart and Circulatory Physiology 306: H1204–H1212. doi: 10.1152/ajpheart.00405.2013 PMID: 24561865
24. Lin XM, O'Malley H, Chen CL, Auerbach D, Foster M, et al. (2015) Scn1b deletion leads to increased tetrodotoxin-sensitive sodium current, altered intracellular calcium homeostasis and arrhythmias in murine hearts. Journal of Physiology-London 593: 1389–1407.

25. Bingen BO, Neshati Z, Askar SF, Kazbanov IV, Ypey DL, et al. (2013) Atrium-specific Kir3.x determines inducibility, dynamics, and termination of fibrillation by regulating restitution-driven alternans. Circulation 128: 2732–2744. doi: 10.1161/CIRCULATIONAHA.113.005019 PMID: 24065610

26. Lomax AE, Rose RA, Giles WR (2003) Electrophysiological evidence for a gradient of G protein-gated K+ current in adult mouse atria. Br J Pharmacol 140: 576–584. PMID: 14522844

27. Wakili R, Voigt N, Kaab S, Dobrev D, Nattel S (2011) Recent advances in the molecular pathophysiology of atrial fibrillation. J Clin Invest 121: 2955–2968. doi: 10.1172/JCI46315 PMID: 21804195

28. Vigmond EJ, Tsoi V, Kuo S, Arevalo H, Kneller J, et al. (2004) The effect of vagally induced dispersion of action potential duration on atrial arrhythmogenesis. Heart Rhythm 1: 334–344. PMID: 15851180

29. Al-Saady NM, Obel OA, Camm AJ (1999) Left atrial appendage: structure, function, and role in thromboembolism. Heart 82: 547–554. PMID: 10525506

30. Galli D, Dominguez JN, Zaffran S, Munk A, Brown NA, et al. (2008) Atrial myocardium derives from the posterior region of the second heart field, which acquires left-right identity as Pitx2c is expressed. Development 135: 1157–1167. doi: 10.1242/dev.014563 PMID: 18272591

31. Webb S, Kanani M, Anderson RH, Richardson MK, Brown NA (2001) Development of the human pulmonary vein and its incorporation in the morphologically left atrium. Cardiol Young 11: 632–642. PMID: 11813915

32. Haissaguerre M, Jais P, Shah DC, Takahashi A, Hocini M, et al. (1998) Spontaneous initiation of atrial fibrillation by ectopic beats originating in the pulmonary veins. N Engl J Med 339: 659–666. PMID: 9725923

33. Lin WS, Tai CT, Hsieh MH, Tsai CF, Lin YK, et al. (2003) Catheter ablation of paroxysmal atrial fibrillation initiated by non-pulmonary vein ectopy. Circulation 107: 3176–3183. PMID: 12821558

34. Sanders P, Jais P, Hocini M, Haissaguerre M (2004) Electrical disconnection of the coronary sinus by radiofrequency catheter ablation to isolate a trigger of atrial fibrillation. Journal of Cardiovascular Electrophysiology 15: 364–368. PMID: 15030429

Appendix 3 - Optical mapping design for murine atrial electrophysiology.

COMPUTER METHODS IN BIOMECHANICS AND BIOMEDICAL ENGINEERING: IMAGING & VISUALIZATION, 2015
http://dx.doi.org/10.1080/21681163.2015.1081079

Taylor & Francis
Taylor & Francis Group

Optical mapping design for murine atrial electrophysiology

T.Y. Yu[a], H. Dehghani[b], K. L. Brain[c], F. Syeda[d], A. P. Holmes[d], P. Kirchhof[d,e,f] and L. Fabritz[d,e,f]

[a]Physical Sciences of Imaging in the Biomedical Sciences (PSIBS), School of Chemistry, College of Engineering and Physical Sciences, University of Birmingham, Birmingham, UK; [b]School of Computer Science, College of Engineering and Physical Sciences, University of Birmingham, Birmingham, UK; [c]Pharmacology and Therapeutics, School of Clinical and Experimental Medicine, College of Medical and Dental Sciences, University of Birmingham, Birmingham, UK; [d]Institute of Cardiovascular Sciences, College of Medical and Dental Sciences, University of Birmingham, Birmingham, UK; [e]Department of Cardiology and Angiology, University Hospital Münster, Münster, Germany; [f]Department of Cardiology, University Hospitals Birmingham NHS Foundation Trust, Birmingham, UK

ABSTRACT

Optical mapping is an important tool for assessment of cardiac electrophysiology. We demonstrate a system for quantification and automatic measurement of electrophysiological parameters in isolated cardiac tissue. The system makes use of voltage sensitive fluorescent dyes. These shift in wavelength in response to millivolt changes in potential across cell membranes located on the left atrium. Automated analysis of the pixel-wise measurements yields information on action potential durations and isochronal maps allowing for high throughput of data analysis. The algorithms that we propose reliably describe activation sequences and allow for quantification of conduction velocities.

ARTICLE HISTORY
Received 13 November 2014
Accepted 5 August 2015

KEYWORDS
Optical mapping; cardiovascular disease; voltage imaging; electrophysiology; action potential duration

CONTACT T.Y. Yu tyy608@bham.ac.uk

Appendix 4 - An automated system using spatial oversampling for optical mapping in murine atria. Development and validation with monophasic and transmembrane action potentials.

Progress in Biophysics and Molecular Biology 115 (2014) 340–348

Contents lists available at ScienceDirect

Progress in Biophysics and Molecular Biology

journal homepage: www.elsevier.com/locate/pbiomolbio

Original research

An automated system using spatial oversampling for optical mapping in murine atria. Development and validation with monophasic and transmembrane action potentials

Ting Yue Yu [a, b], Fahima Syeda [a], Andrew P. Holmes [a], Benjamin Osborne [a], Hamid Dehghani [b, c], Keith L. Brain [d], Paulus Kirchhof [a], Larissa Fabritz [a, *]

[a] Centre for Cardiovascular Sciences, School of Clinical and Experimental Medicine, College of Medical and Dental Sciences, University of Birmingham, UK
[b] Doctoral Training Centre for Physical Sciences of Imaging in the Biomedical Sciences (PSIBS), University of Birmingham, UK
[c] School of Computer Science, College of Engineering and Physical Sciences, University of Birmingham, UK
[d] School of Clinical and Experimental Medicine, College of Medical and Dental Sciences, University of Birmingham, UK

ARTICLE INFO

Article history:
Available online 15 August 2014

Keywords:
Optical mapping
Murine model
Isolated atrium
Conduction velocity
Atrial action potential duration
Atrial fibrillation

ABSTRACT

We developed and validated a new optical mapping system for quantification of electrical activation and repolarisation in murine atria. The system makes use of a novel 2nd generation complementary metal-oxide-semiconductor (CMOS) camera with deliberate oversampling to allow both assessment of electrical activation with high spatial and temporal resolution (128 × 2048 pixels) and reliable assessment of atrial murine repolarisation using post-processing of signals. Optical recordings were taken from isolated, superfused and electrically stimulated murine left atria. The system reliably describes activation sequences, identifies areas of functional block, and allows quantification of conduction velocities and vectors. Furthermore, the system records murine atrial action potentials with comparable duration to both monophasic and transmembrane action potentials in murine atria.

1. Introduction

Atrial fibrillation is the most common sustained arrhythmia in man and a common cause of stroke and cardiac deaths. Although good progress has been made in the characterisation of factors that cause AF (Camm et al., 2012a,b; Schotten et al., 2011; Wakili et al., 2011), there is still an unmet need for better therapies to prevent incident and recurrent AF (Camm et al., 2012a,b; Kirchhof et al., 2013). Unravelling the mechanisms conveying the genetic basis of atrial fibrillation (Benjamin et al., 2009; Ellinor et al., 2012; Gudbjartsson et al., 2007) is a promising and relatively new avenue to novel preventive and therapeutic targets. Genetically altered murine models are popular tools for the study of molecular disease mechanisms, including of atrial fibrillation. Such models allow the characterisation of the functional and molecular consequences of defined genetic alterations, thereby allowing us to identify arrhythmia mechanisms attributable to such modifications. This type of research extends the association studies in patients and populations which are limited by comorbidities, ethical restraints and low sample availability (Riley et al., 2012). The small size of murine hearts, particularly the atria, poses a challenge for detailed electrophysiological assessment, and especially for high density mapping of electrical activation and repolarisation. Evolving knowledge of existence of regional heterogeneities calls for the development of a technique with high spatial resolution, so that the extent of heterogeneity can be identified (Di Diego et al., 2013; Waldeyer et al., 2009). Additionally, the high frequency and fast repolarisation properties of the murine atrium necessitate high temporal resolution.

Optical mapping is an established technique for high spatial and temporal resolution non-contact investigation of electrical excitability of cardiac cells, tissues and whole organs (Efimov et al., 1994; Lee et al., 2011; Rohr and Salzberg, 1994; Salama et al., 1987; Wu et al., 2001). Optical mapping of cardiac tissue uses voltage-sensitive dyes to visualise action potentials as changes in

Abbreviations: ADC, Analogue to digital converter; AF, Atrial fibrillation; APD, Action potential duration; CL, Cycle length; CMOS, Complementary metal-oxide-semiconductor; CV, Conduction velocity; LA, Left atrium; LED, Light emitting diode; MAP, Monophasic action potential; OAP, Optical action potential; SEM, Standard error of the mean; TAP, Transmembrane action potential; TIFF, Tagged image file format.

* Corresponding author. Centre for Cardiovascular Sciences, School of Clinical and Experimental Medicine, College of Medical and Dental Sciences, University of Birmingham, Edgbaston, Birmingham B15 2TT, UK. Tel.: +44 (0)121 414 6938.
E-mail address: L.Fabritz@bham.ac.uk (L. Fabritz).

http://dx.doi.org/10.1016/j.pbiomolbio.2014.07.012

fluorescence, as an index for changes in transmembrane potentials (Salzberg et al., 1973). Numerous improvements have been made to overcome technical difficulties associated with optical mapping of cardiac tissue including removal of contraction artefacts in large and small vertebrates by using uncouplers (Dou et al., 2007; Fedorov et al., 2007; Jou et al., 2010; Wu et al., 1998) and sensitive optical dyes (Efimov and Fahy, 1997; Ehrenberg et al., 1987; Rohr and Salzberg, 1994). As such, this technique has provided important insights into the mechanisms of atrial arrhythmias in murine models (Arora et al., 2003; Blana et al., 2010; Kirchhof et al., 2011a,b). The complex electrophysiology of atrial fibrillation (Eckstein et al., 2013; Kirchhof et al., 2011a,b; Verheule and Tuyls, 2013), renders a higher spatial resolution of murine atrial activation and repolarisation mapping technology desirable. This allows us to pinpoint further, the regional origins and patterns of AF activation (Mandapati et al., 2000). Several foci of AF activation have already been identified in genetically altered mouse models (Benes et al., 2014; Faggioni et al., 2014). However, even with the best available systems, the need for higher spatial and temporal resolution combined with the small signal amplitude generated in the thin atrial murine tissue still poses technical challenges.

To further improve temporal and spatial resolution in cardiac optical imaging of murine atrial tissue, a second-generation complementary metal-oxide-semiconductor (CMOS) camera is utilised and novel algorithms developed to record and analyse atrial activation and repolarisation in the isolated, perfused murine atrium at high spatial resolution. A spatial oversampling technique is implemented to generate high-resolution activation maps at the same time as high quality repolarisation information. The algorithms used to generate isochronal maps and to perform APD measurements are largely automated to limit user bias and to facilitate high throughput analysis. Atrial optical action potentials are compared with epicardial atrial monophasic action potentials and atrial microelectrode transmembrane action potentials from isolated hearts to validate the findings.

2. Methods

2.1. Heart isolation

All surgical procedures were performed according to the Animals (Scientific Procedures) Act, 1986 and were approved by the Home Office and the local authorities. Hearts were rapidly excised by thoracotomy from WT adult mice (3–7 months old), on a 129/Sv or MF1 background, under terminal anaesthesia (200 mg/kg pentobarbital sodium) administered by intraperitoneal injection.

2.2. High resolution mapping using novel methods of automated data processing

Following isolation, hearts were mounted on a vertical Langendorff apparatus (Hugo Sachs, Germany) and the aorta retrogradely perfused with a standard bicarbonate buffered Krebs–Henseleit solution (see below), containing the voltage sensitive dye Di-4-Anepps (50 μM; Biotium, California, USA) and the excitation-contraction uncoupler blebbistatin (5 μM; Cayman Chemical, Michigan, USA), a well-characterised substance used for optical mapping (Fedorov et al., 2007; Kirchhof et al., 2011a,b). The dye was stored in 25 μl aliquots of 5 mg/ml. For each experiment an aliquot was mixed with 1 ml of Krebs solution and injected through a bolus port in the Langendorff system over a period of 5 min. The flow rate of the Krebs solution was kept at 4 ml/min and at 36 °C. After 5 min of infusion, the atria were dissected and placed in a superfusion chamber for image acquisition. A summary of the system set-up used for image acquisition is shown in Fig. 1. Preparations were continuously superfused with Krebs and blebbistatin to reduce contraction and paced incrementally (300 ms–80 ms paced cycle length) via platinum electrodes placed in the tissue bath at twice the diastolic voltage threshold at 2 ms pulse width. Stimuli were generated using an isolated constant voltage stimulator (Digitimer, UK) driven by an analogue to digital converter with spike2 software (Cambridge Electronic Design, UK). The atria were field illuminated by two twin LEDs at 530 nm (Cairn Research, UK). These were required to provide sufficient field illumination from all angles. A lens with a high numerical aperture (Schneider Kreuznach Xenon 0.95/25, NA = 0.52) was used to collect as many photons as possible. Wide field macroscopic images of emitted fluorescence (630 nm) were captured at a sampling frequency of 1 or 2 kHz using a novel, high speed, high resolution camera (128 × 2048 pixels, single pixel area: 6.5 μm by 6.5 μm, ORCA flash 4.0; Hamamatsu, Japan, Figs. 1 and 2). The camera reads the data from the centre of the sensor. Temporal resolution can be increased with reduced spatial resolution only in the vertical direction, as a trade-off. This allows for the full window of the sensor to be used in the horizontal direction. To reduce the read noise of the camera, the 4 × 4 binning option was used (Fig. 2B and C).

Images were extracted and collated using WinFluor V3.4.9 (Dr John Dempster, University of Strathclyde, UK) so that the fluorescence intensity from a specific region of interest (4 × 4 pixels) could be viewed as a single continuous waveform. This permitted the identification and monitoring of a greater number of optical action potentials (OAPs) across the entire surface of the mouse atrium at high spatial resolution. In addition, selected images could be exported into uncompressed Tagged image file format (TIFF) for the generation of whole atrial isochronal activation maps.

For the analysis of OAPs and generation of isochronal activation maps, data were automatically processed using custom made algorithms produced in MATLAB. For measurements of action potential duration (APD), an initial sign change was necessary as the emitted fluorescence intensity is inversely proportional to transmembrane voltage (Loew, 1996). Baseline subtraction was achieved by applying a 'linear top hat filter' to remove any fluorescence drift. At each cycle length, a maximum of 25 action potentials were averaged to calculate the mean action potential waveform for a selected region of interest (Fig. 1B). Previously we found that 25AP signals were sufficient to measure APD reliably. Fewer than 25 APs could be used, but this was dependent on the signal quality from each experiment. For example, a very good signal would require less averaging, but to keep the algorithm consistent 25 signals were routinely used. The baseline (100% repolarisation) was determined as the mean fluorescence signal recorded over 10 ms prior to depolarisation. The point of activation was defined as the peak rate of change (dF/dtmax) and APD30, 50 and 70, were evaluated by measuring the time from dF/dtmax to 30%, 50% and 70% repolarisation respectively (Fig. 1B). For each APD, the value usually falls between sampling time points, 1 ms apart for 1000 fps, 0.5 ms for a 2000 fps. The repolarisation time was estimated by connecting these two closest sampling time points above and below with straight lines. A simple linear equation can be used to determine the time for each APD.

Isochronal activation maps were produced after initially cropping the exported image stack to isolate the region of interest; this was the only step that required user input. Fluorescence intensity from every pixel was automatically analysed in the z (time) axis. The background was removed and signals were smoothed and then filtered using a Savitzky–Golay filter, a moving average filter which preserves signal morphology (Bachtel et al., 2011; Savitzky and Golay, 1964). Signals were differentiated to detect the time of activation, which was repeated until a 2D array (image) was compiled with each element (pixel) corresponding to a specific

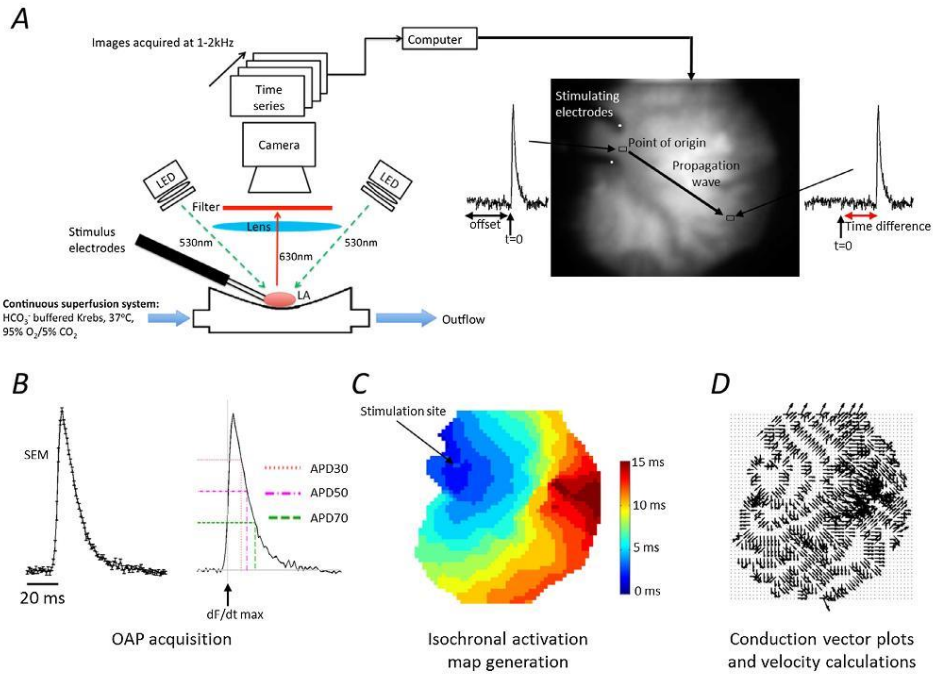

Fig. 1. Summary of the high resolution optical mapping system with automated analysis. **A** represents the schematic of the optical mapping system. The LA samples were excited by four 530 nm LEDs, and filtered through a high NA objective and a 630 nm long pass filter. The electrodes were used for programmed stimulation at 300–80 ms pacing cycle lengths. Images were captured at a frame rate of 1000–2000 per second and recorded on a desktop computer for analysis using Winfluor software. The images above were recorded at 1000 frames per second. The electrodes can be seen on the upper left of the atrial image with the line of activation indicated by the black arrow. The action potentials indicate the time at which the signals have reached that region. **B** This displays the outcome of an averaged signal taken from the left atrium stimulated at 100 ms CL (with standard errors. Adjacent, is the same signal with its action potential durations labelled at APD30, 50 and 70 with the start of activation indicated by dF/dtmax shown. **C** The isochronal map is a colour scale of the time taken to activate at each pixel, from the same atrium as above at 100 ms CL. The time increases in the direction opposite to where the electrodes are placed. **D** Conduction vectors that indicate the direction of the wave are generated from the activation map.

time. The origin of the activation wave was offset to zero ($t = 0$; Fig. 1C). All other time values in relation to the origin could be calculated (Fig. 1C) and then presented in the form of an isochronal map.

For assessment of conduction velocities, the pixel size was measured to be 71 μm and as each pixel represents a time value, the velocity can be measured. The isochronal maps were generated as mentioned above, with each time zone represented with a different colour. From these maps the contours of the wave of propagation were easily interpreted. To ensure accuracy, measurements were always made perpendicular to the wavefront. Two points across several 'time zones', usually a minimum of three, were selected. From the distance and the difference in time between those points, velocity was calculated in cm/second.

2.3. Monophasic action potentials

The new optical mapping system was validated by comparing activation and repolarisation time with two established methods, monophasic action potentials (MAP) (Blana et al., 2010; Kirchhof et al., 2011a,b), and transmembrane action potentials obtained in the same atrial preparations. Briefly, for MAP acquisition, published techniques (Blana et al., 2010; Kirchhof et al., 2011a,b; Knollmann et al., 2001) were employed and MAP recordings were obtained in the intact, perfused heart immediately prior to dissecting the atria for optical mapping. Whole hearts were cannulated and mounted on a vertical Langendorff apparatus (Hugo Sachs, Germany) and retrogradely perfused with standard bicarbonate buffered Krebs–Henseleit solution at 36–37 °C, at constant perfusion pressure (100 ± 5 mmHg) and coronary flow (4 ± 0.5 ml/min). A 2.0 French octapolar mouse electrophysiological catheter with electrodes sized 0.5 mm and spaced at 0.5 mm (CIB'ER MOUSE, NuMED, LLC., N.Y., USA) was inserted into the right atrium for pacing (120 ms–80 ms, 2 ms pulse width). Stable left atrial MAP recordings were obtained using a miniaturised MAP catheter mounted on spring-loaded electrode holder. Voltage signals were amplified, digitised and viewed on a PC loaded with iox2 software (EMKA, France). Measurements of action potential duration (APD) and inter-atrial activation times were acquired using algorithms generated in iox2.

2.4. Transmembrane action potentials

Transmembrane murine atrial action potentials (TAP) were recorded as published (Lemoine et al., 2011) immediately before or after the optical mapping procedure. TAPs were recorded from

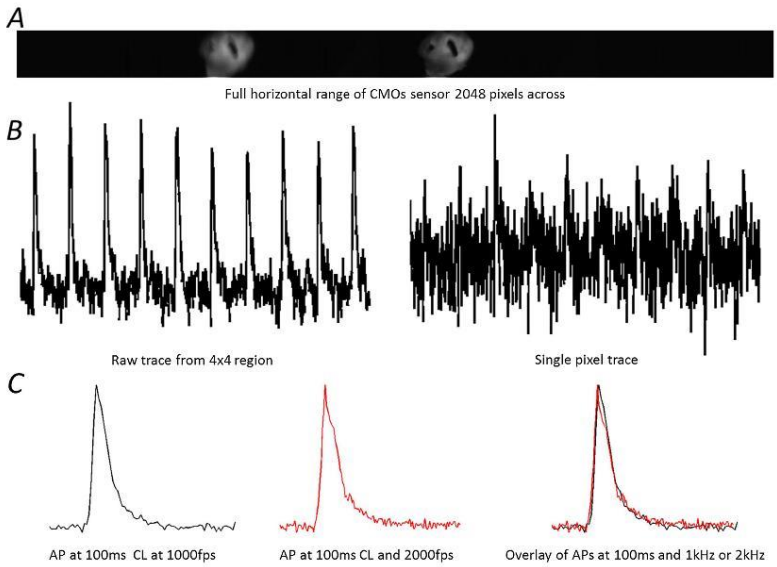

Fig. 2. Examples of raw data from different acquisition techniques. **A** Raw image of the left atria from the ORCA Flash 4.0. Two images can be seen as an image splitter from two different wavelengths focused on the single sensor. Resolution shown here is at 128 × 2048 pixels. **B** Raw traces from the left atria over a period of 1 s showing 10 action potentials. There is less noise in the region of measurement using 4 × 4 pixels (left) compared to single pixels which show very little information, with the action potentials barely visible (right). **C** Comparison of two action potential signals normalised to lie between 0 and 1 taken at 100 ms cycle length (CL) of the same atria and same region of interest but at different acquisition speeds. These signals showed very minute variation in signal as we can see in the overlay.

isolated superfused LA samples prepared as above using borosilicate glass microelectrodes (tip resistance 15–30 MΩ), filled with 3 M KCl. Voltage signals were amplified (Axoclamp 2B; Molecular Devices, USA), digitised and displayed using spike2 software (Cambridge Electronic Design, UK). The sampling frequency was 20 kHz. Preparations were paced successively (300 ms–80 ms) with platinum electrodes at twice the diastolic voltage threshold, with a minimum of 50 APs recorded at each cycle length using an isolated constant voltage stimulator (Digitimer, UK) driven by an analogue to digital converter with Spike2 software (Cambridge Electronic Design, UK). Measurements of APD and intra-atrial activation times were obtained using custom-made spike2 algorithms.

2.5. Solutions

For all experiments a standard bicarbonate buffered Krebs–Henseleit solution was used containing in mM: NaCl 118; $NaHCO_3$ 24.88; KH_2PO_4 1.18; Glucose 5.55; Na-Pyruvate 5; $MgSO_4$ 0.83; $CaCl_2$ 1.8; KCl 3.52, equilibrated with 95% O_2 and 5% CO_2 and heated to 36–37 °C. Under these conditions the pH was maintained at 7.4. For experiments with 1 μM flecainide, the drug was added to the superfusate and circulated for 15 min to reach steady state (Blana et al., 2010) before capturing images.

2.6. Data analysis

Values are expressed as mean ± standard error of mean unless otherwise stated. Statistical analysis was performed using one way Analysis of Variance (ANOVA) with Bonferroni or Dunnett's post hoc analysis where appropriate (GraphPad Prism 5.01). Significance was taken as $p < 0.05$.

3. Results

After development and optimisation of the setup, the quality of OAP recordings was sufficient for generating isochronal maps for conduction measurements from an initial 5/10 to currently 8/10 of the hearts used due to quality criteria, while basic action potential duration measurements could be acquired from all hearts. For a data set to meet the criteria for conduction measurements, the isochronal maps must show a clear direction of wavefront propagation. This allowed for the selection of two points across several 'time zones' for calculation of conduction velocity.

3.1. Optical action potentials

As for TAPs and MAPs, the optically generated action potentials were characterised by a fast depolarisation and a slower repolarisation. The baseline correction adjusted the signal allowing for OAP measurements in all preparations with accuracy (Fig. 3A). Combining several of the oversampled regions, up to four pixels were occasionally required to achieve sufficient signal-to-noise ratios for precise determination of the repolarisation phase of the action potential. OAPs measured using this novel oversampling method exhibited similar morphology and duration characteristics when compared with those recorded using more standard electrophysiology techniques (Fig. 3B and C). At 300 ms CL OAPs at APD50 were 10.9 ± 0.9 ms and APD70 14.7 ± 1.2 ms and showed no

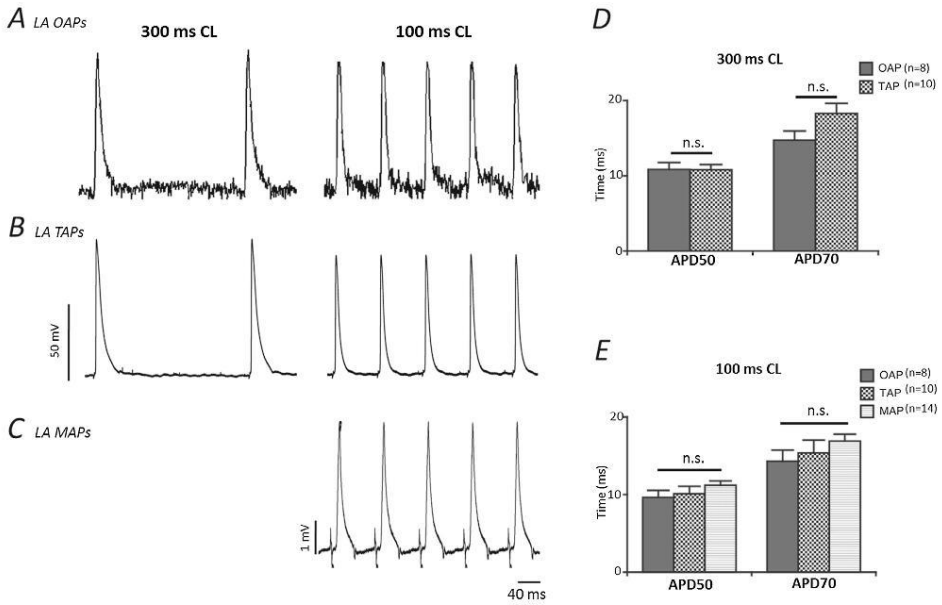

Fig. 3. Comparison of action potentials obtained using the high resolution optical system with other standard electrophysiological techniques. Characteristic raw trace examples of LA (left atrium). **A** optical action potentials (OAP) acquired at 1 kHz. **B** transmembrane (TAP); and **C** monophasic (MAP) action potentials recorded at cycle lengths of 300 ms and 100 ms. **D** and **E** Grouped data showing consistency of optical action potential durations at 50% and 70% repolarisation compared with TAPs and MAPs at 300 ms and 100 ms cycle lengths respectively. Error bars indicate + SEM. Data presented is from 8 regions of interest (ROI) from 8 LAs (OAPs), 10 cells from 5 LAs (TAPs) and 14 recordings from 14 LAs (MAPs).

difference from TAPs at 300 ms cycle lengths (10 cells, 5 atria, Fig. 3D). In another set of experiments, MAPs were recorded from the intact, beating heart just prior to dissection of atrial tissue for OAP measurement. We did not detect a significant difference in APD50 or APD70 between OAPs (9.6 ± 0.9 ms and 14.3 ± 1.4 ms respectively) and TAPs and MAPs at a more physiological paced cycle length of 100 ms (n = 14, Fig. 3E). This degree of uniformity therefore suggests that OAPs obtained using this technique can be used to make accurate and reliable assessments of APDs in the mouse atria.

3.2. Activation maps and conduction velocities

Example isochronal activation maps generated at different cycle lengths for the entire LA are shown in Fig. 4A and demonstrate in greater detail an obvious slowing of the activation spread at shorter cycle lengths. Accordingly, atrial conduction times, measured from the time point of stimulation to the fastest upstroke of the TAP (Fig. 4B) or MAP (Fig. 4C) were prolonged at 100 ms and 80 ms cycle lengths. Fig. 4D illustrates the recording positions of TAP and MAP with respect to the stimulation site. Fig. 4E gives mean conduction velocities (CV), measured with the new optical mapping setup, and throughout the entire left atrium at different paced cycle lengths. CV drops at higher paced cycle length, as expected (CV: 43.0 ± 1.3 cm/s−22.0 ± 4.7 cm/s from 300 ms to 80 ms CL respectively). Fig. 4F illustrates the parallel increase in atrial activation times measured by TAP (left atrial stimulation to mid-LA recording site) and by MAP (right atrial septal stimulation to distant LA recording site). Due to the higher intrinsic rate of the intact, beating heart (including the right atrium and the sinus node), MAP recordings were not available at 300 ms paced cycle length.

When adding the sodium channel blocker flecainide to the superfusion (1 μM), we observed an expected slowing in atrial conduction spread (Fig. 5A and B). The isochronal maps clearly demonstrate that flecainide superfusion produces a well-defined region of functional conduction block in the mid-to inferior left atrium, disturbing the normal pattern of electrical propagation, severely prolonging activation time in certain areas and potentially predisposing to re-entrant arrhythmia (see supplementary video file; Fig. 5B).

Supplementary video related to this article can be found at http://dx.doi.org/10.1016/j.pbiomolbio.2014.07.012.

Thus, in summary, our setup reliably reflects physiological changes in atrial activation and visualises the propagation of electrical activation waves across the entire murine left atrium, as well as allowing for accurate calculation of APD and intra-atrial conduction velocity at any defined region. In addition, this optical mapping system can be used to more definitively trace disordered electrical conduction in the mouse atrium, potentially induced by pharmacological agents, genetic manipulation or features common in certain models of pathology such as heart failure.

4. Discussion

4.1. Main findings

A novel system for optical mapping of electrical activation and repolarisation in the murine atrium is described. The system makes use of new imaging technology, namely a high-resolution 2nd generation CMOS camera, to achieve high temporal and spatial resolution of electrical activation and repolarisation in the murine atrium. It is demonstrated that recording is feasible using

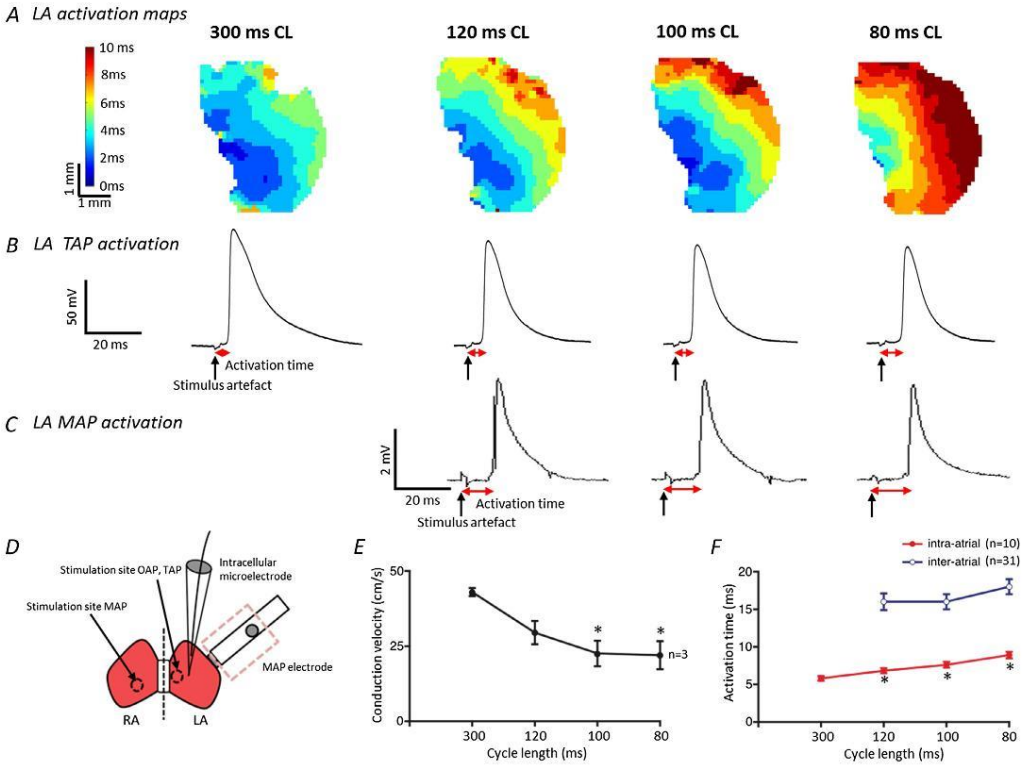

Fig. 4. Activation wave propagation across the murine left atrium and conduction velocities at different pacing cycle lengths. **A** Examples of the activation spread across the same left atrium at different cycle lengths as recorded by the new optical mapping system at 1 kHz. The high resolution isochronal maps indicate that at shorter cycle lengths the activation time across the whole tissue is increased. A similar, but less detailed, pattern of delayed activation at shorter cycle lengths is shown using recordings of **B** TAPs and **C** MAPs, as evidenced by the increase in time from the stimulus artefact to the point of activation (Vmax). **D** A schematic of the atria showing the stimulus and recording sites for the three techniques. When using optical mapping the whole left atrium is imaged and stimulated towards the septum. For TAP recordings the stimulation site is the same but the recording site is approximately in the centre of the tissue. Epicardial left atrial MAP signals were recorded from the intact whole heart and stimulated at the endocardial surface of the right atrium with the octapolar catheter. **E** Mean conduction velocities at different cycle lengths, $n = 3$ LA. Error bars indicate ± SEM, * denotes $P < 0.05$ compared with velocity at 300 ms CL; one way repeated measures ANOVA with Dunnett's post hoc analysis. **F** TAP and MAP activation times at decreasing cycle lengths. Data presented is from 10 cells from 5 LAs (TAPs) and 31 recordings from 31 LAs (MAPs). Error bars indicate ± SEM, * denotes $P < 0.05$ compared with activation time at 300 ms CL; one way ANOVA with Dunnett's post hoc analysis.

the system and shown that the measurements yield comparable action potential waveforms and action potential durations when compared to monophasic and transmembrane atrial action potentials. Furthermore, it is shown that the system is capable of detecting changes in conduction velocity and functional conduction block. In our hands, the oversampling of recordings allows us to maximise the information collected in each experiment, as a higher spatial resolution is conducive to the detection of small activation changes, while larger sampling areas are acceptable for the assessment of atrial repolarisation, where a higher signal to noise ratio may be needed to accurately determine action potential duration. In addition to this, the algorithms used are useful in reducing the time needed for a user to analyse APD measurements and produce activation maps. For example, to correct for baseline shifts, it is common to fit a linear or polynomial equation to the signal (Laughner et al., 2012). In our experiments, these baseline shifts were extremely variable. We therefore had to use a different approach to existing correction methods. Here we use a common top hat filter normally applied to 2D quality images but on a 1D signal on our action potentials. Another example is the detection of $t = 0$ on the isochronal maps. It is a useful tool for speeding up analysis and again, for limiting user bias.

Assessment of murine atrial electrophysiology is an essential tool to understand the functional consequences of defined genetic modifications, including complex gene expression changes e.g. secondary to altered function of transcription factors (Kirchhof et al., 2011a,b; Riley et al., 2012; Wang et al., 2010), or the effects of inhibitory or regulatory RNA molecules. Environmental factors like the effect of training, interventions and chronic or acute drug treatment (Fabritz et al., 2010, 2011) can be assessed with the increased number of pixels in this system in the future, including larger and irregular specimens. The increased spatial resolution in this system will also allow us to identify heterogeneities within the tissue. Imaging of murine embryos should also be possible with this system (Benes et al., 2014).

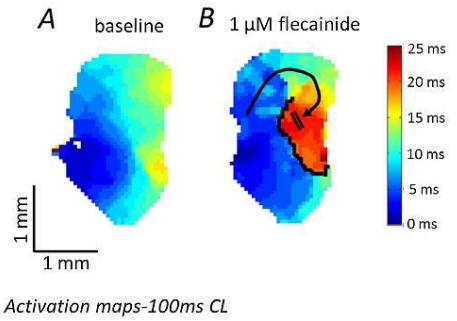

Fig. 5. Functional conduction block (induced by flecainide) in the murine left atrium. **A** Characteristic activation spread across the left atrium under control conditions, taking approximately 15 ms to traverse the whole tissue when paced at 100 ms CL. **B** Disrupted activation wave propagation across the same left atrium following 15 min of 1 μM flecainide infusion. A clearly defined region of functional conduction block develops and is outlined in black. An alternative route of conduction (black arrow) is required and this causes a substantial increase in activation time (25 ms). Both images acquired at 1 kHz sampling.

By building an optical mapping system around a novel 2nd generation oversampling high-resolution CMOS camera with high light sensitivity, we were able to record electrical activation and repolarisation with high accuracy and reliability, yielding information that reflects murine atrial biology (Figs. 2–4). The ORCA camera has very recently been used and shown to capture action potentials in spontaneously spiking HEK cells (Park et al., 2013). Signals from HEK cells occur at approximately 3 APs per second. The pacing rate applied in our experiments in live intact organ tissue was much higher and represented a higher challenge to the camera resolution. The validation data suggest that the system can reliably record atrial repolarisation, making it attractive for the study of arrhythmia mechanisms in genetically altered murine models that mimic inherited arrhythmogenic diseases and/or replicate common gene expression changes associated with common cardiac diseases.

4.2. Technical considerations

Optical mapping of mouse hearts has been used to characterise arrhythmia mechanisms since the beginning of this century. Initially, systems were developed to measure ventricular activation and repolarisation (Baker et al., 2000; Brunner and Kodirov, 2003), and more recently expanded to atrial preparations (Glukhov et al., 2010; Kirchhof et al., 2011a,b; Verheule et al., 2004). One of the most commonly used systems is the custom-made SCIMEDIA system that provides a 100 × 100 pixel field at high temporal resolution (Bezzina et al., 2013; Kirchhof et al., 2011a,b). Especially at high sampling rates, the relatively low signal strength generated by the thin murine atrial tissue has been a challenge. The system developed and validated here uses emerging technology, i.e. a 2nd generation CMOS camera capable of detecting low amplitude light signals at superior spatial resolution (128 × 2048 pixels) and good temporal resolution (1–2 kHz). A higher temporal resolution is needed when capturing quick cellular changes, e.g. action potential depolarisation. A higher spatial resolution is desirable when trying to precisely locate phenomena changing at a lower rate. With this resolution span, each individual pixel provides a signal with a relatively low signal to noise ratio, due to the limited number of light emitting events of the recorded tissue. The spatial oversampling of the signals during data acquisition allows the post-processing of signals to optimise the information per pixel. Specifically, a high spatial resolution is used to assess atrial activation with optimal accuracy and an acceptable signal to noise ratio. The employed algorithm for correction of baseline fluctuation was robust to all types of – sometimes random – changes in baseline fluorescence, thus increasing the reliability of the measurements and the yield of analysable experiments. Reliable assessment of repolarisation, in contrast, was possible using combination of individual signals in the analysis phase, thereby sacrificing some of the spatial resolution, and by signal averaging during steady state pacing. Thus, the proposed new, versatile system allows the adjustment of image parameters after the end of the experiment to suit specific analysis needs, therefore increasing the information yield from each experiment.

This system was capable of recording valid action potential waveforms over a wide range of paced cycle lengths, and with simultaneous recording of action potential durations from all regions of the left atrium. Using the post-processing methods described above, this system will provide detailed insights into the regional differences in atrial action potential duration, and their change in genetically modified models.

The preparation used here was stable over experimental protocols of 1–1.5 h duration, demonstrating that superfusion of the murine atrium is adequate to maintain the integrity of the superfused atrium during acute interventions such as antiarrhythmic drugs (Fig. 5) at bradycardic and physiological cycle lengths. Automated analysis of APD and activation patterns is another important feature of the present system. Semi-automated procedures, involving the investigator in the initial selection of suitable recording periods and in the definition of suitable regions of interest for assessment of repolarisation, combined with automated post-processing of such signals, allows valid, investigator-controlled yet rapid and high-throughput recordings of electrical activation and repolarisation in the intact murine atrium.

4.3. Limitations and further developments

The new optical mapping system can be used to characterise the electrophysiological behaviour of murine atrial tissue in sufficient detail to describe arrhythmogenic changes in electrical activation and repolarisation in murine atria. The isolated superfused, dye-loaded atrium is sufficiently stable to allow the assessment of acute effects of pharmacological interventions such as antiarrhythmic drugs or miRNAs. Cross-over designs, e.g. giving a substance initially and observing the reverse effect during wash out (Blana et al., 2010), can be used in the future to demonstrate stability of the preparation even better. As such, it will be useful to describe arrhythmia mechanisms in genetically modified mice (Riley et al., 2012), especially when paired experiments in genetically modified and wild type mice are done in direct sequence, maintaining blinding during the analysis. The system was stable in assessing a cycle length of 100 ms for several minutes, but for even higher heart rates, a perfusion system would be beneficial to adjust for increased metabolic demand. Assessment of APD needed an uncoupler, but assessment of conduction velocity might be possible without an uncoupler in the near future by filtering techniques following the sharp upstroke of the action potential. Working without an uncoupler physiologically is an advantage especially if working with models of mechano-electrical feedback (Fabritz et al., 2012, 2011; Kohl et al., 1999).

This system seems capable of detecting regional differences in activation (Figs. 4 and 5) and repolarisation (illustrated by the capability to measure action potential duration at one single site in all experiments). The semi-automated analysis combined with the

high and adjustable spatial resolution will allow the generation of regional information quickly and reliably. The software can be further automatised, and source data made compatible with existing analysis platforms for optical activation maps and repolarisation shapes to ensure transferability of the results, ideally in an open access development process. Future developments may make use of calcium-sensitive dyes to assess calcium release patterns in the isolated, superfused atrium.

Use of a 4 × 4 pixel average for a regional measurement can, in theory, affect the upstroke delay as this area is a combination of several cardiomyocytes. Despite this, it is common practice to use a slightly higher regional area to gain signal quality. The signal to noise level does not allow automated analysis of action potential peaks at present with the information from only one pixel. The intensity of emitted light seems the major limitation inhibiting yet finer spatial and temporal resolution in the proposed setup. New optical dyes with higher optical yields may help to further improve resolution and reliability of the system (Lee et al., 2012a,b; Lee et al., 2012a,b). Local stimulation at a defined point within the atrial tissue will allow us to discern longitudinal and transverse conduction properties, and enable programmed stimulation protocols. Fixation of the tissue at the end of the experiment, which was not done in the present study, will allow us to relate regional electrophysiological changes (e.g. conduction block, or differences in action potential duration) to histological changes.

4.4. Conclusions

Using the techniques described above, murine atria but also ventricular neonatal or embryonal whole hearts may be investigated in the future, driving new insight into inborn errors leading to cardiomyopathy, heart failure and arrhythmias.

This novel technique for optical mapping and analysis of optical action potentials was developed as a tool for experimentation with murine cardiac atrial electrophysiology and will help to drive insights into how genetic changes and environmental factors influence atrial activation and repolarisation properties, thereby helping to elucidate mechanisms of atrial arrhythmias.

Funding

Preliminary data award (LF) of Research Development Fund, University of Birmingham; Engineering and Physical Sciences Research council funds the PSIBS doctoral training centre EP/F50053X/1, University of Birmingham (TY); UoB starter grant (LF, PK). BmedSci intercalation (BO, FS, LF), EUTRAF and BHF.

Editors' note

Please see also related communications in this issue by Seo et al. (2014) and Verheule et al. (2014).

Acknowledgements

We thank Genna Riley and Sarah Hopkins for help with breeding of murine models. We thank Sander Verheule, Peter Kohl and Patrizia Camelliti for advice on optical mapping techniques. Alan Race for computational and Prem Kumar for logistical support.

References

Arora, R., Verheule, S., Scott, L., Navarrete, A., Katari, V., Wilson, E., et al., 2003. Arrhythmogenic substrate of the pulmonary veins assessed by high-resolution optical mapping. Circulation 107, 1816–1821. http://dx.doi.org/10.1161/01.Cir.0000058461.86339.7e.

Bachtel, A.D., Gray, R.A., Stohlman, J.M., Bourgeois, E.B., Pollard, A.E., Rogers, J.M., 2011. A novel approach to dual excitation ratiometric optical mapping of cardiac action potentials with di-4-ANEPPS using pulsed LED excitation. IEEE Trans. Biomed. Eng. 58, 2120–2126. http://dx.doi.org/10.1109/TBME.2011.2148719.

Baker, L.C., London, B., Choi, B.-R., Koren, G., Salama, G., 2000. Enhanced dispersion of repolarization and refractoriness in transgenic mouse hearts promotes reentrant ventricular tachycardia. Circ. Res. 86, 396–407. http://dx.doi.org/10.1161/01.RES.86.4.396.

Benes, J., Ammirabile, G., Sankova, B., Campione, M., Krejci, E., Kvasilova, A., et al., 2014. The role of connexin40 in developing atrial conduction. Fed. Eur. Biochem. Sci. Lett. 588, 1465–1469. http://dx.doi.org/10.1016/j.febslet.2014.01.032.

Benjamin, E.J., Rice, K.M., Arking, D.E., Pfeufer, A., van Noord, C., Smith, A.V., et al., 2009. Variants in ZFHX3 are associated with atrial fibrillation in individuals of European ancestry. Nat. Genet. 41, 879–881. http://dx.doi.org/10.1038/ng.416.

Bezzina, C.R., Barc, J., Mizusawa, Y., Remme, C.A., Gourraud, J.-B., Simonet, F., et al., 2013. Common variants at SCN5A-SCN10A and HEY2 are associated with Brugada syndrome, a rare disease with high risk of sudden cardiac death. Nat. Genet. 45, 1044–1049. http://dx.doi.org/10.1038/ng.2712.

Blana, A., Kaese, S., Fortmuller, L., Laakmann, S., Damke, D., van Bragt, K., et al., 2010. Knock-in gain-of-function sodium channel mutation prolongs atrial action potentials and alters atrial vulnerability. Heart Rhythm 7, 1862–1869. http://dx.doi.org/10.1016/j.hrthm.2010.08.016.

Brunner, M., Kodirov, S., 2003. In vivo gene transfer of Kv1. 5 normalizes action potential duration and shortens QT interval in mice with long QT phenotype. Am. J. Physiol. Heart Circ. Physiol., 194–203, 02115.

Camm, A.J., Al-Khatib, S.M., Calkins, H., Halperin, J.L., Kirchhof, P., Lip, G.Y.H., et al., 2012a. A proposal for new clinical concepts in the management of atrial fibrillation. Am. Heart J. 164, 292–302.e1. http://dx.doi.org/10.1016/j.ahj.2012.05.017.

Camm, A.J., Lip, G.Y.H., De Caterina, R., Savelieva, I., Atar, D., Hohnloser, S.H., et al., 2012b. 2012 focused update of the ESC Guidelines for the management of atrial fibrillation: an update of the 2010 ESC Guidelines for the management of atrial fibrillation. Developed with the special contribution of the European Heart Rhythm Association. Eur. Heart J. 33, 2719–2747. http://dx.doi.org/10.1093/eurheartj/ehs253.

Di Diego, J.M., Sicouri, S., Myles, R.C., Burton, F.L., Smith, G.L., Antzelevitch, C., 2013. Optical and electrical recordings from isolated coronary-perfused ventricular wedge preparations. J. Mol. Cell. Cardiol. 54, 53–64. http://dx.doi.org/10.1016/j.yjmcc.2012.10.017.

Dou, Y., Arlock, P., Arner, A., 2007. Blebbistatin specifically inhibits actin-myosin interaction in mouse cardiac muscle. Am. J. Physiol. Cell Physiol., 1148–1153. http://dx.doi.org/10.1152/ajpcell.00551.2006.

Eckstein, J., Zeemering, S., Linz, D., Maesen, B., Verheule, S., van Hunnik, A., et al., 2013. Transmural conduction is the predominant mechanism of breakthrough during atrial fibrillation: evidence from simultaneous endo-epicardial high-density activation mapping. Circ. Arrhythm. Electrophysiol. 6, 334–341. http://dx.doi.org/10.1161/CIRCEP.113.000342.

Efimov, I., Fahy, G., 1997. High resolution fluorescent imaging does not reveal a distinct atrioventricular nodal anterior input channel (fast pathway) in the rabbit heart during sinus rhythm. J. Cardiovasc. Electrophysiol. 8, 295–306.

Efimov, I.R., Huang, D.T., Rendt, J.M., Salama, G., 1994. Optical mapping of repolarization and refractoriness from intact hearts. Circulation 90, 1469–1480.

Ehrenberg, B., Farkas, D.L., Fluhler, E.N., Lojewska, Z., Loew, L.M., 1987. Membrane potential induced by external electric field pulses can be followed with a potentiometric dye. Biophys. J. 51, 833–837. http://dx.doi.org/10.1016/S0006-3495(87)83410-0.

Ellinor, P.T., Lunetta, K.L., Albert, C.M., Glazer, N.L., Ritchie, M.D., Smith, A.V., et al., 2012. Meta-analysis identifies six new susceptibility loci for atrial fibrillation. Nat. Genet. 44, 670–675. http://dx.doi.org/10.1038/ng.2261.

Fabritz, L., Damke, D., Emmerich, M., Kaufmann, S.G., Theis, K., Blana, A., et al., 2010. Autonomic modulation and antiarrhythmic therapy in a model of long QT syndrome type 3. Cardiovasc. Res. 87, 60–72. http://dx.doi.org/10.1093/cvr/cvq029.

Fabritz, L., Fortmuller, L., Yu, T.Y., Paul, M., Kirchhof, P., 2012. Can preload-reducing therapy prevent disease progression in arrhythmogenic right ventricular cardiomyopathy? Experimental evidence and concept for a clinical trial. Prog. Biophys. Mol. Biol. 110, 340–346. http://dx.doi.org/10.1016/j.pbiomolbio.2012.08.010.

Fabritz, L., Hoogendijk, M.G., Scicluna, B.P., van Amersfoorth, S.C., Fortmueller, L., Wolf, S., et al., 2011. Load-reducing therapy prevents development of arrhythmogenic right ventricular cardiomyopathy in plakoglobin-deficient mice. J. Am. Coll. Cardiol. 57, 740–750. http://dx.doi.org/10.1016/j.jacc.2010.09.046.

Faggioni, M., Savio-Galimberti, E., Venkataraman, R., Hwang, H.S., Kannankeril, P.J., Darbar, D., et al., 2014. Suppression of spontaneous ca elevations prevents atrial fibrillation in calsequestrin 2-null hearts. Circ. Arrhythm. Electrophysiol. 7, 313–320. http://dx.doi.org/10.1161/CIRCEP.113.000994.

Fedorov, V.V., Lozinsky, I.T., Sosunov, E.A., Anyukhovsky, E.P., Rosen, M.R., Balke, C.W., et al., 2007. Application of blebbistatin as an excitation-contraction uncoupler for electrophysiologic study of rat and rabbit hearts. Heart Rhythm 4, 619–626. http://dx.doi.org/10.1016/j.hrthm.2006.12.047.

Glukhov, A., Flagg, T., Fedorov, V., 2010. Differential K ATP channel pharmacology in intact mouse heart. J. Mol. Cell. Cardiol. 48, 152–160. http://dx.doi.org/10.1016/j.yjmcc.2009.08.026.

Gudbjartsson, D.F., Arnar, D.O., Helgadottir, A., Gretarsdottir, S., Holm, H., Sigurdsson, A., et al., 2007. Variants conferring risk of atrial fibrillation on chromosome 4q25. Nature 448, 353–357. http://dx.doi.org/10.1038/nature06007.

Jou, C.J., Spitzer, K.W., Tristani-Firouzi, M., 2010. Blebbistatin effectively uncouples the excitation-contraction process in zebrafish embryonic heart. Cell. Physiol. Biochem. 25, 419–424. http://dx.doi.org/10.1159/000303046.

Kirchhof, P., Breithardt, G., Aliot, E., Al Khatib, S., Apostolakis, S., Auricchio, A., et al., 2013. Personalized management of atrial fibrillation: proceedings from the fourth Atrial Fibrillation competence NETwork/European Heart Rhythm Association consensus conference. Europace 15, 1540–1556. http://dx.doi.org/10.1093/europace/eut232.

Kirchhof, P., Kahr, P., Kaese, S., 2011a. PITX2c is expressed in the adult left atrium, and reducing Pitx2c expression promotes atrial fibrillation inducibility and complex changes in gene expression. Circ. Cardiovasc. Genet. http://dx.doi.org/10.1161/CIRCGENETICS.110.958058.

Kirchhof, P., Marijon, E., Fabritz, L., Li, N., Wang, W., Wang, T., et al., 2011b. Overexpression of cAMP-response element modulator causes abnormal growth and development of the atrial myocardium resulting in a substrate for sustained atrial fibrillation in mice. Int. J. Cardiol. http://dx.doi.org/10.1016/j.ijcard.2011.10.057.

Knollmann, B.C., Katchman, A.N., Franz, M.R., 2001. Monophasic action potential recordings from intact mouse heart: validation, regional heterogeneity, and relation to refractoriness. J. Cardiovasc. Electrophysiol. 12, 1286–1294.

Kohl, P., Hunter, P., Noble, D., 1999. Stretch-induced changes in heart rate and rhythm: clinical observations, experiments and mathematical models. Prog. Biophys. Mol. Biol. 71, 91–138. http://dx.doi.org/10.1016/S0079-6107(98)00038-8.

Laughner, J.I., Ng, F.S., Sulkin, M.S., Arthur, R.M., Efimov, I.R., 2012. Processing and analysis of cardiac optical mapping data obtained with potentiometric dyes. Am. J. Physiol. Heart Circ. Physiol. 303, H753–H765. http://dx.doi.org/10.1152/ajpheart.00404.2012.

Lee, P., Bollensdorff, C., Quinn, T.A., Wuskell, J.P., Loew, L.M., Kohl, P., 2011. Single-sensor system for spatially resolved, continuous, and multiparametric optical mapping of cardiac tissue. Heart Rhythm 8, 1482–1491. http://dx.doi.org/10.1016/j.hrthm.2011.03.061.

Lee, P., Taghavi, F., Yan, P., Ewart, P., Ashley, E.A., Loew, L.M., et al., 2012a. In situ optical mapping of voltage and calcium in the heart. PLoS One 7, e42562. http://dx.doi.org/10.1371/journal.pone.0042562.

Lee, P., Yan, P., Ewart, P., Kohl, P., Loew, L.M., Bollensdorff, C., 2012b. Simultaneous measurement and modulation of multiple physiological parameters in the isolated heart using optical techniques. Pflugers Arch. 464, 403–414. http://dx.doi.org/10.1007/s00424-012-1135-6.

Lemoine, M.D., Duverger, J.E., Naud, P., Chartier, D., Qi, X.Y., Comtois, P., et al., 2011. Arrhythmogenic left atrial cellular electrophysiology in a murine genetic long QT syndrome model. Cardiovasc. Res. 92, 67–74. http://dx.doi.org/10.1093/cvr/cvr166.

Loew, L.M., 1996. Potentiometric dyes: imagingelectrical activity of cell membranes. Pure Appl. Chem. 68, 1405–1409. http://dx.doi.org/10.1351/pac199668071405.

Mandapati, R., Skanes, A., Chen, J., Berenfeld, O., Jalife, J., 2000. Stable microreentrant sources as a mechanism of atrial fibrillation in the isolated sheep heart. Circulation 101, 194–199. http://dx.doi.org/10.1161/01.CIR.101.2.194.

Park, J., Werley, C.A., Venkatachalam, V., Kralj, J.M., Dib-Hajj, S.D., Waxman, S.G., et al., 2013. Screening fluorescent voltage indicators with spontaneously spiking HEK cells. PLoS One 8, e85221. http://dx.doi.org/10.1371/journal.pone.0085221.

Riley, G., Syeda, F., Kirchhof, P., Fabritz, L., 2012. An introduction to murine models of atrial fibrillation. Front. Physiol. 3, 296. http://dx.doi.org/10.3389/fphys.2012.00296.

Rohr, S., Salzberg, B.M., 1994. Multiple site optical recording of transmembrane voltage (MSORTV) in patterned growth heart cell cultures: assessing electrical behavior, with microsecond resolution, on a cellular and subcellular scale. Biophys. J. 67, 1301–1315. http://dx.doi.org/10.1016/S0006-3495(94)80602-2.

Salama, G., Lombardi, R., Elson, J., 1987. Maps of optical action potentials and NADH fluorescence in intact working hearts. Am. J. Physiol. 252, H384–H394.

Salzberg, B.M., Davila, H.V., Cohen, L.B., 1973. Optical recording of impulses in individual neurones of an invertebrate Central nervous system. Nature 246, 508–509. http://dx.doi.org/10.1038/246508a0.

Savitzky, A., Golay, M.J.E., 1964. Smoothing and differentiation of data by simplified least squares procedures. Anal. Chem. 36, 1627–1639. http://dx.doi.org/10.1021/ac60214a047.

Schotten, U., Verheule, S., Kirchhof, P., Goette, A., 2011. Pathophysiological mechanisms of atrial fibrillation: a translational appraisal. Physiol. Rev. 91, 265–325. http://dx.doi.org/10.1152/physrev.00031.2009.

Seo, K., Inagaki, M., Hidaka, I., Fukano, H., Sugimachi, M., Hisada, T., Nishimura, S., Sugiura, S., 2014. Relevance of cardiomyocyte mechano-electric coupling to stretch-induced arrhythmias: Optical voltage/calcium measurement in mechanically stimulated cells, tissues and organs. Prog. Bio. Mol. Biol. 115 (2-3), 129–139. http://dx.doi.org/10.1016/j.pbiomolbio.2014.07.008.

Verheule, S., Sato, T., Everett, T., Engle, S.K., Otten, D., Rubart-von der Lohe, M., et al., 2004. Increased vulnerability to atrial fibrillation in transgenic mice with selective atrial fibrosis caused by overexpression of TGF-beta1. Circ. Res. 94, 1458–1465. http://dx.doi.org/10.1161/01.RES.0000129579.59664.9d.

Verheule, S., Tuyls, E., 2013. Loss of continuity in the thin epicardial layer because of endomysial fibrosis increases the complexity of atrial fibrillatory conduction. Circ. Arrhythm. Electrophysiol., 202–211. http://dx.doi.org/10.1161/CIRCEP.112.975144.

Verheule, S., Eckstein, J., Linz, D., Maesen, B., Bidar, E., Gharaviri, A., Schotten, U., 2014. Role of endo-epicardial dissociation of electrical activity and transmural conduction in the development of persistent atrial fibrillation. Prog. Bio. Mol. Biol. 115 (2-3), 173–185. http://dx.doi.org/10.1016/j.pbiomolbio.2014.07.007.

Wakili, R., Voigt, N., Kääb, S., Dobrev, D., Nattel, S., 2011. Recent advances in the molecular pathophysiology of atrial fibrillation. J. Clin. Invest. 121, 2955–2968. http://dx.doi.org/10.1172/JCI46315.

Waldeyer, C., Fabritz, L., Fortmueller, L., Gerss, J., Damke, D., Blana, A., et al., 2009. Regional, age-dependent, and genotype-dependent differences in ventricular action potential duration and activation time in 410 Langendorff-perfused mouse hearts. Basic Res. Cardiol. 104, 523–533. http://dx.doi.org/10.1007/s00395-009-0019-1.

Wang, J., Klysik, E., Sood, S., 2010. Pitx2 prevents susceptibility to atrial arrhythmias by inhibiting left-sided pacemaker specification. Proc. Natl. Acad. Sci., 1–6. http://dx.doi.org/10.1073/pnas.0912585107.

Wu, J., Biermann, M., Rubart, M., Zipes, D.P., 1998. Cytochalasin D as excitation-contraction uncoupler for optically mapping action potentials in wedges of ventricular myocardium. J. Cardiovasc. Electrophysiol. 9, 1336–1347.

Wu, J., Olgin, J., Miller, J., Zipes, D., 2001. Mechanisms underlying the reentrant circuit of atrioventricular nodal reentrant tachycardia in isolated canine atrioventricular nodal preparation using optical mapping. Circ. Res., 1189–1195.

Appendix 5 - PITX2 modulates atrial membrane potential and reduced PITX2 potentiates the antiarrhythmic effects of sodium-channel blockers.

Fahima Syeda PhD[1*], Andrew P Holmes PhD[1*], Ting Y Yu Msc[1,2], Samantha Tull PhD[1], Stefan Michael Kuhlmann[1], Davor Pavlovic DPhil[1], Daniel Betney BMedSc[1], Genna Riley DPhil[1], Jan P Kucera MD[4], Florian Jousset PhD[4], Joris R. de Groot MD[5], Stephan Rohr MD[4], Nigel Brown PhD[3], Larissa Fabritz MD[1,6-8], Paulus Kirchhof MD[1,6-9]

*contributed equally

1. Institute of Cardiovascular Sciences, University of Birmingham
2. Physical Sciences of Imaging in the Biomedical Sciences
3. St George's Hospital Medical School
4. Department of Physiology, University of Bern, Switzerland
5. Heart Center, Department of Cardiology, Academisch Medisch Centrum, Amsterdam, Netherlands
6. Department of Cardiovascular Medicine, University Hospital Muenster, Germany
7. Atrial Fibrillation NETwork, Muenster, Germany
8. University Hospitals Birmingham NHS Foundation Trust
9. Sandwell and West Birmingham Hospitals NHS Trust

Correspondence address:

Professor Paulus Kirchhof
Institute of Cardiovascular Sciences, University of Birmingham and
SWBH and UHB NHS Trusts
IBR, room 139
Wolfson Drive
Birmingham, B15 2TT
United Kingdom
phone: ++44 121 414 7042

e-mail: p.kirchhof@bham.ac.uk

Conflicts of interest

T Y Yu: none. A P Holmes: none. S P Tull: none. D Betney: none. F Jousset: none. J P Kucera: none. S Rohr: none. S M Kuhlmann: none. D Pavlovic: none. G Riley is currently employed by Bio-Techne (R&D Products). L Fabritz has received further institutional research grant support from DFG and Gilead Inc. P Kirchhof has received further research support from German Centre for Heart Research, from several drug and device companies active in atrial fibrillation, and has received honoraria from several such companies. F Syeda, L Fabritz, and P Kirchhof are listed as inventors on a patent (WO2015/140571) held by University of Birmingham on genotype specific antiarrhythmic drug therapy of atrial fibrillation.

Abstract

Background Antiarrhythmic drugs are widely used to treat patients with atrial fibrillation, but the mechanisms conveying their variable effectiveness are not known. Recent data suggest that PITX2 may have an important role in regulating gene expression and electrical function of the adult left atrium.

Objectives We determined left atrial PITX2 expression in AF patients requiring rhythm control therapy. We furthermore assessed the effects of PITX2 on left atrial electrophysiology and the effect of antiarrhythmic drugs.

Methods Left atrial PITX2 mRNA levels were measured in 95 patients undergoing thoracoscopic AF ablation. The effects of flecainide, a sodium channel blocker, and d,l-sotalol, a potassium channel blocker, were studied in littermate mice with normal and reduced PITX2 by electrophysiological study, optical mapping, and patch clamp studies. PITX2-dependent mechanisms of antiarrhythmic drug action were studied in HEK cells expressing human Na channels and by modelling human action potentials.

Results Flecainide (1µmol/L) was more effective in suppressing atrial arrhythmias in atria with reduced PITX2 mRNA levels ($Pitx2c^{+/-}$). Resting membrane potential was more depolarized in $Pitx2c^{+/-}$ atria, and TASK-2 gene and protein expression were decreased.

This resulted in enhanced post-repolarization refractoriness (refractoriness beyond 90% repolarisation) and a more effective sodium channel inhibition. Defined holding potentials eliminated differences in flecainide's effects between wildtype and Pitx2c$^{+/-}$ atrial cardiomyocytes. More positive holding potentials replicated the increased effectiveness of flecainide in blocking human $Na_v1.5$ channels in HEK293 cells. Computer modelling reproduced an enhanced effectiveness of sodium channel block when resting membrane potential was slightly depolarized.

Conclusions PITX2 modulates atrial resting membrane potential and thereby alters the effectiveness of Na channel blockers such as flecainide. PITX2 and ion channels regulating the resting membrane potential may provide novel targets for antiarrhythmic drug development and companion therapeutics in AF.

Abbreviations

AAD- Antiarrhythmic drug

Key words

Pitx2, atrial fibrillation, antiarrhythmic drugs, sodium channel, electrophysiology, drug targets, personalized medicine

Introduction

Atrial fibrillation (AF) causes cardiovascular deaths, frequent hospitalizations and cognitive decline even in anticoagulated and rate controlled patients (1,2). Antiarrhythmic drug (AAD) therapy remains the most commonly used treatment to maintain sinus rhythm in AF patients, but the effectiveness of AADs is limited (3). Unfortunately, we lack a basic understanding of why antiarrhythmic drugs prevent AF over long periods in some patients, but not others (4,5). Identifying factors that modify the effects of AADs would allow the selection of responsive patients and could help to guide development of novel AADs (6).

PITX2 is a transcription factor that regulates the development of the left atrium and other parts of the chest. Its c isoform is expressed in the adult left atrium and regulates the expression of left atrial ion channels (7-9). Low atrial Pitx2 expression renders mice susceptible to AF and shortens the left atrial action potential (8,10,11). Here, we studied how variations in atrial PITX2 expression modify the effects of AADs.

We detected variable left atrial PITX2 mRNA expression in AF patients requiring rhythm control therapy. We found that low PITX2 enhances the effect of flecainide, mediated by a more positive resting membrane potential (RMP). We identified reduced TASK-2 expression as a possible driver of this effect and replicated these effects in cells expressing human Na channels and in a human atrial AP model.

Methods

Study approval. All experiments were conducted under the Animals (Scientific Procedures) Act, 1986, approved by the Home Office (PPL number 30/2967) and by the institutional review board at the University of Birmingham. Analyses of human atrial tissue were approved by the Institutional Review Board of the Academic Medical Center, Amsterdam, Netherlands. All patients provided written informed consent.

Human DNA extraction and SNP analysis. Left atrial appendage (LAA) was excised in 95 patients undergoing bilateral thoracoscopic AF ablation using an endoscopic stapling device (Endo Gia stapler, Tyco Healthcare Group, North Haven, CT), snap frozen in liquid

nitrogen and stored at -80°C (12). DNA was extracted from using DNAeasy and PITX2 mRNA content was quantified by rtPCR.

Murine studies. Adult mice (12-16 weeks) on an MF1 background with normal or reduced (Pitx2c$^{+/-}$ (8)) atrial PITX2c expression were studied.

Arrhythmia inducibility, action potential duration, and activation times. Left atrial epicardial monophasic action potentials (MAP) were recorded from Langendorff-perfused (4ml.min^{-1}, 37°C) beating murine hearts as described (8,13). Programmed stimulation was performed at baseline and with flecainide (Sigma, 1µmol/L) or d,l-sotalol (Sigma, 10µmol/L) Arrhythmia inducibility and ERP were measured by using single RA extrastimuli after steady state pacing in 1ms decrements (8,13).
Transmembrane action potentials were recorded using borosilicate glass microelectrodes from isolated murine left atria as published (14). Resting membrane potential, action potential duration, upstroke velocity, and activation times were analysed and compared between groups (13,15,16).

Modelling of the electrophysiological consequences of different resting membrane potentials. We used the human atrial cell model of Courtemanche, Ramirez and Nattel (17). Simulations were run in model atrial cell strands of 100 cells (cell length 100µm). To reach steady state, the 5 leftmost cells of the strand were paced (S1) for 2 minutes at 1000 and 500 ms basic cycle length. A premature stimulation (S2) was applied to determine the ERP and CV was measured from cells 25-75. RMP was measured as the minimum diastolic potential during pacing at basic cycle length. Values for all other parameters were measured from the 50th cell. Post-repolarization refractoriness was calculated as the difference between APD at -60mV repolarization and ERP.

Na^+ current recordings in murine left atrial cardiomyocytes and HEK293 cells expressing the human $Na_v1.5$ channel. Murine hearts were removed under terminal anaesthesia and cell isolation was performed as published (18)For I_{Na} recordings, murine left atrial cardiomyocytes or HEK293 cells stably expressing the human Nav1.5 channel (SB ion channels, UK) were superfused at 5ml.min^{-1}, 22±0.5 °C with a solution containing in mM: NaCl 130, CsCl 5, HEPES 10, $CaCl_2$ 1.8, MgCl 1.2 and glucose 10, pH 7.4 (CsOH). 100µM $CdCl_2$ was added to block L-type Ca^{2+} currents. Whole cell patch clamp recordings

were obtained in voltage clamp mode using borosilicate glass pipettes (tip resistance 1–3 MΩ, pipette solution CsCl 115, NaCl 5, HEPES 10, EGTA 10, MgATP 5, $MgCl_2$ 0.5 and TEA 10, pH 7.2). Na^+ currents were elicited at 100ms steps to -10mV from holding potentials of -100 to -65mV using an Axopatch 1D amplifier (Molecular Devices, USA) and a CED micro1401 driven by Signal v6 (CED, UK).

Standard I_{K1} currents were isolated using 50μM $BaCl_2$ and applying 10mV step depolarisations (500ms) from -120mV to +50mV (18). For background K^+ current measurements, the external solution contained in mM: NaCl 130, KCl 5.4, $CaCl_2$ 1, $MgCl_2$ 1, HEPES 10, TEA 10, 4-AP 5, glibenclamide (2μM), $BaCl_2$ (100μM), $NiCl_2$ 2 and glucose 5.5 (pH 7.4 with NaOH), to block voltage-gated K^+ and Ca^{2+} channels and I_{K1} and I_{KATP}. Currents were measured in response to a 5s voltage ramp from -80 to 0mV. Background TASK-like K^+ current was isolated with 10mM $BaCl_2$. Full details are presented in the supplementary methods

mRNA and protein concentration of atrial ion channels. Murine right and left atria were harvested and immediately snap frozen. We extracted RNA and produced cDNA from snap frozen murine left and right atria, (SuperScript® VILO™, Life Technologies, UK). We quantified the expression of 20 major atrial ion channels and genes with suspected PITX2-dependent regulation (9) using custom-designed 96-well TLDA plates (Life Technologies). Western immunoblotting was performed by incubation of left atrial tissue lysates with antibodies detecting TASK-2 , $K_v1.6$, Na/K ATPase alpha-1 , Na/K ATPase alpha-2, Na/Ca exchanger 1 , Serca2a, $Na_v1.5$, or calnexin), and developed using enhanced chemiluminescence (Amersham, UK). For details of antibodies, see Supplementary Methods

Optical action potential and calcium transient recordings left atria. Mouse hearts were rapidly excised under terminal anaesthesia, mounted on a Langendorff apparatus, and perfused with either Di-4-Anepps (50 μmol/L; Biotium, California, USA) or Rhod-2 acetoxymethyl ester (5μmol/L) at 36-37°C for 10 minutes. The LA was isolated and signals recorded as described previously (14).. Ca^{2+} transients were obtained independently of voltage measurements. Optical action potentials and Ca^{2+} transients were analyzed for

APD, activation spread, longitudinal conduction velocity, and calcium transients using custom-made MATLAB algorithms (The MathWorks, USA, (14)).

Statistics. All experiments were performed and analysed blinded to genotype in littermate pairs of mice. Categorical data were compared using Fisher's exact test. Numerical data were compared by two-sided paired t tests (e.g. measurements before and after perfusion of flecainide or sotalol) and Wilcoxon signed-rank tests. Multiple measurements were assessed by repeated measures analysis of variance followed by multiple comparison (Bonferroni t-test) if the overall test was significant. Two-sided p values <0.05 were considered significant. Boxplots depict individual measurements (points), mean and SEM. Statistics and figures were created using GraphPad Prism 5.

Results

PITX2 / PITX2c mRNA levels in human left atrial tissue by SNP status. PITX2 mRNA varied markedly in human left atrial tissue harvested from patients undergoing combined endocardial and thoracoscopic AF ablation (n=95, Figure 1, Table 1 (12)), suggesting that a 50% lowered PITX2 expression defines a large, potentially clinically relevant group of AF patients. This did not correlate with AF risk based on SNP haplotype (Table 2), although we found reduced PITX2 levels in patients with 5 risk alleles.

Flecainide suppresses atrial arrhythmias in Pitx2c$^{+/-}$ hearts. Flecainide completely suppressed induced atrial arrhythmias in hearts with reduced PITX2 expression (Pitx2c$^{+/-}$, 0/17 hearts with atrial arrhythmias), but less in hearts with normal PITX2 expression (3/12 hearts with atrial arrhythmias, Figure 2A-C). Flecainide prolonged effective refractory periods (ERP) and post-repolarization refractoriness (PRR; calculated as the difference between the ERP and APD90) more in hearts with reduced PITX2 expression (Figure 2D and E, Table 3). Pitx2c$^{+/-}$ hearts had shorter atrial action potentials as expected (8). Flecainide abolished APD differences between Pitx2c$^{+/-}$ and wildtype left atria by prolonging early repolarization (APD30, APD50 and APD70, Table 3). Atrial PITX2 expression did not modulate the effects of sotalol on atrial APD or ERP (Table 4).

Atria with low Pitx2c expression show a more depolarized resting membrane potential. Resting membrane potentials (RMP) were slightly depolarized in left atrial cells with reduced Pitx2c expression (Figures 3A and B, mean depolarization 1.2– 2.4mV, all $p<0.05$). DV/dt_{max} was not significantly affected by atrial PITX2 levels (100ms paced CL wild type: 104.4± 4.3 V/s; $Pitx2c^{+/-}$: 93.7 ± 4.5 V/s). Flecainide altered atrial RMP (Figure 3B) and reduced action potential amplitude (100ms CL: wildtype baseline 77.5± 1.2 mV, n=30, wildtype flecainide 71.3 ± 1.2 mV, n=31; $Pitx2c^{+/-}$ baseline 73.4 ±1.3 mV, n=22, $Pitx2c^{+/-}$ flecainide 65.1 ± 1.45 mV, n=24), consistent with its sodium channel blocking effect.

Resting membrane potential differences explain the differential effect of flecainide in atria with reduced Pitx2c expression. Atrial PITX2 expression did not modify Na^+ currents (I_{Na}) recorded from isolated cardiomyocytes at holding potentials ranging from -100 to -65mV (Figure 4A-C). Peak sodium current (I_{Na}) was reduced at more depolarized holding potentials ($P<0.001$; WT: -100mV: 96 ± 4; -80mV: 72 ± 5; -75mV: 59± 5 ; -70mV: 43 ± 4; -65mV 30± 3 pA/pF, n = 40, N = 7 . $Pitx2c^{+/-}$: -100mV: 91 ± 4; -80mV: 60 ± 4; -75mV: 48± 4 ; -70mV: 35 ± 4 ; -65mV 24± 3 pA/pF, n = 41, N = 10). Flecainide inhibited I_{Na} better at more positive holding potentials (-100mV: 49± 3 %; -80mV: 58 ± 4 %; -75mV: 63 ± 4 %; -70mV: 68 ± 5 % n=; -65mV 75± 5 % n = 86, N = 17) in cells from atria with normal or reduced PITX2 expression, suggesting that the greater efficiency of flecainide in atria with reduced Pitx2c expression is secondary to RMP depolarization (Figure 4C). Consistent with this, flecainide inhibited human Nav1.5 channels more potently in more depolarized HEK cells channels (-65 – -75 mV, Figure 4D-E).

PITX2 regulates expression of KCNK5 channels and modifies background leak currents. Kcna6 and Kcnk5 mRNA expression were reduced in $Pitx2c^{+/-}$ murine left atria (Figure 5A, Supplementary table 1) while mRNA concentrations of 20 ion channels or related genes were not altered. Kv1.6 protein expression was unaltered and expression of TASK-2 was reduced in murine atria with reduced PITX2 expression (Figure 5B). $Na_v1.5$ mRNA and protein expression were not changed (Figures 5A and B). Background leak currents, which include TASK-related currents were reduced in $Pitx2c^{+/-}$ murine atria, while I_{K1} did not differ between genotypes (Figure 7).

Depolarizing the RMP in a human atrial model mimics the effects of flecainide in atria with reduced Pitx2c expression. We simulated a depolarized RMP in the Courtemanche AP model by a 25% reduction in I_{K1}. This reduced the RMP at 500ms paced cycle length by 2mV from–79.9 mV ("normal PITX2") to -77.9 mV ("low PITX2"). Sodium channels recovered from inactivation more slowly upon partial I_{Na} block (50 or 60%, Figure 6A). Furthermore, PRR was enhanced in the "low PITX2" model (Figure 4B and Table 5). I_{Na} inhibition reduced upstroke velocity (dV/dt_{max}) and conduction velocity in both models. Action potential simulations reproduced the prolongation of post-repolarization refractoriness (Figure 4B).

Pitx2 does not modify the effects of flecainide on left atrial electrical conduction and calcium handling. Reduced Pitx2 expression did not alter atrial conduction velocities or activation patterns (Supplementary Figure 1A-C, Table 6), consistent with published data (8). As expected, 1µmol/L flecainide decreased atrial conduction velocities without differences between atria with normal or reduced Pitx2c expression (Supplementary Figures 1B and C). Ca^{2+} relaxation times at 50% relaxation were not different in atria with reduced or normal PITX2 expression (Supplementary Figures 1D and E). Flecainide (1µmol/L) shortened 50% Ca^{2+} relaxation times by approximately 10% and decreased the Ca^{2+} transient amplitude by approximately 50% in atria with normal and reduced Pitx2c expression (Supplementary Figure 1E and F). Also, we did not find changes in expression of Na/Ca exchanger, Serca2a or Na/K ATPase alpha-1 and alpha-2 subunit protein in atria with normal and reduced Pitx2c expression (Supplementary Figure 2).

Discussion

Main findings. We demonstrate that left atrial Pitx2 mRNA concentrations vary in patients with AF requiring rhythm control therapy. Furthermore, flecainide increases post-repolarization refractoriness and suppresses arrhythmias more effectively in atria with halved Pitx2 expression, mediated by a more depolarized resting membrane potential. Drug-induced PRR is thought to prevent premature excitation as reactivation can then only occur after complete repolarisation, after the vulnerable period of excitability (19,20). We found similar effects in cells expressing human sodium channels and in the Courtemanche Nattel model of human atrial action potentials.

Thus, our study highlights modulation of the atrial resting membrane potential by PITX2, possibly mediated by background currents such as TASK-2, as a target for AAD therapy, including atrial-selective therapy. Furthermore, our results suggest that markers for atrial PITX2 expression can be used to stratify sodium channel blocker therapy.

Small changes in the atrial resting membrane potential cause marked post-repolarization refractoriness induced by flecainide. We identified low atrial PITX2 expression as an important determinant of the antiarrhythmic effects of Na channel blockers: Low left atrial Pitx2 mRNA depolarized the atrial RMP (Figure 3), consistent with another, earlier report (11). A depolarized RMP increased flecainide-induced post-repolarization refractoriness (Figure 2)(21-25). The conduction-slowing effect of flecainide was not modulated by reduced atrial PITX2 (Supplementary Figure 1), an important surrogate for drug safety. Both the modelling experiments (Figure 6) and the experiments in HEK cells expressing human sodium channels (Figure 4, Table 4) confirm that small changes in resting membrane potential can markedly modulate sodium channel inhibition.

The resting membrane potential: A potential target for antiarrhythmic drug or companion drug development. Open-state sodium channel blockers such as flecainide or propafenone bind preferentially to sodium channels integrated in membranes with slightly depolarized resting potentials, where more channels are in the open or inactivated state (26,27). Our data suggest that AAD combinations that combine a sodium channel blocker with a membrane potential modifying substance, such as amiodarone (28) or the combination of dronedarone and ranolazine (24,29,30), may have synergistic antiarrhythmic effects because they modulate the atrial resting membrane potential and thereby enhance the effect of sodium channel blockade. Further studies of such drug combinations are warranted. Our data also suggest that such combined effects may be of special relevance in patients who have a depolarized resting membrane potential, e.g. secondary to low left atrial PITX2. As PITX2 expression is confined to the left atrium in the heart, AAD therapy that leverages modifications in RMP may achieve “atrial specific” antiarrhythmic drug therapy.

Molecular mechanism of depolarized resting membrane potential in atria with reduced Pitx2c. RMP is maintained by an intricate balance of different transmembrane currents and closely related to the potassium equilibrium potential. We identified that PITX2 modifies expression of the genes encoding $K_v1.6$ and TASK-2 (Figure 5). Complete deletion of Pitx2 regulates other potassium and sodium channels such as *Kcnj2* (8,31), which alter the RMP, but these were not responsible for the depolarized RMP observed in our study. Two-pore domain potassium channels, such as TASK-2, contribute to the RMP in a variety of cells including skeletal and cardiac muscle (32,33). So far, an altered function of the TASK-1 channel and of I_{K1} has been implicated in atrial remodelling and atrial fibrillation (34,35). Here we demonstrate that TASK-2 is expressed in atrial myocardium (Figure 5B), suggesting that a reduced function of TASK-2 could depolarize the RMP (Figures 2&6, (8,11)), in analogy to the effect of TASK-2 in neuronal and cartilage tissue (36,37).

Developing clinical markers for patients with a depolarized RMP. While it will be challenging to directly assess left atrial RMP in AF patients, our data suggest that differences in atrial RMP could explain the effectiveness of sodium channel blockers in carriers of common gene variants on chromosome 4q25 (38), although left atrial PITX2c levels are modulated by factors other than SNP status (Table 1). It seems desirable to develop and validate drivers that modify the RMP and clinical markers for patients prone to a depolarized atrial RMP to select appropriate AADs for individual patients in the future, thus paving the way to a stratified or personalized antiarrhythmic drug therapy selection (6,39).

Limitations. We provide robust evidence that left atrial Pitx2 expression varies in AF patients, and that reduced Pitx2c expression enhances the antiarrhythmic effects of sodium channel blockers by modulating the atrial resting membrane potential. Our study was partly motivated by the assumption that gene variants on chromosome 4q25 modify Pitx2 expression, an assumption that has not been definitively proven (9,11,40,41). Our analysis here and that of others indicate that SNP status does not always correlate with Pitx2 levels(42,43). Our findings are relevant to AAD therapy even if the presumed link

between PITX2 expression and genetic variants on chromosome 4q25 proves elusive. Validating our findings in patients is desirable but will be challenging as access to fresh left atrial cardiomyocytes is limited.

Further studies exploring the relevance of TASK channels for the atrial resting membrane potential are warranted.

Perspectives

Competency in Medical Knowledge. Antiarrhythmic drugs are commonly used to prevent symptomatic AF recurrences, but their effectiveness varies. This study identifies the atrial resting membrane potential as an important modulator determining the effects of sodium channel blockers. PITX2, a transcription factor linked to left-right asymmetry in the chest during development, modulates the expression of left atrial ion channels maintaining the resting potential.

Translational Implications.

What's known? AADs only prevent recurrent AF in approximately half of AF patients, while putting all patients at risk of side effects. The reasons why AADs are variably effective are unknown.

What's new? We identified PITX2 as a modulator of the atrial resting membrane potential, probably via TASK2. A slight depolarization of the atrial resting membrane potential markedly enhances the antiarrhythmic effects of sodium channel blockers. Within the limitations of an experimental study, our data suggest that sodium channel blockers are an attractive AAD therapy in AF patients with reduced PITX2 expression, as the enhanced post-repolarization refractoriness counters the PITX2-induced shortening of the atrial action potential. Our data also underpin the use of modifiers of the atrial resting membrane potential as companion therapeutics for sodium channel blockers.

What's next? Markers for a depolarized atrial resting membrane potential may in the future help to select AAD therapy. Our study calls for investigations of the use of sodium channel blockers as antiarrhythmic agents of first choice in AF patients with low atrial

PITX2 levels. Ion channels regulating resting membrane potential may provide novel targets for the development ofAADs and/or for the development of companion therapeutics to existing compounds, e.g. targeting TASK-2 channels.

Author contributions

PK and LF designed the study and interpreted results. FS designed, performed and analysed experiments and wrote the paper with help from all authors. APH, TYY, ST, DB, DP, SMK, JPK, FJ, and SR designed, performed and analysed experiments. GR coordinated experiments. NB provided the murine embryos and contributed to the design and interpretation of the results. JRdG provided human left atrial tissue samples.

Sources of funding. This work was supported by European Union (EUTRAF 25105 to PK and SR, grant agreement No 633193 [CATCH ME] to PK and LF), British Heart Foundation (FS/13/43/30324 to PK and LF), Leducq Foundation to PK, Physical Science of Imaging In Biomedical Sciences (PSIBS) University of Birmingham for TY to LF (EP/F50053X/1), DFG (FA 413 3/1) to LF, Swiss National Science Foundation (138297) to SR, and Boehringer Ingelheim Foundation to SMK. JRdG is supported by NWO/ZonMW VIDI grant 016.146.310.

Acknowledgements

We thank Sarah Hopkins, Syeeda Nashitha Kabir, Pushpa Patel and Charles Carey for technical support, Marta Coric for help with HEK cells and Ilaria Piccini for advice on TLDA.

References

1. Chugh SS, Havmoeller R, Narayanan K et al. Worldwide epidemiology of atrial fibrillation: a Global Burden of Disease 2010 Study. Circulation 2014;129:837-47.
2. January CT, Wann LS, Alpert JS et al. 2014 AHA/ACC/HRS guideline for the management of patients with atrial fibrillation: a report of the American College of Cardiology/American Heart Association Task Force on Practice Guidelines and the Heart Rhythm Society. J Am Coll Cardiol 2014;64:e1-76.
3. Camm AJ, Lip GY, De Caterina R et al. 2012 focused update of the ESC Guidelines for the management of atrial fibrillation: an update of the 2010 ESC Guidelines for the management of atrial fibrillation--developed with the special contribution of the European Heart Rhythm Association. Europace 2012;14:1385-413.
4. Kirchhof P, Andresen D, Bosch R et al. Short-term versus long-term antiarrhythmic drug treatment after cardioversion of atrial fibrillation (Flec-SL): a prospective, randomised, open-label, blinded endpoint assessment trial. Lancet 2012;380:238-46.
5. Schotten U, Verheule S, Kirchhof P, Goette A. Pathophysiological mechanisms of atrial fibrillation: a translational appraisal. Physiological reviews 2011;91:265-325.
6. Fabritz L, Guasch E, Antoniades C et al. Expert consensus document: Defining the major health modifiers causing atrial fibrillation: a roadmap to underpin personalized prevention and treatment. Nat Rev Cardiol 2015.
7. Li N, Dobrev D, Wehrens XH. PITX2: a master regulator of cardiac channelopathy in atrial fibrillation? Cardiovasc Res 2016.
8. Kirchhof P, Kahr PC, Kaese S et al. PITX2c is expressed in the adult left atrium, and reducing Pitx2c expression promotes atrial fibrillation inducibility and complex changes in gene expression. Circulation Cardiovascular genetics 2011;4:123-33.
9. Kahr PC, Piccini I, Fabritz L et al. Systematic Analysis of Gene Expression Differences between Left and Right Atria in Different Mouse Strains and in Human Atrial Tissue. PloS one 2011;6:e26389.
10. Wang J, Klysik E, Sood S, Johnson RL, Wehrens XH, Martin JF. Pitx2 prevents susceptibility to atrial arrhythmias by inhibiting left-sided pacemaker specification. Proceedings of the National Academy of Sciences of the United States of America 2010;107:9753-8.
11. Chinchilla A, Daimi H, Lozano-Velasco E et al. PITX2 insufficiency leads to atrial electrical and structural remodeling linked to arrhythmogenesis. Circulation Cardiovascular genetics 2011;4:269-79.
12. Krul SP, Driessen AH, van Boven WJ et al. Thoracoscopic video-assisted pulmonary vein antrum isolation, ganglionated plexus ablation, and periprocedural confirmation of ablation lesions: first results of a hybrid surgical-electrophysiological approach for atrial fibrillation. Circulation Arrhythmia and electrophysiology 2011;4:262-70.
13. Blana A, Kaese S, Fortmuller L et al. Knock-in gain-of-function sodium channel mutation prolongs atrial action potentials and alters atrial vulnerability. Heart rhythm : the official journal of the Heart Rhythm Society 2010;7:1862-9.
14. Yu TY, Syeda F, Holmes AP et al. An automated system using spatial oversampling for optical mapping in murine atria. Development and validation with monophasic and transmembrane action potentials. Prog Biophys Mol Biol 2014;115:340-8.
15. Yu TY, Syeda F, Holmes AP et al. An automated system using spatial oversampling for optical mapping in murine atria. Development and validation with monophasic and transmembrane action potentials. Progress in biophysics and molecular biology 2014.
16. Lemoine MD, Duverger JE, Naud P et al. Arrhythmogenic left atrial cellular electrophysiology in a murine genetic long QT syndrome model. Cardiovasc Res 2011;92:67-74.

17. Courtemanche M, Ramirez RJ, Nattel S. Ionic mechanisms underlying human atrial action potential properties: insights from a mathematical model. The American journal of physiology 1998;275:H301-21.
18. Holmes AP, Yu TY, Tull S et al. A Regional Reduction in Ito and IKACh in the Murine Posterior Left Atrial Myocardium Is Associated with Action Potential Prolongation and Increased Ectopic Activity. PloS one 2016;11:e0154077.
19. Kirchhof P, Fabritz L, Franz MR. Post-repolarization refractoriness versus conduction slowing caused by class I antiarrhythmic drugs - antiarrhythmic and proarrhythmic effects. Circulation 1998;97:2567-2574.
20. Milberg P, Frommeyer G, Uphaus T et al. Electrophysiologic profile of dronedarone on the ventricular level: beneficial effect on postrepolarization refractoriness in the presence of rapid phase 3 repolarization. Journal of cardiovascular pharmacology 2012;59:92-100.
21. Frommeyer G, Schmidt M, Clauss C et al. Further insights into the underlying electrophysiological mechanisms for reduction of atrial fibrillation by ranolazine in an experimental model of chronic heart failure. European journal of heart failure 2012;14:1322-31.
22. Milberg P, Frommeyer G, Ghezelbash S et al. Sodium channel block by ranolazine in an experimental model of stretch-related atrial fibrillation: prolongation of interatrial conduction time and increase in post-repolarization refractoriness. Europace 2013.
23. Fukuda K, Watanabe J, Yagi T et al. A sodium channel blocker, pilsicainide, produces atrial post-repolarization refractoriness through the reduction of sodium channel availability. Tohoku J Exp Med 2011;225:35-42.
24. Burashnikov A, Sicouri S, Di Diego JM, Belardinelli L, Antzelevitch C. Synergistic effect of the combination of ranolazine and dronedarone to suppress atrial fibrillation. Journal of the American College of Cardiology 2010;56:1216-24.
25. Kirchhof P, Engelen M, Franz MR et al. Electrophysiological effects of flecainide and sotalol in the human atrium during persistent atrial fibrillation. Basic Res Cardiol 2005;100:112-21.
26. Anno T, Hondeghem LM. Interactions of flecainide with guinea pig cardiac sodium channels. Importance of activation unblocking to the voltage dependence of recovery. Circulation research 1990;66:789-803.
27. Nitta J, Sunami A, Marumo F, Hiraoka M. States and sites of actions of flecainide on guinea-pig cardiac sodium channels. European journal of pharmacology 1992;214:191-7.
28. Singh BN, Singh SN, Reda DJ et al. Amiodarone versus sotalol for atrial fibrillation. N Engl J Med 2005;352:1861-72.
29. Burashnikov A, Di Diego JM, Zygmunt AC, Belardinelli L, Antzelevitch C. Atrial-selective sodium channel block as a strategy for suppression of atrial fibrillation. Ann N Y Acad Sci 2008;1123:105-12.
30. Reiffel JA, Camm AJ, Belardinelli L et al. The HARMONY Trial: Combined Ranolazine and Dronedarone in the Management of Paroxysmal Atrial Fibrillation: Mechanistic and Therapeutic Synergism. Circulation Arrhythmia and electrophysiology 2015.
31. Tao Y, Zhang M, Li L et al. Pitx2, an Atrial Fibrillation Predisposition Gene, Directly Regulates Ion Transport and Intercalated Disc Genes. Circulation Cardiovascular genetics 2014.
32. Reyes R, Duprat F, Lesage F et al. Cloning and expression of a novel pH-sensitive two pore domain K+ channel from human kidney. The Journal of biological chemistry 1998;273:30863-9.
33. Enyedi P, Czirjak G. Molecular background of leak K+ currents: two-pore domain potassium channels. Physiological reviews 2010;90:559-605.
34. Harleton E, Besana A, Chandra P et al. TASK-1 current is inhibited by phosphorylation during human and canine chronic atrial fibrillation. Am J Physiol Heart Circ Physiol 2015;308:H126-34.

35. Liang B, Soka M, Christensen AH et al. Genetic variation in the two-pore domain potassium channel, TASK-1, may contribute to an atrial substrate for arrhythmogenesis. J Mol Cell Cardiol 2014;67:69-76.
36. Clark RB, Kondo C, Belke DD, Giles WR. Two-pore domain K(+) channels regulate membrane potential of isolated human articular chondrocytes. J Physiol 2011;589:5071-89.
37. Kindler CH, Paul M, Zou H et al. Amide local anesthetics potently inhibit the human tandem pore domain background K+ channel TASK-2 (KCNK5). The Journal of pharmacology and experimental therapeutics 2003;306:84-92.
38. Ellinor PT, Lunetta KL, Albert CM et al. Meta-analysis identifies six new susceptibility loci for atrial fibrillation. Nat Genet 2012;44:670-5.
39. Kirchhof P, Sipido KR, Cowie MR et al. The continuum of personalized cardiovascular medicine: a position paper of the European Society of Cardiology. Eur Heart J 2014;35:3250-7.
40. Gore-Panter SR, Hsu J, Barnard J et al. PANCR, the PITX2 Adjacent Noncoding RNA, Is Expressed in Human Left Atria and Regulates PITX2c Expression. Circ Arrhythm Electrophysiol 2016;9.
41. Holmes AP, Kirchhof P. Pitx2 Adjacent Noncoding RNA: A New, Long, Noncoding Kid on the 4q25 Block. Circ Arrhythm Electrophysiol 2016;9.
42. Holmes AP, Kirchhof P. Pitx2 Adjacent Noncoding RNA: A New, Long, Noncoding Kid on the 4q25 Block. Circulation Arrhythmia and electrophysiology 2016;9:e003808.
43. Gore-Panter SR, Hsu J, Hanna P et al. Atrial Fibrillation Associated Chromosome 4q25 Variants Are Not Associated with PITX2c Expression in Human Adult Left Atrial Appendages. PloS one 2014;9:e86245.

Figure Legends

Figure 1

Pitx2 mRNA expression as a fraction of actin in human left atrial appendages taken from atrial fibrillation patients undergoing thoracoscopic AF ablation therapy

Figure 2

A Image and schematic representation of the Langendorff perfused heart.

B Atrial arrhythmia inducibility in isolated, beating wildtype and Pitx2c$^{+/-}$ hearts. Flecainide abolished atrial arrhythmia inducibility in Pitx2c$^{+/-}$ hearts only *p<0.05 flecainide vs baseline (Fisher's exact test). Baseline: WT n= 16, Pitx2c$^{+/-}$ n= 21. Flecainide: WT n= 12, Pitx2c$^{+/-}$ n= 17

C Representative trace of AF induced during programmed stimulation at baseline, showing reduced severity of arrhythmias with 1µmol/L flecainide in Pitx2c$^{+/-}$ atria. S2= single extrastimulus

D Effects of flecainide on atrial effective refractory period (ERP), in wildtype and Pitx2c$^{+/-}$ isolated, beating hearts. Shown is the difference (ms) in ERP between baseline and 1µmol/L flecainide at 80-120ms paced cycle length (CL) following a single extra stimulus (S2). Horizontal lines represent mean ± SEM. Wildtype (open circles) n=10-11, Pitx2c$^{+/-}$ (closed circles) n= 11-13, individual values are displayed, *p<0.05 between genotypes across all CL, 2-way ANOVA. Data points for each genotype have been offset at each cycle length for clarity.

E Schematic representation of the overall effects of 1µmol/L flecainide on ERP. Flecainide prolongs ERP in both genotypes, this effect is more pronounced in Pitx2c$^{+/-}$ atria than in wildtype. Flecainide causes post-repolarization refractoriness (PRR), the difference between ERP (black and red lines) and APD90 (blue lines), in wildtype and Pitx2c$^{+/-}$ atria. Flecainide-induced PRR in Pitx2c$^{+/-}$ is almost 3 times that of wildtype atria. *p<0.05 wildtype vs Pitx2c$^{+/-}$ $^{\#}$p<0.05 Baseline vs 1µmol/L flecainide.

Figure 3

A Schematic representation of sharp microelectrode electrode recordings from the superfused whole left atrium (LA).

B Resting membrane potential (RMP) in wildtype and Pitx2c$^{+/-}$ left atria (LA) at baseline (black; n wildtype =30, Pitx2c$^{+/-}$=31) and with 1µmol/L flecainide (red; n wildtype=22,

Pitx2c$^{+/-}$=23). Pitx2c$^{+/-}$ LA have depolarized RMP; the difference between wildtype and Pitx2c$^{+/-}$ is exaggerated with flecainide. Horizontal lines represent mean ± SEM. 2-way repeated measures ANOVA *p<0.05, ***p<0.001 across all cycle lengths. Individual values are also shown. Data points for each genotype have been offset at each cycle length for clarity.

C Maximum upstroke velocity (dV/dt_{max}) in wildtype and Pitx2c$^{+/-}$ left atria at baseline (black; n widltype=30, Pitx2c$^{+/-}$=31) and with 1µmol/L flecainide (red; n wildtype=22, Pitx2c$^{+/-}$=24). Flecainide brings about a difference in dV/dt_{max} between wildtype and Pitx2c$^{+/-}$ LA. Horizontal lines represent mean ± SEM. 2-way repeated measures ANOVA. **p<0.01 Individual values are also shown. Data points for each genotype have been offset at each cycle length for clarity.

Figure 4

A Schematic representation of patch clamp experiments carried out in isolated atrial cardiomyocytes. Human embryonic kidney (HEK) cells were patch clamped using the same setup.

B Representative traces showing sodium current (I_{Na}) measured by patch clamping, in isolated atrial cardiomyocytes at baseline (black) and with 1µmol/L flecainide (red), at increasing holding potentials (-100 to -65 mV). Horizontal line = 1 ms, vertical line = 40pA/pF

C Percentage reduction in peak I_{Na} caused by 1µmol/L flecainide in atrial CM from wildtype and Pitx2c$^{+/-}$ LA. Reduction in peak I_{Na} is enhanced with increased holding potentials, irrespective of the origin of the cardiomyocytes. Wildtype n= 10; Pitx2c$^{+/-}$ n = 9

D Representative traces showing sodium currents (I_{Na}) in $Na_v1.5$-transfected HEK cells at baseline (black) and with 1µmol/L flecainide (red) at increasing holding potentials (-100 to -65 mV).

E Percentage reduction in peak I_{Na} caused by 1µmol/L flecainide in $Na_v1.5$-transfected HEK cells. Reduction in peak I_{Na} was enhanced with increased holding potentials. The greatest difference in % reduction was between -70mV and -65mV.

Figure 5

A Relative quantity (RQ) of mRNA of selected ion channels in left atria from Pitx2c$^{+/-}$ and wild-type mice**.** Expression levels were measured relative to wildtype sample 1. Kcnk5

encodes TASK-2, Kcna6 encodes $K_V1.6$ and Scn5a encodes $Na_V1.5$. WT = 6, Pitx2c$^{+/-}$ = 6. *p<0.05 Student's t-test. See Supplementary Table 1 for all ion channels measured.

B Quantity of TASK-2, $K_V1.6$ and $Na_V1.5$ proteins relative to calnexin (arbitrary units). Representative immunoblots are displayed below the corresponding dot plot. WT = 7, Pitx2c$^{+/-}$ = 8. *p<0.05 Student's t-test. Molecular weights: TASK-2 55 kDa; $K_V1.6$ 58 kDa; $Na_V1.5$ 248 kDa.

Figure 6

A Propagated action potentials (top) simulated with the Courtemanche-Ramirez-Nattel model modified to reflect the action potential characteristics of murine Pitx2c$^{+/-}$ atria and the effect of 60% I_{Na} block at pacing cycle lengths of 500 and 1000 ms, with 2 minutes prepacing, and corresponding time courses of the product of the two inactivation gates *h* and *j* of I_{Na} (bottom), reflecting I_{Na} availability.

B Effects of reduced sodium conductance (g_{Na}) on post-repolarization refractoriness in the simulations. Reduction in g_{Na} caused PRR in the reference model and Pitx2c deficiency model. After reducing g_{Na}, PRR was greater in the Pitx2c deficiency model than in the reference model (red lines).

Figure 7

A Representative traces showing I_{K1} currents (50µmol/L Ba^{2+}) measured by patch clamping, in isolated wildtype and Pitx2c$^{+/-}$ atrial cardiomyocytes at test potentials ranging from -120 to 50mV.

B I_{k1} currents in atrial cardiomyocytes from wildtype and Pitx2c$^{+/-}$ LA at test potentials ranging from -120 to 50mV. There is no significant difference between genotypes.

C Representative traces showing background leak currents (10mmol/L Ba^{2+}) in isolated wildtype and Pitx2c$^{+/-}$ atrial cardiomyocytes.

D Background leak currents in atrial cardiomyocytes from wildtype and Pitx2c$^{+/-}$ LA at test potentials ranging from -120 to 50mV. Pitx2c$^{+/-}$ cardiomyocytes had significantly reduced background currents

Table 1. Baseline characteristics of atrial fibrillation patients. Left atrial appendages were collected from these patients.

Baseline Characteristics	
Patients, n	101
Age (years)	59.7±8.4 (40-76)
Male, n (%)	79 (78)
CHA_2DS_2VASc-score (mean).	1.3 (0-6)
Congestive heart failure, n (%)	6 (6)
Hypertension, n (%)	34 (34)
Age ≥ 75, n (%)	1 (1)
Diabetes, n (%)	9 (9)
Stroke/TIA/Embolus, n (%)	10 (10)
Vascular disease, n (%)	10 (10)
Female gender, n (%)	22 (22)
Age ≥ 65, n (%)	31 (31)
CHA_2DS_2VASc-score = 0, n (%)	60 (59)
CHA_2DS_2VASc-score = 1, n (%)	24 (24)
CHA_2DS_2VASc-score ≥ 2, n (%)	17 (17)
Previous catheter PVI, n (%)	20 (20)
Type AF	
Paroxysmal, n (%)	44 (44)
Persistent, n (%)	56 (55)
Longstanding Persistent, n (%)	1 (1)
AF duration (years)	6.0 (1-35)
Anti-arrhythmic drugs,	
Class IA, n (%)	4 (4)
Class IC, n (%)	33 (33)
Class II, n (%)	53 (52)
Class III, n (%)	41 (41)
Class IV, n (%)	17 (17)
Digoxin, n (%)	15 (15)
Anticoagulants (before PVI procedure),	
Coumarins, n (%)	89 (88)
Antiplatelets, n (%)	6 (6)

AF: atrial fibrillation, PVI: pulmonary vein isolation, TIA: transient ischemic attack

Table 2: Effects of flecainide on refractoriness and repolarization in PITX2-deficient (Pitx2c$^{+/-}$) and wildtype mouse hearts.

All values are given as mean±SEM. # indicate significant compared to baseline, * indicate significant differences compared to wildtype. Number of atria are in brackets. CL= cycle length

					Wildtype				Pitx2c$^{+/-}$			
Paced (ms)	CL	120		100		80		120		100		80
Left atrial effective refractory period (ms)												
	Baseline	Flecainide	Baseline	Flecainide	Baseline	Flecainide	Baseline	Flecainide	Baseline	Flecainide	Baseline	Flecainide
	23.5±2.3(11)	29.8±3.0(11)	22.2±2.1(11)	29.6±3.3(11)	21.9±2.4(10)	28.7±3.5(10)*	30.5±2.4(11)	38.5±3.3(11)#	28.0±2.3(13)	40.2±2.8(13)#	27.5±2.5(13)	41.2±3.0(13)*#
Left atrial monophasic action potential duration (ms)												
	Baseline	Flecainide	Baseline	Flecainide	Baseline	Flecainide	Baseline	Flecainide	Baseline	Flecainide	Baseline	Flecainide
APD50	10.2±1.3(8)	14.5±1.7(8)	10.8±1(8)	11.9±1.6(8)	10.4±0.7(7)	12.0±1.1(7)	12.4±1.1(15)	14.4±1.3(15)	11.5±1.0(15)	12.4±1.1(15)	10.6±0.9(11)	10.3±1.0(11)
APD70	17.8±2.2(9)	23±2.1(9)	18.4±1.6(9)	18.7±2.2(9)	18.1±1.2(8)	18.1±1.9(8)	18.0±1.6(15)	19.2±1.8(15)	16.0±1.4(13)	16.2±1.4(13)	14.9±1.0(10)*	13.1±0.7(10)
APD90	31.3±3.0(8)	37.4±2.8(8)	31.5±2.5(9)	29.9±2.9(9)	31.0±1.4(8)	28.4±2.7(8)	28.3±2.2(13)	29.9±2.2(13)	27.4±2.2(13)	26.6±1.5(13)	26.8±1.7(10)	23.1±1.4(10)
Left atrial transmembrane action potential duration (ms)												
	Baseline	Flecainide	Baseline	Flecainide	Baseline	Flecainide	Baseline	Flecainide	Baseline	Flecainide	Baseline	Flecainide
APD30	4.5±0.1(30)	5.5±0.3(22)	4.5±0.1(30)	5.4±0.3(22)	4.4±0.1(30)	5.2±0.3(22)	4.0±0.1(31)	4.7±0.2(24)	3.9±0.1(31)	4.6±0.2(24)	3.8±0.1(31)*	4.4±0.2(24)
APD50	6.7±0.2(30)	8.2±0.5(22)	6.6±0.2(30)	8.0±0.4(22)	6.4±0.2(30)	7.8±0.5(22)	5.9±0.2(31)	7.1±0.4(24)	5.7±0.2(31)	7.0±0.4(24)	5.6±0.2(31)*	6.7±0.3(24)
APD70	10.5±0.4(30)	12.7±0.8(22)	10.1±0.4(30)	12.1±0.7(22)	9.6±0.4(30)	11.8±0.7(22)	8.9±0.4(31)	10.7±0.6(24)	8.6±0.4(31)	10.3±0.6(24)	8.3±0.3(31)*	9.8 ± 0.5(24)
APD90	20.9±1.0(30)	23.4±1.5(22)	19.9±0.9(30)	22.2±1.4(22)	18.4±0.8(30)	21.6±1.3(22)	17.6±0.9(31)	20.3±1.1(24)	16.5±0.8(31)	19.2±1.0(24)	15.7±0.8(31)*	17.9±0.9(24)
Left atrial optical action potential duration (ms)												
	Baseline	Flecainide	Baseline	Flecainide	Baseline	Flecainide	Baseline	Flecainide	Baseline	Flecainide	Baseline	Flecainide
APD30	6.1±0.3(10)	7.3±0.6(6)	6.4±0.8(10)	5.9±1.0(6)	6.1±0.4(10)	6.9±1.3(6)	4.9±0.4(10)	7.7±0.9(8)	4.6±0.3(10)	5.4±0.7(8)	4.3±0.4(10)*	5.7±0.7(8)
APD50	8.5±0.6(10)	10.7±1.2(6)	8.9±1.1(10)	8.5±1.2(6)	8.3±0.7(10)	10.3±1.8(6)	6.9±0.4(10)	10.0±1.0(8)	6.6±0.4(10)	8.1±0.9(8)	6.1±0.4(10)*	8.0±0.9(8)
APD70	11.7±1.2(10)	15.0±2.1(6)	12.5±1.5(10)	12.8±1.7(6)	11.5±1.1(10)	14.4±2.5(6)	9.4±0.0(10)	13.3±1.2(8)	9.4±0.6(10)	11.6±1.5(8)	9.1±0.5(10)*	11.2 ± 1.2(8)

Table 3: Electrophysiological effects of sotalol (10μmol/L) in Pitx2c$^{+/-}$ and wildtype left atria.

All values are given as mean±SEM; number of atria are in brackets

Wildtype				Pitx2c$^{+/-}$			
120		100		120		100	
Left atrial effective refractory period							
Baseline	Sotalol	Baseline	Sotalol	Baseline	Sotalol	Baseline	Sotalol
38.7±7.8(7)	33.9±6.3(7)	32.2±6.1(6)	29.2±5.3(6)	39.3±4.0(4)	26.8±3.5(4)	37.0±5.7(4)	24.0±3.7(4)
Left atrial action potential duration							
Baseline	Sotalol	Baseline	Sotalol	Baseline	Sotalol	Baseline	Sotalol
11.5±1.2(9)	13.4±1.2(9)	10.9±2.0(7)	12.2±1.3(7)	10.8±1.1(7)	11.2±1.0(7)	8.3±0.9(4)	11.1±1.7(4)
17.6±2.2(9)	20.0±1.9(9)	16.0±1.3(7)	18.2±2.3(7)	16.5±1.6(7)	17.3±1.2(7)	13.0±1.5(4)	17.0±1.9(4)
30.7±3.2(9)	33.5±2.7(9)	29.0±1.9(7)	30.9±3.2(7)	29.7±2.7(7)	31.2±2.0(7)	23.8±2.8(4)	29.6±2.9(4)

Table 4: Electrophysiological effects of reduced sodium conductance in a human atrial model of PITX2 deficiency

	Wildtype model		Pitx2c-deficiency model	
Paced cycle length (ms)	500	1000	500	1000
g_{Na}	**Resting membrane potential (mV)**			
100%	-79.92	-81.28	-77.90	-79.61
50%	-79.6	-81.12	-77.33	-79.37
40%	-79.43	-81.01	-76.99	-79.23
g_{Na}	**Action potential duration at repolarization to -60 mV (ms)**			
100%	217	253	206	226
50%	239	266	233	239
40%	248	273	245	245
g_{Na}	**Effective refractory period (ms)**			
100%	266	301	261	280
50%	308	335	316	320
40%	327	352	342	339
g_{Na}	**Post-repolarization refractoriness (ms)**			
100%	49	48	55	54
50%	69	69	83	81
40%	79	79	97	94
gNa	**Conduction velocity (cm/s)**			
100%	49.5	50.0	50.3	50.5
50%	36.9	37.0	37.5	37.5
40%	32.9	32.7	33.0	33.1

Table 5. Electrical activation time and conduction velocity in Pitx2c$^{+/-}$ and wildtype left atria. All values are given as mean±SEM; number of atria are in brackets.

	Wildtype					Pitx2c$^{+/-}$				
Paced cycle length (ms)	1000	300	120	100	80	1000	300	120	100	80
Activation time (ms)	6±0.3(22)	6±0.3(22)	9±0.5(22)	12±1.0(22)	16±1.4(22)	6±0.2	7±0.3	12±0.9	13±0.9	18±1.2
Conduction Velocity (cm/s)	----	30±1.8(8)	25±2.4(8)	25±1.9(8)	23±1.9(8)	---	29±1.5(8)	26±1.6(8)	25±1.6(8)	23±1.6(8)

Table 6: **PITX2c expression in LA tissue obtained from AF ablation patients**. This dataset was grouped according to the number of high-risk SNP alleles of SNP1 rs2200733, SNP2 rs6838973 and SNP3 rs1448818. These three SNPs are located close to the PITX2 gene. Data were divided into 0-6 high-risk alleles. The data demonstrated that there were no trends in mRNA expression associated with increasing number of risk alleles.

Risk Alleles	Min.	25% IQR	Median	75% IQR	Max.	Mean	SEM	N
0	3.22	3.22	3.69	5.22	5.22	4.04	0.6	3
1	1.83	2.96	4.25	6.25	7.16	4.54	0.5	13
2	2.05	2.65	3.78	4.75	7.11	3.94	0.3	22
3	1.12	2.74	3.72	4.92	7.42	3.83	0.4	17
4	2.13	3.00	4.29	5.41	7.73	4.39	0.5	10
5	1.94	1.96	2.66	4.66	5.12	3.10	0.7	4
6	4.95	4.95	4.95	4.95	4.95	4.95	0	1

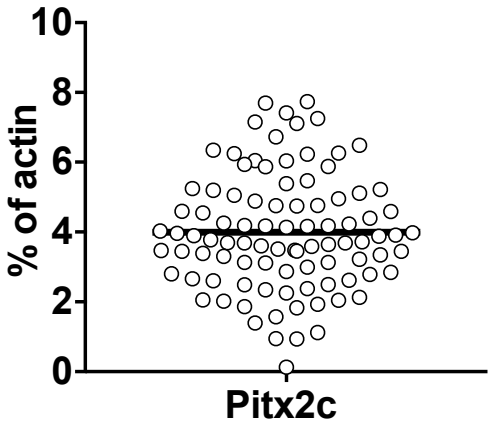

Figure 1

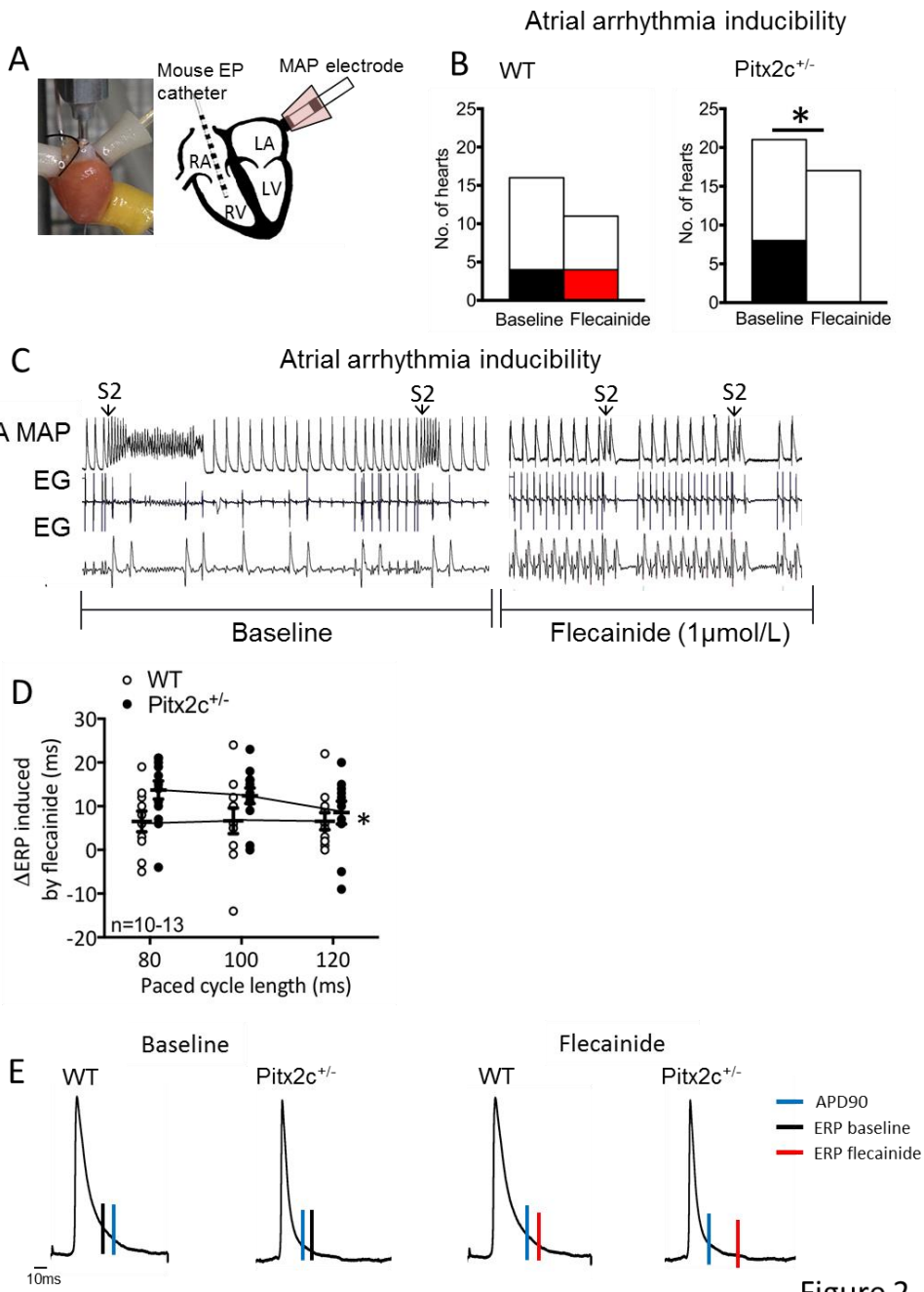

Figure 2

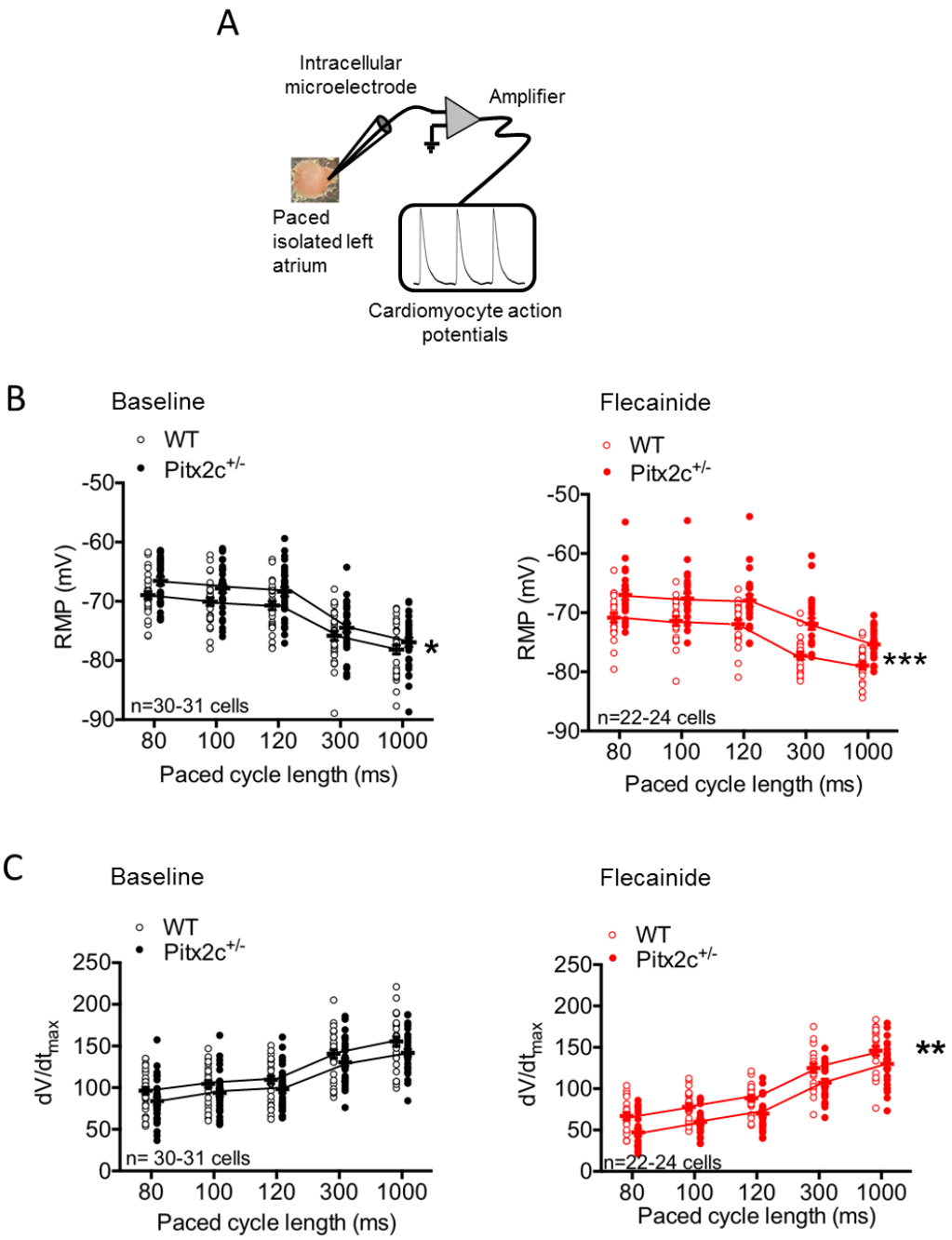
A
Intracellular microelectrode
Amplifier
Paced isolated left atrium
Cardiomyocyte action potentials
B
Baseline
WT
Pitx2c+/-
RMP (mV)
-50
-60
-70
-80
-90
n=30-31 cells
*
80
100
120
300
1000
Paced cycle length (ms)
Flecainide
WT
Pitx2c+/-
RMP (mV)
n=22-24 cells
***
Paced cycle length (ms)
C
Baseline
WT
Pitx2c+/-
dV/dtmax
250
200
150
100
50
0
n= 30-31 cells
Paced cycle length (ms)
Flecainide
WT
Pitx2c+/-
dV/dtmax
n=22-24 cells
**
Paced cycle length (ms)

Figure 3

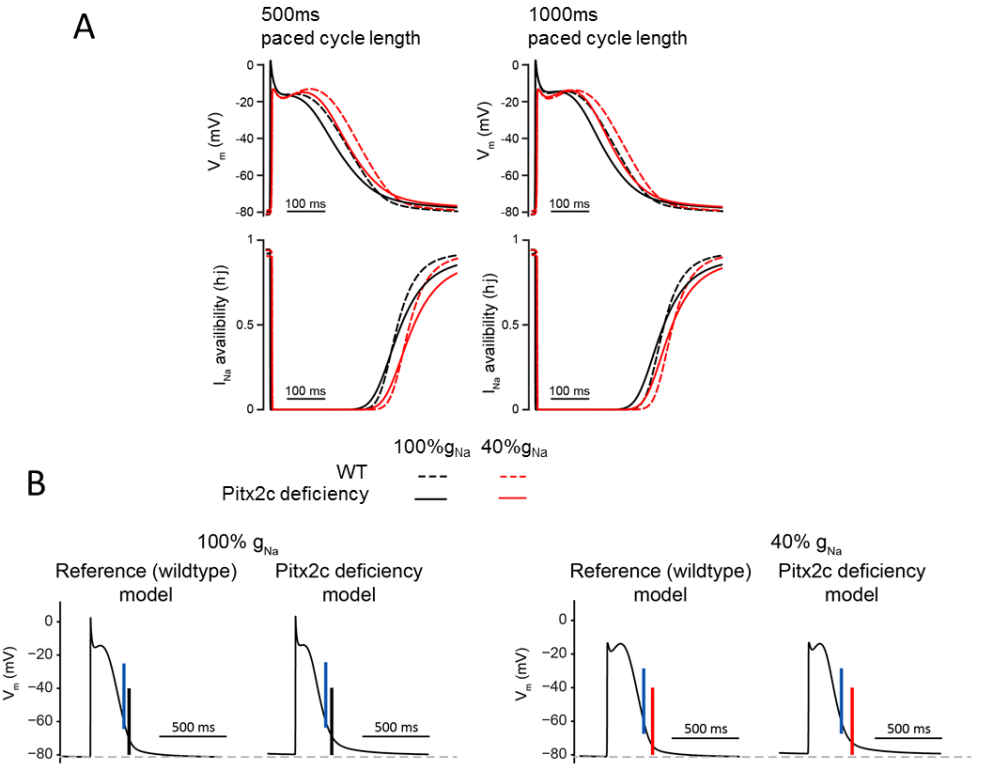

Figure 4

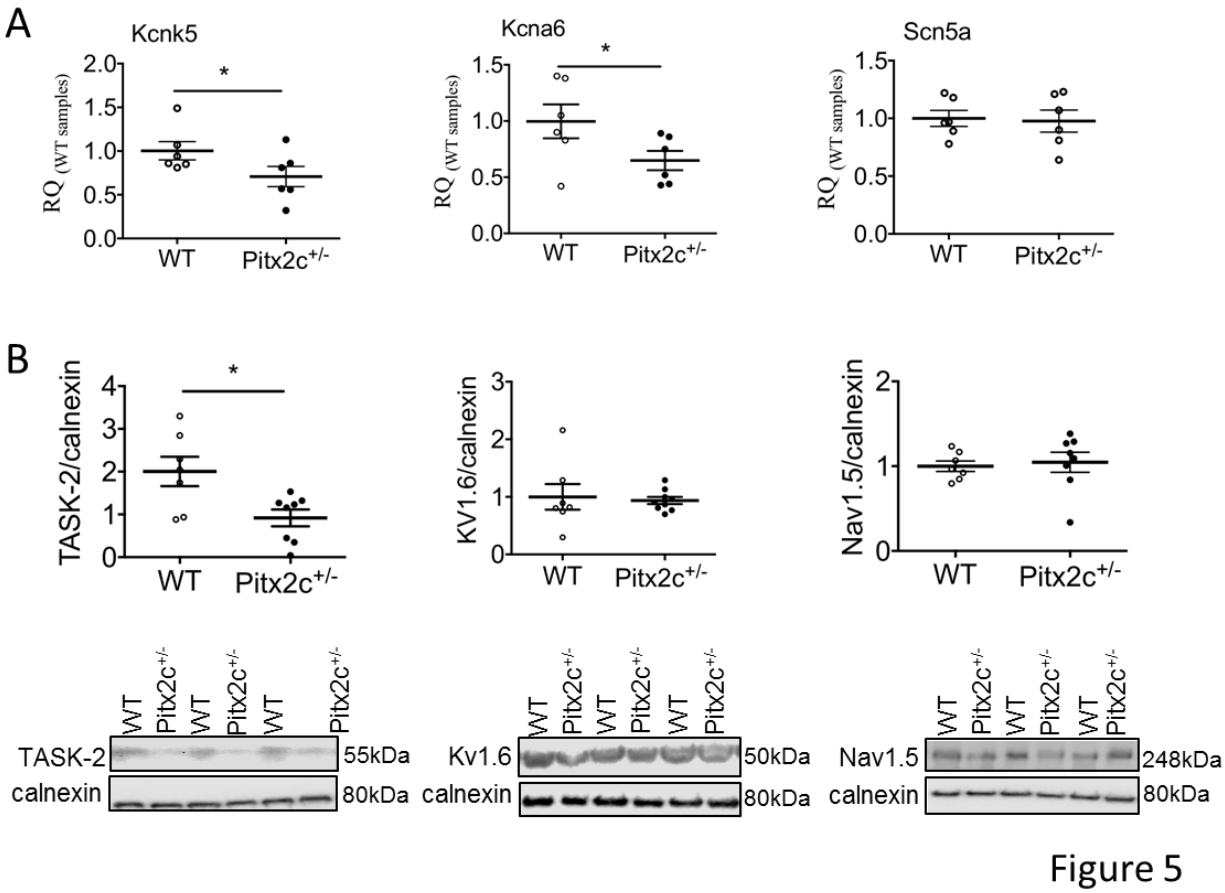

Figure 5

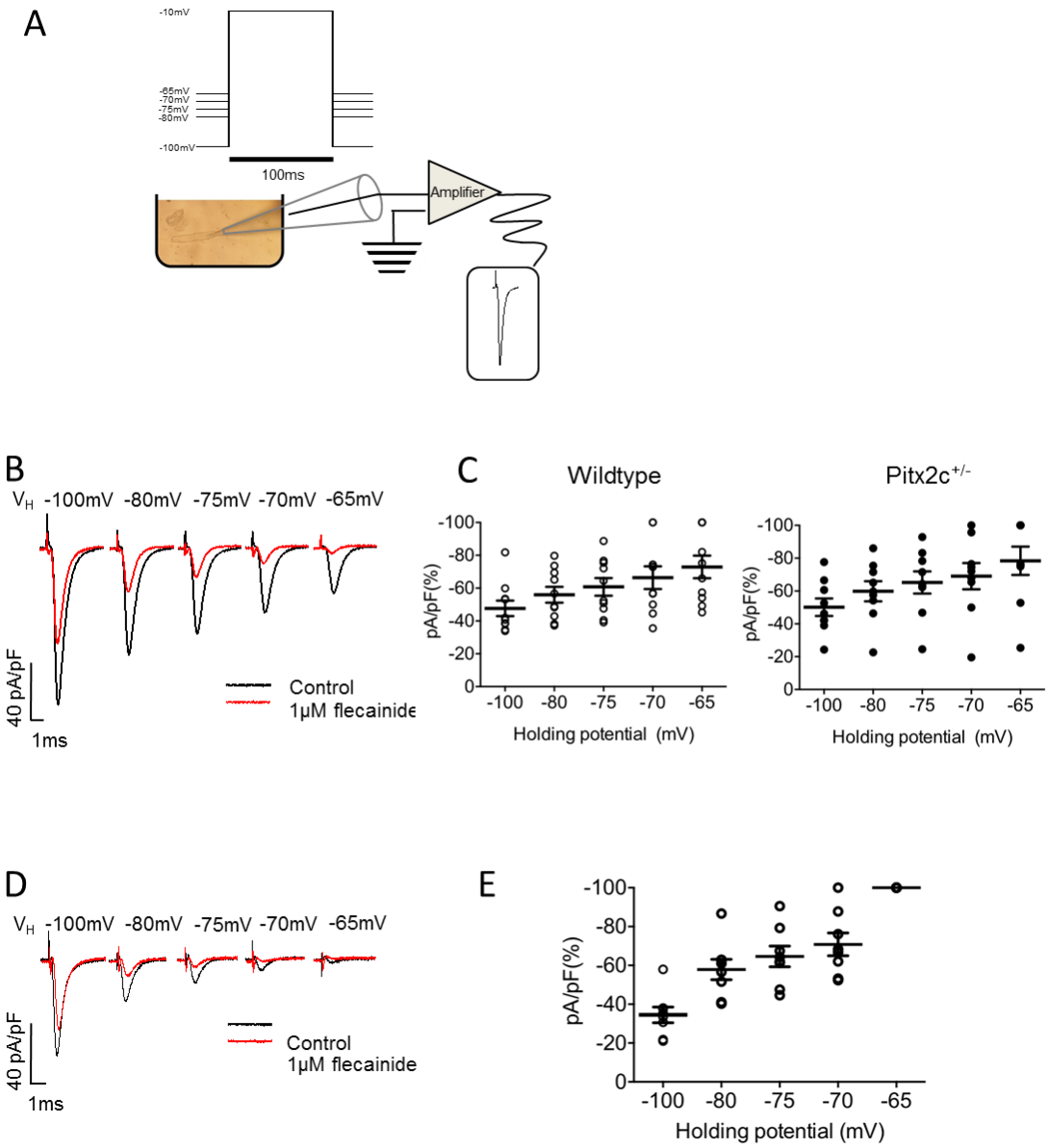
A
-10mV
-65mV
-70mV
-75mV
-80mV
-100mV
100ms
Amplifier
B
V_H -100mV -80mV -75mV -70mV -65mV
40 pA/pF
1ms
Control
1μM flecainide
C
Wildtype
Pitx2c+/-
pA/pF(%)
-100
-80
-60
-40
-20
0
-100 -80 -75 -70 -65
Holding potential (mV)
D
V_H -100mV -80mV -75mV -70mV -65mV
40 pA/pF
1ms
Control
1μM flecainide
E
pA/pF(%)
-100
-80
-60
-40
-20
0
-100 -80 -75 -70 -65
Holding potential (mV)

Figure 6

Appendix 6 - Can preload-reducing therapy prevent disease progression in arrhythmogenic right ventricular cardiomyopathy? Experimental evidence and concept for a clinical trial.

Progress in Biophysics and Molecular Biology 110 (2012) 340–346

Contents lists available at SciVerse ScienceDirect

Progress in Biophysics and Molecular Biology

journal homepage: www.elsevier.com/locate/pbiomolbio

Review

Can preload-reducing therapy prevent disease progression in arrhythmogenic right ventricular cardiomyopathy? Experimental evidence and concept for a clinical trial

Larissa Fabritz [a,b,*], Lisa Fortmüller [b], Ting Y. Yu [a,c], Matthias Paul [b], Paulus Kirchhof [a,b]

[a] Centre for Cardiovascular Sciences, School of Clinical and Experimental Medicine, College of Medical and Dental Sciences, University of Birmingham, United Kingdom
[b] Department of Cardiology and Angiology, University Hospital Münster, Germany
[c] Physical Sciences of Imaging in the Biomedical Sciences, Doctoral Training Centre, School of Chemistry, University of Birmingham, United Kingdom

ARTICLE INFO

Article history:
Available online 27 August 2012

Keywords:
Preload
Arrhythmogenic right ventricular cardiomyopathy (ARVC)
Sudden death
Athletes
Sports medicine
Mechanical cell–cell contacts

ABSTRACT

Arrhythmogenic right ventricular cardiomyopathy (ARVC) is an inherited cardiomyopathy and a leading cause of sudden cardiac death in a young population. ARVC is especially common in young athletes. Mutations in different desmosomal genes have been identified causing dysfunctional cell–cell contacts. Reduced myocardial expression of plakoglobin in cell–cell contact complexes appears to associate with disease manifestation in patients harbouring mutations within other cell–cell contact genes. Experimental data suggest that preload reduction may be a simple and effective intervention to prevent disease progression and ventricular arrhythmias in ARVC. This review discusses the potential effects of this innovative approach and describes the design of the first controlled trial of preload-reducing therapy in patients with ARVC.

Contents

1. The medical problem

Arrhythmogenic right ventricular cardiomyopathy (ARVC) alongside hypertrophic cardiomyopathy (Kaltman et al., 2011), is one of the leading causes of sudden death in the Young, and one of the main causes of unexpected death in athletes (Corrado et al., 2006; Marcus et al., 2010). The prevalence of ARVC is estimated at 1:1000 in Europe (Sen-Chowdhry et al., 2010). Every year, at least one

* Corresponding author. Centre for Cardiovascular Sciences, School of Clinical and Experimental Medicine and SWBH NHS Trust, College of Medical and Dental Sciences, University of Birmingham, Wolfson Drive, Edgbaston Birmingham B15 2TT, UK. Tel.: +44 121 414 6259, +44 121 414 6938; fax: +44 121 414 8867.
E-mail address: L.Fabritz@bham.ac.uk (L. Fabritz).

0079-6107/$ – see front matter © 2012 Elsevier Ltd. All rights reserved.
http://dx.doi.org/10.1016/j.pbiomolbio.2012.08.010

professional cyclist, football/soccer or basketball player makes headline news due to sudden cardiac death during a race or a match secondary to ARVC. Practice of competitive sports clearly co-segregates with ARVC, suggesting that strong physical training, and especially endurance sports such as cycling, swimming or long-distance running, accelerates disease development in patients (Corrado et al., 2006; Heidbuchel et al., 2003).

2. Evidence of disease mechanism

In the majority of patients with ARVC, mutations in genes encoding proteins of mechanical intercellular connections have been identified, leading to the recognition of ARVC as a "disease of the desmosome" (Asimaki et al., 2007; Gerull et al., 2004; Sen-Chowdhry et al., 2007; Syrris et al., 2007; van Tintelen et al., 2006). Among those with predominant autosomal-dominant mode of inheritance (Sen-Chowdhry et al., 2010) are plakophilin, desmoplakin, desmoglein, desmocollin, and plakoglobin. Mutations within plakophilin-2 were the first to be identified in a considerably large proportion of patients with ARVC (Gerull et al., 2004; van Tintelen et al., 2006), however, penetrance and clinical disease manifestation were variable (Dalal et al., 2006; Lahtinen et al., 2011) outside of specific, often recessive subforms such as Naxos disease or Carvajal syndrome (Norgett et al., 2000; Protonotarios et al., 2001).

Recent reports suggest that desmoglein-2 mutations harbour dual effects by: a) modifying the interaction with n-cadherin at the myocardial cell–cell contacts, thereby possibly reducing plakoglobin binding to the cell–cell contact complexes (Gehmlich et al., 2010; Syrris et al., 2007), and b) inducing cardiomyocyte necrosis and cardiac fibrosis (Kant et al., 2012; Pilichou et al., 2009). Similarly, both electrophysiological alterations (e.g. conduction slowing), and structural changes (i.e. fibrofatty replacement) are found (Gomes et al., 2012). Of note, the electrophysiological changes precede structural alterations in desmoplakin mutants (Gomes et al., 2012).

Analyses of right ventricular endomyocardial biopsies and cardiac post-mortem specimen from ARVC patients carrying different desmosomal gene defects identified reduced plakoglobin expression (Asimaki et al., 2009) thereby indicating that a reduction of this desmosomal protein could pathophysiologically be regarded as the "final common pathway" in ARVC and may also be utilized to discriminate ARVC from other cardiomyopathies (Asimaki et al., 2011).

3. Evidence from disease models

Several elegant studies in genetically modified mice have shown that genetic disruption of desmoplakin, plakoglobin, and desmoglein is sufficient to replicate the phenotype of ARVC (Garcia-Gras et al., 2006; Gehmlich et al., 2011; Kirchhof et al., 2006; Krusche et al., 2011; Pilichou et al., 2009). Disease expression differs in models carrying different genetic defects: right ventricular dysfunction and ventricular arrhythmias are predominantly observed in plakoglobin-deficient mice (Kirchhof et al., 2006); biventricular fibrosis is most prominently detected in desmoplakin-deficient mice (Garcia-Gras et al., 2006); and cardiomyocyte necrosis/fibrosis are found in desmoglein-mutant mice (Krusche et al., 2011; Pilichou et al., 2009).

More recent data confirm that cardiomyocyte-directed deletion of plakoglobin (i.e. >80% reduction of plakoglobin expression by induced heart-directed deletion) causes the histological changes of ARVC including fibrosis and heart failure (Li et al., 2011), while heterozygous deletion of plakoglobin (i.e. reducing plakoglobin content to approximately 50%) provokes the complete functional phenotype of ARVC without histological alterations (Kirchhof et al., 2006). Consequently, it could be hypothesised that lack of plakoglobin at the mechanical cell–cell contacts is responsible for the functional changes in ARVC, including right ventricular enlargement, right ventricular dysfunction, and right ventricular conduction slowing, while dislocation of plakoglobin to the nuclear compartment in the cell, e.g. secondary to decreased plakoglobin binding at the cell membrane, may confer some of the structural changes which are summarised as fibro-fatty infiltration (Garcia-Gras et al., 2006), and may be the late reflection of cardiomyocyte necrosis (Pilichou et al., 2009).

This might also explain the sequence of changes associated with desmoglein mutants whereby functional electrophysiological changes precede structural alterations (Gomes et al., 2012).

To summarise, the different models support a cascade of events by which a genetically conferred reduction of plakoglobin in the intercellular connections results in "early" functional defects such as ventricular arrhythmias and right heart dilation, while a more marked reduction of plakoglobin and/or a translocation of plakoglobin to the nucleus appears to be associated with the later development of fibrosis, cardiomyocyte necrosis and other structural changes induced by mutated cell–cell contact proteins.

In the plakoglobin-deficient model, endurance exercise training markedly accelerates the development of ARVC (Kirchhof et al., 2006), thereby corroborating the clinical suspicion that chronically increased right ventricular preload as provoked by endurance sports expedites disease progression (Corrado et al., 2006; Heidbuchel et al., 2003). Of note, athletes with right ventricular arrhythmias show reduced right ventricular function when compared to athletes without arrhythmias (Ector et al., 2007). Even in otherwise healthy endurance athletes, intense exercise has recently been shown to cause transient right ventricular dysfunction and structural remodelling in magnetic resonance imaging (La Gerche et al., 2012).

4. The need for a disease-modifying therapy in ARVC

At present, no therapy is available to prevent disease progression in ARVC patients. Management, therefore, focuses on reducing the risk of sudden death by antiarrhythmic drug therapy, implantation of a defibrillator, catheter ablation to prevent frequent arrhythmia recurrences, or a combination of these (Sen-Chowdhry et al., 2010; Wichter et al., 2004). Antiarrhythmic drug therapy is needed in addition to defibrillator therapy in many ARVC patients to reduce the burden of ventricular arrhythmias (Marcus et al., 2009; Wichter et al., 2004), and catheter ablation of ventricular tachycardias is performed regularly as palliation in patients with frequent shocks (Carbucicchio et al., 2008). Although the use of 3D-electroanatomic mapping systems and epicardial ablation strategies are associated with longer VT-free survival, recurrence rates remain considerable (Philips et al., 2012). Furthermore, many patients, though not eligible for defibrillator implantation, are still at increased risk of sudden death (Corrado et al., 2010). Complications associated with defibrillator therapy are higher in ARVC patients due to the diffuse or segmental progressive right ventricular fibro-fatty replacement of viable myocardium (Marcus et al., 2009; Wichter et al., 2004). Antiarrhythmic therapy also harbours specific therapy-associated problems: 1. Antiarrhythmic drug therapy is still widely empiric and often relies on sotalol and amiodarone, two agents with well-known cardiac and extracardiac toxicity (Marcus et al., 2009). 2. Even when managed in specialised centres with diligent intra- and perioperative management of implantable cardioverter-defibrillator (ICD) recipients, frequent defibrillator-related complications (affecting up to 45% of patients during long-term follow-up; (Tavernier et al., 2001; Wichter et al., 2004)) and a high prevalence of adequate defibrillator shocks due to disease progression are still unresolved clinical problems in this cohort of relatively young, active, and otherwise healthy individuals. Furthermore, the

improved longevity of ARVC patients on antiarrhythmic management leads to more patients experiencing the later stages of the disease, characterised by progressive right heart failure, at times even requiring heart transplant therapy.

A therapeutic intervention that could slow or possibly even halt progression of ARVC is therefore desperately needed. The recent elucidation of the molecular cause of ARVC in patients and models may allow us to devise such a therapy based on the pathophysiological effects of reduced cell–cell contacts.

5. The physiological role of preload in the heart

Preload is related to right atrial pressure. The most important determinant of right atrial pressure is venous return. This is affected by venous tone and volume of circulating blood, and can be reduced by a single dose of a nitrate (Marmor et al., 1989). Right ventricular function is especially susceptible to changes in preload, as evidenced by marked variations in right ventricular function and cardiac output depending on respiration phase (inspiration or expiration) (Caplin et al., 1989; Olsen et al., 1985), postural position (Guazzi et al., 1995), in response to fluid challenge (Squara et al., 1997), or in response to exercise (La Gerche et al., 2012) in humans. Model systems in engineering can help to study isolated intact cardiomyocytes subjected to dynamic changes in mechanical load (Iribe et al., 2007).

Due to its ellipsoid geometry, left ventricular preload can be calculated based on the Law of Laplace: left ventricular end-diastolic pressure × left-ventricular end-diastolic radius (measured at the ventricular midpoint) divided by 2 times the left ventricular wall thickness.

LVEDP * LVEDR/(2*h), applied e.g. in Martin and Haines (1970). When preload is given, this formula can, conversely, be used to determine wall strain of the left ventricle.

6. Right ventricular preload

As discussed above, the right ventricle is more susceptible to acute changes in preload than the left ventricle due to the comparably thinner wall that bestows higher compliance (Caplin et al., 1989; Guazzi et al., 1995; Olsen et al., 1985; Squara et al., 1997). It was the right rather than the left ventricle of endurance athletes which was affected by temporal dysfunction after a peak exercise as detected in magnetic resonance imaging (La Gerche et al., 2012).

While the ellipsoid shape of the left ventricle allows a valid estimation of left ventricular wall stress by Laplace's formula (see section 5), the complex anatomy of the right ventricle renders estimation of right ventricular wall stress more difficult: Fig. 1 illustrates a CT-based model of right ventricular anatomy (Fig. 1 left, see online data for moving sequence), provides two simplified schemes of increase in right ventricular preload (Fig. 1, center) and an experimental example of acute change in right ventricular size during instantaneous increase in preload by volume challenge in murine echocardiography (Fig. 1, right). Ellipsoid or crescent-like volume assumptions have been evaluated to estimate right ventricular volume (Aebischer et al., 1998): In principle, the concepts of preload that have been developed to understand left ventricular function are comparable in the right ventricle. Right ventricular end-diastolic pressure can be directly measured by catheterisation (Braunschweig et al., 2002; Stevenson et al., 2010). The thickness of the right ventricle (h in the equation) is 1/3 to 1/10 of left ventricular thickness (Hauser et al., 1985; Outhred et al., 1970), with the thinner areas in the apical region. The anatomy and morphology of the right ventricle is markedly different from an ellipsoid, hence forming predilection points for increased local wall stretch (Fig. 1, center). The shape of the right ventricle has been described as a pyramid or a crescent (Aebischer et al., 1998; Ector et al., 2007; Song, 2011). We have previously published and validated a formula that estimates right ventricular volume based on echocardiographically accessible right ventricular diameters (Kirchhof et al., 2006). This formula assumes a right ventricular shape delineated by two convex ellipsoids that are curved in the same direction, generating a "shell-like" or "crescent" (Aebischer et al., 1998) right ventricular shape that wraps around the left ventricle (Fig. 1, lower left panel). Similar assumptions have been applied later in a quantitative angiographic study of right ventricular function in endurance athletes (Ector et al., 2007).

We hypothesise that the edges of the right ventricular chamber may be exposed to more regional wall movement, stretch and preload when compared to other areas within the right ventricular anatomy, or when compared to any area within an ellipsoid structure (Fig. 1). This physiological consideration would suggest that the corners of the right ventricular shape, i.e. the inferior wall close to the right ventricular apex, the superior area (outflow tract), and the inferior area, would be exposed to increased stretch. First magnetic resonance data in humans support this: In normal subjects with normal load, and also in patients with tetralogy of Fallot, the apical area and the outflow tract are exposed to high strain rates compared to the inflow tract, when assessed by magnetic resonance techniques (Auger et al., 2012; Zhong et al., 2012), While these observations await validation in larger cohorts and in ARVC patients, it is worth noting that the predilection spots for right ventricular changes in ARVC are found in the "triangle of ARVC", almost exactly matching the areas that would be predicted to be exposed to increased mechanical load, strain and stretch in the right ventricle. Along these lines, diagnosing right ventricular wall thinning, right ventricular dysfunction and right ventricular outflow tract enlargement was a better predictor of disease than diagnosis of fatty infiltration (Tandri et al., 2006).

In summary, the reduced right ventricular wall thickness and the non-ellipsoid anatomy of the right ventricular cavity render the right ventricle, and focused regions therein more exposed to preload and regional aggravation to preload when compared to the left ventricle (Fig. 1).

7. Pharmacological preload reduction

Venous vasodilators reduce venous return and therefore cardiac preload (Cohn, 1987; Holtz et al., 1978; Marmor et al., 1989; McDonald et al., 1993). Although most vasodilator drugs dilate both veins and arteries, some drugs, such as organic nitrates, are relatively selective for venous return. This could conceptually increase their tolerability when compared to afterload-reducing substances, especially in young, active individuals. Venous dilation increases venous compliance by relaxing the venous smooth muscle. Increased compliance decreases the mean circulatory filling pressure resulting in a small decrease in right atrial pressure. Thereby, venous dilation decreases right ventricular preload (Cohn, 1987; Holtz et al., 1978; Marmor et al., 1989; McDonald et al., 1993). Diuretics, in contrast, can reduce preload by reducing systemic blood volume (Kraus et al., 1990).

8. Preload-reducing therapy to prevent disease progression in arrhythmogenic right ventricular cardiomyopathy

After we observed that the full functional phenotype of ARVC develops in mice with heterozygous deletion of plakoglobin (Kirchhof et al., 2006), we started to devise an intervention that could reduce the mechanical load delivered to the genetically weakened mechanical cell–cell connections. We tested whether a preload reducing therapy could slow progression of ARVC in this

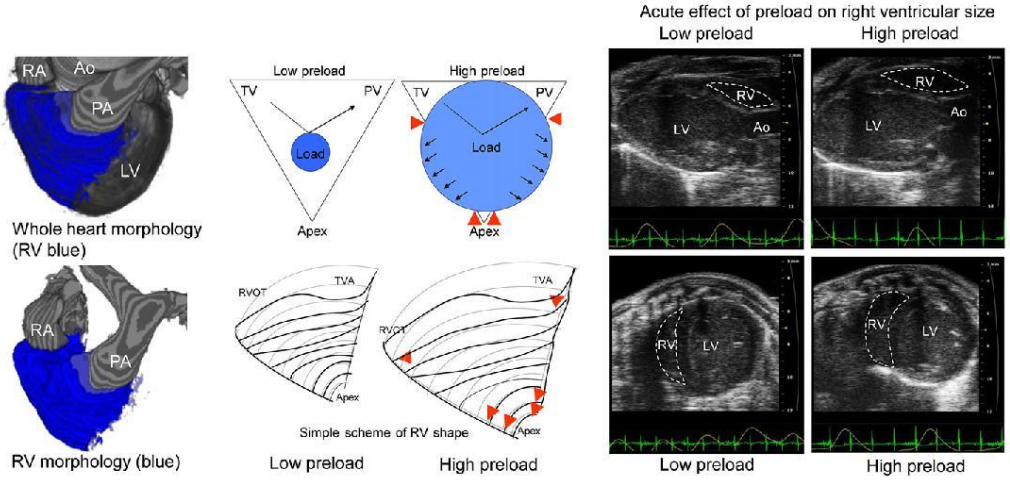

Fig. 1. Right ventricular shape and preload. Left: models depicting the shape of heart and right ventricle generated from computed tomography data by image reconstruction algorithms. The blue areas indicate the right ventricle. The upper panel shows the entire heart in a supero-anterior view, the lower image shows an anterior view of the right ventricle curved around the ellipsoid left ventricle. In order to create the 3D model of the human heart, example data was extracted from the OsiriX archive (Cardiac CT64). Due to the nature of the image acquisition process in clinical CT scans, areas of non interest could be excluded using manual thresholding but images with poor contrast required manual segmentation performed using ImageJ. Atria, right and left ventricle (LV), Aorta (Ao) and pulmonary artery (PA) were manually isolated from each other. Converting the images from greyscale to binary allowed for better visualisation of the right ventricle. The image sequence is stacked together using the ImageJ 3D viewer plugin. Bottom left: All areas have been excluded apart from the right ventricle and right atrium (RA), along with the pulmonary artery (PA). Center: simple schemes of changes in right ventricular preload. Scheme of unloaded (centre left) and loaded (centre right) right ventricle. Changes in preload may result in differences in stretch depending on the tissue location in the RV. Apex, outflow tract/anterior infundibulum may be especially prone to stretch-induced disease. Red arrows point to areas with increased potential for stretch-induced stress as a fixed and thinned area is exposed to stretch. TV, Tricuspid valve, PV pulmonary valve, RVOT right ventricular outflow tract, TVA, Tricuspid valve area. Right: Example of the acute effects of low preload (left) and high preload (right) on right ventricular size in a wild-type mouse visualised by 2-dimensional right ventricular echocardiography in the long axis view (upper row) and short axis view (lower row). The measurements were obtained before and after an acute volume administration (2 ml NaCl i.p.) accompanied with decrease in heart rate. Ao, Aorta, LV, left ventricle, RV, right ventricle, area marked by dotted line: estimated right ventricular 2-dimensional extensions in that particular plane.

plakoglobin-deficient model by assessing the effect of chronic therapy with nitrates (Holtz et al., 1978; McDonald et al., 1993), and diuretics (Kraus et al., 1990) on right ventricular size and function in heterozygous plakoglobin-deficient mice. In this controlled, and blinded trial, preload reduction using a fixed combination of nitrates and diuretics was well tolerated and prevented development of ARVC, rendering preload-treated heterozygous plakoglobin-deficient mice undistinguishable from their wild-type littermates (Fabritz et al., 2011): Preload reduction prevented right ventricular enlargement, right ventricular conduction slowing, and the induction of right ventricular arrhythmias (Fabritz et al., 2011). The flow chart of the preclinical trial is depicted next to the flow chart of the planned clinical trial in Fig. 2. To date, this remains the only example directly testing this therapy to date, but experimental studies in other models are planned or ongoing.

9. Could preload-reducing therapy prevent disease progression in patients with arrhythmogenic right ventricular cardiomyopathy? Design of the PreVENT-ARVC trial

The observation that preload reduction prevents disease manifestation in heterozygous plakoglobin-deficient mice subjected to training raises the question whether such a therapy could be beneficial for patients with ARVC. In an editorial on the study of preload-reducing therapy in the plakoglobin-deficient mouse model (Fabritz et al., 2011), Hugh Calkins commented: "It therefore paves the ground for …strategies focused on prevention of disease development in susceptible individuals, prevention of progression and development of clinically manifest disease, and the development of approaches to reverse ARVD in affected individuals." (Calkins, 2011). The editorial also notes that "there has never been a prospective randomized clinical trial of any therapeutic modality for treatment of patients at risk of or affected by ARVD", while also mentioning that some of the beneficial effects of preload reduction could possibly also be obtained by angiotensin-converting-enzyme inhibition or ß-adrenoceptor-blockade (Calkins, 2011), the latter being part of standard ARVC therapy. Both of these also significantly decrease afterload and warrant further investigations in different experimental models of ARVC and controlled trials in ARVC patients as well.

These preclinical data suggest that preload reduction may be a simple and effective intervention to prevent disease progression and the occurrence of potentially life threatening ventricular arrhythmias in patients with ARVC. The fact that the preclinical study was done with clinically available substances and the finding that many patients with ARVC display reduced myocardial plakoglobin expression (Asimaki et al., 2009) suggest that a clinical trial of preload reduction could be feasible.

However, such a trial would have to address several questions: Treating patients who are susceptible to ARVC or have established ARVC with a diuretic may, as eluded to by Calkins, carry potential risks associated with electrolyte depletion and nitrate intolerance in addition to the well-recognized side effects of nitrate therapy. Nitrates are well-tolerated in patients with coronary artery disease or global heart failure, but it is not clear whether the known side-effects render such a therapy tolerable in young patients with

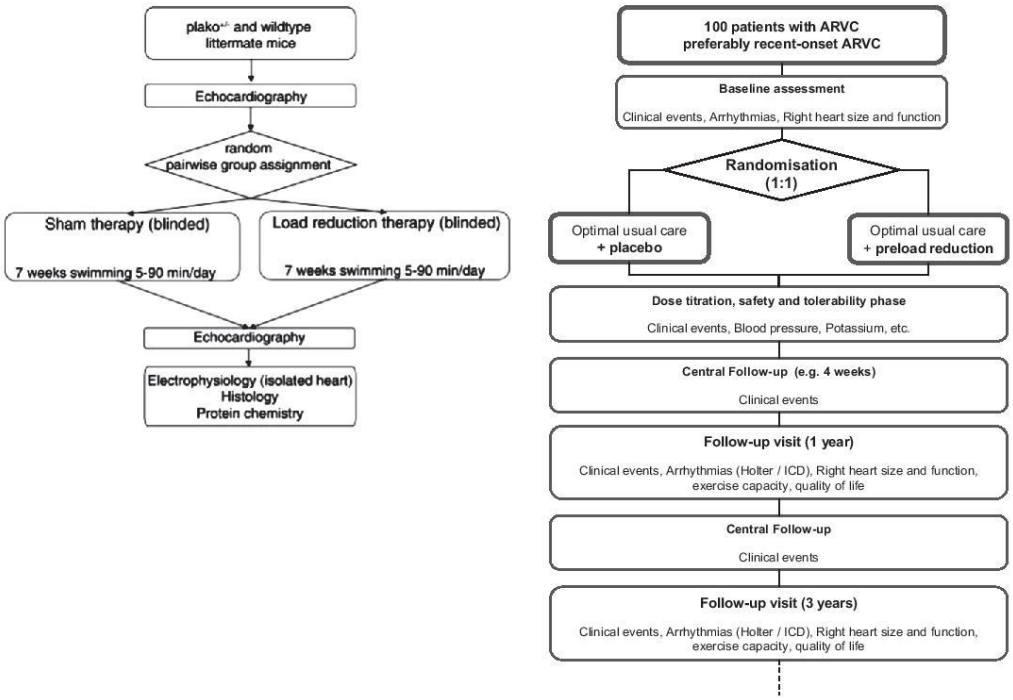

Fig. 2. Flow charts. Left: Flow chart of preclinical trial in a murine model of Arrhythmogenic right ventricular cardiomyopathy that has shown prevention of disease by preload reduction (from Fabritz et al., JACC, 2011). Right: Flow chart of the PreVENT-ARVC® trial, a trial of preload reduction in patients with recently diagnosed ARVC. Primary outcomes of the main trial will be the time to the first occurrence of life-threatening ventricular arrhythmias or death. The safety outcomes of the initial phase, tolerability, side effects, and changes in blood pressure, can help adjust dosing of the trial intervention, and confirm tolerability of preload reduction in patients with ARVC.

overwhelmingly selective right heart dysfunction. It is also unclear whether established substances to improve systolic left ventricular function such as ß-adrenoceptor-blockers or angiotensin-converting-enzyme inhibitors, could evoke similar results as preload reduction with nitrates and diuretics in ARVC (Calkins, 2011). Preload-reducing therapy given on top of usual care which often includes ß-adrenoceptor-blockers may therefore have less obvious beneficial effects and possibly more unwanted effects.

Another consideration is that the preclinical study (Fabritz et al., 2011) initiated preload reduction prior to full disease manifestation, while a clinical trial would only be feasible in patients with already established disease. Finally, the therapy was tested in only one animal model, harbouring a genetic defect that is not associated with structural right ventricular changes. To test the effect of training and preload reduction in experimental models of ARVC developing overt structural abnormalities, e.g. a desmoglein 2 mutant (Krusche et al., 2011), would therefore particularly be of interest.

Estimation of event rates taken from ARVC registries and assumptions on the potential effects of preload reduction in patients with ARVC suggest that such a trial could be feasible with approximately one hundred ARVC patients. Together with expert colleagues from dedicated ARVC clinics from across Germany, we are initiating this controlled clinical trial testing preload reduction therapy in patients with ARVC (PreVENT-ARVC®). In this trial, patients will be randomised to either optimal standard management or to optimal standard management supplemented by preload reduction (Fig. 2). Based on the considerations discussed above, we have initiated a monocentric safety run-in phase, which will soon commence at the University Hospital Münster, Germany, with ARVC patients carrying an implanted cardioverter-defibrillator to establish the maximal tolerated dosage and to assess the profile of potential side effects (Fig. 2).

The clinical trial intervention mimics the preclinical intervention by applying a combination of nitrates and diuretics in the active therapy group. To maximise tolerability, a long-acting nitrate that does not induce nitrate tolerance will be used (PETN) rather than isosorbid nitrates in alternation with molsidomine. A combination of a thiazide diuretic and a potassium-saving diuretic will be used instead of furosemide. PreVent-ARVC® plans to enrol patients with recently diagnosed ARVC in an attempt to start therapy as early as possible. Even with this prospect, it is far too early to predict whether this innovative and first causal therapeutic approach will mark the corner stone in the clinical management of patients with ARVC.

Editors' note

Please see also related communications in this issue by Kim et al. (2012) and Pellis et al. (2012).

Acknowledgements

Joachim Gerss, and Sabine Jürgensmeyer for help with planning of the PreVENT-ARVC trial, and Genna Riley, Fahima Syeda and Stavros Apostolakis for discussions and reading of the manuscript. We thank Steve Watson, Stuart Egginton and Hamid Dehghani for co-supervision of Ting Y. Yu.

Supported by funds from SFB656 Mobil (LF, PK); DFG FA 413/3-1(LF); starter grant (PK, LF) and preliminary data award (LF) of Research Development Fund, University of Birmingham; Engineering and Physical Sciences Research council funds the PSIBS doctoral training centre, University of Birmingham (TY); and IMF (PA 1 2 11 27, MP, LF), Medical Faculty, University of Münster, Germany.

Appendix A. Supplementary material

Supplementary data related to this article can be found at http://dx.doi.org/10.1016/j.pbiomolbio.2012.08.010.

References

Aebischer, N., Meuli, R., Jeanrenaud, X., Koerfer, J., Kappenberger, L., 1998. An echocardiographic and magnetic resonance imaging comparative study of right ventricular volume determination. Int. J. Card. Imaging 14, 271–278.

Asimaki, A., Syrris, P., Wichter, T., Matthias, P., Saffitz, J.E., McKenna, W.J., 2007. A novel dominant mutation in plakoglobin causes arrhythmogenic right ventricular cardiomyopathy. Am. J. Hum. Genet. 81, 964–973.

Asimaki, A., Tandri, H., Duffy, E.R., Winterfield, J.R., Mackey-Bojack, S., Picken, M.M., Cooper, L.T., Wilber, D.J., Marcus, F.I., Basso, C., Thiene, G., Tsatsopoulou, A., Protonotarios, N., Stevenson, W.G., McKenna, W.J., Gautam, S., Remick, D.G., Calkins, H., Saffitz, J.E., 2011. Altered desmosomal proteins in granulomatous myocarditis and potential pathogenic: links to arrhythmogenic right ventricular cardiomyopathy. Circ. Arrhythm Electrophysiol.

Asimaki, A., Tandri, H., Huang, H., Halushka, M.K., Gautam, S., Basso, C., Thiene, G., Tsatsopoulou, A., Protonotarios, N., McKenna, W.J., Calkins, H., Saffitz, J.E., 2009. A new diagnostic test for arrhythmogenic right ventricular cardiomyopathy. N. Engl. J. Med. 360, 1075–1084.

Auger, D.A., Zhong, X., Epstein, F.H., Spottiswoode, B.S., 2012. Mapping right ventricular myocardial mechanics using 3D cine DENSE cardiovascular magnetic resonance. J. Cardiovasc. Magn. Reson. 14, 4.

Braunschweig, F., Linde, C., Eriksson, M.J., Hofman-Bang, C., Ryden, L., 2002. Continuous haemodynamic monitoring during withdrawal of diuretics in patients with congestive heart failure. Eur. Heart J. 23, 59–69.

Calkins, H., 2011. Use of mouse models to evaluate novel therapeutic approaches to treatment of arrhythmogenic right ventricular cardiomyopathy the future is now. J. Am. Coll. Cardiol. 57, 751–752.

Caplin, J.L., Flatman, W.D., Dyke, L., Wiseman, M.N., Dymond, D.S., 1989. Influence of respiratory variations on right ventricular function. Br. Heart J. 62, 253–259.

Carbucicchio, C., Santamaria, M., Trevisi, N., Maccabelli, G., Giraldi, F., Fassini, G., Riva, S., Moltrasio, M., Cireddu, M., Veglia, F., Della Bella, P., 2008. Catheter ablation for the treatment of electrical storm in patients with implantable cardioverter-defibrillators: short- and long-term outcomes in a prospective single-center study. Circulation 117, 462–469.

Cohn, J.N., 1987. Role of nitrates in congestive heart failure. Am. J. Cardiol. 60, 39H–43H.

Corrado, D., Basso, C., Pavei, A., Michieli, P., Schiavon, M., Thiene, G., 2006. Trends in sudden cardiovascular death in young competitive athletes after implementation of a preparticipation screening program. JAMA 296, 1593–1601.

Corrado, D., Calkins, H., Link, M.S., Leoni, L., Favale, S., Bevilacqua, M., Basso, C., Ward, D., Boriani, G., Ricci, R., Piccini, J.P., Dalal, D., Santini, M., Buja, G., Iliceto, S., Estes 3rd, N.A., Wichter, T., McKenna, W.J., Thiene, G., Marcus, F.I., 2010. Prophylactic implantable defibrillator in patients with arrhythmogenic right ventricular cardiomyopathy/dysplasia and no prior ventricular fibrillation or sustained ventricular tachycardia. Circulation 122, 1144–1152.

Dalal, D., James, C., Devanagondi, R., Tichnell, C., Tucker, A., Prakasa, K., Spevak, P.J., Bluemke, D.A., Abraham, T., Russell, S.D., Calkins, H., Judge, D.P., 2006. Penetrance of mutations in plakophilin-2 among families with arrhythmogenic right ventricular dysplasia/cardiomyopathy. J. Am. Coll. Cardiol. 48, 1416–1424.

Ector, J., Ganame, J., van der Merwe, N., Adriaenssens, B., Pison, L., Willems, R., Gewillig, M., Heidbuchel, H., 2007. Reduced right ventricular ejection fraction in endurance athletes presenting with ventricular arrhythmias: a quantitative angiographic assessment. Eur. Heart J. 28, 345–353.

Fabritz, L., Hoogendijk, M.G., Scicluna, B.P., van Amersfoorth, S.C., Fortmueller, L., Wolf, S., Laakmann, S., Kreienkamp, N., Piccini, I., Breithardt, G., Noppinger, P.R., Witt, H., Ebnet, K., Wichter, T., Levkau, B., Franke, W.W., Pieperhoff, S., de Bakker, J.M., Coronel, R., Kirchhof, P., 2011. Load-reducing therapy prevents development of arrhythmogenic right ventricular cardiomyopathy in plakoglobin-deficient mice. J. Am. Coll. Cardiol. 57, 740–750.

Garcia-Gras, E., Lombardi, R., Giocondo, M.J., Willerson, J.T., Schneider, M.D., Khoury, D.S., Marian, A.J., 2006. Suppression of canonical Wnt/beta-catenin signaling by nuclear plakoglobin recapitulates phenotype of arrhythmogenic right ventricular cardiomyopathy. J. Clin. Invest. 116, 2012–2021.

Gehmlich, K., Asimaki, A., Cahill, T.J., Ehler, E., Syrris, P., Zachara, E., Re, F., Avella, A., Monserrat, L., Saffitz, J.E., McKenna, W.J., 2010. Novel missense mutations in exon 15 of desmoglein-2: role of the intracellular cadherin segment in arrhythmogenic right ventricular cardiomyopathy? Heart Rhythm 7, 1446–1453.

Gehmlich, K., Syrris, P., Peskett, E., Evans, A., Ehler, E., Asimaki, A., Anastasakis, A., Tsatsopoulou, A., Vouliotis, A.I., Stefanadis, C., Saffitz, J.E., Protonotarios, N., McKenna, W.J., 2011. Mechanistic insights into arrhythmogenic right ventricular cardiomyopathy caused by desmocollin-2 mutations. Cardiovasc. Res. 90, 77–87.

Gerull, B., Heuser, A., Wichter, T., Paul, M., Basson, C.T., McDermott, D.A., Lerman, B.B., Markowitz, S.M., Ellinor, P.T., Macrae, C.A., Peters, S., Grossmann, K.S., Michely, B., Sasse-Klaassen, S., Birchmeier, W., Dietz, R., Breithardt, G., Schulze-Bahr, E., Thierfelder, L., 2004. Mutations in the desmosomal protein plakophilin-2 are common in arrhythmogenic right ventricular cardiomyopathy. Nat. Genet. 36, 1162–1164.

Gomes, J., Finlay, M., Ahmed, A.K., Ciaccio, E.J., Asimaki, A., Saffitz, J.E., Quarta, G., Nobles, M., Syrris, P., Chaubey, S., McKenna, W.J., Tinker, A., Lambiase, P.D., 2012. Electrophysiological abnormalities precede overt structural changes in arrhythmogenic right ventricular cardiomyopathy due to mutations in desmoplakin-A combined murine and human study. Eur. Heart J.

Guazzi, M., Pepi, M., Maltagliati, A., Celeste, F., Muratori, M., Tamborini, G., 1995. How the two sides of the heart adapt to graded impedance to venous return with head-up tilting. J. Am. Coll. Cardiol. 26, 1732–1740.

Hauser, A.M., Dressendorfer, R.H., Vos, M., Hashimoto, T., Gordon, S., Timmis, G.C., 1985. Symmetric cardiac enlargement in highly trained endurance athletes: a two-dimensional echocardiographic study. Am. Heart J. 109, 1038–1044.

Heidbuchel, H., Hoogsteen, J., Fagard, R., Vanhees, L., Ector, H., Willems, R., Van Lierde, J., 2003. High prevalence of right ventricular involvement in endurance athletes with ventricular arrhythmias. Role of an electrophysiologic study in risk stratification. Eur. Heart J. 24, 1473–1480.

Holtz, J., Bassenge, E., Kolin, A., 1978. Hemodynamic and myocardial effects of long-lasting venodilation in the conscious dog: analysis of molsidomine in comparison with nitrates. Basic Res. Cardiol. 73, 469–481.

Iribe, G., Helmes, M., Kohl, P., 2007. Force-length relations in isolated intact cardiomyocytes subjected to dynamic changes in mechanical load. Am. J. Physiol. Heart Circ. Physiol. 292, H1487–H1497.

Kaltman, J.R., Thompson, P.D., Lantos, J., Berul, C.I., Botkin, J., Cohen, J.T., Cook, N.R., Corrado, D., Drezner, J., Frick, K.D., Goldman, S., Hlatky, M., Kannankeril, P.J., Leslie, L., Priori, S., Saul, J.P., Shapiro-Mendoza, C.K., Siscovick, D., Vetter, V.L., Boineau, R., Burns, K.M., Friedman, R.A., 2011. Screening for sudden cardiac death in the young: report from a national heart, lung, and blood institute working group. Circulation 123, 1911–1918.

Kant, S., Krull, P., Eisner, S., Leube, R.E., Krusche, C.A., 2012. Histological and ultrastructural abnormalities in murine desmoglein 2-mutant hearts. Cell Tissue Res.

Kim, D.Y., White, E., Saint, D.A., 2012. Increased mechanically-induced ectopy in the hypertrophied heart. Prog. Biophys. Mol. Biol. 110 (2–3), 331–339.

Kirchhof, P., Fabritz, L., Zwiener, M., Witt, H., Schafers, M., Zellerhoff, S., Paul, M., Athai, T., Hiller, K.H., Baba, H.A., Breithardt, G., Ruiz, P., Wichter, T., Levkau, B., 2006. Age- and training-dependent development of arrhythmogenic right ventricular cardiomyopathy in heterozygous plakoglobin-deficient mice. Circulation 114, 1799–1806.

Kraus, P.A., Lipman, J., Becker, P.J., 1990. Acute preload effects of furosemide. Chest 98, 124–128.

Krusche, C.A., Holthofer, B., Hofe, V., van de Sandt, A.M., Eshkind, L., Bockamp, E., Merx, M.W., Kant, S., Windoffer, R., Leube, R.E., 2011. Desmoglein 2 mutant mice develop cardiac fibrosis and dilation. Basic Res. Cardiol. 106, 617–633.

La Gerche, A., Burns, A.T., Mooney, D.J., Inder, W.J., Taylor, A.J., Bogaert, J., Macisaac, A.I., Heidbuchel, H., Prior, D.L., 2012. Exercise-induced right ventricular dysfunction and structural remodelling in endurance athletes. Eur. Heart J. 33, 998–1006.

Lahtinen, A.M., Lehtonen, E., Marjamaa, A., Kaartinen, M., Helio, T., Porthan, K., Oikarinen, L., Toivonen, L., Swan, H., Jula, A., Peltonen, L., Palotie, A., Salomaa, V., Kontula, K., 2011. Population-prevalent desmosomal mutations predisposing to arrhythmogenic right ventricular cardiomyopathy. Heart Rhythm 8, 1214–1221.

Li, D., Liu, Y., Maruyama, M., Zhu, W., Chen, H., Zhang, W., Reuter, S., Lin, S.F., Haneline, L.S., Field, L.J., Chen, P.S., Shou, W., 2011. Restrictive loss of plakoglobin in cardiomyocytes leads to arrhythmogenic cardiomyopathy. Hum. Mol. Genet. 20, 4582–4596.

Marcus, F.I., McKenna, W.J., Sherrill, D., Basso, C., Bauce, B., Bluemke, D.A., Calkins, H., Corrado, D., Cox, M.G., Daubert, J.P., Fontaine, G., Gear, K., Hauer, R., Nava, A., Picard, M.H., Protonotarios, N., Saffitz, J.E., Sanborn, D.M., Steinberg, J.S., Tandri, H., Thiene, G., Towbin, J.A., Tsatsopoulou, A., Wichter, T., Zareba, W., 2010. Diagnosis of arrhythmogenic right ventricular cardiomyopathy/dysplasia: proposed modification of the Task Force Criteria. Eur. Heart J. 31, 806–814.

Marcus, G.M., Glidden, D.V., Polonsky, B., Zareba, W., Smith, L.M., Cannom, D.S., Estes 3rd, N.A., Marcus, F., Scheinman, M.M., 2009. Efficacy of antiarrhythmic

drugs in arrhythmogenic right ventricular cardiomyopathy: a report from the North American ARVC Registry. J. Am. Coll. Cardiol. 54, 609–615.
Marmor, A., Krakauer, J., Schneeweiss, A., 1989. Effects of a single dose of isosorbide-5-mononitrate on the left ventricular diastolic function in systemic hypertension. Am. J. Cardiol. 63, 1235–1239.
Martin, R.R., Haines, H., 1970. Application of Laplace's law to mammalian hearts. Comp. Biochem. Physiol. 34, 959–962.
McDonald, K.M., Francis, G.S., Matthews, J., Hunter, D., Cohn, J.N., 1993. Long-term oral nitrate therapy prevents chronic ventricular remodeling in the dog. J. Am. Coll. Cardiol. 21, 514–522.
Norgett, E.E., Hatsell, S.J., Carvajal-Huerta, L., Cabezas, J.C., Common, J., Purkis, P.E., Whittock, N., Leigh, I.M., Stevens, H.P., Kelsell, D.P., 2000. Recessive mutation in desmoplakin disrupts desmoplakin-intermediate filament interactions and causes dilated cardiomyopathy, woolly hair and keratoderma. Hum. Mol. Genet. 9, 2761–2766.
Olsen, C.O., Tyson, G.S., Maier, G.W., Davis, J.W., Rankin, J.S., 1985. Diminished stroke volume during inspiration: a reverse thoracic pump. Circulation 72, 668–679.
Outhred, K.G., McKenzie, H.I., White, K.H., 1970. Some findings on the post-mortem association of right ventricular wall thickness and chronic obstructive bronchitis, pneumoconiosis, emphysema and tuberculosis. Med. J. Aust. 2, 950–954.
Pellis, T., Pausler, D., Gaiarin, M., Franceschino, E., Epstein, A., Boulin, C., Kohl, P., 2012. Off-patient assessment of pre-cordial impact mechanics among medical professionals in north-east Italy for emergency cardiac resuscitation. Prog. Biophys. Mol. Biol. 110 (2–3), 390–396.
Philips, B., Madhavan, S., James, C., Tichnell, C., Murray, B., Dalal, D., Bhonsale, A., Nazarian, S., Judge, D.P., Russell, S.D., Abraham, T., Calkins, H., Tandri, H., 2012. Outcomes of catheter ablation of ventricular tachycardia in arrhythmogenic right ventricular Dysplasia/Cardiomyopathy (ARVD/C). Circ. Arrhythm Electrophysiol.
Pilichou, K., Remme, C.A., Basso, C., Campian, M.E., Rizzo, S., Barnett, P., Scicluna, B.P., Bauce, B., van den Hoff, M.J., de Bakker, J.M., Tan, H.L., Valente, M., Nava, A., Wilde, A.A., Moorman, A.F., Thiene, G., Bezzina, C.R., 2009. Myocyte necrosis underlies progressive myocardial dystrophy in mouse dsg2-related arrhythmogenic right ventricular cardiomyopathy. J. Exp. Med. 206, 1787–1802.
Protonotarios, N., Tsatsopoulou, A., Anastasakis, A., Sevdalis, E., McKoy, G., Stratos, K., Gatzoulis, K., Tentolouris, K., Spiliopoulou, C., Panagiotakos, D., McKenna, W., Toutouzas, P., 2001. Genotype-phenotype assessment in autosomal recessive arrhythmogenic right ventricular cardiomyopathy (Naxos disease) caused by a deletion in plakoglobin. J. Am. Coll. Cardiol. 38, 1477–1484.
Sen-Chowdhry, S., Morgan, R.D., Chambers, J.C., McKenna, W.J., 2010. Arrhythmogenic cardiomyopathy: etiology, diagnosis, and treatment. Annu. Rev. Med. 61, 233–253.
Sen-Chowdhry, S., Syrris, P., Ward, D., Asimaki, A., Sevdalis, E., McKenna, W.J., 2007. Clinical and genetic characterization of families with arrhythmogenic right ventricular dysplasia/cardiomyopathy provides novel insights into patterns of disease expression. Circulation 115, 1710–1720.
Song, Z.Z., 2011. A possible diagnosis of isolated right ventricular hypertrabeculation/noncompaction in an elderly man by three-dimensional echocardiography. Int. J. Cardiol. 147, e4–e7.
Squara, P., Journois, D., Estagnasie, P., Wysocki, M., Brusset, A., Dreyfuss, D., Teboul, J.L., 1997. Elastic energy as an index of right ventricular filling. Chest 111, 351–358.
Stevenson, L.W., Zile, M., Bennett, T.D., Kueffer, F.J., Jessup, M.L., Adamson, P., Abraham, W.T., Manda, V., Bourge, R.C., 2010. Chronic ambulatory intracardiac pressures and future heart failure events. Circ. Heart Fail. 3, 580–587.
Syrris, P., Ward, D., Asimaki, A., Evans, A., Sen-Chowdhry, S., Hughes, S.E., McKenna, W.J., 2007. Desmoglein-2 mutations in arrhythmogenic right ventricular cardiomyopathy: a genotype-phenotype characterization of familial disease. Eur. Heart J. 28, 581–588.
Tandri, H., Castillo, E., Ferrari, V.A., Nasir, K., Dalal, D., Bomma, C., Calkins, H., Bluemke, D.A., 2006. Magnetic resonance imaging of arrhythmogenic right ventricular dysplasia: sensitivity, specificity, and observer variability of fat detection versus functional analysis of the right ventricle. J. Am. Coll. Cardiol. 48, 2277–2284.
Tavernier, R., Gevaert, S., De Sutter, J., De Clercq, A., Rottiers, H., Jordaens, L., Fonteyne, W., 2001. Long term results of cardioverter-defibrillator implantation in patients with right ventricular dysplasia and malignant ventricular tachyarrhythmias. Heart 85, 53–56.
van Tintelen, J.P., Entius, M.M., Bhuiyan, Z.A., Jongbloed, R., Wiesfeld, A.C., Wilde, A.A., van der Smagt, J., Boven, L.G., Mannens, M.M., van Langen, I.M., Hofstra, R.M., Otterspoor, L.C., Doevendans, P.A., Rodriguez, L.M., van Gelder, I.C., Hauer, R.N., 2006. Plakophilin-2 mutations are the major determinant of familial arrhythmogenic right ventricular dysplasia/cardiomyopathy. Circulation 113, 1650–1658.
Wichter, T., Paul, M., Wollmann, C., Acil, T., Gerdes, P., Ashraf, O., Tjan, T.D., Soeparwata, R., Block, M., Borggrefe, M., Scheld, H.H., Breithardt, G., Bocker, D., 2004. Implantable cardioverter/defibrillator therapy in arrhythmogenic right ventricular cardiomyopathy: single-center experience of long-term follow-up and complications in 60 patients. Circulation 109, 1503–1508.
Zhong, L., Gobeawan, L., Su, Y., Tan, J.L., Ghista, D., Chua, T., Tan, R.S., Kassab, G., 2012. Right ventricular regional wall curvedness and area strain in patients with repaired tetralogy of Fallot. Am. J. Physiol. Heart Circ. Physiol. 302, H1306–H1316.